

**STUDY OF RADIATION DAMAGE AND DEFECT EVOLUTION IN  
NANOSTRUCTURED METALS VIA ATOMISTIC AND MESO-SCALE  
SIMULATION TECHNIQUES**

A Dissertation  
Presented to  
The Academic Faculty

By

Daniel Vizoso

In Partial Fulfillment  
of the Requirements for the Degree  
Doctor of Philosophy in the  
School of Mechanical Engineering  
Department of Nuclear and Radiological Engineering

Georgia Institute of Technology  
Université de Paris-Saclay

December 2021

© Daniel Vizoso 2021

**STUDY OF RADIATION DAMAGE AND DEFECT EVOLUTION IN  
NANOSTRUCTURED METALS VIA ATOMISTIC AND MESO-SCALE  
SIMULATION TECHNIQUES**

Thesis committee:

Dr. Chaitanya Deo  
School of Nuclear Engineering  
*Georgia Institute of Technology*

Dr. Surya Kalidindi  
School of Mechanical Engineering  
*Georgia Institute of Technology*

Dr. Gianguido Baldinozzi  
SPMS  
*Centrale Supelec*

Dr. Laurent Capolungo  
MST-8  
*Los Alamos National Lab*

Dr. Remi Dingreville  
Center for Integrated Nanotechnologies  
*Sandia National Laboratories*

Dr. Celine Hin  
School of Materials Science and Engineer-  
ing  
*Virginia Polytechnic Institute and State  
University*

Dr. Preet Singh  
School of Materials Science and Engineer-  
ing  
*Georgia Institute of Technology*

Date approved: December 2nd, 2021



## ACKNOWLEDGMENTS

I would like to thank the members of my thesis committee for their help in preparation of this document – Remi Dingreville and Chaitanya Deo, for their assistance in the preparation of several of the presented chapters, Gianguido Baldinozzi and Vassilis Pontikis, who have helped me tremendously both in work and in life during my stay in France.

Special thanks are due to the friends and colleagues who made this work possible. Paul Burke provided frequent assistance in the preparation of any programming work. Elton Chen laid the groundwork for several of my projects, and his assistance sped up my progress considerably.

Any views and conclusions contained herein are those of the author, and do not necessarily represent the official positions, express or implied, of the funders.

The work performed in section 3.3 was supported by a public grant overseen by the French National research Agency (ANR) as part of the « Investissements d’Avenir » program, through the “ADI 2019” project funded by the IDEX Paris-Saclay, ANR-11-IDEX-0003-02.

## TABLE OF CONTENTS

<b>Acknowledgments</b>	iii
<b>List of Tables</b>	viii
<b>List of Figures</b>	xi
<b>List of Acronyms</b>	xviii
<b>Summary</b>	xx
<b>Chapter 1: Introduction and Background</b>	1
1.1 Motivation	1
1.2 Computational Approaches to Studying Radiation Damage	3
1.2.1 Molecular Statics and Dynamics	3
1.2.2 Phase Field	5
1.3 Goal and Scientific Questions	6
1.4 Dissertation Outline	7
<b>Chapter 2: Atomistic Characterization of Nano-scale Radiation-Induced Defects</b>	9
2.1 Determination of vacancy formation energies in binary UZr alloys using special quasirandom structure methods [22]	10
2.1.1 Introduction and Motivation	10

2.1.2	Methods . . . . .	14
2.1.3	Results and Discussion . . . . .	18
2.1.4	Conclusions . . . . .	24
2.2	Scaling laws and stability of nano-sized defect clusters in niobium via atomistic simulations and statistical analysis [21] . . . . .	26
2.2.1	Introduction . . . . .	26
2.2.2	Methodology . . . . .	29
2.2.3	Geometrical configurations and energetics of nano-sized defect clusters . . . . .	35
2.2.4	Conclusions . . . . .	48
<b>Chapter 3: Examination of Radiation Damage in Radiation-Tolerant Microstructures . . . . .</b>		<b>49</b>
3.1	Size-dependent radiation damage mechanisms in nanowires and nanoporous structures [24] . . . . .	50
3.1.1	Introduction . . . . .	50
3.1.2	Computational Methods . . . . .	53
3.1.3	Experimental Methods . . . . .	60
3.1.4	Results: Mechanisms of Radiation Damage Accumulation in Nanowires	61
3.1.5	Discussion: Comparison of Radiation Tolerance Between Nanowires and Nanoporous Structures . . . . .	75
3.1.6	Conclusions . . . . .	79
3.2	Impact of Radiation Damage on the Mechanical Behavior of Nanoporous Metallic Foams Studied Via Atomistic Simulation Techniques . . . . .	81
3.2.1	Introduction . . . . .	81
3.2.2	Methodology . . . . .	83

3.2.3	Results . . . . .	85
3.2.4	Conclusions . . . . .	98
3.3	Molecular Statics Investigation into the Stability of the 4H Phase of Gold at 0 K Using the EGTB Interatomic Potential . . . . .	100
3.3.1	Introduction . . . . .	100
3.3.2	LAMMPS Implementation . . . . .	101
3.3.3	Interatomic Potential Validation . . . . .	104
3.3.4	Investigation of the Stability of the 4H Hexagonal Phase in Gold . .	106
3.3.5	Conclusions . . . . .	110
 <b>Chapter 4: Computational Study of Radiation-Induced Segregation Mechanisms in Metallic Alloys . . . . .</b>		 111
4.1	Phase Field Examination of Radiation Induced Segregation in Binary Alloy Systems . . . . .	111
4.1.1	Introduction . . . . .	111
4.1.2	Phase Field Model for Radiation-Induced Segregation in Binary Al- loys . . . . .	115
4.1.3	Results . . . . .	125
4.1.4	Discussion . . . . .	137
4.1.5	Conclusions . . . . .	140
 <b>Chapter 5: Conclusions . . . . .</b>		 143
 <b>Appendices . . . . .</b>		 145
Appendix A: Appendix for Section 2.1 . . . . .		146
Appendix B: Appendix for Section 2.2 . . . . .		152

Appendix C: Appendix for Section 3.1 . . . . .	164
Appendix D: Appendix for Section 3.2 . . . . .	177
Appendix E: Appendix for Chapter 4 . . . . .	180
Appendix F: French Summary . . . . .	184
<b>References . . . . .</b>	<b>188</b>

## LIST OF TABLES

2.1	Vacancy formation energies in bcc uranium . . . . .	11
2.2	Vacancy formation energies in bcc zirconium . . . . .	11
2.3	Probability of zirconium inhabiting a number of nearest neighbor positions in U-Zr alloy . . . . .	20
2.4	Helium-vacancy cluster formation energies. First column describes the type of helium-vacancy cluster, second column provides the calculated binding energy and the third column lists values found in the literature. . . . .	46
2.5	Helium defect binding energies. NNS: nearest neighboring site; 2NNS: second nearest neighboring site. . . . .	47
3.1	Number of ROAC events inserted at each time step for various structures in both gold and niobium. . . . .	57
3.2	Material constants for the modified NRT-dpa defect production model in Equa- tion 3.1 and Equation 3.2. . . . .	59
3.3	EGTB Potential Parameters . . . . .	104
3.4	Defect Formation Energies . . . . .	105
3.5	Surface Energies ( $\text{mJ/m}^{-2}$ ) . . . . .	105
3.6	Elastic Properties . . . . .	106
3.7	4H Surface Energies . . . . .	107
3.8	Structure Cohesive Energies . . . . .	108
4.1	Comparison of existing phase field radiation-induced segregation models . .	115

A.1	Uranium vacancy formation energy in SQS and random structures . . . . .	150
A.2	Zirconium vacancy formation energy in SQS and random structures . . . . .	150
A.1	All possible nearest neighbor configurations with 4 Zr and 4 U around a vacancy . . . . .	151
B.1	Formation, $E^f$ , and binding, $E^b$ energies of defects in bulk Nb investigated via DFT in the literature. NNS: nearest neighboring site; 2NNS: second nearest neighboring site. . . . .	152
B.2	Formation, $E^f$ , and binding, $E^b$ energies of defects in Nb via MD in the literature. NNS: nearest neighboring site; 2NNS: second nearest neighboring site. . . . .	155
B.1	Supercell size ( $L$ ) and number of atoms ( $N$ ) used for point defect formation energy simulations. Supercell sizes are given in units of lattice constants. . .	157
B.2	Supercell size ( $L$ ) and number of atoms ( $N$ ) used for vacancy cluster formation energy simulations as a function of the cluster size ( $V_n$ ). Supercell sizes are given in units of lattice constants. . . . .	157
B.3	Supercell size ( $L$ ) and number of atoms ( $N$ ) used for interstitial cluster formation energy simulations as a function of the cluster size ( $I_n$ ). Supercell sizes are given in units of lattice constants. . . . .	157
B.1	Formation energies of single vacancies and vacancy clusters containing up to four vacancies. NNS: nearest neighboring site; 2NNS: second nearest neighboring site. . . . .	158
B.2	Formation energy, $E^f(V_n)$ , (in eV) for vacancy clusters as a function of the size ( $V_n$ ) for three interatomic potential tested. . . . .	158
B.3	Formation energies of self-interstitial point defects. . . . .	159
B.4	Formation energy, $E^f(I_n)$ , (in eV) of interstitial clusters as a function of the cluster size ( $I_n$ ) for three interatomic potential tested. . . . .	159
B.5	Binding energies for small vacancy clusters of up to size four. NNS: nearest neighbor site; 2NNS: second nearest neighbor site. For vacancy clusters of size three or four, results correspond to configuration (a) illustrated in Figure 2.7 (a) and Figure 2.7 (g). . . . .	161

B.6	Minimum binding energy, $E^b(V_n)$ , (in eV) for vacancy clusters as a function of the cluster size ( $V_n$ ) for three interatomic potentials. . . . .	161
B.7	Minimum, average, and maximum binding energies, $E^b(I_n)$ , (in eV) for interstitial clusters as a function of the cluster size ( $I_n$ ). . . . .	162
C.1	Diameters, lengths, and numbers of atoms in simulations of Au and Nb nanowires . . . . .	164
C.2	Structure parameters for nanoporous simulations . . . . .	165
C.3	Structure parameters for bulk simulations . . . . .	166
C.4	Material constants for the modified NRT defect production model in Equation C.4, Equation C.5, and Equation C.6 . . . . .	171
C.5	List of MD PKA simulation parameters: $E_{PKA}$ - initial energy of recoil, $N_{\text{simulation}}$ - Number of simulations performed, $L^{\text{Au}}$ - Simulation cell size in lattice units for gold, $N_{\text{atoms}}^{\text{Au}}$ - Total number of atoms within the computation domain. . . . .	171
E.1	List of General Parameters . . . . .	180
E.2	List of Elastic Parameters . . . . .	181
E.3	Parameters for ARC-DPA Equations . . . . .	182
E.4	Dislocation Parameters . . . . .	182
E.5	Coefficients for Determining Onsager Coefficients . . . . .	183



## LIST OF FIGURES

1.1	(a) Defects created by a 20 keV PKA in Cu. Simulation box is approximately 25x25x25 nm. Red atoms are hcp, white atoms are disordered. (b) Voids formed under neutron irradiation at 510° C in stainless steel to a final dose of $4.7 \times 10^{22}$ n.cm <sup>-2</sup> . (c) Stress-strain curves of iron after receiving varying neutron doses. . . . .	2
1.2	Illustration of the length and time scales associated with radiation damage and computational techniques. Taken from Deo, Chen, and Dingreville [10]	4
2.1	Plots of the vacancy formation energy for the removal of zirconium calculated for SQS and random structures of U-Zr alloy ranging from 0% to 100% U. Bars represent the standard deviation in the measured vacancy formation energies. . . . .	18
2.2	Plots of the vacancy formation energy for the removal of uranium calculated for SQS and random structures of U-Zr alloy ranging from 0% to 100% U. Bars represent the standard deviation in the measured vacancy formation energies. . . . .	19
2.3	Plots of the vacancy formation energy for removing a: (a) zirconium and (b) uranium atom from a U-10%Zr alloy. Each data point represents a vacancy formation energy for a particular configuration of Zr atoms in the nearest neighbor sites as specified by the x-axis position. . . . .	21
2.4	Configuration $E_v$ of zirconium vacancies for different atom percentages . . .	22
2.5	Configuration $E_v$ of uranium vacancies for different atom percentages . . .	23
2.6	Survey of (a) formation ( $E^f$ ) and (b) binding ( $E^b$ ) energies for small vacancy clusters. (c) Survey of formation energies of self-interstitial atoms in different configurations. References are marked in parenthesis, with hollow symbols denoting MD simulation results, and solid symbols denoting DFT simulation results. . . . .	28

2.7	(a)–(f): Tri-vacancy configurations. (g)–(j): Tetra-vacancy configurations. White spheres represent niobium atoms, and blue spheres represent vacancies. Sub-letter by each configuration corresponds to its formation energy in Table B.1 in Appendix B section B.3. . . . .	35
2.8	Predicted minimum energy vacancy (top row) and interstitial (bottom row) cluster configurations with fifty vacancies/interstitials for all three interatomic potential tested. Left to right: structures obtained from the Johnson ((a) and (d)), Ackland ((b) and (e)) and Fellingner ((c) and (f)) potentials. In (a)–(c), atoms on the surface of the vacancy void are illustrated with white balls and surfaces of the cavities are rendered with blue surfaces. In (d)–(f), green dislocation segments correspond to $1/2\langle 111 \rangle$ dislocations, magenta dislocation segments correspond to $\langle 100 \rangle$ dislocations. . . . .	37
2.9	Formation energies for (a) vacancy and (b) interstitial cluster defects as a function of cluster size. Triangle, square and circle symbols correspond to the Johnson, Ackland and Fellingner interatomic potentials respectively. . . .	38
2.10	Binding energies for (a) vacancy and (b) interstitial cluster defects as a function of cluster size. Triangle, square and circle symbols correspond to the Johnson, Ackland and Fellingner interatomic potentials respectively. . . .	41
2.11	(a) Normalized formation energies per (a) vacancy ( $E^f/V_n$ ) and per (b) interstitial ( $E^f/I_n$ ) as a function of the binding energy for all cluster sizes simulated. Triangle, square and circle symbols correspond to the Johnson, Ackland and Fellingner interatomic potentials respectively. . . . .	42
2.12	RDFs of interstitial clusters containing 25 interstitials produced using the (a) Johnson, (b) Ackland, and (c) Fellingner potentials, from left to right. RDFs have been smoothed using a Gaussian filter. . . . .	43
2.13	Parity plots shown for the linear models of actual versus predicted formation ((a)–(c)) and binding ((d)–(f)) energies produced using the Johnson ((a) and (d)), Ackland ((b) and (e)), and Fellingner ((c) and (f)) interatomic potentials for Nb. . . . .	44
2.14	(a) Formation and (b) vacancy binding energies of a helium-vacancy cluster as a function of cluster size and helium-to-vacancy ratio ( $n/m$ ). Triangle, square and filled circle symbols correspond to $n/m = 1/2, 2, 4$ respectively. . . .	47

3.1	(a)-(b) Examples of structure types considered in this work. The nanowire represented in (a) has a diameter of 10 nm. The nanoporous structure in (b) has an average ligament size of 12 nm. Structures displayed in (a) and (b) correspond to renders after irradiation. (c) Primary recoil spectrum used from sampling recoil energies in the consecutive cascade simulations and accelerated radiation-damage accumulation simulations. . . . .	55
3.2	(a) Number of atoms sputtered in 3-nm gold and niobium nanowires due to a single 3 keV cascade initiated at a random distance from the surface. Error bars show the standard deviation around the average value. (b) Fraction of atoms sputtered in 3nm gold and niobium nanowires as a function of the number of consecutive cascades. Almost 20% of the atoms are sputtered off the nanowires after only 100 cascades. Equivalent damage levels (measured in dpa) are indicated for 50 and 100 consecutive cascades. Gold and niobium data are represented with circle and square symbols respectively. .	62
3.3	Evolution of defect accumulation after multiple consecutive cascades in 3-nm gold and niobium nanowires. (a) and (d) After 10 cascades, (b) and (e) after 50 cascades, and (c) and (f) after 100 cascades. White atoms represent disordered structures and red atoms denote atoms in the HCP configuration. Blue atoms are identified as BCC. Lattice atoms are not shown. . . . .	63
3.4	Defect structures in 30-nm gold and niobium nanowires at various damage levels (measured in dpa): (a) and (d) 0.1 dpa; (b) and (e) 0.5 dpa; and (c) and (f) 1.0 dpa. White atoms represent disordered structures and red atoms denote atoms in the HCP configuration. Lattice atoms are not shown. . . .	65
3.5	Evolution of point defect concentration ((a) and (b)) and dislocation density ((c) and (d)) as a function of the damage level (measured in dpa) in gold and niobium nanowires of different sizes. . . . .	66
3.6	Evolution of the dislocation density in 30-nm (a) gold and (b) niobium nanowires as a function of the damage level (measured in dpa). Superimposed images show the dislocation structures at 0.001 dpa (A inset), 0.01 dpa (inset B), 0.5 dpa (inset C), and 1.0 dpa (inset D). . . . .	67
3.7	Dose transition from a mechanism of defect accumulation to defect saturation for both gold (circle symbol) and niobium (square symbol) nanowires as a function of the diameter of the nanowire. . . . .	69
3.8	Defect structures in 10-nm gold nanowires at various damage levels (measured in dpa): (a) 0.1 dpa; (b) 0.5 dpa; and (c) 1.0 dpa. White atoms represent disordered structures and red atoms denote atoms in the HCP configuration. Lattice atoms are not shown. . . . .	70

3.9	Mechanism of motion of $1/6\langle 112 \rangle$ Shockley dislocation along $\{111\}$ planes leading to FCC-to-HCP phase transformation: (a) state prior occurrence of $1/6\langle 112 \rangle$ Shockley dislocation. (b) Motion of $1/6\langle 112 \rangle$ Shockley dislocation along $\{111\}$ plane. (c) Stacking fault merging with adjacent stacking faults. White atoms represent disordered structures and red atoms denote atoms in the HCP configuration. Lattice atoms are not shown. Green dislocation line corresponds to $1/6\langle 112 \rangle$ Shockley dislocations. . . . .	71
3.10	Evolution of the HCP phase fraction as a function of the damage level (measured in dpa) in gold nanowires of different sizes. . . . .	72
3.11	Point defect concentration (vacancies and interstitials) formed in Au and Nb 20-nm nanowires due to a single cascade at different recoil energies as a function of the distance between the initial location of the PKA and the free surface. Error bars show the standard deviation around the average values. . . . .	73
3.12	Defect structures at 0.10 dpa in a single crystal ((a) and (d)), and in the vicinity of a ligament within a nanoporous structure ((b) and (e)) in gold and niobium, as predicted from the atomistic simulations. White atoms represent disordered structures, and red atoms represent HCP atoms. Lattice atoms are not shown. (c) and (f) show corresponding TEM images of gold and niobium nanoporous structures respectively. . . . .	74
3.13	(a) Experimental characterization of radiation damage in nanoporous gold irradiated with 1.7 MeV $\text{Au}^{3+}$ ions to 18.6 dpa (fluence $5.49 \cdot 10^{14}$ ions/cm <sup>2</sup> ). (b) Real-time TEM observations of the damage evolution in nanoporous niobium, irradiated with 1.7 MeV $\text{Au}^{3+}$ ions for 40 s. . . . .	76
3.14	(a)-(b): Evolution of dislocation density as a function of the damage level (measured in dpa) in gold and niobium nanostructures. . . . .	78
3.15	Stress-strain curves for pristine gold and niobium nanowires under tension and compression. Wire diameters are provided in the legends. . . . .	86
3.16	Images of 10 nm nanowires pre and post yielding under tension. Atoms are colored according to lattice type: blue is BCC, green is FCC, red is HCP, and white is disordered. . . . .	87
3.17	Images of 10 nm nanowires pre and post yielding under compression. Atoms are colored according to lattice type: blue is BCC, green is FCC, red is HCP, and white is disordered. . . . .	89

3.18	Stress-strain curves for irradiated gold and niobium nanowires with diameters of 10 nm under tension and compression. Dose levels are provided in the legends. . . . .	90
3.19	Stress-strain curves for irradiated gold and niobium nanowires with diameters of 40 nm under tension and compression. Dose levels are provided in the legends. . . . .	91
3.20	Cross-section of a 40 nm diameter niobium nanowire irradiated to a dose of 0.11 dpa under compression. Atoms have been made semi-transparent and are colored according to their structure: blue is BCC, white is disordered. Dislocations are colored according to their type: green is $\frac{1}{2} \langle 111 \rangle$ , magenta is $\langle 100 \rangle$ . The current applied strain to the nanowire is shown in the caption of each image. . . . .	93
3.21	Renders of a 30 nm diameter niobium nanowire irradiated to a dose of 0.50 dpa under tension. Atoms are colored according to their structure: blue is BCC, white is disordered. Dislocations are colored according to their type: green is $\frac{1}{2} \langle 111 \rangle$ , magenta is $\langle 100 \rangle$ . The current applied strain to the nanowire is shown in the caption of each image. . . . .	94
3.22	SFT found in a 20 nm diameter gold nanowire irradiated to a dose of 0.5 dpa under compression. Lattice atoms have been removed, with the atoms shown being HCP. Dislocations are colored according to their type: green is $\frac{1}{2} \langle 111 \rangle$ , magenta is $\langle 100 \rangle$ . The current applied strain to the nanowire is shown in the caption of each image. . . . .	96
3.23	Stress-strain plot and renders of a 20 nm diameter gold nanowire irradiated to a final dose of 0.05 dpa under tension. In the renders, only HCP atoms are shown in red. Dislocations are colored according to their type: green is $\frac{1}{2} \langle 111 \rangle$ , magenta is $\langle 100 \rangle$ . . . . .	97
3.24	Cross-section images of a 10 nm gold nanowire at 1 dpa under compression. Applied strain is shown in the caption of each image. Atoms are colored by structure type: green is FCC, red is HCP, white is disordered. . . . .	98
3.25	Cross-section images of a 10 nm gold nanowire at 1 dpa under tension. Applied strain is shown in the caption of each image. . . . .	99
3.26	Renders of a 2x6 nm 4H hexagonal phase gold nanoribbon. Lattice orientations are provided for each image. . . . .	107
3.27	Plots of the calculated cohesive energy for spheres with different radii. The x axis represents the ratio of the surface area to the solid volume of the sphere, and is equivalent to three divided by the radius. . . . .	109

4.1	Plot of point defect concentrations as a function of dose for three different dose rates. The legend for (c) describes the marks for (a) and (b). . . . .	127
4.2	Plot of the total defect cluster concentration (i.e., the sum of the concentrations of vacancy clusters and interstitial clusters) for simulations with different dose rates. . . . .	128
4.3	Plot of the fraction of solute trapped at segregation sites. Segregation sites are nodes where the concentration of the solute is greater than 0.25%, which is the maximum initial concentration. . . . .	129
4.4	Plots of the concentration of the solute species at three different dose levels for simulations with different dose rates. . . . .	131
4.5	Plot of point defect concentrations as a function of dose for three different dose rates in systems containing a dislocation. The legend for (c) describes the marks for (a) and (b). . . . .	132
4.6	Plot of the fraction of solute trapped at segregation sites for simulations containing dislocations. Segregation sites are nodes where the concentration of the solute is greater than 0.25%, which is the maximum initial concentration. . . . .	133
4.7	Plots of the concentration of the solute species at three different dose levels for simulations with dislocations and different dose rates. . . . .	135
4.8	Plot of the fraction of solute trapped at segregation sites for simulations with varying grid sizes. Segregation sites are nodes where the concentration of the solute is greater than 0.25%, which is the maximum initial concentration. . . . .	136
4.9	Plot of point defect concentrations as a function of dose for two different damage insertion methods at a dose rate of 1 dpa/month ( $3.858\,02 \times 10^{-7}$ dpa/s)	138
4.10	Plot of the total defect cluster concentration for simulations irradiated using Frenkel pair insertion. . . . .	139
4.11	Plot of the fraction of solute trapped at segregation sites for simulations irradiated using Frenkel pair insertion. Segregation sites are nodes where the concentration of the solute is greater than 0.25%, which is the maximum initial concentration. . . . .	140

C.1	Examples of defect structures left behind in the core region of Au and Nb nanowires, 50 ps after the initiation of a 3 keV PKA event. Red atoms are HCP, and white atoms are disordered atoms. . . . .	174
C.2	Evolution of defect accumulation after multiple consecutive cascades in small FCC Au nanowires. (a) After 10 cascades, (b) after 50 cascades, and (c) after 100 cascades. . . . .	175
C.3	Evolution of defect accumulation after multiple consecutive cascades in small BCC Nb nanowires. (a) After 10 cascades, (b) after 50 cascades, and (c) after 100 cascades. . . . .	176
D.1	Stress-strain curves for irradiated gold and niobium nanowires with diameters of 14 nm under tension and compression. Dose levels are provided in the legends. . . . .	177
D.2	Stress-strain curves for irradiated gold and niobium nanowires with diameters of 20 nm under tension and compression. Dose levels are provided in the legends. . . . .	178
D.3	Stress-strain curves for irradiated gold and niobium nanowires with diameters of 30 nm under tension and compression. Dose levels are provided in the legends. . . . .	179

## LIST OF ACRONYMS

<b>ARC</b>	Athermal-Recombination-Corrected
<b>ATAT</b>	Alloy Theoretic Automated Toolkit
<b>BCC</b>	Body Centered Cubic
<b>CD</b>	Cluster Dynamics
<b>CNA</b>	Common Neighbor Analysis
<b>DD</b>	Dislocation Dynamics
<b>DFT</b>	Density Functional Theory
<b>dpa</b>	Displacements per Atom
<b>DXA</b>	Dislocation Extraction Analysis
<b>EAM</b>	Embedded Atom Method
<b>EGTB</b>	Electron-Gas-Tight-Binding
<b>FCC</b>	Face Centered Cubic
<b>FP</b>	Frenkel pair
<b>HCP</b>	Hexagonal Close-Packed
<b>kMC</b>	Kinetic Monte Carlo
<b>LAMMPS</b>	Large-scale Atomic/Molecular Massively Parallel Simulator
<b>MD</b>	Molecular Dynamics
<b>MEAM</b>	Modified Embedded Atom Method
<b>MS</b>	Molecular Statics
<b>NRT</b>	Norgett-Robinson-Torrens
<b>PC</b>	Principal Component
<b>PCA</b>	Principal Component Analysis



**PKA** Primary Knock-on Atom  
**RDF** Radial Distribution Function  
**RIS** Radiation-Induced Segregation  
**ROAC** Reduced-Order Accelerated Cascade  
**rpa** Replacements per Atom  
**SFT** Stacking Fault Tetrahedra  
**SIA** Self Interstitial Atom  
**SQS** Special Quasirandom Structures  
**SRIM** Stopping and Range of Ions in Matter  
**TEM** Transmission Electron Microscopy  
**ZBL** Ziegler-Biersack-Littmark

## SUMMARY

The ultimate intent of this dissertation is to use computational techniques to explore the atomistic mechanisms and characteristics of radiation damage formation, and how these properties and behaviors contribute to the radiation tolerance of nanostructured materials. The need for materials that can withstand radiation environments for extended periods of time has increased as we have developed more advanced nuclear technologies. Both experiments and computational simulations have shown that nanostructured materials with high densities of defect sinks such as grain boundaries or free surfaces have enhanced radiation tolerance, being able to withstand high radiation doses without accumulating radiation damage in the same ways as conventionally structured materials. In order to understand the mechanisms by which these materials exhibit radiation tolerance, as well as to be able to predict how these materials will evolve in time when exposed to a radiation environment, thorough characterization of the properties, formation behavior, and accumulation behavior of radiation damage is necessary. To that end, we have used computational techniques to study radiation damage across the range of length- and time-scales within which it develops, with an emphasis on considering the impact that microstructure and defect configuration have on the formation and evolution of radiation damage.

We began with an examination of the properties of radiation-induced defects. In uranium-zirconium alloy, we examined how both the arrangements of the atoms within the lattice as well as the composition of the alloy impacted the value of the vacancy formation energy. Vacancies are one of the two fundamental point defects produced under irradiation, and they play a significant role in the evolution of materials under irradiation due to the importance of vacancies in the process of diffusion. Through this study, we observed how basic material properties can be very sensitive to small changes in local atomic configurations and showed the importance of considering both alloy composition and local atomic configuration when characterizing material properties in alloys.

We then examined how the properties of defect clusters varied with the size of the cluster as well as the configuration of the cluster in pure niobium. Previous studies of the properties of defect clusters have primarily focused on the ground state properties of such clusters, and have explored a limited range of cluster sizes. In systems under dynamic or non-equilibrium conditions such as systems at temperature or systems under irradiation, there is a high likelihood that some defects may not be in their ground state configuration. Therefore, the primary goal of this study was to examine how the properties of defect clusters, such as formation and binding energies, varied with both the size and the configuration of the cluster, and found that non-ground state configurations can be thermally stable depending on the configuration.

Moving from the study of defect properties, we then performed a study of the mechanisms of radiation damage accumulation in nanoporous niobium and gold. Nanoporous structures have very high surface-to-volume ratios where the free surfaces are able to serve as perfect sinks for any radiation damage that is produced within the solid volume of the structure. In this study, we examined how the length-scale of the nanoporous structure impacted the accumulation mechanisms of radiation damage, and observed a strong size effect where nanoporous systems with the correct length scale for the irradiation conditions would display a degree of radiation tolerance. We also observed size-dependent damage mechanisms where systems with certain size characteristics would experience unique changes to their microstructure. We then followed this study with an examination of how the mechanical behavior of these nanoporous systems were effected by the irradiation process. We found that, while nanoporous systems may be resistant to the accumulation behavior of radiation damage in conventional materials, there was an effect on the mechanical response of nanoporous structures due to the damage to the surfaces within the nanostructure as well as the formation of various radiation-induced defects within the ligaments and the nodes of the structures. Therefore, while radiation may not affect these materials in the same way that it affects conventionally structured materials, it does have an impact on the

microstructure that can adversely effect the materials properties.

We then focused on the computational technique of molecular dynamics, and worked on the implementation and validation of the newly developed EGTB interatomic potential into the molecular dynamics code LAMMPS. Interatomic potentials control the accuracy of molecular dynamics simulations, and it is of vital importance that proper care is taken when selecting an interatomic potential to ensure that the features of the intended simulation will be properly reproduced by the chosen potential. The EGTB potential is capable of accurately predicting surface energies, fundamental defect characteristics, and material phonon behavior, making it an ideal interatomic potential for the simulation of complex microstructures under highly non-equilibrium conditions, such as nanostructured materials under irradiation.

Finally, we provide an example of how atomistically-determined characteristics of radiation damage can be used by proposing a phase field model for radiation-induced segregation. Phase field techniques use coupled partial differential equations to simulate the spatio-temporal evolution of species, where the interactions between the species are described via rate terms. The proposed model allows for the study of how material properties as well as radiation conditions impact the development of radiation-induced segregation, a degradation process in which the homogeneously mixed elements in an alloy begin to separate, which can drastically impact the mechanical properties of the material. This model was used to study how radiation conditions such as dose rate and incident particle type impact the development of radiation-induced segregation.

# CHAPTER 1

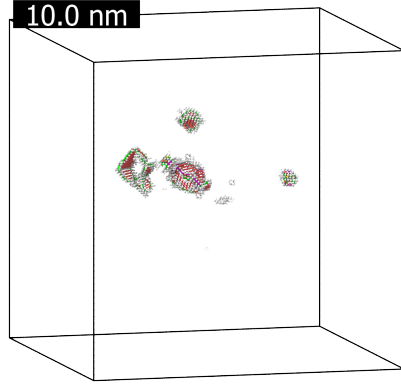
## INTRODUCTION AND BACKGROUND

### 1.1 Motivation

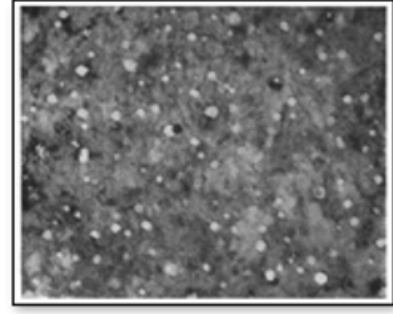
It is well understood that materials exposed to radiation fields experience significant changes to their microstructures through the formation of defects [1–5]. When incident radiation interacts with the atoms within a material, some particles (known as Primary Knock-on Atom (PKA)) are displaced from their lattice positions and are given some kinetic energy. As these energetic particles move, they displace additional atoms, resulting in the formation of collision cascades. These cascades grow until the particles lack the energy required to displace additional atoms, after which the remaining kinetic energy is dissipated to the rest of the material through thermal oscillation. Radiation-induced defects are left behind in the lattice after collision cascades, which can range in size from point defects to defect clusters depending on the energy of the incident radiation. An example of the defect structure produced by a single damage event with an energy of 20 keV is shown in Figure 1.1a. These damage events typically evolve over the course of tens of picoseconds, with length-scales on the order of nanometers.

As the amount of radiation damage accumulates within a material due to consecutive events, networks of larger defect structures can form, such as the network of voids seen in Figure 1.1b. Consecutive damage events can also induce certain radiation-induced degradation mechanisms, such as segregation in alloys as well as amorphization or phase transformations. Such processes can develop over the course of microseconds to days depending on the material and the irradiation conditions, with the length-scales of such processes typically being on the order of hundreds of nanometers to hundreds of micrometers.

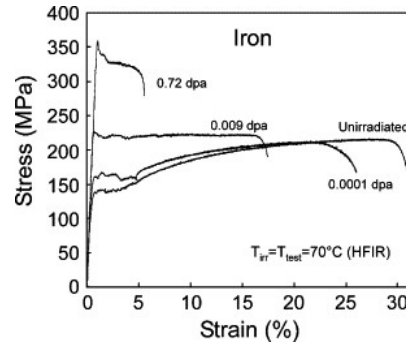
Continued exposure to radiation damage can eventually lead to the degradation pro-



(a)



(b) Image taken from Cawthorne and Fulton [8]



(c) Image taken from Eldrup et al. [9]

Figure 1.1: (a) Defects created by a 20 keV PKA in Cu. Simulation box is approximately 25x25x25 nm. Red atoms are hcp, white atoms are disordered. (b) Voids formed under neutron irradiation at 510° C in stainless steel to a final dose of  $4.7 \times 10^{22} \text{ n.cm}^{-2}$ . (c) Stress-strain curves of iron after receiving varying neutron doses.

cesses that significantly alter the performance of the material, such as low temperature radiation hardening and embrittlement, radiation-induced and -modified solute segregation and phase stability, irradiation creep, void swelling, and high-temperature helium embrittlement [3, 6]. Depending on the material and the irradiation conditions, such degradation processes develop over the course of seconds to years, and on length-scales rangin from centimeters to meters. These degradation mechanisms can result in accelerated corrosion when the material is in a corrosive environment [7], or result in premature failure of the component due to changes in its mechanical response, as illustrated in Figure 1.1c.

Therefore, it is imperative that materials that are to be used in radiation environments must have some means of either reducing the amount of damage that forms due to irradi-

ation or a means to annihilate those defects before they are able to coalesce and change the properties of the material. This need is even greater for materials that will be used in advanced nuclear systems such as Gen IV fission reactors, fusion reactors, or for space applications, where materials must be able to withstand higher radiation doses than are seen in currently operating nuclear reactors [3].

## **1.2 Computational Approaches to Studying Radiation Damage**

To ensure that material selection or design is able to meet the needs of advanced nuclear systems, it is imperative that the mechanisms by which radiation damage is produced are well understood. It is also important to understand how the damage that is produced impacts the aging of the material over its life-cycle. While the impact of radiation damage on materials can be examined via experiment, characterization of the properties of defect formation as well as the properties of the defects themselves must predominately be done at the atomistic scale using computational techniques. There exists a number of different atomistic simulation techniques, each with their own strengths and weaknesses. These computational techniques are tuned to explore different length and time-scales, as shown in Figure 1.2. In this dissertation, two computational techniques were employed: molecular statics/dynamics, and phase field simulations.

### 1.2.1 Molecular Statics and Dynamics

Classical Molecular Statics (MS) or Molecular Dynamics (MD) are frequently used computational tools for the simulation of condensed matter and molecules [11, 12]. In classical MS and MD, atoms or molecules are treated as point masses and their spatio-temporal evolution is determined through the solution of Newton's equations of motion[13–15]. The physics of the interactions between individual atoms is contained within an interatomic potential energy function, which must be uniquely developed for specific material systems [16, 17].

These interatomic potentials can vary significantly in their complexity, with the two general categories of potentials being pair-wise potentials and many-body potentials. An example of a pair-wise potential would be the Lennard-Jones potential [18], which is shown in the following equation,

$$U(r) = 4\epsilon \left[ \left( \frac{\sigma}{r} \right)^{12} - \left( \frac{\sigma}{r} \right)^6 \right]. \quad (1.1)$$

In this expression,  $\sigma$  and  $\epsilon$  are fitting parameters, and  $r$  is the distance between atom pairs. Since this equation is only a function of individual interatomic distances, it can be computed by iterating through the list of all atom pairs. Many-body potentials such as the Modified Embedded Atom Method (MEAM) [19] or Electron-Gas-Tight-Binding (EGTB) [20] potentials introduce terms where operations are performed on the sum of all of the atoms pair-wise interactions. Therefore, when computing potential energies and forces using many-body potentials, one must iterate through every atom individually rather than being able to iterate through the list of atom pairs. The derivatives of the potential energy curves provide the forces between atoms, which can be repulsive or attractive depending on the distance between the two atoms and the shape of the potential energy curve.

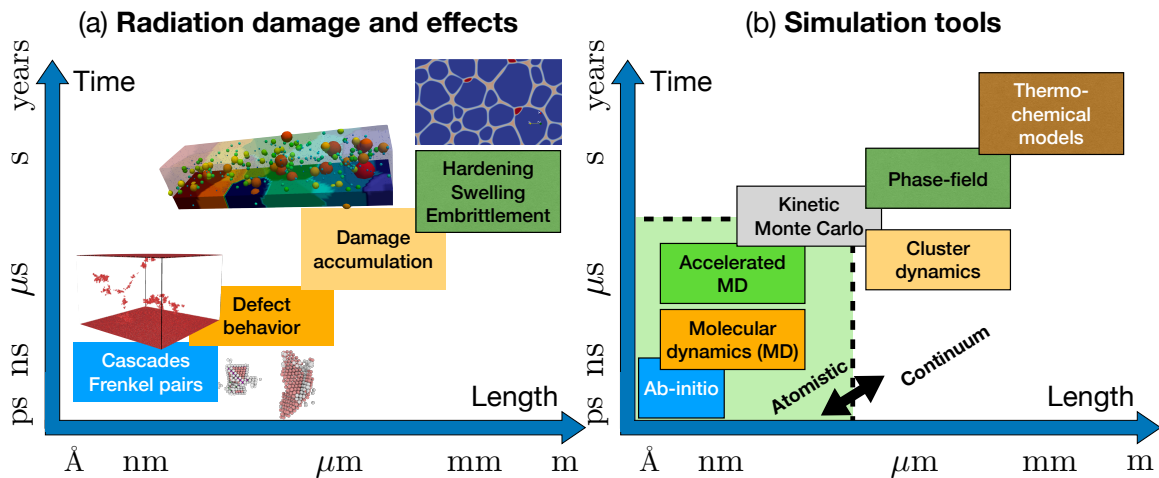


Figure 1.2: Illustration of the length and time scales associated with radiation damage and computational techniques. Taken from Deo, Chen, and Dingreville [10]



Additional discussion on the MEAM potential format is provided in Appendix A, and a discussion on the EGTB potential is provided in the final section of Chapter 3.

Molecular statics simulations involve the solving of the interatomic potential energy function for a particular configuration of atoms without considering atomic motion. Such simulations are typically paired with a minimum energy search function, which gradually adjusts atomic positions until a minimum energy configuration has been found. Together, these techniques can be used for the measurement and evaluation of a material's ground-state properties, including parameters such as lattice constants, defect formation energies, and migration barriers [21, 22].

Molecular dynamics simulations introduce to molecular statics the evolution of atomic positions in time based off of interatomic forces, allowing for the examination of temperature dependant properties or the evaluation of how a material system evolves during dynamic processes. Materials at temperature are modelled by applying a Boltzmann distribution of velocities to the atoms and evolving the system in time via Newton's equations of motion. MD simulations allow for the study of dynamic atomistic processes, such as radiation damage cascades [23], the accumulation of radiation damage due to consecutive events [23, 24], mechanical loading [25, 26], and many more.

### 1.2.2 Phase Field

The phase-field method is a continuum method approach to modeling and predicting meso-scale material morphology and microstructural evolution in non-equilibrium conditions [27–29]. In this method, the microstructure is described as a set of conserved or non-conserved field variables that are themselves continuous across the described system. These fields are evolved in time and space using the Cahn-Hilliard nonlinear diffusion equation and the Allen-Cahn relaxation equation, or versions of these equations that have been modified to capture unique physics. With the thermodynamic and kinetic information of specific material systems, it is possible to predict the evolution of arbitrary microstructures through com-

plex processes such as solidification, phase transformation, grain growth, vapor-deposition, and surface corrosion [27, 30]. Being a meso-scale technique, phase field simulations must be connected to the material systems that they seek to simulate through material parameters that are used in the partial differential equations.

### 1.3 Goal and Scientific Questions

Atomistic techniques such as molecular statics and dynamics are inherently limited to small simulation sizes (several hundred atoms for very large Density Functional Theory (DFT) simulations and hundreds of millions of atoms for very large MD simulations [24]) and very short time scales (on the order of tens of nanoseconds for typical dynamics simulations [24] and microseconds for very long dynamics simulations, such as simulations of protein folding [31, 32]). Recent advances in coarse-grained simulation techniques (such as phase field methods) allow for the simulation of materials over more engineering-relevant length- and time-scales, yet they require accurate quantification and parameterization of intrinsic thermodynamic quantities in order to predict the spatiotemporal evolution of the material [21, 23].

Therefore, the central goal of this dissertation is:

- **To examine the formation and accumulation behavior of radiation damage in various materials in order to understand the fundamental mechanisms that allow for some microstructures to be radiation tolerant.**

To accomplish this goal, both atomistic and continuum scale computational techniques will be employed to probe the varying time and length scale phenomena associated with the formation and accumulation of radiation damage.

In addressing this goal, we seek to examine a series of scientific questions about the relationship between the microstructure of a material and the formation and accumulation of radiation damage. Starting at the atomistic scale, the first question is:

**Q1** How does local atomic arrangement impact the formation and accumulation behavior of radiation-induced defects?

Through an examination of the impact that local atomic arrangement has on defect properties, we can gain a better understanding of how defects will form and accumulate in various materials. Expanding the consideration from isolated defects to defect accumulation leads to the second question:

**Q2** What does defect formation and evolution look like in a radiation-tolerant material?

An atomistic examination of defect accumulation in a material that has experimentally been observed to be radiation tolerant will allow us observe the fundamental mechanisms that contribute to this tolerance, as well as allow us to explore how this tolerance evolves with continued damage. Continuing to increase the time and length scale considered, the third question becomes:

**Q3** How do defect characteristics affect continuum scale models of radiation-induced degradation mechanisms, such as radiation induced segregation?

Using our understanding that we have gained from addressing the first two questions, we will present a case study of how atomistic-scale characteristics of defect formation can be used to model processes that can't be probed directly using atomistic methods.

## **1.4 Dissertation Outline**

In the following chapters, we will be discussing various tasks that address the ultimate goal of understanding defect formation and accumulation and their relationship with material degradation. These chapters are ordered such that each chapter considers a regime of radiation damage formation and accumulation that has increased in length and time scale. Due to the wide range of computational techniques employed in the various tasks described in this dissertation, each chapter will have their own methods sections describing the specific implementations of those techniques.

In Chapter 2, two studies of the impact of local atomic configuration on the formation and growth properties of radiation-induced defects are provided. The first study (section 2.1) examines how a fundamental defect property (the energy required to form a vacancy) depends on the local arrangement of atoms in a U-Zr binary alloy [22]. The second study (section 2.2) examines how defect properties change in niobium as the size and configuration of those defects change [21].

In Chapter 3, two studies are presented that examine radiation damage accumulation in a radiation-tolerant material. The first study (section 3.1) examines the mechanisms behind the radiation tolerance of nanoporous gold and niobium [24]. The second study (section 3.2) continues from the previous study and examines how the accumulation of radiation damage impacts the mechanical behavior of nanoporous gold and niobium under compressive and tensile loading. Finally, in section 3.3 we discuss the implementation and validation of a recently developed interatomic potential into the frequently used molecular dynamics code Large-scale Atomic/Molecular Massively Parallel Simulator (LAMMPS), and provide a case-study of its use in examining the stability of the 4H hexagonal phase in gold.

Chapter 4 presents a phase field study of Radiation-Induced Segregation (RIS) in a binary alloy. This study focuses on how the conditions of irradiation, including dose rate and incident radiation type, can impact the onset and evolution of RIS, while also considering how pre-existing microstructural defects can alter this behavior. The proposed model serves as an example of how meso-scale simulation techniques are informed by the characterization of radiation-induced damage performed using atomistic techniques.

Finally, the concluding remarks of this dissertation are provided in Chapter 5.

## **CHAPTER 2**

### **ATOMISTIC CHARACTERIZATION OF NANO-SCALE RADIATION-INDUCED DEFECTS**

In this chapter, we seek to address the first question posed in Chapter 1,

**Q1** How does local atomic arrangement impact the formation and accumulation behavior of radiation-induced defects?

To address this question, we have first examined how a fundamental defect property, such as the vacancy formation energy, can be impacted by the configuration of atoms in their nearest neighbor sites in an alloy using as an example the uranium-zirconium alloy system. This study sought to provide a methodology to address the shortcoming that is typically seen in atomistic evaluations of defect properties in alloys, where only an ensemble average or minimum value is provided without providing the context of the full distribution.

Then, we examined how the formation and binding energies of vacancy and interstitial clusters change with the size of the cluster as well as the configuration of the cluster. Similar to the objective of the previous study, this study sought to provide a methodology for including the consideration of defect configuration when characterizing the properties of clusters of radiation induced defects.

Through these two studies, we have shown how the material properties that influence the formation of radiation damage can vary significantly within a material depending on the local atomic environment. With careful consideration of elemental arrangement and the local microstructure, it should be possible to design materials that are more resistant to the formation and accumulation of radiation damage. These findings are presented in such a way that they can be deployed as input parameters in meso-scale simulation techniques.

## 2.1 Determination of vacancy formation energies in binary UZr alloys using special quasirandom structure methods [22]

### 2.1.1 Introduction and Motivation

The use of predictive models to examine defect production and migration in metallic systems requires a thorough understanding of the energetics of defect formation and migration. In fully miscible alloys, atomistic properties are heavily dependent on local atomic configurations, and can vary significantly across the volume of even a homogeneous alloy mixture. One such atomistic property is the vacancy formation energy ( $E_v^f$ ), which is a very important material property that is frequently required for continuum and Monte Carlo simulations of materials [28, 29, 33]. It plays a significant role in governing the diffusion and formation of point defects in materials, and must accurately be parameterized for the specific material system to allow for representative simulations. In alloy systems, such as the U-Zr alloy system examined in this work, the vacancy formation energy is a function of local atomic arrangement and must be tracked separately for the two species, since continuum methods such as phase field or Monte Carlo methods must track which species is removed to form the defect. The  $E_v^f$  for elemental uranium has been explored extensively in both experiments and computational calculations, with a mono-vacancy formation energy of  $1.20 \pm 0.25$  eV being reported by Matter, Winter, and Triftshäuser [34].  $E_v^f$  in Zr metal has not been studied as extensively, with different authors reporting values over a large range of energies (1.68 eV by Korzhavyi et al. [35] and 2.1 eV by Le Bacq, Willaime, and Pasturel [36]). Additional reported values for  $E_v^f$  in elemental uranium and zirconium are provided in Table 2.1 and Table 2.2.

For this work, the MEAM interatomic potential for U-Zr developed by Moore et al. [37] was used. This potential was developed to simulate  $\gamma$ -U-Zr alloys at operational temperatures. The uranium portion of this potential was designed to recreate the properties of  $\gamma$ -phase uranium at high temperatures, but was also fit to the elastic properties and lattice

Table 2.1: Vacancy formation energies in bcc uranium

Date	Reference	Method	Vacancy Formation Energy (eV)
2017	Current Work	MEAM	1.34
2015	[37]	MEAM	1.16
2013	[38]	DFT	1.38
2013	[39]	EAM	2.2-3.0
2011	[40]	EAM	1.52
2012	[16]	MEAM	1.61
2008	[41]	DFT	1.08
1980	[34]	PAS	$1.20 \pm 0.25$

Table 2.2: Vacancy formation energies in bcc zirconium

Date	Reference	Method	Vacancy Formation Energy (eV)
2017	Current Work	MEAM	2.074
2015	[37]	DFT-PBE	1.8
2015	[37]	MEAM	2.07
1999	[36]	DFT	2.10
1999	[35]	<i>ab initio</i>	1.68
1991	[42]	EAM	2.1

constant of  $\gamma$ -phase uranium at 0 K. However, the  $\gamma$ -phase of pure uranium is unstable at 0 K, and must be stabilized through the application of an external pressure. Due to this mechanical instability, calculations of properties by other common simulation methods such as DFT or *ab initio* calculations cannot be performed, due to their reliance on the presence of an equilibrium state at 0 K [37]. Through the use of a volume or pressure constraint in molecular dynamics simulations, simulations of pure  $\gamma$ -phase uranium at 0K can be performed. It is also important to note that the presence of a small atom percentage of an alloying element can stabilize the  $\gamma$ -phase of uranium, meaning that all of the studied U-Zr alloy compositions in this work were stable without requiring additional constraints.

It is common practice in MS modeling of metallic alloys to populate the lattice structure via random atom placement. Bulk material properties of crystals generated in this way can closely mimic the properties of real crystals; however, due to the finite nature of any modeled supercell, the random population of lattice sites may deviate from “perfect” randomness on a local scale. To address this issue, Wei et al. [43] proposed a method

of generating Special Quasirandom Structures (SQS) that would more closely mimic the configuration average of an infinite perfectly random  $A_{1-x}B_x$  alloy, and can be generated in sizes as small as  $N = 8$ . SQS “supercells” can be generated, and then combined into a larger lattices if bulk properties needed to be tested. The process of generating SQS is provided in Wei et al. [43], where multisite correlation functions are used to determine if a randomly generated microstructure mimics the ensemble averages that would be expected for an infinite random alloy. This is done to ensure that there are no regions within the randomly generated microstructure that statistically would be considered not random, thereby ensuring that properties determined using SQS are representative of a homogeneously mixed alloy. In their original work, Wei et al. [43] found that a supercell size of  $N = 8$  was sufficient to mimic the first and second nearest neighbor correlation functions for a binary alloy, and  $N = 64$  was sufficient to mimic the correlation functions for the third nearest neighbors. For this work, SQS’s of 2000 atoms and 250 atoms were developed using the stochastic SQS generation system that was implemented in the `mcSQS` code by Walle et al. [44]. The 250 atom structures were then repeated to produce a single system containing 2000 atoms.

For any alloy, there exists a distribution of possible vacancy formation energies due to the species arrangement and thermal oscillations of the atoms in the neighboring sites [45]. For this task, to examine the impact of different configurations of nearest neighbor sites on vacancy formation energy, all 256 possible nearest neighbor configurations for a binary bcc alloy were examined for each atom percentage and vacancy type tested. However, not all configurations are equally likely to occur in all alloys with differing atom percentages (e.g. all eight nearest neighbor lattice positions of a vacancy in a U-10%Zr alloys being filled by Zr atoms, etc.)

In a perfectly random binary alloy, the probability of an atom of species A inhabiting any given lattice position can be defined by the concentration of that species in the bulk lattice,  $C_A$ , while the probability of species B inhabiting the same lattice position can be



defined as the concentration of species B in the lattice,  $C_B$ . For a number of lattice positions  $z$ , the probability that  $i$  lattice positions are inhabited by species A and  $z - i$  lattice positions are inhabited by species B can be defined as

$$C_A^i C_B^{z-i}. \quad (2.1)$$

This probability refers to the probability of  $i$  species A atoms and  $z - i$  species B atoms inhabiting specific lattice positions. For each species distribution in  $z$  lattice positions, with  $i$  atoms of species A and  $z - i$  atoms of species B, the total number of configurations with that species distribution can be described by the following expression:

$$\frac{z!}{i!(z-i)!}. \quad (2.2)$$

Finally, the expression that defines the probability of having a specific species distribution in  $z$  lattice positions in a binary alloy can be expressed as the product of the probability of having the species distribution in a particular configuration and the total number of possible configurations for that species distribution, resulting in a binomial probability distribution [46],

$$P = \frac{z!}{(z-i)!i!} C_A^i C_B^{z-i} \text{ for } (0 \leq i \leq z). \quad (2.3)$$

In a BCC structure, there are eight first nearest neighbor sites and six second nearest neighbor sites. For a binary BCC alloy, there then exist 256 unique first nearest neighbor configurations and 104 unique second nearest neighbor configurations, combining for a total of 26,624 unique local configurations around a single atomic position, which in a binary system can be one of two different species. To account for this, the results of all possible configurations were compared with results for the configurations with atom percentages that were reasonable when compared to the atom percentage of the alloy as a whole.

All MS simulations were performed with a supercell consisting of 10 x 10 x 10 unit

cells held in a microcanonical, or NVE, ensemble.

### 2.1.2 Methods

#### *Interatomic Potential of U-Zr*

MS simulations model interactions between atoms via interatomic potential functions that are used to calculate the force on any atom in the system caused by the other  $N-1$  atoms in the system. A primary advantage of interatomic potential functions over first principle calculations is that potentials can be used for the calculation of larger scale atomic properties at temperature, as well as the ability to perform calculations on systems with many atoms. This is particularly advantageous for materials such as  $\gamma$ -uranium, which is mechanically unstable at 0 K [37]. For this work, a MEAM interatomic potential was used which was fit to various physical properties determined using a combination of experimental methods and first principles calculations [16]. MEAM potentials are modified versions of Embedded Atom Method (EAM), which are semi-empirical potentials that express the cohesive energy in terms of embedding energies, with the atoms in the system being embedded in an electron gas. The difference between MEAM and EAM potentials is that MEAM potentials account for angular forces, which are present in certain materials that form directional bonds [16]. Full descriptions and comparisons of EAM and MEAM potentials have been completed in other works [16, 17], and only a short description of the theory will be included here. A more complete description of MEAM potentials is also provided in Appendix A, paraphrased from Beeler et al. [16]. The general equation for the interatomic potential for both EAM and MEAM is shown by equation Equation 2.4.

$$E = \sum_i [F_i(\bar{\rho}_i) + \frac{1}{2} \sum_{j \neq i} \phi_{ij}(R_{ij})]. \quad (2.4)$$

In this equation,  $E$  represents the total potential energy energy of the system,  $\phi_{ij}$  represents the pair potential between atoms  $i$  and  $j$ ,  $\bar{\rho}$  is the effective electron density, and  $F_i$  is the

embedding function, which introduces many-body effects. For EAM potentials, the background electron density is taken to be the linear superposition of the spherically averaged atomic electron densities ( $\rho^0$ ), whereas in MEAM, angular effects are considered [16].

Vacancy formation energies can be calculated for a bulk lattice using the following equation,

$$E_v^f = E_{(n-1)} - \frac{n-1}{n} E_{(n)}, \quad (2.5)$$

where  $E_{(n-1)}$  is the energy of the system with a single vacancy,  $E_{(n)}$  is the energy of the reference lattice, and  $n$  is the total number of atoms in the reference lattice [16]. This equation was used due to the emphasis of this work on the impact of local atomic configuration and alloy composition on the value of the vacancy formation energy with respect to irradiation, rather than desiring a global minimum value for use in determining the concentration of thermal vacancies [47, 48].

### *SQS Generation Procedures*

For the generation of SQS, three input files were used with the `mcsqs` code from the Alloy Theoretic Automated Toolkit (ATAT) [49]. The first input file (by default `rndstr.in`, but this can be changed with the `-l=filename` option in the command line) defines the structure of the alloy and the ratio of the components. This input file must be made by the user. The second input file (by default `clusters.out`, but this can be changed with the `-cf=filename` option in the command line) tells the code what clusters must be considered while generating the SQS. This input file can be generated by code by using the command

$$mcsqs - 2 = \dots - 3 = \dots$$

where -2 and -3 define the ranges of pairs and triplets, while in the same directory as `rndstr.in`. For the purpose of this work, the range of pairs was set to 6 Angstroms, and the range of triplets was set to 8 Angstroms. The third input file used was `sqscell.out`,

which defines the supercell that `mcsqs` will use while generating the SQS. This input file is required only if the user requires a supercell of a specific shape. For the purpose of this work, a cubic supercell was used, to allow for ease of comparison between the SQS structure and the randomly generated cubic structures that were made using LAMMPS. To generate the SQS, the command

$$mcsqs -n = \dots -rc$$

must be used, where `-n` defines the number of atoms that will be placed within the supercell, and `-rc` tells the code to use the supercell defined in `sqscell.out`. For the code to work, the value for `-n` must be an integer, and the number of atoms must match with the size of the supercell provided in `sqscell.out`.

To run multiple ATAT sequences in parallel, the command `-ip=...` can be added to the previous command, with an integer following the equals sign. This integer will be appended to the names of the output files produced by the code. The produced SQS will be found in the output file `bestsqs(i).out`, which will have the dimensions of the unit cell and the supercell, and then the xyz location and type of each atom in the supercell in units of the specified lattice parameter. The file `bestcorr.out` tracks the correlations of the best SQS that has been found. For the purpose of this work, the code was stopped after the first SQS was generated.

### *Molecular Statics Procedures*

**Random Structures** All of the random structures used for this work were produced by LAMMPS. To produce a random structure, the dimensions of the supercell must be given in terms of unit cells, and the lattice parameter of the unit cell must be provided. Also, the structure of the unit cell must be specified (Body Centered Cubic (BCC), Face Centered Cubic (FCC), etc...). LAMMPS will produce a homogeneous structure with the specified

dimensions and structure. To create a random alloy, the `set` command is used, which allows the user to specify what percentage of atoms should be replaced by a specified atom type. Each alloy was minimized to energy (unitless) and force (eV/Angstrom) stopping tolerances of  $1.0 \times 10^{-15}$ . After running the initial minimization on the as-generated crystal, the atom at the center of the supercell was removed, and the alloy was again run for one time-step, then minimized to the same tolerance limits. For each random supercell generated by LAMMPS, the calculation of the vacancy formation energy was performed for both zirconium and uranium vacancies by setting the atom type of the atom that was to be removed to the desired element. Twenty random structures were tested for each alloy concentration. To prevent the mechanical instability of pure uranium at 0 K from influencing the results of simulations performed with pure uranium, the energy minimization step was only performed on the first nearest neighbors and second nearest neighbors of the vacancy, while the rest of the atoms in the supercell were fixed in space.

**SQS Structures** LAMMPS has the ability to import supercell structures through the use of the `read_data` command. After the supercell structure is read into the LAMMPS, the same process for the determination of the vacancy formation energy was used. For the 2000 atom SQS structures, a MATLAB script was used that determined the atom type of the atom at the center of the supercell, and found the xyz coordinates of the closest atom to the center of the supercell that was of the other type. For the 250 atom SQS structures, the atom at the center supercell was removed, and random atoms within the structure were chosen until an atom of the different type was found. Then, two runs were performed for each SQS, one where the atom at the center of the supercell was removed, and then a run where an atom of the opposite type was removed. In this way, the structure of the SQS was preserved. For the sqs structures, 16 structures containing 2000 atoms and 20 structures containing 250 atoms were generated for each alloy concentration.

### 2.1.3 Results and Discussion

Using LAMMPS, vacancy formation energies were calculated for the random structures and the SQS by minimizing the energy of the lattice as it was produced, then removing an atom from the center of the structure, minimizing the energy, and then taking the difference between the energies before and after the removal of the atom, as described by Equation 2.5 in subsection 2.1.2. All of these simulations were performed at a temperature of 0 K.

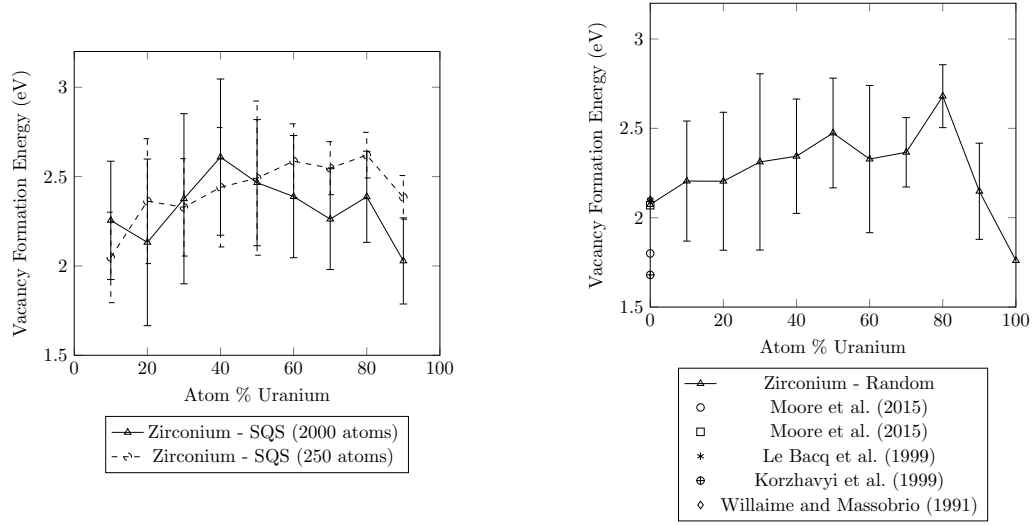


Figure 2.1: Plots of the vacancy formation energy for the removal of zirconium calculated for SQS and random structures of U-Zr alloy ranging from 0% to 100% U. Bars represent the standard deviation in the measured vacancy formation energies.

Figure 2.1 and Figure 2.2 compare the vacancy formation energies for the removal of zirconium and uranium atoms, respectively, for structures that were generated using the SQS method and by random atom placement. SQS can not be generated for pure metals, so only a single LAMMPS simulation was performed to determine the  $E_v^f$  of uranium and zirconium in pure uranium and zirconium metals. Tabulated results for the  $E_v^f$  in the pure

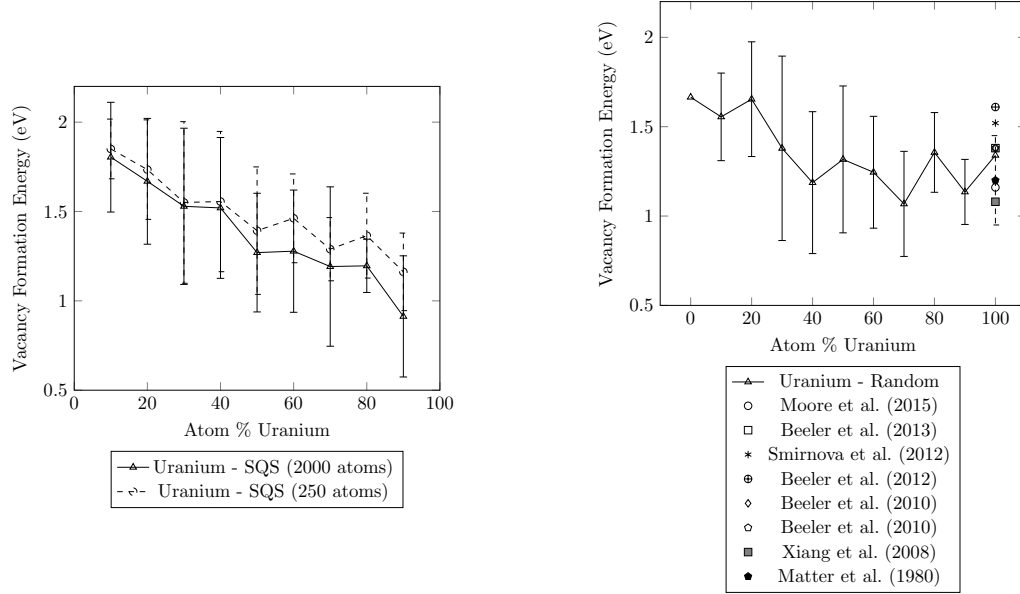


Figure 2.2: Plots of the vacancy formation energy for the removal of uranium calculated for SQS and random structures of U-Zr alloy ranging from 0% to 100% U. Bars represent the standard deviation in the measured vacancy formation energies.

metals can be seen in Table 2.1 and Table 2.2, compared with results from other works. The value of 1.34 eV obtained for the uranium  $E_v$  in pure uranium at 0K agrees well with the value of 1.38 eV produced by Beeler et al. [38] using a MEAM potential for  $\gamma$ -uranium in LAMMPS.

For the  $E_v^f$  of zirconium, the value seems to be fairly constant with changing atom percent of uranium, with any variation in the lines being within two standard deviations. The value of 2.074 eV obtained for the zirconium  $E_v^f$  in pure zirconium matches very well with the results of 2.07 eV and 2.10 eV attained by Moore et al. [37], Le Bacq, Willaime, and Pasturel [36] and Willaime and Massobrio [42], respectively.

The results for the vacancy formation energies of the 2000 atom SQS structures and the random structures were in good agreement. The  $E_v^f$  for the 250 atom SQS structures tended to be higher than those from the random and the 2000 atom SQS structures at higher

Table 2.3: Probability of zirconium inhabiting a number of nearest neighbor positions in U-Zr alloy

Configuration (U-Zr)	0-8	1-7	2-6	3-5	4-4	5-3	6-2	7-1	0-8
Number of Configurations	1	8	27	56	72	56	28	8	1
Atom Percent Zr	Probabilities								
10	0.4305	0.3826	0.1488	0.0331	0.0046	0.0004	2.268e-5	7.200e-7	1.000e-8
20	0.1678	0.3355	0.2936	0.1468	0.0459	9.175e-3	1.147e-3	8.192e-5	2.560e-6
30	0.0574	0.1977	0.2965	0.2541	0.1361	0.0467	1.225e-3	1.122e-3	6.651e-5
40	0.0168	0.0896	0.2090	0.2787	0.2322	0.1239	0.0413	7.863e-3	6.554e-4
50	3.906e-3	0.0313	0.1094	0.2188	0.2734	0.2188	0.1094	0.0313	3.906e-3
60	6.554e-4	7.864e-3	0.0413	0.1239	0.2322	0.2787	0.2090	0.0896	0.0168
70	6.656e-5	1.225e-3	0.0100	0.0467	0.1361	0.2541	0.2965	0.1977	0.0576
80	2.560e-6	8.192e-5	1.147e-3	9.175e-3	0.0459	0.1468	0.2936	0.3355	0.1678
90	1.000e-8	7.200e-7	2.268e-5	4.082e-4	4.593e-3	0.0331	0.1488	0.3826	0.4305

uranium percentages; however, this difference never exceeded more than one standard deviation, indicating that it was not a true difference in the properties between the structures. One important note is that random alloys produced by LAMMPS do not have exact atom percentages, with the atom percentages for each run being randomly distributed around the specified composition, with a maximum deviation of a few percentage points. Atom percentages for SQS structures are exact.

To examine the impact of local configuration on the vacancy formation energy, all possible nearest neighbor configurations were tested for the U-Zr alloy system for both uranium and zirconium vacancies. It has been shown in previous studies that the vacancy formation energy in binary alloys is highly dependent on the species distribution in both the first and second nearest neighbor sites [50]. For the simulations performed for this work only the first nearest neighbor configurations were varied, while keeping the second nearest neighbor configurations as they were generated. Therefore, the impact of second nearest neighbor configurations on the vacancy formation energy cannot be determined from the collected data.

It is important to note that not all local atomic configurations are equally likely in an alloy with a set concentration. For example based on the probabilities provided in Table 2.3, a U-10%Zr alloy will have a 96.2% chance that there will be three or fewer zirconium atoms in nearest neighbor sites, and a 99.55% chance that there will be four or fewer zirconium atoms in nearest neighbor positions. Therefore, when considering the impact that



different configurations have on the average vacancy formation energy for a given material composition, it is valid to sample configurations based on their probability of occurring.

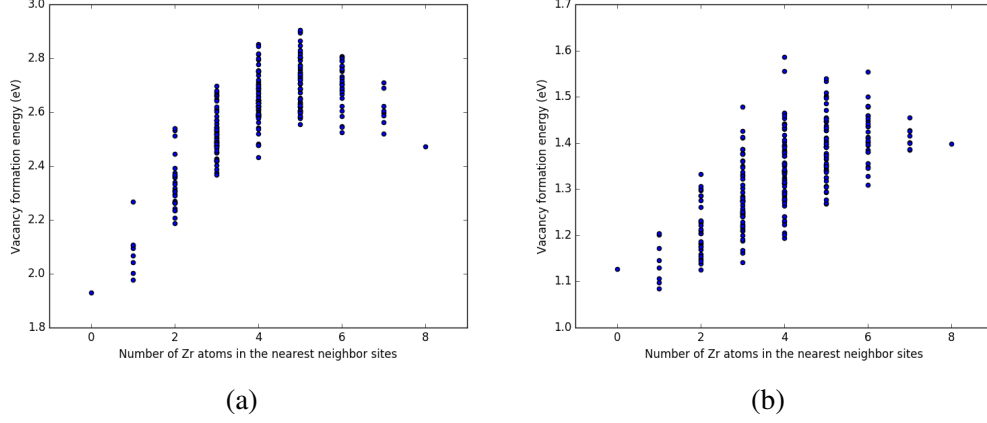


Figure 2.3: Plots of the vacancy formation energy for removing a: (a) zirconium and (b) uranium atom from a U-10%Zr alloy. Each data point represents a vacancy formation energy for a particular configuration of Zr atoms in the nearest neighbor sites as specified by the x-axis position.

Figure 2.3a and Figure 2.3b show the vacancy formation energy as a function of local atomic composition and configuration calculated for a zirconium and uranium vacancy in U-10%Zr alloy, respectively. Each data point represents the  $E_v^f$  for a particular nearest neighbor configuration with the number of Zr atoms in nearest neighbor sites specified along the x-axis. The plots of the  $E_v^f$  results for the 256 configurations at different atom percentages can be seen in Figure 2.4 and Figure 2.5. All of the simulations for Figure 2.4 and Figure 2.5 were performed in randomly generated supercells with the nearest neighbors adjusted manually.

By examining Figure 2.3a and Figure 2.3b, it can be seen that the energy required to remove either a uranium or zirconium atom from a U-10%Zr alloy generally increases as the total number of Zr atoms in nearest neighbor positions increases. In the case of removal of Zr, there is a slight drop in  $E_v^f$  as the number of zirconium atoms in nearest neighbor sites increases from five atoms to eight atoms, while the trend in the removal of uranium consistently increases with increasing zirconium atoms in nearest neighbor positions. This

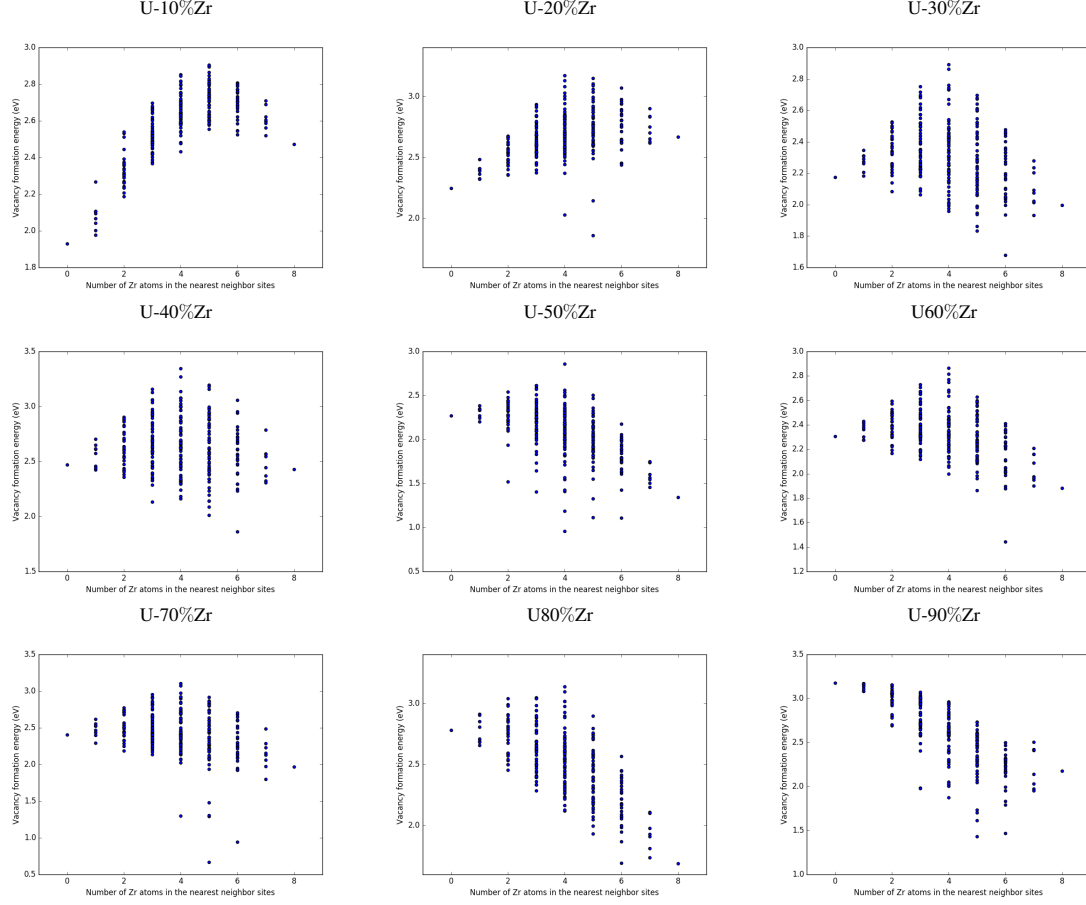


Figure 2.4: Configuration  $E_v$  of zirconium vacancies for different atom percentages

trend could be interpreted as an increase in the vacancy formation energy near positions where the local atomic concentrations deviate significantly from the composition of the alloy. This is exact trend is observed in Figure 2.4, where the U-10%Zr, U-20%Zr, U-80%Zr, and U-90%Zr alloy compositions all show the trend of increasing  $E_v^f$  as the local composition differs significantly from that of the alloy. For the middle concentrations (U-30%Zr to U-70%Zr), very similar trends are observed where there is a slight decreasing trend in  $E_v^f$  with an increasing number of zirconium nearest neighbors. In the case of the dependence of  $E_v^f$  on local atomic composition for the removal of uranium atoms, the same trend is observed for all alloy compositions, where the energy required to form a vacancy by removing a uranium atom always increases as the number of zirconium nearest neighbors increases.

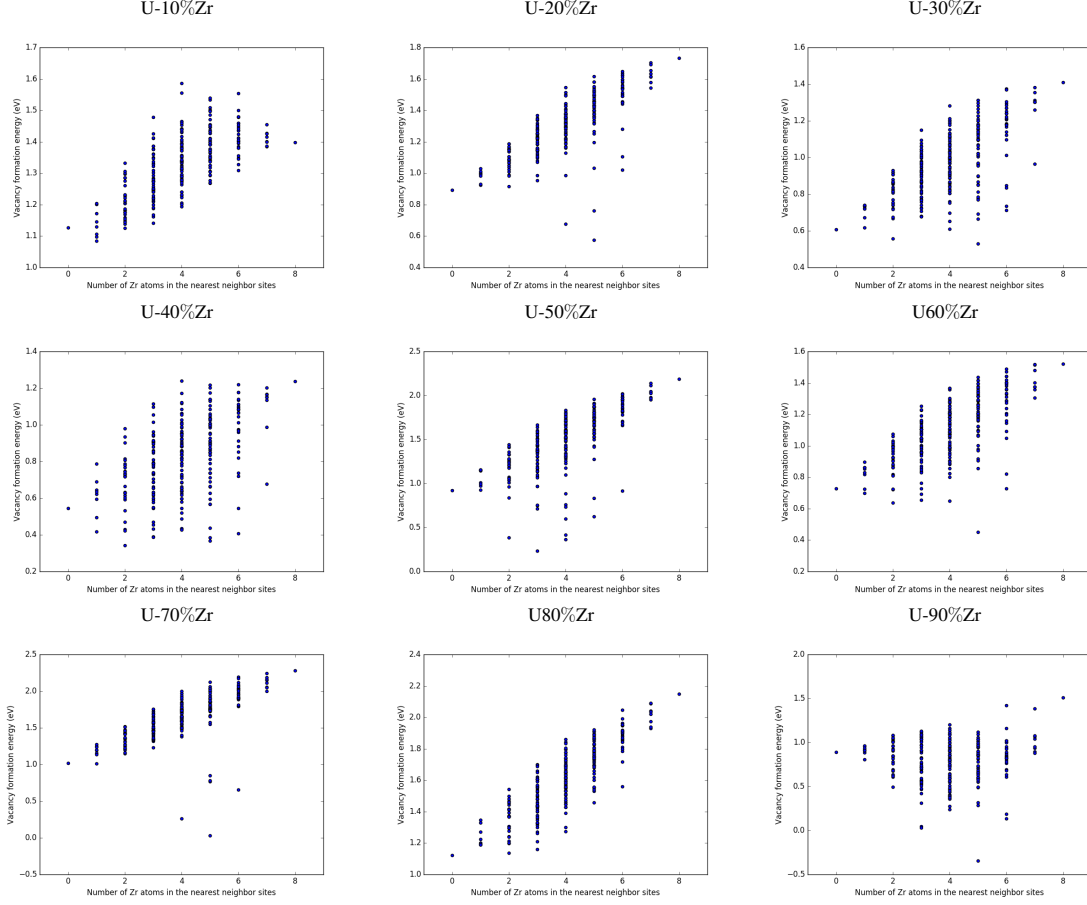


Figure 2.5: Configuration  $E_v$  of uranium vacancies for different atom percentages

In some of the plots in Figure 2.4 and Figure 2.5, some data points can be seen to lie well below the rest of the data points for a specific number of uranium atoms in nearest neighbor positions. In the case of the U-90%Zr and U-70%Zr plots in Figure 2.5, two configurations containing five uranium atoms and three zirconium atoms actually had negative vacancy formation energies. These data points represent systems that have particularly high energy arrangements of the species in their reference configurations. When the vacancy is introduced into the lattice of these structures, the introduction of the vacancy results in a smaller increase, or in the cases of the configurations which resulted in negative vacancy formation energies, actually results in the total energy of the system decreasing (i.e., becoming more stable).

Determining specific trends in how the local arrangement of the species (i.e., species

clumped together or distributed evenly across the nearest neighbor sites) impacts the formation energy of vacancies is difficult, particularly since this will also depend on the composition and arrangement of the second nearest neighbor atoms, which were not manipulated in this study, as well as the alloy composition. Examination of specific configurations by hand was performed for a series of initial alloy compositions and configurations, and it was determined that  $E_v^f$  is higher when the different species are grouped together into adjacent nearest neighbor sites, and that  $E_v^f$  decreases as the species are spread out as much as possible.

#### 2.1.4 Conclusions

The formation energies of uranium and zirconium vacancies in U-Zr binary bcc alloys were determined using MS simulations with a MEAM potential. Non-linear dependence on atom percent was observed for both uranium and zirconium vacancies. Good agreement was found for the  $E_v^f$  of both pure uranium and pure zirconium with the works of Beeler et al. [38, 51] and Matter, Winter, and Triftshäuser [34] for uranium and Moore et al. [37], Le Bacq, Willaime, and Pasturel [36], and Willaime and Massobrio [42] for zirconium.

The impact of crystal generation method on  $E_v^f$  was examined by generating the alloys both as random alloys and as SQS. It was found that, for the supercell size used in our MS simulations, there is no statistically significant difference between the vacancy formation energies in the crystals generated by the two methods. This indicates that the supercell size used in our simulations was sufficiently large to mimic a truly random structure. Additional work could be performed to determine the supercell size where a random alloy ceases to perform similarly to SQS structures, which are intended to mimic perfectly random systems.

The effect of local atomic configuration on  $E_v^f$  was examined by varying the configuration of atoms in the nearest neighbor sites around a vacancy in U-Zr alloys. It was observed that for both uranium and zirconium, the configuration of nearest neighbor atoms did have

a noticeable impact on the  $E_v^f$ . The removal energy of uranium was found to increase with increasing Zr nearest neighbors up until an atom fraction of 90% Zr, where no strong dependence on nearest neighbor configuration was found. The removal energy of zirconium was found to increase with increasing Zr nearest neighbors in low atom percent Zr alloys, and decrease with increasing Zr nearest neighbors in alloys with Zr atom percentages higher than percent. It was observed that  $E_v^f$  increased when the nearest neighbors were arranged in a manner that grouped atoms of the same species together, while  $E_v^f$  was found to decrease as the species were evenly distributed across the nearest neighbor sites.

With a better understanding of the  $E_v^f$  in  $\gamma$ -U-Zr alloys, additional work can be performed with the examination of defect diffusion via vacancies, as well as the formation of defects due to radiation damage events. This work could also support the development or improvement of conventional interatomic potentials for alloys, or as a possible data source for machine learning interatomic potentials or machine learning-based simulation techniques. Further insight into the relationship between the  $E_v^f$  and local atomic configuration could be explored through the use of DFT simulations.

## 2.2 Scaling laws and stability of nano-sized defect clusters in niobium via atomistic simulations and statistical analysis [21]

### 2.2.1 Introduction

There are three common geometric configurations for clusters of vacancies and Self Interstitial Atoms (SIAs) created by energetic particle irradiation in BCC metals: two two-dimensional (2D) planar dislocation loop configurations (faulted and perfect) for both vacancies and interstitials and one three-dimensional (3D) configuration occurring only for vacancies in the form of cavities (typically faceted) [52].

The thermodynamic stability and evolution of these defect clusters depend on the nature (vacancy versus interstitial), the geometry (2D or 3D clusters), the size and the density of these clusters and their interplay with the microstructure. For example, Marinica, Willaime, and Crocombette [53] demonstrated that, in iron (Fe), the orientation of self-interstitial atoms dumbbells changes from  $\langle 110 \rangle$  to  $\langle 111 \rangle$  depending on the number of interstitials included. Similarly, Morishita, Sugano, and Wirth [54] showed that the growth and shrinkage mechanisms of helium–vacancy clusters in iron depend on the size of these clusters.

Advances in coarse-grained computational models elucidating the evolution of the aforementioned defect clusters are seemingly continuous. These include atomistic and object-oriented kinetic Monte Carlo (akMC/okMC) [55, 56], Cluster Dynamics (CD) [57] or Dislocation Dynamics (DD) [58, 59]. These modeling techniques require an accurate quantification and parameterization of intrinsic thermodynamic quantities such as the formation energy ( $E^f$ ) or the binding energy ( $E^b$ ) for all the defect configurations and for a broad range of cluster sizes in order to predict the spatiotemporal evolution and distribution of these defects in microstructures. Parameterization of the formation and binding energies are routinely performed using DFT or MD [60–65]. On one hand, DFT calculations are numerically limited to predicting the structure and energetics of elementary clusters containing only a small number of defects. For example, Dézerald et al. [66] were limited

to study the stability of small ring and loop configurations of di-, tri-, tetra- and octa-interstitial clusters with C15 Laves phase structure in Fe using DFT simulations, when the same research group [67] later on developed a discrete-continuum model to predict scaling laws for larger nano-sized C15 clusters. On the other hand, results obtained from MD simulations using different interatomic potentials (EAM, MEAM, etc...) can be qualitatively different from one another for the same property of interest or predict different stable defect configurations. For instance, Osetsky et al. [68] showed that, when using different types of interatomic potentials (short-ranged versus long-ranged), the stability of a self interstitial in BCC-Fe was dependent on the range of the potential used. Results from their short-ranged potentials predicted the  $\langle 110 \rangle$  dumbbell as the stable configuration while in the case of the long-ranged potential, their results predicted the  $\langle 111 \rangle$  crowdion as the stable configuration.

Energetics and stability of defect clusters in various bcc metals (Fe, W, and V) have been extensively studied using DFT and MD [62, 65, 67, 69–78]. Unfortunately, there are fewer studies of the energetics of vacancy and interstitial clusters in niobium (Nb) for various defect configurations and sizes. Nb is a refractory BCC metal with important applications in engineered alloys for radiation resistant materials in helium- (He) or sodium- (Na) cooled Generation IV reactors [79], compact space reactors [80–84], advanced fission reactor [85–87], and fusion reactor concepts [87, 88]. The accurate predictions of scaling laws for the structure and energetics of defect clusters are therefore important in the context of coarse-grained modeling for understanding the behavior of Nb-based nanostructured alloys [89, 90]. As shown in Figure 2.6a, Figure 2.6b and Figure 2.6c, we can see that, across all the data sources and between the two modeling techniques used (DFT versus MD), there is a large scatter in the predicted formation and binding energies and that only data for small sizes of cluster configurations are available. Additionally, predictions of the stability of (small) cluster configurations differ depending on the technique used. For example, looking at the configuration yielding the minimum formation energy of interstitial

dumbbells, DFT sources [60, 62, 91] as well as Finkenstadt et al. [92], which employed tight-binding MD, predict that the minimum energy configuration in Nb is the  $\langle 111 \rangle$  crowdion. However, the rest of the MD sources [71, 72, 91, 93] predict the  $\langle 110 \rangle$  dumbbell to be the lowest energy dumbbell. It should be noted that data on helium-vacancy and helium clusters is also scarce. Note that all the results shown in Figure 2.6 are tabulated in Appendix section B.1.

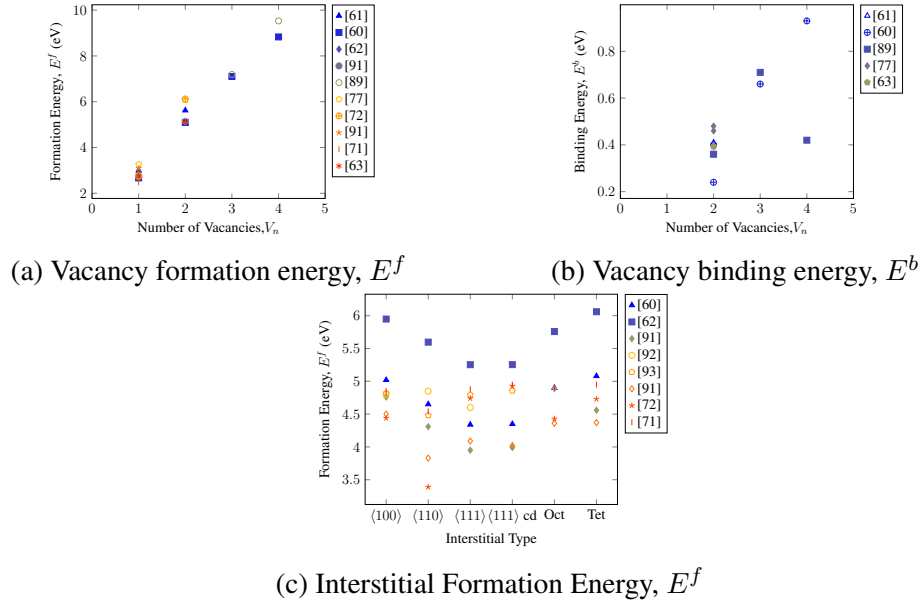


Figure 2.6: Survey of (a) formation ( $E^f$ ) and (b) binding ( $E^b$ ) energies for small vacancy clusters. (c) Survey of formation energies of self-interstitial atoms in different configurations. References are marked in parenthesis, with hollow symbols denoting MD simulation results, and solid symbols denoting DFT simulation results.

Given the current discrepancy and scarcity of available data, the aim of this work is to systematically investigate the size and configuration dependence of (large) nano-sized vacancy and interstitial defect clusters on the stability of these defects in Nb using MD simulations. The largest sizes correspond to defect sizes visible by Transmission Electron Microscopy (TEM) and of relevance to coarse-grained computational modeling of microstructure evolution. In order to generalize our results and evaluate the stability of the various defect configurations, we compare three different EAM interatomic potentials. These results are integrated into a statistical analysis of the various defect configurations



to predict the formation and binding energies of interstitial clusters as a function of both their size and geometry. This section is organized as follows. The first subsection, subsection 2.2.2 describes the key aspects of the interatomic potential used and generation of the various defect cluster configurations. The analysis of the configurations and energetics of vacancy and interstitial nano-sized defect clusters is provided in subsection 2.2.3. This is followed by the analysis of the relative predictability of the formation and binding energies as a function of the configuration and size. Then, we present a discussion of the role of helium and metastable configurations on the stability of vacancy and interstitial clusters. Finally, conclusions are given in subsection 2.2.4.

## 2.2.2 Methodology

### *Description of interatomic potentials*

We used the MD code LAMMPS [94] in order to evaluate the formation and binding energies of vacancy and interstitial defect clusters in Nb. There are many EAM type interatomic potentials for bcc Nb available in the literature, see for example [61, 91–93, 95–97]. For this work, we selected three potentials that have been used for modeling defect evolution.

The first potential is a force-matched EAM potential developed by Fellingner, Park, and Wilkins [91] for pure Nb. This potential was fit to a database of DFT forces, energies, and stresses from *ab initio* MD simulations for the cohesive energy, lattice parameter, bulk modulus, elastic constants and stacking fault energy of BCC Nb. This potential predicts the  $\langle 110 \rangle$  dumbbell as the most stable interstitial configuration.

The second potential is a Finnis-Sinclair type potential developed by [93] and later improved by Zhang et al. [95] for Cu-Nb binary system. It was fit to the elastic constants, the lattice parameter, as well as the cohesive and stacking fault energies. This potential showed that it could predict crystal structures comparably to other potentials [61, 93, 97] as well as predicting the  $\langle 110 \rangle$  dumbbell as the most stable interstitial structure in the original paper. We will henceforth refer to this potential as the Ackland [93] potential.

Finally, the last potential is based on the EAM potential initially developed by Johnson and Oh [97] and later improved by Demkowicz and Hoagland [96]. This potential was used to model collision cascades in Cu-Nb-He systems. The single-element Nb potential was fit to the elastic constants, the lattice parameter, the cohesive energy of BCC Nb, the difference in cohesive energy between Nb in the BCC and FCC structures and the relaxed vacancy formation energy in the BCC phase. This potential predicted that the most stable interstitial structure configuration is the  $\langle 100 \rangle$  dumbbell in the original paper. We will henceforth refer to this potential as the Johnson potential [97]. We emphasize that, despite being fitted to similar physical and thermodynamic properties, these three potentials are qualitatively different since they predict different stable configurations and energetics for elementary defect configurations.

We performed simulations in pure Nb with all three potentials, while our simulations involving He were performed using the modified version of the Johnson and Oh potential [96].

### *Generation of defect clusters*

We simulated vacancy and interstitial clusters of sizes up to fifty defects and small helium-vacancy and helium clusters of sizes up to ten defects. The largest sizes correspond to defect sizes visible by TEM and of relevance to coarse-grained computational modeling of microstructure evolution. The size of our simulation cell was dependent on the size of the defect being simulated as listed in Table B.1 of Appendix B. For all simulations, we used periodic boundary conditions to simulate a defect cluster isolated in the bulk. All Nb simulations were performed with a lattice constant of 3.30 Å.

**Point defects** We performed all point defect simulations by forming a perfect lattice, minimizing the energy of the lattice using the conjugate gradient method, introducing the point defect at the center of the supercell, and then minimizing the energy of the supercell again.

The parameters for the minimization were a stopping energy (unit-less) and force (eV/Å) tolerance of  $1.0 \times 10^{-15}$ , and the maximum number of iterations for the minimizer was set to 200,000. Unless stated otherwise, the above parameters and minimization method were used for all energy minimization procedures. We list the sizes of the supercell used for point defect formation simulations in Table B.1 of Appendix B .

**Vacancy clusters** We used two different methods to generate vacancy cluster configurations. The first method was designed to capture all possible configurations of a vacancy cluster of a given size, so as to preserve metastable states for implementation into a coarse-grained simulation such as Kinetic Monte Carlo (kMC) or CD. This method consisted of defining a region in the center of the supercell, then creating a list of all possible iterations of a set number of atoms within that region that did not exceed a second nearest neighbor distance from any other atom in the list. Duplicate orientations were removed by comparing the sets of inter-vacancy distances for each vacancy within the cluster. If a set of inter-vacancy distances matched the set of a different cluster, the clusters were assumed to be identical, and only one was tested. This method of cluster generation is computationally expensive, with the number of possible configurations for the cluster increasing exponentially with cluster size. Due to this limitation, this method of vacancy cluster generation was only used for small clusters with four vacancies or less.

The second method of vacancy cluster generation was designed to find the minimum energy configuration for a vacancy cluster with a large number of vacancies. For this method, a vacancy was introduced in the center of the supercell, and the potential energy of each atom within the supercell was evaluated [98]. The atom with the highest potential energy was then removed, and the process was repeated until the desired cluster size was reached. If multiple atoms were found to have the same potential energy, each of those atoms was removed individually, and the final vacancy cluster configuration with the lowest formation energy was used to progress the simulation. This cluster generation method

does not necessarily find the minimum energy configuration for a vacancy cluster of large size, but it does produce low energy vacancy clusters that can be considered of relevance to a rate-theory or kMC model of defect formation. This method was used to generate configurations of vacancy clusters containing up to fifty vacancies.

In order to find the minimum energy cluster configuration, the vacancy clusters produced by the second method were subsequently taken through a thermal quenching process, where the system temperature was equilibrated at 300 K using a Nose-Hoover thermostat for 10 ps, quenched from 300K to 10K for another 10 ps, and finally minimized using conjugate gradient minimization. The change in positions was accepted [98, 99] if the total energy of the system is reduced by the change, or if a random seed is larger than  $\exp(-\Delta E/k_B T)$ , where  $\Delta E$  is the energy difference between the formation energy of the adjusted cluster and the formation energy of the previous iterations cluster,  $k_B$  is the Boltzmann constant, and  $T$  is the system temperature used. This process was repeated until the change in energy between iterations was below a set threshold value, or if a certain number of iterations has occurred. For all vacancy clusters where this operation was performed, no significant changes in cluster geometry were observed. The supercells used for the simulation of vacancy clusters are listed in Table B.2 of Appendix B.

**Self-interstitial atom clusters** Self-interstitial atom clusters were generated by introducing the desired number of atoms into a small region with a radius of two lattice dimensions, then minimizing the energy of the system. After the initial minimization, the temperature of the system was equilibrated at 300 K for 10 ps using a Nose-Hoover thermostat, then quenched from 300 K to 10 K over the course of 5 ps. The energy of the system was then minimized using the conjugate gradient method, resulting in the final interstitial cluster configurations used for the calculations of the formation and binding energies. The supercell sizes used for the interstitial cluster simulations can be seen in Table B.3 of Appendix B.

**Helium-vacancy clusters** We considered small helium-vacancy of size up to ten defects. Helium-vacancy clusters were generated by taking the minimum-energy orientations for the vacancy clusters from the first method of vacancy cluster generation, and randomly placing the desired number of helium atoms within spheres of an approximate radius of 1.3 Å located at the center of the vacancies. For each number of vacancies and helium atoms, 100 different random placements of the helium atoms were simulated, in an attempt to observe possible metastable states. All helium-vacancy cluster simulations were performed in a supercell of  $30 \times 30 \times 30$  lattice units containing 54,000 atoms of Nb in the perfect lattices.

**Helium clusters** Helium clusters are classified as clusters of helium atoms located at interstitial sites in the bulk lattice that have not displaced any of the lattice atoms. Once the helium cluster is large enough to displace an atom, the helium cluster is classified as a helium-vacancy cluster. Helium clusters were formed by randomly placing a set number of helium atoms in to a spherical region within an interstitial site in the lattice with an approximate radius of 1.3 Å. For each cluster size, one hundred different random placements were simulated in an attempt to search for local minima. All helium cluster simulations were performed in a supercell of  $40 \times 40 \times 40$  lattice units and 128,000 atoms of Nb in the perfect lattices. All helium defect simulations were performed using the modified version of the Ackland interatomic potential by Demkowicz and Hoagland [96].

#### *Calculation of defect cluster formation and binding energies*

The formation energies  $E^f$  of point defects such as single vacancies, self-interstitial atoms in tetrahedral and octahedral sites, and self-interstitial dumbbells are defined as follows [100]:

$$E^f(j_1) = E_{N \pm 1} - \frac{N \pm 1}{N} E_N \quad (2.6)$$

where  $j_1$  is either a single vacancy or interstitial,  $E_{N\pm 1}$  is the energy of the system containing the point defect,  $E_N$  is the energy of the perfect lattice,  $N$  is the number of atoms in the perfect lattice, and the  $\pm$  corresponds to a summation in the case of an interstitial and a subtraction in the case of a vacancy respectively. For He interstitials, the formation energy is given by Hayward and Deo [98],

$$E^f(\text{He}_1) = E_{N+\text{He}} - E_N + N_{\text{He}}E(\text{He}), \quad (2.7)$$

where  $E_{N+\text{He}}$  is the energy of the supercell containing the He interstitial,  $N$  is the number of atoms in the perfect lattice,  $E_N$  is the energy of the reference lattice containing no defects,  $N_{\text{He}}$  is the number of He interstitial atoms, and  $E(\text{He})$  is the energy of a He atom in an empty supercell (taken to be zero). The formation energies of defect clusters and helium-vacancy clusters of size  $n$  are calculated in a very similar fashion such that [100],

$$E^f(j_n) = E_{N\pm n} - \frac{N \pm n}{N} E_N, \quad (2.8)$$

where  $j_n$  is either a vacancy or interstitial cluster,  $N$  is the number of atoms in the perfect lattice,  $n$  is the number of defects in the cluster,  $E_{N\pm n}$  is the energy of the lattice containing the defect cluster,  $E_N$  is the energy of the perfect lattice, and  $\pm$  corresponds to a summation in the case of an interstitial cluster and a subtraction in the case of a vacancy cluster respectively.

The thermal stability of defect clusters is described by the binding energy  $E^b$  of a vacancy, an interstitial, or a helium to a defect cluster of size  $n$  and it is calculated by [100]:

$$E^b(j_n) = E^f(j_1) + E^f(j_{n-1}) - E^f(j_n). \quad (2.9)$$

#### *Defect cluster configuration analysis*

We extracted and characterized the stable defect clusters configurations using a combi-

nation of the Common Neighbor Analysis (CNA) defect analysis and Radial Distribution Function (RDF), as implemented in the OVITO software [101]. We used a binning distance of 0.01 Å and a cutoff distance of 7 Å for the RDF. RDFs were subsequently smoothed using a Gaussian filter with a standard deviation of 3.7 Å and truncation point of 3.5 standard deviations. In order to generalize our results and to be statistically representative, we generated fifty configurations for each defect cluster size ranging from single point defect configurations to large defect clusters containing fifty defects for the three interatomic potentials considered, resulting in a total of 1,800 simulations.

### 2.2.3 Geometrical configurations and energetics of nano-sized defect clusters

#### *Defect cluster geometrical configurations*

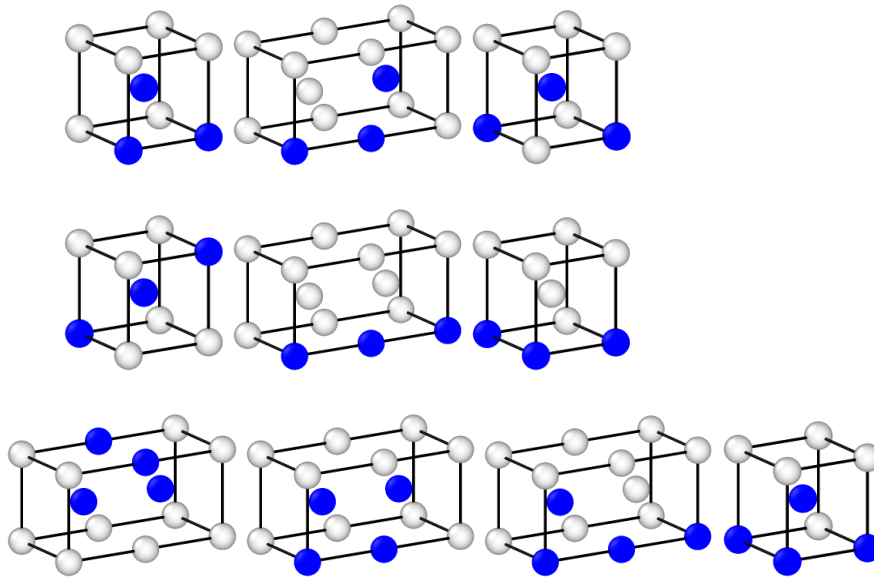


Figure 2.7: (a)–(f): Tri-vacancy configurations. (g)–(j): Tetra-vacancy configurations. White spheres represent niobium atoms, and blue spheres represent vacancies. Sub-letter by each configuration corresponds to its formation energy in Table B.1 in Appendix B section B.3.

We generated single vacancies and their clusters containing up to four vacancies for six tri-vacancy configurations (see Figure 2.7 (a)–(f)) and four tetra-vacancy configurations (see Figure 2.7 (g)–(j)). For single interstitial, we generated five different configura-

tions, namely the three dumbbell configurations ( $\langle 100 \rangle$ ,  $\langle 110 \rangle$ , and  $\langle 111 \rangle$ ) along with the octohedral and tetrahedral configurations. As tabulated in Table B.1 and Table B.3 in Appendix B section B.3, regardless of the potential used, our simulations predicted that the trivacancy configuration shown in Figure 2.7 (a) and the tetravacancy configuration shown in Figure 2.7 (g) to be the most stable configurations. However, we observed differences on the most stable interstitial configuration depending on the interatomic potential. Our results using the Johnson potential predicted the  $\langle 100 \rangle$  dumbbell to be the most stable interstitial configuration, while results for both the Ackland and the Feller potential predicted the  $\langle 110 \rangle$  dumbbell to be the most stable interstitial configuration. Our simulations that used the Feller potential also predicted that an interstitial in the tetrahedral interstitial position would have nearly the same formation energy as the  $\langle 110 \rangle$  dumbbell. In contrast to this work and other MD works, all of the results from DFT sources (see list in Table B.1 in Appendix B section B.1) predicted that the  $\langle 111 \rangle$  dumbbell is the configuration with the lowest energy interstitial configuration, followed in increasing order by the  $\langle 111 \rangle$  crowdion, the tetrahedral interstitial site, the  $\langle 110 \rangle$  dumbbell, the  $\langle 100 \rangle$  dumbbell, and finally the octahedral interstitial site [60, 62, 91].

Larger vacancy clusters containing up to fifty vacancies were computed via the growth method described in subsection 2.2.2. Our simulations resulted in 3D faceted void configurations consisting of only  $\{100\}$  and  $\{110\}$  surfaces with various shape ratios depending on the interatomic potential used (see Figure 2.8). The Ackland potential predicted an elongated faceted void configuration for vacancy clusters, while the Feller and Johnson potentials predicted faceted spherical nano-sized vacancy voids. For these large vacancy cluster sizes (i.e., greater than four vacancies), we generated one hundred different initial configurations which all lead to the same final configuration after minimization for each of the three interatomic potential tested. Therefore, none of the potential we tested resulted in metastable configurations for vacancy clusters.

Large interstitial clusters (i.e., clusters comprising at least two interstitials or more)



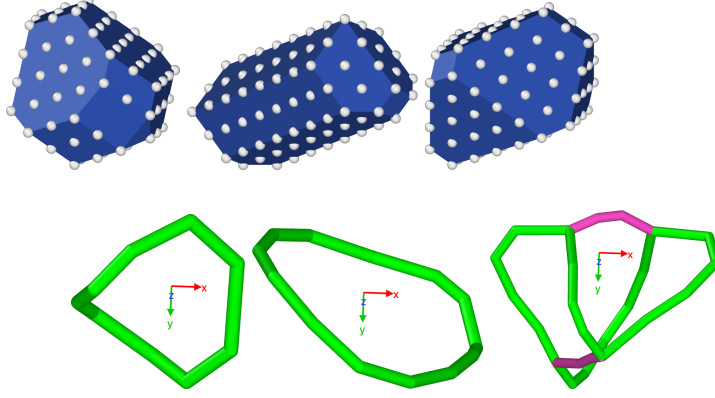


Figure 2.8: Predicted minimum energy vacancy (top row) and interstitial (bottom row) cluster configurations with fifty vacancies/interstitials for all three interatomic potential tested. Left to right: structures obtained from the Johnson ((a) and (d)), Ackland ((b) and (e)) and Fellingner ((c) and (f)) potentials. In (a)–(c), atoms on the surface of the vacancy void are illustrated with white balls and surfaces of the cavities are rendered with blue surfaces. In (d)–(f), green dislocation segments correspond to  $\frac{1}{2}\langle 111 \rangle$  dislocations, magenta dislocation segments correspond to  $\langle 100 \rangle$  dislocations.

were generated using the method described in subsection 2.2.2. Our simulations resulted in 2D  $\frac{1}{2}\langle 111 \rangle$  planar dislocation loop configurations for the Ackland and Johnson potentials, while our results with the Fellingner potential showed a crossover between  $\frac{1}{2}\langle 111 \rangle$  and  $\langle 100 \rangle$  loops. Using this method, we produced fifty different (metastable) cluster configurations for each interatomic potential. Thus, each of the potentials we tested resulted in multiple metastable configurations for interstitial clusters. These configurations are consistent with those found in iron for example [102].

### *Formation energy*

We present the formation energies of both vacancy and interstitial clusters as a function of their size in Figure 2.9 for the three interatomic potential tested. This data is tabulated in Table B.1–Table B.2 for vacancies and in Table B.3–Table B.4 for interstitials in Appendix B section B.3. The asymptotic values and functional forms for the formation energies of vacancies ( $E^f(V_n)$ ) and interstitials ( $E^f(I_n)$ ) as a function of the number of

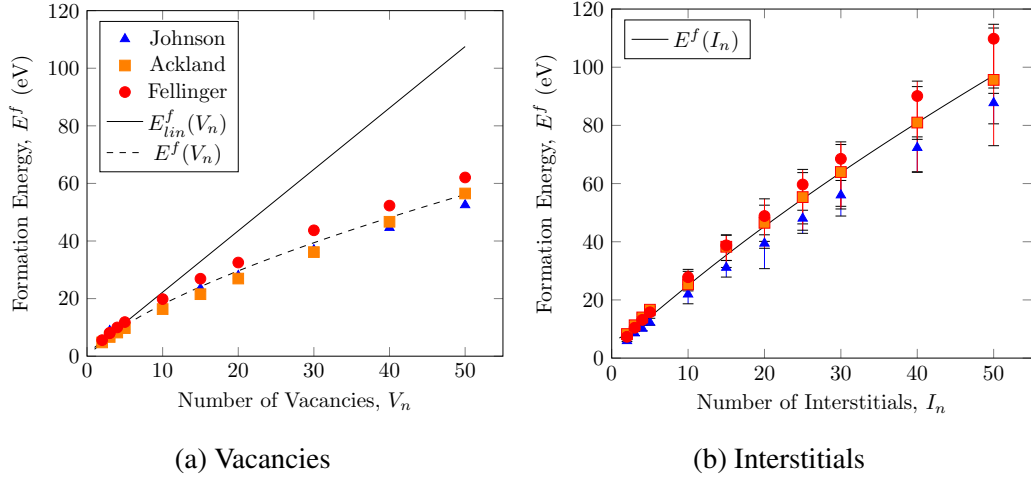


Figure 2.9: Formation energies for (a) vacancy and (b) interstitial cluster defects as a function of cluster size. Triangle, square and circle symbols correspond to the Johnson, Ackland and Fellinger interatomic potentials respectively.

vacancies  $V_n$  and interstitials  $I_n$  respectively are given by,

$$E^f(V_n) = E_{v,0}^f \left[ 1 - A_v V_n^{\frac{2}{3}} \right], \quad (2.10)$$

$$E^f(I_n) = E_{i,0}^f \left[ 1 + A_i \sqrt{I_n} \ln(I_n) - B_i \sqrt{I_n} \right], \quad (2.11)$$

where  $E_{v,0}^f$  and  $A_v$  are the fitting coefficients for the vacancy formation energy and  $E_{i,0}^f$ ,  $A_i$ ,  $B_i$  are the fitting coefficients for the interstitial formation energy. The functional form for the vacancy formation energy was chosen to reflect the fact that the energetic properties of vacancy clusters are primarily dominated by surface effects [103]. The functional form for the interstitial formation energy is meant to capture the competition between elastic effects (through coefficient  $A_i$ ) and surface effects (through coefficient  $B_i$ ) [67]. These functions were fit to the average of the formation energies calculated from our atomistic simulations using the three different interatomic potentials with the following fitting coefficients  $E_{v,0}^f = -1.872$  eV and  $A_v = 2.284$  for vacancies and  $E_{i,0}^f = 1.570$  eV,  $A_i = -1.574$ , and  $B_i = -0.343$ . The linear fit  $E_{lin}^f(V_n)$  in Figure 2.9a represents the linear functional fit using the formation energies for small vacancy clusters (size four and smaller) found in literature using DFT and MD results (as tabulated in Table B.1–Table B.2 in Appendix B sec-

tion B.1).

Our results for the formation energy of vacancies  $E^f(V_n)$  indicate that all three potentials predicted the same configurational ranking for the different tri- and tetra-vacancy configurations. Our simulation results for the minimum energy configurations for small vacancy clusters are in agreement with those from DFT simulations [60]. Our results are also in agreement with those of Dunn et al. [89] who found the exact same values for the formation energies of single, di-, and tri-vacancies; although they do not mention the corresponding tri-vacancy configuration.

Comparing the different fits in Figure 2.9, it is immediately apparent that the use of the linear model fit to the formation energies of the small vacancy clusters overestimates the formation energies of the large vacancy cluster substantially. As indicated by the goodness of fit between Equation 2.10 and the data from our atomistic simulations, the scaling law for the formation energy of vacancy clusters is governed by surface effects, while the scaling law for the formation energy of interstitial clusters is governed by both surface and elastic effects. The variation in the formation energy of interstitial clusters for all the configuration tested remain relatively small indicating the predominance of elastic effects [67] as the size of an interstitial cluster increases as compared to surface effects from the variation in the geometrical configurations.

### *Binding energy*

The binding energies for small vacancy clusters of up to size four were computed for various vacancy-vacancy reactions ( $V+V \rightarrow V_2$ ;  $V+V_2 \rightarrow V_3$ ;  $V_3+V \rightarrow V_4$ ;  $V+V+V+V \rightarrow V_4$ ;  $V_2+V_2 \rightarrow V_4$ ) within these small clusters as listed in Table B.5 in Appendix B section B.4, whereas the binding energies for larger vacancy clusters of sizes greater than size four were computed via the growth method representing the reaction of a single vacancy with a random site from the larger vacancy cluster. The asymptotic values and functional forms for the formation energies of vacancies ( $E^b(V_n)$ ) and interstitials ( $E^b(I_n)$ ) as a func-

tion of the number of vacancies  $V_n$  and interstitials  $I_n$  respectively are given by,

$$E^b(V_n) = E_{v,\text{sat}}^b [1 - C_v \exp(D_v V_n)], \quad (2.12)$$

$$E^b(I_n) = E_{i,\text{sat}}^b [1 - C_i \exp(D_i I_n)], \quad (2.13)$$

where  $(E_{v,\text{sat}}^b, C_v, D_v)$  and  $(E_{i,\text{sat}}^b, C_i, D_i)$  are the fitting coefficients for the vacancy and interstitial binding energies respectively. The functional form for the binding energy is meant to capture the fact that the binding of an atom to a large cluster (vacancy or interstitial) as the size of the cluster increases should approach the energy required to remove an atom from a free surface. These functions were fit to the average of the binding energies calculated from our atomistic simulations using the three different interatomic potentials with the following fitting coefficients  $E_{v,\text{sat}}^b = 1.570$  eV,  $C_v = -1.574$ , and  $D_v = -0.343$  and  $E_{i,\text{sat}}^b = 4.13594$  eV,  $C_i = -1.419$ , and  $D_i = -0.280$ .

Concerning the binding energy of vacancies, it is worth noting that all three potentials predicted that the nearest neighbor configuration for the di-vacancy to be the most stable. This prediction is consistent with the MD results of Hu, Shu, and Zhang [72], but contradicts the results of Cerdeira et al. [60] and Derlet, Nguyen-Manh, and Dudarev [61], both of which are DFT works that predict that the second nearest neighbor configuration of the di-vacancy to be more stable.

As shown in Figure 2.10, the scaling law for the binding energy of vacancy and interstitial clusters as the size increases saturates for cluster sizes greater than fifteen vacancies/interstitials respectively. The binding energy for vacancy clusters saturates at an approximate value of  $E_{v,\text{sat}}^b = 1.570$  eV, while the binding energy for interstitial clusters saturates at an approximate value of  $E_{i,\text{sat}}^b = 4.136$  eV. Both the binding energies increase with cluster size, and, at any size, the binding energy for vacancy clusters is on average smaller than that for interstitial clusters. This suggests that large stable vacancy clusters in Nb are thermally less stable than interstitial clusters, and that vacancy clusters can more

easily dissociate than interstitial clusters. However, given the large variation in binding energy depending on the geometrical configuration of large interstitial clusters and the interatomic potential used, some metastable configurations of interstitial clusters can be less stable than vacancy clusters for the same cluster size, notably at intermediate sizes ranging from ten to thirty defects.

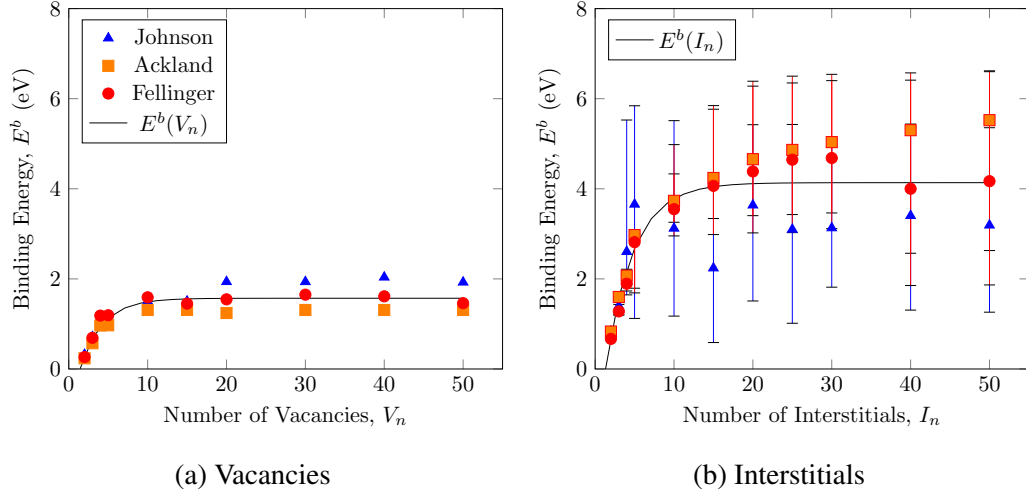


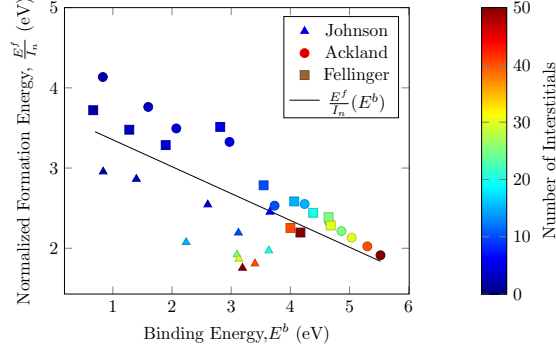
Figure 2.10: Binding energies for (a) vacancy and (b) interstitial cluster defects as a function of cluster size. Triangle, square and circle symbols correspond to the Johnson, Ackland and Fellingner interatomic potentials respectively.

In Figure 2.11, we plot the correlation between the formation energy per defect irrespective of the size of the cluster against the binding energy for the corresponding cluster. As clearly illustrated, we found the binding energy is inversely correlated with formation energy at any size.

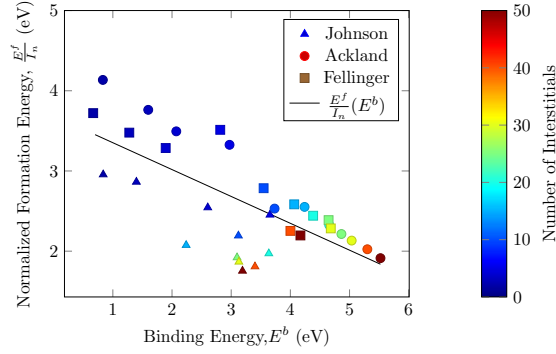
#### *Role of metastable configurations on the stability of nano-sized defect clusters*

When considering the range of possible metastable configurations with their respective energies predicted for interstitial clusters, we noted that the functional forms proposed in Equation 2.11 and Equation 2.13 are not able to capture this configurational complexity.

In order to predict the formation and binding energies of large interstitial clusters while accounting for the variation in the geometrical configuration of these (2D) clusters, we per-



(a) Vacancies



(b) Interstitials

Figure 2.11: (a) Normalized formation energies per (a) vacancy ( $E^f/V_n$ ) and per (b) interstitial ( $E^f/I_n$ ) as a function of the binding energy for all cluster sizes simulated. Triangle, square and circle symbols correspond to the Johnson, Ackland and Fellingner interatomic potentials respectively.

formed a Principal Component Analysis (PCA) [104] on the RDF of these clusters as it provides a suitable set of spatial correlations for the statistical quantification of the interstitial cluster structure. PCA provides an objective identification of reduced-order representations of the cluster structure by linearly transforming the high dimensionality of the structure of the cluster into an orthonormal basis where the axes are ordered according to the observed variance among the elements of the dataset. Hence, by knowing the size and geometrical configuration of a interstitial cluster via the RDF, a linear regression model can be trained to predict both the formation and binding energies of other interstitial clusters containing the same number of SIAs using only the statistical characterization of these clusters.

As an example, fifty different interstitial cluster configurations containing twenty five interstitials were created for the three niobium potentials used in this work. We show in Figure 2.12 examples of RDFs smoothed using a Gaussian filter.

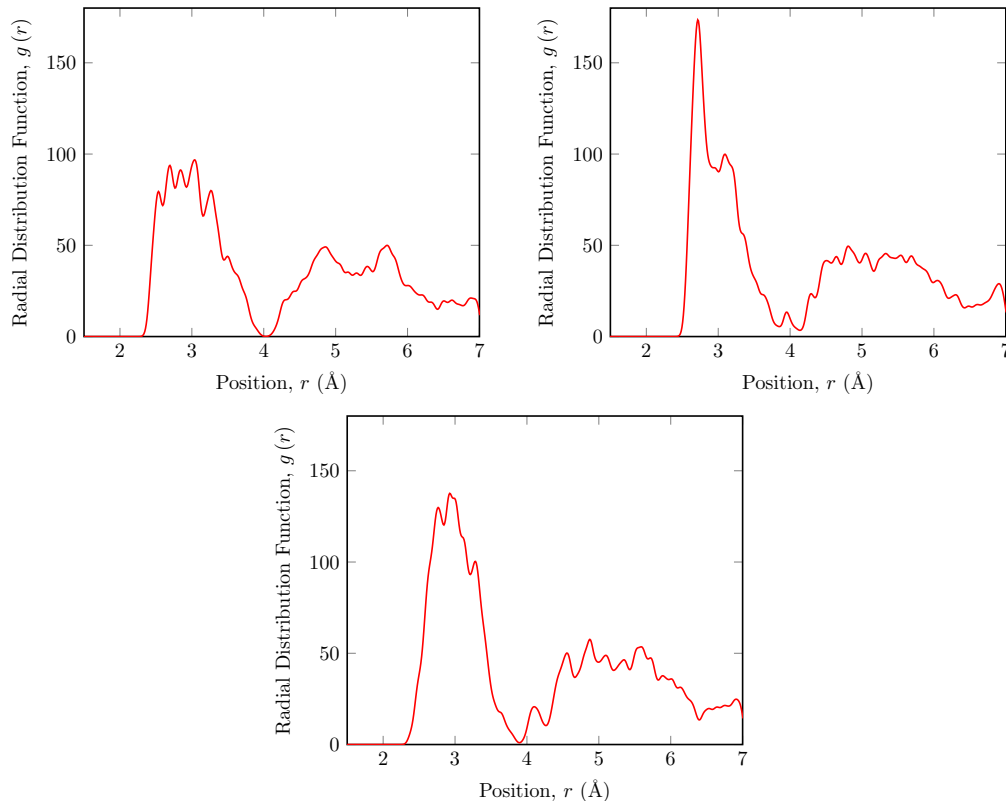


Figure 2.12: RDFs of interstitial clusters containing 25 interstitials produced using the (a) Johnson, (b) Ackland, and (c) Feller potentials, from left to right. RDFs have been smoothed using a Gaussian filter.

The PCA was then performed on the smoothed RDFs, and a linear regression model for each interatomic potential was fit to the Principal Component (PC) scores. We show the parity plots of the models in Figure 2.13 for both the formation ((a)–(c)) and binding ((d)–(f)) energies. Our results show that a linear model can predict formation and binding energies of interstitial clusters when trained on a statistical characterization of those clusters, with mean squared error values of 1.27 eV, 0.87 eV, and 0.41 eV for the formation energy models built with the Johnson, Ackland, and Feller potentials respectively, and with mean squared error values of 0.05 eV, 0.07 eV, and 0.11 eV for the binding energy

models built with the Johnson, Ackland, and Feller potentials respectively.

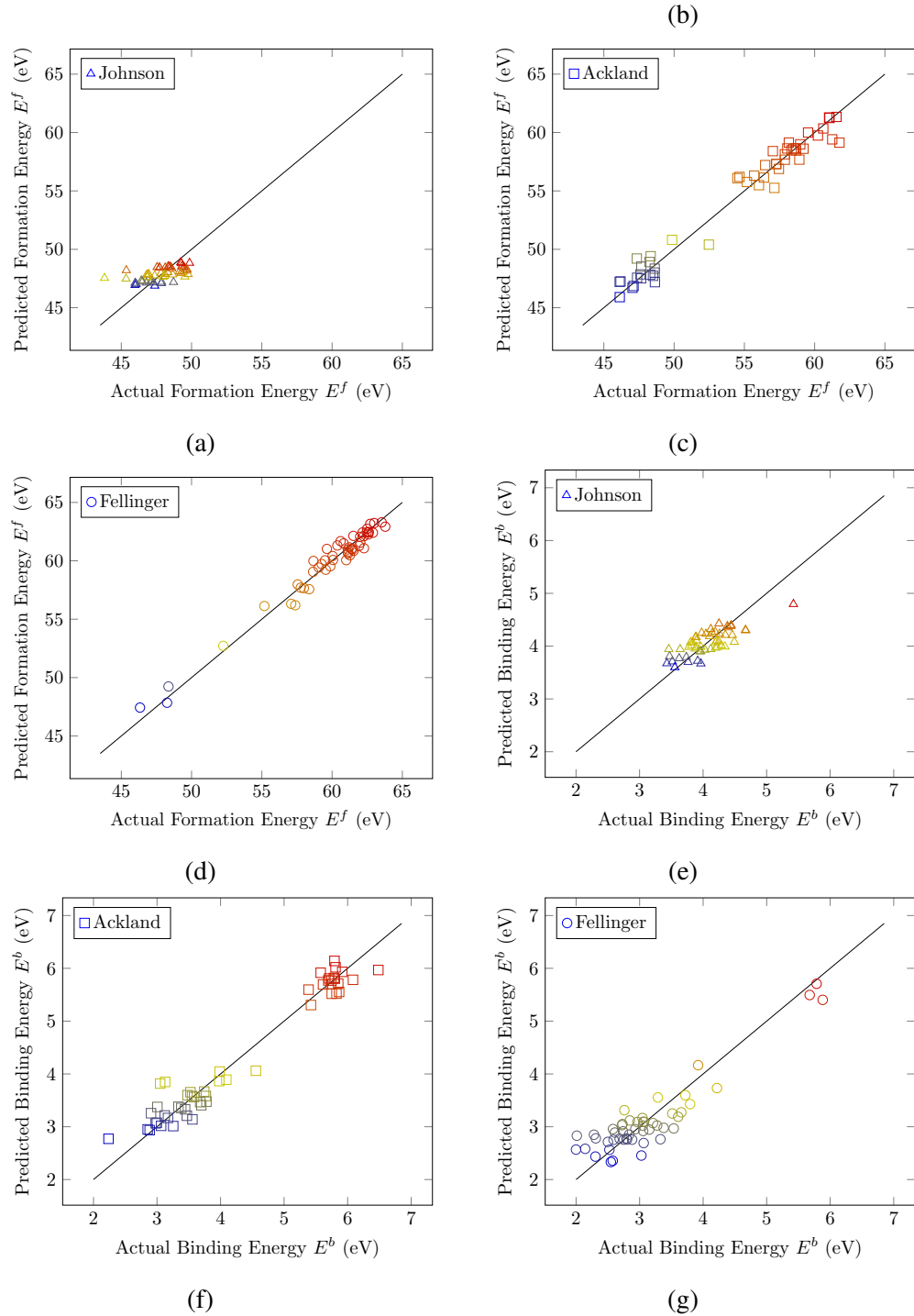


Figure 2.13: Parity plots shown for the linear models of actual versus predicted formation ((a)–(c)) and binding ((d)–(f)) energies produced using the Johnson ((a) and (d)), Ackland ((b) and (e)), and Feller ((c) and (f)) interatomic potentials for Nb.



It is interesting to note however that the model trained on interstitial clusters produced using the Johnson/Demkowicz potential [96, 97] produces a spread in the predicted energies compared to the actual energies and are more energetically localized compared to the other two potentials. Thus, results for the Johnson/Demkowicz potential indicate that the PC scores of the RDFs of these clusters do not capture the information needed to predict formation energy, while they do suffice for the interstitial clusters produced using the Ackland and Feller potentials. The main explanation for the spread in the predicted energy from the Johnson potential stems from the large variation in (metastable) geometrical configurations predicted by this potential (some configurations are predicted as 2D  $1/2\langle 111 \rangle$  loops other as crossovers between  $1/2\langle 111 \rangle$  and  $\langle 100 \rangle$  loop) as compared to the Ackland and Feller potentials which predict consistently the type of 2D structures among the fifty realizations generated. Overall results obtained with Ackland interatomic potential provide the best for both the formation and binding energies with a  $R^2$  value of 0.97 for the formation energy (Johnson/Demkowicz: 0.31; Feller: 0.97) and 0.95 for the binding energy (Johnson/Demkowicz: 0.60; Feller: 0.84).

In the original work of Alexander et al. [67], the coefficients of Equation 2.11 were fit to specific dislocation loop types. Here, we show that these coefficients can be inferred from one type to the other based on the geometrical configuration.

#### *Role of helium on the stability of nano-sized defect clusters*

When helium is introduced into a vacancy cluster, both the formation and binding state of that cluster are drastically changed. We present the minimum formation energies of helium interstitials, helium bubbles, and helium-vacancy clusters in Table 2.4. We found good agreement between our predictions and those found in the literature for small helium-vacancy clusters calculated from DFT simulations [60]. For the sake of simplicity, we refer to helium-vacancy clusters via the nomenclature  $\text{He}_n\text{V}_m$ , where  $n$  is the number of helium atoms and  $m$  is the number of vacancies in the helium-vacancy cluster. A cluster

Table 2.4: Helium-vacancy cluster formation energies. First column describes the type of helium-vacancy cluster, second column provides the calculated binding energy and the third column lists values found in the literature.

Defect Type	Formation energy $E^b$ (eV)	Literature
He - Octahedral	3.520	3.43[60] 3.26[70] 3.71[106]
He - Tetrahedral	3.617	3.15[60] 3.05[70] 3.45[106] 3.55[89]
He - Substitutional	3.679	4.27[60] 3.74[89]
2 He - Interstitial	6.651	6.24[60]
3 He - Interstitial	9.466	9.25[60]
4 He - Interstitial	12.313	11.69[60]
He <sub>1</sub> V <sub>2</sub>	6.112	6.19[60] 5.90[89]
He <sub>1</sub> V <sub>3</sub>	7.686	
He <sub>2</sub> V <sub>1</sub>	5.508	5.91[60]
He <sub>3</sub> V <sub>1</sub>	7.387	7.77[60]
He <sub>4</sub> V <sub>1</sub>	9.127	9.68[60]
He <sub>2</sub> V <sub>2</sub>	6.508	7.43[60]
He <sub>3</sub> V <sub>2</sub>	7.819	9.10[60]
He <sub>4</sub> V <sub>2</sub>	9.284	10.20[60]
He <sub>5</sub> V <sub>2</sub>	10.804	
He <sub>6</sub> V <sub>2</sub>	12.222	
He <sub>7</sub> V <sub>2</sub>	13.718	
He <sub>8</sub> V <sub>2</sub>	15.231	

noted He<sub>1</sub>V<sub>1</sub> corresponds to a substitutional He atoms in the Nb lattice. A helium-vacancy cluster noted as He<sub>n</sub>V<sub>m</sub> corresponds to  $n$  He atoms in a void constituted of  $m$  vacancies.

For larger clusters, as illustrated in Figure 2.14 (a), the formation energy of a helium-vacancy cluster, He<sub>n</sub>V<sub>m</sub>, of size  $n + m$  increases as the helium-to-vacancy ratio  $n/m$  increases, where the ratio is defined independently of the cluster size. In other words, only small helium bubbles can form in bulk niobium in accordance with experimental observations [105].

The binding energies of a vacancy to a small helium-vacancy cluster, He<sub>n</sub>V<sub>m</sub>, for  $m = [1, 4]$  were computed for various helium-vacancy reactions as listed in Table 2.5. This allows for a direct comparison to the binding energy of a vacancy to a pure vacancy cluster. In Figure 2.14, we show the role of helium-to-vacancy ratio  $n/m$  on the stability of vacancy clusters. The ratio is defined independently of the helium-vacancy cluster size. Similar to observations in other bcc systems [107], our results indicate that the addition of a vacancy

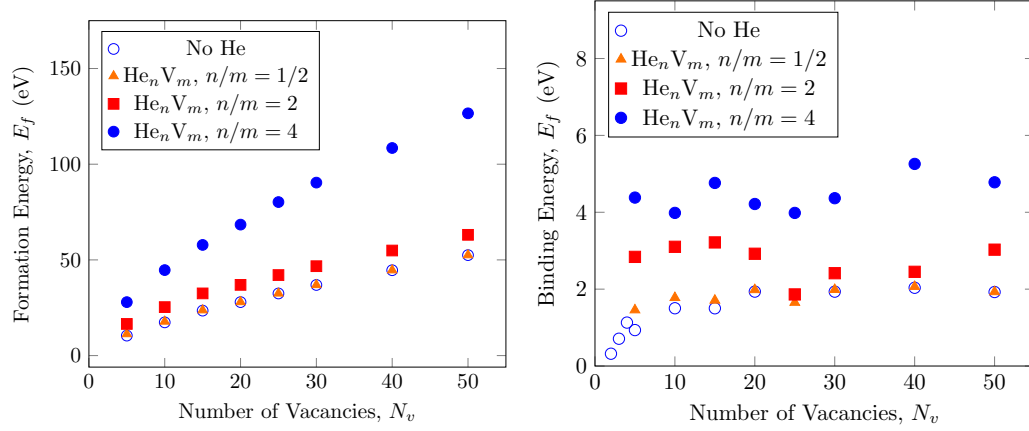


Figure 2.14: (a) Formation and (b) vacancy binding energies of a helium-vacancy cluster as a function of cluster size and helium-to-vacancy ratio ( $n/m$ ). Triangle, square and filled circle symbols correspond to  $n/m = 1/2, 2, 4$  respectively.

to a vacancy cluster gradually increases the binding energy with helium-to-vacancy ratios, as a result primarily of the change of geometrical configuration. Helium appears to have a significant effect on the binding of vacancies to a bubble.

Table 2.5: Helium defect binding energies. NNS: nearest neighboring site; 2NNS: second nearest neighboring site.

Reaction	Binding energy $E^b$ (eV)	Literature
$\text{He}_{\text{oct}}^{\text{int}} + V \rightarrow \text{He}_1\text{V}_1$	2.588	
$\text{He}_{\text{tet}}^{\text{int}} + V \rightarrow \text{He}_1\text{V}_1$	2.691	1.54[60] 2.57[89]
$\text{He}_{\text{oct}}^{\text{int}} + \text{V}_2(\text{nns}) \rightarrow \text{He}_1\text{V}_2(\text{nns})$	2.803	
$\text{He}_{\text{tet}}^{\text{int}} + \text{V}_2(\text{nns}) \rightarrow \text{He}_1\text{V}_2(\text{nns})$	2.906	
$\text{He}_{\text{oct}}^{\text{int}} + \text{V}_2(2\text{nns}) \rightarrow \text{He}_1\text{V}_2(2\text{nns})$	2.588	
$\text{He}_{\text{tet}}^{\text{int}} + \text{V}_2(2\text{nns}) \rightarrow \text{He}_1\text{V}_2(2\text{nns})$	2.692	2.05[60] 2.80[89]
$\text{He}_1\text{V}_1 + V \rightarrow \text{He}_1\text{V}_2(\text{nns})$	0.571	
$\text{He}_1\text{V}_1 + V \rightarrow \text{He}_1\text{V}_2(2\text{nns})$	0.320	0.75[60] 0.59[89]
$\text{He}_{\text{oct}}^{\text{int}} + \text{V}_3(a) \rightarrow \text{He}_1\text{V}_3(a)$	3.021	
$\text{He}_{\text{tet}}^{\text{int}} + \text{V}_3(a) \rightarrow \text{He}_1\text{V}_3(a)$	3.125	2.38[60] 3.04[89]
$\text{He}_1\text{V}_2(\text{nns}) + V \rightarrow \text{He}_1\text{V}_3(a)$	0.928	
$\text{He}_1\text{V}_2(2\text{nns}) + V \rightarrow \text{He}_1\text{V}_3(a)$	1.180	0.99[60] 0.95[89]
$\text{He}_{\text{oct}}^{\text{int}} + \text{V}_4(a) \rightarrow \text{He}_1\text{V}_4(g)$	3.021	
$\text{He}_{\text{tet}}^{\text{int}} + \text{V}_4(a) \rightarrow \text{He}_1\text{V}_4(g)$	3.125	2.38[60] 3.04[89]

#### 2.2.4 Conclusions

In this task, we investigated the formation and binding energies of vacancy and interstitial clusters in niobium via MD simulations using three different interatomic potentials. The main results were the development of scaling laws of both of these energies as a function of the size and geometrical configurations allowing us to treat various cases of 3D vacancy and 2D interstitial clusters. Our results show that the size dependence of vacancy and interstitial clusters can be approximated by a functional form that accounts for bulk and surface effects as well as some considerations of elastic interactions.

Our study shows that large vacancy clusters form 3D faceted void configurations consisting of only  $\{100\}$  and  $\{110\}$  surfaces with various shape ratios depending on the interatomic potential used, while large interstitial clusters form 2D  $\frac{1}{2}\langle 111 \rangle$  planar dislocation loops or crossovers between  $\frac{1}{2}\langle 111 \rangle$  and  $\langle 100 \rangle$  loops depending on the interatomic potential used. From the interpretation of a statistical analysis of the spatial correlations of interstitial cluster geometrical configurations, the predictability and reliability of these potentials can be assessed, where the interatomic potential designated as the Ackland potential seems to provide the best agreement with existing data on energetics of defects and predictability across the various metastable configurations of defects.

Regarding the stability of helium–vacancy clusters, our results show that, based on the binding energies of a vacancy to the helium–vacancy clusters, helium can increase the binding energy of a vacancy to a helium–vacancy cluster.

Taken together, these results and conclusions, our parameterized functional forms for the formation and binding energies are valid for a very broad range of defect sizes and configurations making it possible to be used directly in a coarse-grained modeling strategy such as Monte Carlo, cluster dynamics or dislocation dynamics that look at defect accumulation and evolution in microstructures [90, 108].

# **CHAPTER 3**

## **EXAMINATION OF RADIATION DAMAGE IN RADIATION-TOLERANT MICROSTRUCTURES**

In this chapter, we seek to address the second question posed in Chapter 1,

**Q2** What does defect formation and evolution look like in a radiation-tolerant material?

First we present in section 3.1 a study of radiation damage formation and accumulation mechanisms in gold and niobium nanowires and nanoporous structures, with the intent of examining how those mechanisms change with the length-scale of the microstructures. Through this study, we determined unique damage accumulation mechanisms based on the length-scale and element of the structures, and discuss the nature of radiation tolerance in these structure types.

In section 3.2 we present a study examining the impact of radiation damage on the mechanical behavior of nanowires. We discuss how the defects introduced to the surface and bulk regions of these microstructures change their response to mechanical loading. We also note how the accumulation of radiation damage in these radiation tolerant microstructures allows for a different impact on the mechanical behavior of the materials compared to those observed in conventional microstructures.

This chapter is concluded in section 3.3 with a short summary of the implementation of a new interatomic potential into the molecular dynamics code LAMMPS, as well as a study using this new potential to examine the stability of the 4H hexagonal phase in gold at 0 K. This interatomic potential is able to accurately reproduce material surface energies as well as thermal properties, making it an ideal potential for use in studying complex microstructures in highly non-equilibrium conditions, such as irradiation.

### **3.1 Size-dependent radiation damage mechanisms in nanowires and nanoporous structures [24]**

#### 3.1.1 Introduction

Nanostructured materials have attracted significant interest due to the reported improved tolerance to radiation damage compared to conventional coarse-structured materials [4, 109, 110]. Such behavior is correlated with the high density of interfaces (free surfaces, grain/phase boundaries) in these nanostructured materials, which act as sinks for radiation-induced defects. Metallic nanoporous materials and nanowires are of particular interest because of their abundance of free surfaces. Free surfaces serve as perfect damage sinks, allowing for the continuous annihilation of defects as they are produced. In turn, this seemingly continuous annihilation process prevents the agglomeration of small defects into larger defect clusters that can otherwise degrade mechanical, electrical, or thermal properties [4, 111]. However, the exact details about the mechanisms at the origin of radiation damage in these structures remain elusive due to their transient nature and the atomic scale at which they occur.

It has been previously reported that radiation damage in gold (Au) nanoporous materials depends on the ligament size and irradiation conditions [25, 112–119]. For instance, Bringa et al. [112] used atomistic models to determine that nanowires below some critical size experienced irradiation-induced melting with minimum damage, while nanowires above an upper critical size behaved as bulk materials and accumulated defects. Their results showed that this critical size is a function of the recoil energy of the cascade interacting with the nanowire.

Similarly, Ruestes et al. [116] explored heavy-ion irradiation effects on nanoporous gold structures using atomistic simulations and showed that the ligament morphology changes in the irradiated region is caused by local melting. These simulation predictions are confirmed by the experimental observations of Gomes et al. [118] and Hu et al. [119]. The

Ga-ion irradiation experiments in gold nanoporous networks by Gomes et al. [118] showed that the irradiated samples presented a thickening of the width of ligaments and a reduction in the ligament length resulting in an overall densification of the nanoporous network. More recently, Hu et al. [119] performed gold and carbon ion irradiations on nanoporous gold to study the effect of ion species on the irradiation-induced changes in these structures. Their observations showed that heavy-ion irradiation (gold ions) had a greater effect on modifying the surface morphologies of ligaments while light-ion irradiation (carbon ions) tends to cause coarsening of the ligaments.

In terms of damage accumulation, Briot et al. [117] experimentally observed that, in nanoporous gold, and for a broad range of irradiation conditions (46 keV, 1.7 MeV, and 10 MeV Au-ion irradiation), ligaments with a diameter less than 25 nm exhibited little-to-no visible defect accumulation. They also observed the absence of a denuded region near the surface above this critical ligament size, indicating that the radiation tolerance of nanoporous materials is dependent not only on the extrinsic length scale of the ligaments, but also on a capillary length scale, which is determined by the surface curvature of the ligaments.

In addition to these size-dependent cases of radiation damage, irradiated nanostructured materials can also experience phase changes such as amorphization or transitions to another crystalline state. For instance, Sprouster et al. [120] and later Siva et al. [121] showed that the irradiation of cobalt nanoparticles and thin films by moderate-energy gold ions transforms the FCC cobalt phase into a Hexagonal Close-Packed (HCP) phase. This effect has also been observed in other FCC material systems. For example, ion irradiation of gold [122] and nickel [123] nanocrystalline films displayed a similar phase transformation from an FCC structure to a stabilized HCP structure. As a general rule, these observations indicate that nanostructured materials in a wide range of FCC metals can phase transform with suitable irradiation conditions, and that this transformation mechanism is size-dependent. At the same time, this additional phenomenon further complicates

our understanding on the origins of the mechanisms resulting in radiation tolerance at the nanoscale.

To date, the majority of the computational studies examining the origins of the radiation tolerance of nanoporous materials has focused on gold nanowires as an abstraction of nanoporous FCC systems [26, 112, 113, 124–126] and on tungsten or iron for BCC systems [127, 128]. These studies were based on atomistic simulations and they were limited to a small number of single radiation events interacting with nanowires of various sizes. For example, Fu et al. [113] performed atomistic simulations of a gold nanowire and examined the accumulation of damage due to consecutive PKAs, considering however only up to six consecutive PKAs.

These foundational computational efforts provide insights on the unitary mechanisms responsible for the response of nanowires exposed to single radiation events. However, understanding the compounding mechanisms at the origin of the radiation tolerance of these low-dimensional nanomaterials to higher damage levels (also referred to as dose in the remainder of this section) remains limited partially due to the inability of consecutive PKA simulations to reach large damage levels, and we therefore have to rely primarily on experimental observations. The complex interplay between the multiple defect interaction mechanisms and size effects are inextricably linked to each other but hard to observe experimentally, generally only through in-situ ion irradiation TEM.

Herein, we study the mechanisms of damage accumulation up to large damage levels (measured in displacement-per-atom or dpa) in nanowires of sizes ranging from 3 nm to 40 nm and in nanoporous materials in model FCC gold and BCC niobium (Nb) using a combination of accelerated multi-cascade atomistic simulations [23] and in-situ ion irradiation microscopy observations. We chose these two classes of materials primarily because the nature of radiation-induced defects between FCC and BCC materials is substantially different [129–131]. Indeed, the mobility of both interstitial and vacancy clustering depends on the dislocation character, the crystal structure, and the stacking-fault energy.



For instance, Stacking Fault Tetrahedras (SFTs) are only found in FCC structures. Gold nanowires and nanoporous structures are taken as an exemplar FCC metallic system [25, 112, 113, 117], while niobium is a refractory BCC metal with important applications in nuclear systems [88, 132, 133]. However, there are currently little to no publications examining the radiation response of niobium nanostructures via experimental or computational means. The comparison between nanowires and nanoporous structures enables us to gain insights into the damage accumulation mechanisms in complex nanoporous structures.

We also compare the efficiency of these structures to mitigate radiation damage to that seen in single crystals. In subsection 3.1.2, we present the methodology for generating the various nanostructures and simulating radiation damage. In subsection 3.1.3, we describe our ion irradiation experiments of gold and niobium nanoparticles and nanoporous nanostructures using in-situ TEM. In subsection 3.1.4, we examine size-dependent mechanisms of damage accumulation up to large damage levels in gold and niobium nanowires. In subsection 3.1.5, we compare the radiation response and associated radiation tolerance between single crystal, nanowires, and nanoporous structures, and give credence to our modeling predictions through comparison with the experimental observations made via in-situ TEM.

### 3.1.2 Computational Methods

We used the open-source molecular dynamics simulation code LAMMPS [15] to perform all of our radiation-damage atomistic simulations. We conducted these simulations to gain insights into the mechanisms of radiation damage accumulation in single crystals, nanowires, and nanoporous structures in both FCC (Au) and BCC (Nb) nanostructures. The simulation workflow is composed of two steps: (i) create and equilibrate the structures (single crystal, nanowire, nanoporous structures), and (ii) accumulate radiation-induced damage in these structures. We extracted and analyzed the defect and dislocation configurations accumulating during these simulations using a combination of CNA, Wigner-Seitz

defect analysis, and Dislocation Extraction Analysis (DXA), as implemented in the OVITO software [101, 134]. The central features for each step in our workflow are presented below. Additional details are provided in the Appendix C.

### *Description of Interatomic Interactions*

We used two EAM interatomic potentials developed by Foiles, Baskes, and Daw [135] and Ackland et al. [136] to describe the interatomic interactions in gold and niobium respectively. The gold interatomic potential was fit to the formation energies of vacancy defects amongst other parameters and was found to closely match low-index surface energies, as well as the formation and migration energies of vacancies and self-interstitials. This interatomic potential has been successfully used in other studies to simulate radiation damage in gold nanowires and nanoporous structures [113, 125, 126]. The niobium interatomic potential was developed for the simulation of defects, free surfaces, and grain boundaries and proved to be the best suited to study the formation and evolution of defects during radiation as compared to other interatomic potentials [21].

In order to simulate displacement-cascade collisions, we overlaid the gold interatomic potential with a short-range repulsive term (nuclear stopping) via the Ziegler-Biersack-Littmark (ZBL) [137, 138] universal screening function. Adding the ZBL overlay provides a strong repulsive force at short distances which prevents atoms from getting too close during high-energy cascades. We chose ZBL switching function parameters of  $r_1 = 0.4617 \text{ \AA}$  (distance where the ZBL switching function begins) and  $r_2 = 1.20 \text{ \AA}$  (global cutoff for ZBL interaction) [125], as implemented in LAMMPS. The niobium interatomic potential already contained a close-range repulsion term and was not modified for short-range interactions. For both gold and niobium interatomic potentials, we also included the effects of electronic stopping as a frictional drag force which is linearly proportional to the atomic velocity [139, 140]. This frictional force was applied to atoms with kinetic energy  $\geq 3.79 \text{ eV}$  for gold and  $\geq 7.48 \text{ eV}$  for niobium.

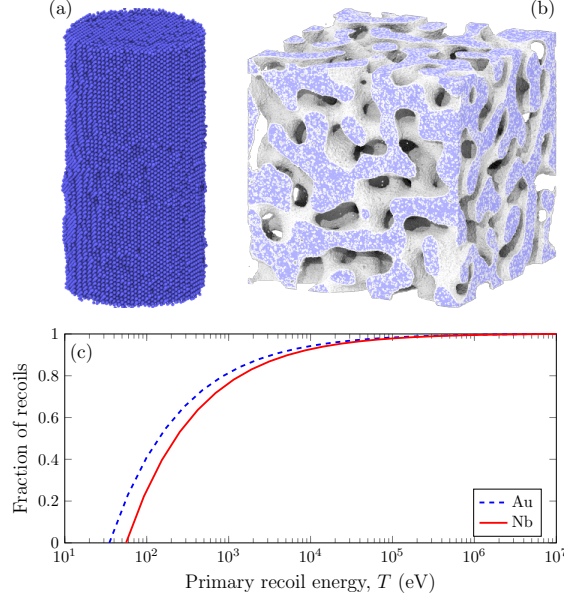


Figure 3.1: (a)-(b) Examples of structure types considered in this work. The nanowire represented in (a) has a diameter of 10 nm. The nanoporous structure in (b) has an average ligament size of 12 nm. Structures displayed in (a) and (b) correspond to renders after irradiation. (c) Primary recoil spectrum used from sampling recoil energies in the consecutive cascade simulations and accelerated radiation-damage accumulation simulations.

### *Construction of Nanowires and Nanoporous Structures*

Figure 3.1(a) and (b) illustrate examples of the structures considered in this work for both gold and niobium. We simulated nanowire structures as a simplified representation of ligaments seen in nanoporous structures, where nodes are excluded. Nanowires are commonly used to approximate the nanoporous materials. We also simulated single crystals to provide a baseline for the radiation damage. Finally, we simulated actual nanoporous structures to be compared with the nanowire and single crystal results, as well as our experiments performed in nanoporous thin films.

We generated gold and niobium nanowires by creating cylindrical columns of atoms with diameters of 3, 10, 14, 20, 30, and 40 nm. For all of these nanowires, we chose to have a fixed aspect ratio with the length of the wire taken as twice the diameter. The longitudinal direction of the nanowire is along the  $\langle 100 \rangle$  crystallographic direction for both gold and niobium. The simulation cell is periodic along the longitudinal direction. These models

contain between  $\sim 2,400$  to 5.9 million atoms depending on the diameter of the nanowire. After constructing the initial nanowire system at 0 K, we thermalized the simulation cell using an isobaric-isothermal (NPT) ensemble at 300 K and zero pressure. Additional details on the construction of the nanowires are provided in Note 1 of Appendix C.

We constructed gold and niobium nanoporous structures via our three-dimensional (3D) in-house phase-field model for the spinodal decomposition of a binary alloy with a 50-50 phase fraction [27, 141]. We populated the voxelated, phase-field-based, nanoporous model with either FCC (Au) or BCC (Nb) atomic lattices for one of the phases using nanoSCULPT for structures with a porosity of approximately 45% [142]. Using the open-source software FoamExplorer [143], we determined that the initial average diameters of the gold and niobium nanoporous structures after temperature equilibration were  $10.6 \pm 3.9$  nm and  $11.2 \pm 4.3$  nm respectively corresponding to the ligament size found in our experimental nanoporous microstructures synthesized by dealloying [117]. The 3D, phase-field-based, gold and niobium nanoporous structures are periodic in all directions with dimensions  $\sim 125 \text{ nm} \times 125 \text{ nm} \times 125 \text{ nm}$ , containing  $\sim 50$  million atoms. After constructing the initial nanoporous structures at 0 K, we equilibrated the simulation cell using an NPT ensemble at 300 K and zero pressure. After equilibrating the nanoporous structures to the desired temperature, the nanostructures were analyzed to determine if the equilibration process had resulted in the formation of any dislocations. For both the gold and niobium nanoporous structures, no dislocations were detected. In the case of the gold nanostructure, no stacking faults were found. Additional details on the construction of the nanoporous structures are provided in Note 2 of Appendix C.

We also generated cubic single-crystal structures of gold and niobium with dimensions of  $\sim 59 \text{ nm} \times 59 \text{ nm} \times 59 \text{ nm}$ . The simulation cell is periodic in all directions. After constructing the initial single-crystal structures at 0 K, we equilibrated the simulation cell using an isochoric ensemble (NVT) held at 300 K. Additional details are provided in Note 3 of Appendix C.

Table 3.1: Number of ROAC events inserted at each time step for various structures in both gold and niobium.

Structure	Au		Nb	
	ROAC events	Dose rate (dpa.s <sup>-1</sup> )	ROAC events	Dose rate (dpa.s <sup>-1</sup> )
10-nm nanowire	100	$5.3 \times 10^7$	100	$8.8 \times 10^7$
20-nm nanowire	100	$6.8 \times 10^6$	100	$1.1 \times 10^7$
30-nm nanowire	500	$1.0 \times 10^7$	300	$9.7 \times 10^6$
40-nm nanowire	1,000	$8.5 \times 10^6$	500	$6.8 \times 10^7$
Single crystal	3,000	$1.3 \times 10^7$	3,000	$2.1 \times 10^7$
Nanoporous	20,000	$1.9 \times 10^7$	18,000	$2.7 \times 10^7$

### *Simulation of Radiation Damage*

After creating and equilibrating the various nanostructures, we simulated displacement cascades and the accumulation of radiation-induced defects up to a given damage level (up to 1 dpa) using a combination of two different techniques. For the very small nanowires (*i.e.*, diameter = 3 nm), we performed consecutive explicit PKA events with recoil energies sampled from the primary recoil spectrum shown in Figure 3.1(c). We simulated up to 100 consecutive cascades for these small nanowires since, as discussed in the subsequent sections, their behavior is primarily dominated by sputtering (see additional details on the PKA simulations in Notes 4 and 5 of Appendix C). In the consecutive-cascades simulations, each PKA event is inserted into the atomistic system every 50 ps, resulting in a total simulation time of 5 ns. However, simulating a series of consecutive single PKA events is computationally too expensive to reach large damage levels as the ones targeted in this study (*i.e.*, 1 dpa). Instead, for the larger nanowires (*i.e.*, diameter  $\geq 10$  nm), we used a recently developed accelerated, multi-cascade method (namely the Reduced-Order Accelerated Cascade (ROAC)) to simulate the accumulation of radiation damage in all the nanostructures [23].

The ROAC method [23] introduces collision cascades as core-shell atomic structures approximating a displacement cascade by considering the Athermal-Recombination-Corrected (ARC) Displacements per Atom (dpa) in the shell, and the Replacements per Atom (rpa)

atomic mixing in the core. Depending on the size of the simulation cell and the energy of the recoil events, the ROAC method can model large dose accumulation, three to four orders of magnitude faster than performing consecutive PKA simulations, thus enabling us to reach large damage levels. Indeed, in this method, we simultaneously simulate multiple, isolated recoil events at once, provided that the core regions do not overlap. We list in Table 3.1 the number of ROAC events inserted at each time interval for the various structures considered.

We calibrated the core-shell structures for a broad range of recoil energies by performing explicit PKA simulations in bulk gold and niobium, and then combining results from these PKA simulations with an extension of the Norgett-Robinson-Torrens (NRT) dpa model [144, 145] to estimate cascade defect production efficiency (ARC-dpa) and mixing effects (rpa). In the ROAC method, at equally-spaced time intervals, we randomly inserted  $N$  recoil events in the various nanostructures studied with recoil energies sampled from the primary recoil spectrum shown in Figure 3.1(c). Sampling from this recoil spectrum is meant to reproduce our experimental irradiation conditions described in subsection 3.1.3. In the case of nanowires and nanoporous nanostructures, the ROAC events were inserted as long as they did not overlap with the free surface of the wire. In the case of the 10-nm nanowires, due to the small size of the atomic system and the associated high probability of a cascade interacting with the free surface, we adopted a hybrid simulation strategy. In this case, if a ROAC event did overlap with the free surface, we instead performed an explicit PKA event near the surface for that specific cascade event. As discussed later, for this small size of nanowires, this hybrid approach resulted in a small amount of sputtering at the surface, but the 10-nm wire remained nonetheless stable.

The damage level,  $N_{\text{dpa}}$ , was calculated according to the extension of the NRT model [145] to estimate the number of displaced atoms caused by each ROAC event with energy  $T$  such

Table 3.2: Material constants for the modified NRT-dpa defect production model in Equation 3.1 and Equation 3.2.

	$E_d$ (eV)	$b_{\text{dpa}}$	$c_{\text{dpa}}$
<b>Au</b>	35.0	$-1.044 \pm 0.0957$	$0.220 \pm 0.0095$
<b>Nb</b>	56.0	$-0.485 \pm 0.0270$	$0.172 \pm 0.0155$

that,

$$N_{\text{dpa}} = \begin{cases} 0 & \text{for } T < E_d \\ 1 & \text{for } E_d < T < \frac{2E_d}{0.8} \\ \frac{0.8T}{2E_d} \xi_{\text{dpa}}(T) & \text{for } \frac{2E_d}{0.8} < T < \infty \end{cases} \quad (3.1)$$

and,

$$\xi_{\text{dpa}}(T) = \frac{1 - c_{\text{dpa}}}{(2E_d/0.8)^{b_{\text{dpa}}}} T^{b_{\text{dpa}}} + c_{\text{dpa}}, \quad (3.2)$$

$$\xi_{\text{rpa}}(T) = \left[ \frac{b_{\text{rpa}}^{c_{\text{rpa}}}}{(2E_d/0.8)^{c_{\text{rpa}}}} + 1 \right] \frac{T^{c_{\text{rpa}}}}{b_{\text{rpa}}^{c_{\text{rpa}}} + T^{c_{\text{rpa}}}}, \quad (3.3)$$

where  $E_d$  is the threshold displacement energy, and  $b_{\text{dpa}}$ ,  $c_{\text{dpa}}$ ,  $b_{\text{rpa}}$ , and  $c_{\text{rpa}}$  are material specific constants determined from MD simulations or experiments. The function  $\xi_{\text{dpa}}(T)$  represents the fraction of surviving defects due to athermal recombination, while  $\xi_{\text{rpa}}(T)$  represents the number of atoms that are displaced and return to lattice positions within the thermal spike. The threshold displacement energy for niobium was taken from Chen, Deo, and Dingreville [23], while the threshold displacement energy for gold was taken from Bauer and Anderman [146]. The coefficients used in this work are shown in Table 3.2. Since we calculated the number of displaced atoms directly from the atomic system, our measure of radiation damage implicitly accounts for the free surfaces and shapes of the atomic systems studied. Additional details of the ROAC method are provided in Notes 6 and 7 of Appendix C.

In both the consecutive-cascades and ROAC simulations, the recoil spectrum was chosen to match the energy spectrum used in the majority of the experiments discussed below,

however due to intrinsic time scales associated with molecular dynamics, the simulated dose rate is several orders of magnitude higher ( $\sim 1.0 \times 10^7$  dpa.s<sup>-1</sup>, see individual simulated dose rates for each structure in Table 3.1) than the one seen in the ion irradiation experiments ( $\sim 2.9 \times 10^{-3}$  dpa.s<sup>-1</sup>). Therefore, our results do not capture slower mechanisms (*e.g.* diffusion of point defects and small clusters) occurring at larger time scales. The degree to which missing these mechanisms will impact the accumulation of radiation damage is expected to increase as the length-scale of the microstructures increase. Ultimately, it is expected that the defect densities that are observed in our simulations will be higher than those that would occur in systems irradiated at experimental dose rates, with the possibility that the size regime where we observe radiation tolerance also being restricted to a smaller range of structural sizes. As pointed out in Chen, Deo, and Dingreville [23], the inability for the atomistic timescale to accurately reach characteristic times associated with diffusion processes does restrict our methodology to capture the interaction and clustering of point defects and small clusters at low damage levels as the ones studied here.

### 3.1.3 Experimental Methods

We compared our modeling results to in-situ TEM ion irradiation experiments of gold and niobium nanoporous thin films [117, 147] and gold nanoparticles and nanorods [148, 149]. These experiments and the analysis of the irradiated samples was performed by collaborators to this project. The gold nanoporous films were produced via chemical dealloying of gold-silver (Au-Ag) alloy samples deposited via physical vapor deposition onto sodium-chloride substrate and floated off [117]. Similarly, the niobium nanoporous films were produced via thermal dealloying of niobium-magnesium (Nb-Mg) alloy samples [147]. In both cases, the synthesis of gold and niobium nanoporous films via these routes provides excellent control of the external dimensions of the sample as well as ligament size in the nanometer regime, for comparison to the simulation results. The gold nanoparticles and nanorods were produced by Nanopartz, Inc. (Loveland, CO) and drop cast on TEM grids



with a carbon film support.

In order to characterize the dynamics and stability of these nanoporous films under radiation conditions, we exposed them to ion irradiation during real time TEM observation. All of the in-situ TEM experiments were completed using bright-field imaging at the in-situ ion irradiation TEM facility at Sandia National Laboratories [150]. For the radiation experiments, we used heavy ion irradiation produced from a 6 MV tandem accelerator with either gold or niobium ions at energies sufficient to create significant damage in the nanoparticles and nanoporous films. For the 1.7 MeV Au<sup>3+</sup> beam used to irradiate the gold and niobium nanoporous films in our experiments, the predicted dose rate is approximately  $\sim 2.9 \times 10^{-3}$  dpa.s<sup>-1</sup> [117] as estimated with the Stopping and Range of Ions in Matter (SRIM) software [138].

#### 3.1.4 Results: Mechanisms of Radiation Damage Accumulation in Nanowires

Our simulations reveal three primary radiation-induced damage mechanisms in gold and niobium nanowires depending on the size and crystallography of the wires. For very small nanowires, the dominant behavior is primarily governed by sputtering. For large sizes, the primary mechanism for damage accumulation is based on the formation and accumulation of point defects to form dislocation loops and defect clusters. Finally, for a narrow range of wire diameters, coined as the Goldilocks zone, gold nanowires experience an FCC-to-HCP phase transformation, not observed in smaller or larger sizes. In addition to these radiation-induced mechanisms, we also discuss the origin of surface roughening seen in both FCC and BCC nanowires regardless of the size of the nanowire. In what follows, we describe each mechanism in detail.

##### *Sputtering at small sizes*

We begin by investigating the mechanism of defect accumulation in small nanowires with a 3-nm diameter. Figure 3.2 quantifies the amount of sputtering seen in these small gold

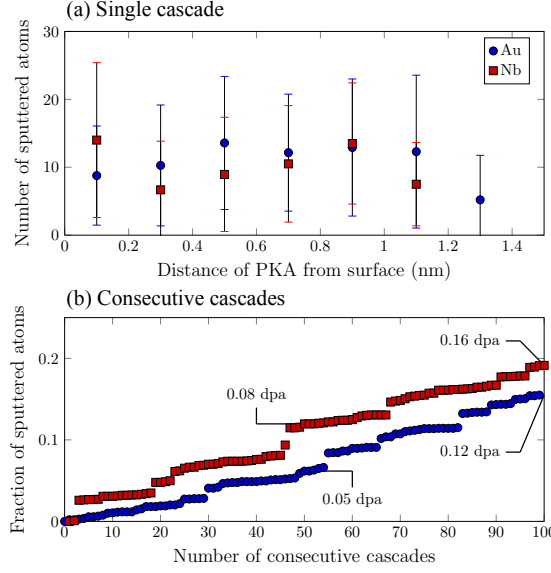


Figure 3.2: (a) Number of atoms sputtered in 3-nm gold and niobium nanowires due to a single 3 keV cascade initiated at a random distance from the surface. Error bars show the standard deviation around the average value. (b) Fraction of atoms sputtered in 3nm gold and niobium nanowires as a function of the number of consecutive cascades. Almost 20% of the atoms are sputtered off the nanowires after only 100 cascades. Equivalent damage levels (measured in dpa) are indicated for 50 and 100 consecutive cascades. Gold and niobium data are represented with circle and square symbols respectively.

and niobium nanowires during the interaction with both single and consecutive cascades respectively. Our results show that, for such small sizes, regardless of where a cascade is initiated with respect to the free surface, atoms are sputtered from the wire, and sputtering is the dominant damage mechanism. This corollary is even more relevant as the probability of cascade/surface interaction increases with the amount of radiation damage. Figure 3.3 presents snapshots of the type of defects that accumulated after 10, 50, and 100 consecutive cascades in 3-nm gold and niobium nanowires respectively. In this figure, we only represented the surface of the nanowire and atoms not in their lattice positions. First, these simulations demonstrate that, for the 3-nm wires, large craters are formed at the surface of the wires. In fact, our single cascade results showed that, depending on the recoil energy, even a single cascade can obliterate and create large craters in those wires, in agreement with other studies [112, 151] and our own experimental observations [148, 149]. These sputtering results point to the fact that small nanowires are not stable enough to survive a

large amount of radiation. This is not the case for larger nanowires (*i.e.*, diameter  $\geq 10$  nm), for which sputtering is limited to a material- and energy-dependent region from the free surface (see Note 8 of Appendix C and subsection 3.1.4). For the large nanowires, outside this surface sputtering region, the cascade created by a PKA is too far away from the surface to cause any atom to be sputtered off the free surface of the wire, and therefore large nanowires can sustain some surface damage due to sputtering while remaining relatively stable [148, 152]. Second, in addition to sputtering, the small nanowires, both in gold and niobium, experience amorphization of the entire wire upon being struck by consecutive cascades (generally after 50 or more cascades), especially in the 3-nm configuration. This is a direct consequence of the relative size of the thermal spike during the development of a cascade with respect to the (small) size of the wire. In the case of the gold nanowires, as seen in Figure 3.3(a)-(c), some stacking faults form early on through the wire, but they are rapidly replaced by an amorphous region throughout the entire cross section of the wire (see additional information in Note 8 of Appendix C).

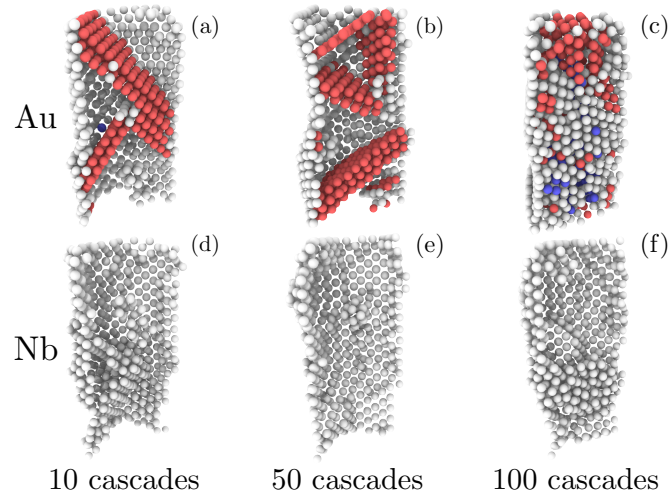


Figure 3.3: Evolution of defect accumulation after multiple consecutive cascades in 3-nm gold and niobium nanowires. (a) and (d) After 10 cascades, (b) and (e) after 50 cascades, and (c) and (f) after 100 cascades. White atoms represent disordered structures and red atoms denote atoms in the HCP configuration. Blue atoms are identified as BCC. Lattice atoms are not shown.

Despite the orders of magnitude difference in the temporal scale between the simula-

tions and the experiments, previous experimental studies [148, 149, 151, 153] exploring the radiation stability of gold nanoparticles and nanorods confirm that the radiation damage seen in small nanoparticles (*i.e.*, with characteristic dimensions  $<10$  nm) is dominated by sputtering. It has been determined from these experiments that, when the ion strike did result in a PKA, the structural impact to gold nanoparticles was extensive and found to be highly dependent on the size and crystallographic orientation of those nanoparticle [148, 149]. For instance, the impact of the length scale on the extent of sputtering can be seen in Fig. 3 in Bufford and Hattar [148] for gold nanoparticles with nominal diameters of 5, 20 and 60 nm irradiated with 46 keV gold ions. In these experiments, the larger nanoparticles were dominated by surface sputtering, while the smallest particles were completely obliterated by the radiation events, resulting in the formation of five smaller nanoparticles. Similar experimental observations have been made in other FCC systems such as silver (Ag) nanowires [152]. Besides the observations that can be made on sputtering, it is nonetheless difficult to experimentally observe the rapid amorphization and possible phase change that can occur in the first 5 ns in these small nanostructures as seen in our simulations. However, there is evidence that many crystalline materials experience short-term amorphization as a result of ion beam modification [154]. Taken together, these experimental observations provide confirmation of the dominance of sputtering in small gold nanoparticles and potential for amorphization seen in our simulations.

#### *Dislocation-dominated mechanisms at larger sizes*

The mechanism of radiation damage accumulation for the larger nanowires (*i.e.*, diameter  $\geq 14$  nm) is different. Figure 3.4 shows snapshots of the type of defects that accumulated at 0.1 dpa, 0.5 dpa, and 1.0 dpa in 30-nm gold and niobium nanowires. Here again, we only represented the surface of the nanowire and atoms not in their lattice positions. For gold nanowires of sizes greater than 14 nm (see for instance Figure 3.4(a)-(c)), our results show that small SFTs and a few stacking faults are formed in the wires, along with a high density

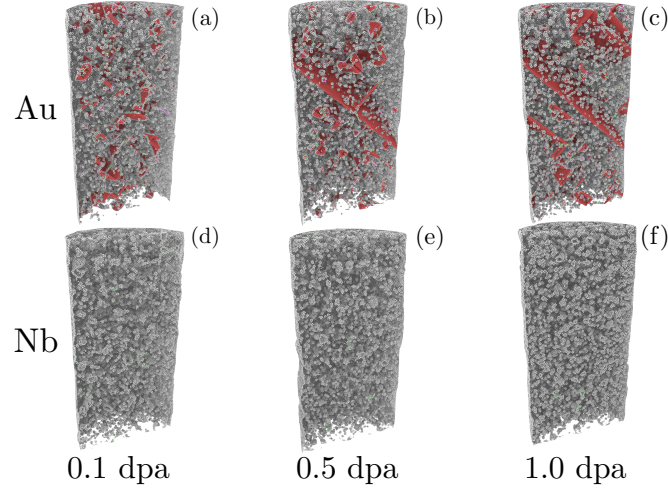


Figure 3.4: Defect structures in 30-nm gold and niobium nanowires at various damage levels (measured in dpa): (a) and (d) 0.1 dpa; (b) and (e) 0.5 dpa; and (c) and (f) 1.0 dpa. White atoms represent disordered structures and red atoms denote atoms in the HCP configuration. Lattice atoms are not shown.

of small point defects uniformly distributed across the wire. In the niobium nanowires, regardless of the size of the wire, our results show that small vacancy clusters are distributed throughout the nanowire, and there is little-to-no change in the defect type as the damage level increases. This mechanism is illustrated in Figure 3.4 (d)-(f). We confirmed and quantified these observations in Figure 3.5 by comparing the concentration of point defects and dislocation density as a function of the dose for different sizes of nanowires in both gold and niobium. As seen in Figure 3.5(a) and (b), our simulation results show that the point defect concentration increases with the dose, with minor differences in concentration for sizes between 14 nm and 40 nm. We made the same observation for the evolution of the dislocation density as a function of damage level (see Figure 3.5(c) and (d)).

In the case of gold nanowires, for diameters greater than or equal to 14 nm, the total dislocation density gradually increased with increasing radiation damage, with the predominant types of dislocations being  $1/6\langle 112 \rangle$  (Shockley dislocations) and  $1/6\langle 100 \rangle$  dislocations (stair-rod dislocations), respectively. The stair-rod dislocations are mainly present in the form of SFTs. As the diameter of the gold nanowires increases, more stable SFTs are created within the core-region of the nanowire, resulting in an increase in the equilibrium

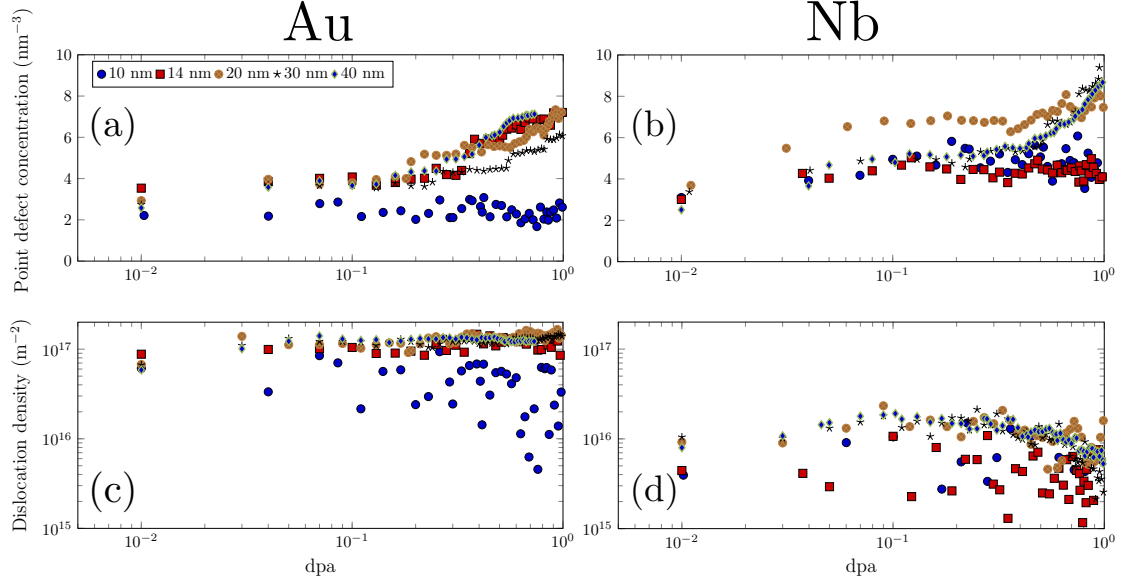


Figure 3.5: Evolution of point defect concentration ((a) and (b)) and dislocation density ((c) and (d)) as a function of the damage level (measured in dpa) in gold and niobium nanowires of different sizes.

dislocation densities with increasing nanowire diameter (see Figure 3.5(c)). Defect accumulation in gold nanowires follows a two-step process: (i) an accumulation of small SFTs (see insets A and B in Figure 3.6(a)) followed by (ii) a saturation of dislocations, where SFTs are surrounded by partial and full Shockley dislocations (see insets C and D in Figure 3.6(a)). In this case, SFTs are locked-in within the core of the nanowires and their mobility is drastically reduced by the forest of surrounding Shockley dislocations. This mechanism is illustrated in Figure 3.6(a) at various damage levels (*i.e.*, 0.001 dpa, 0.01 dpa, 0.5 dpa, and 1.0 dpa) for a 30-nm gold nanowire. Although experimental observations highlight the impact of cratering in nanoparticles and nanorods of these dimensions, it has been observed that SFTs, as predicted by our simulations, are also created during heavy-ion irradiation of nanowires [155]. Additionally, the predictions on defect evolution from our model corroborate with experimental observations of silver nanowires irradiated up to 1 dpa [152]. In these experiments, no significant change in the average defect cluster density was observed between 0.5 dpa and 1 dpa, confirming the two-step process of damage accumulation in gold nanowires.

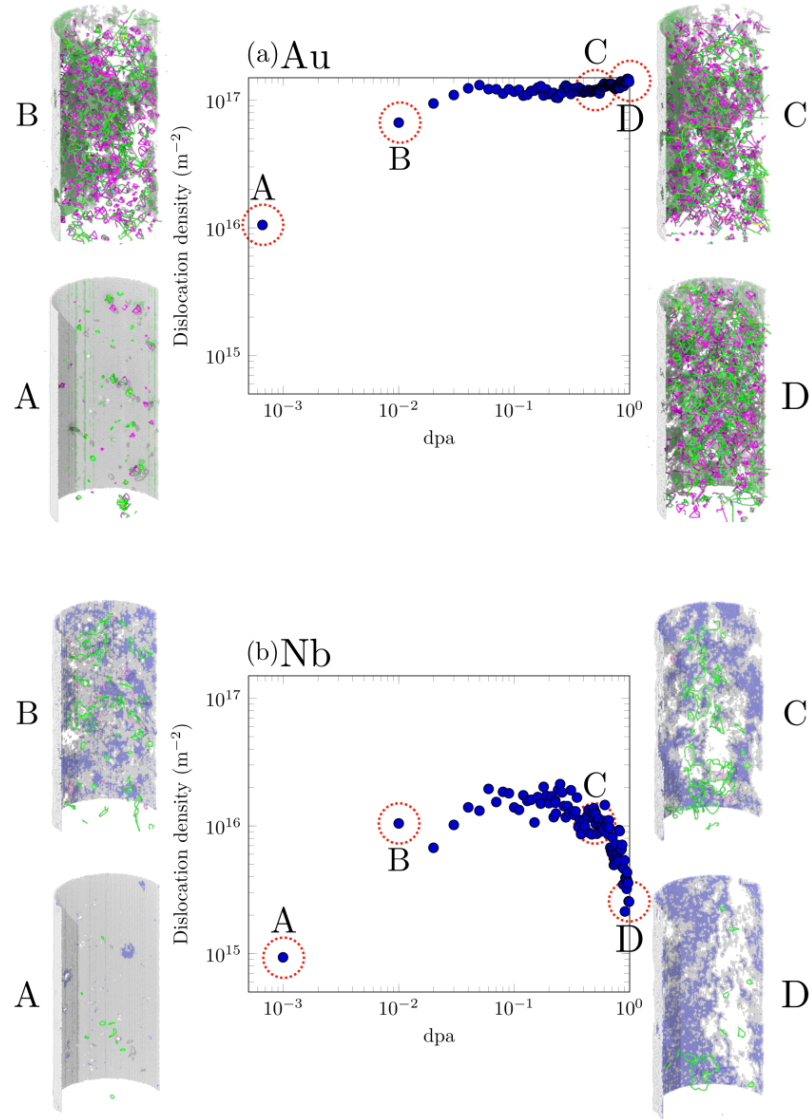


Figure 3.6: Evolution of the dislocation density in 30-nm (a) gold and (b) niobium nanowires as a function of the damage level (measured in dpa). Superimposed images show the dislocation structures at 0.001 dpa (A inset), 0.01 dpa (inset B), 0.5 dpa (inset C), and 1.0 dpa (inset D).

In the case of niobium nanowires, for all diameters, the primary type of dislocation accumulating in the nanowires are  $1/2\langle 111 \rangle$  dislocation loops. These loops are energetically more stable than other types of loops and their presence is in agreement with experimental observations of radiation-induced defect formation in other common BCC metals [21, 156, 157] and in recent atomistic models of BCC nanowires [127, 128]. In niobium nanowires, similar to what is seen in bulk niobium [23, 158] and other BCC metals [158–160], we observe an “S-shaped” radiation response consisting of three primary stages: (i) an accumulation of small dislocations at low damage (see inset A in Figure 3.6(b)), (ii) a saturation of the density of dislocations (see insets B and C in Figure 3.6(b)), and (iii) a coalescence of small dislocations into large dislocation loops (see inset D in Figure 3.6(b)). The first stage at low damage levels consists of the production of small dislocation loops, formed by the clustering of point defects and the production of distributed point defects. This stage is followed by a saturation regime when the dislocation density reaches a sufficient concentration, and the formation of small dislocations loops becomes more frequent. At a medium-to-high damage level, small dislocation loops start to coalesce to form larger loops and the density decreases. In this coalescence process, the loss of dislocation content is due to a combination of (i) dislocation reorganization, (ii) annihilation of dislocations reaching the free surface, and (iii) annealing of dislocations already present due to the interaction with ROAC events (local melting) being inserted. These stages correspond to experimental observations of radiation damage in single-crystal, bulk niobium [161] in which numerous small defects are observed at low doses, clustering into fewer, larger ones with continued irradiation.

As seen in Figure 3.7, in both the gold and niobium nanostructures, we observe that the transition from rapid accumulation of dislocations to a saturation process is size-dependent. The saturation regime is a natural consequence of the competition between defect accumulation and defect annihilation, but it corresponds to a regime where the population of defects has a different characteristic size than in the accumulation regime. Smaller nanowires ex-



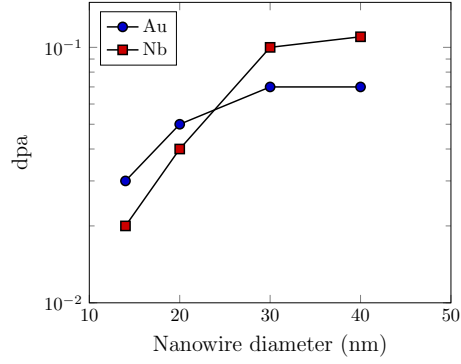


Figure 3.7: Dose transition from a mechanism of defect accumulation to defect saturation for both gold (circle symbol) and niobium (square symbol) nanowires as a function of the diameter of the nanowire.

perience a saturation of dislocation density at earlier damage levels than larger nanowires due to a confinement effect and a higher probability of ROAC events to promote the annealing of dislocations as the dose increases. For example, in niobium, 14-nm nanowires experience this transition at 0.02 dpa, while it occurs at 0.11 dpa in the case of the 40-nm nanowires. As indicated by the evolution of the total dislocation densities in Figure 3.6, this size-dependent transition is also accompanied by a change in the characteristic size of the defects (dislocation loops and defect clusters) from small, dispersed defects to large extended network of dislocation loops in both gold and niobium with the addition of uniformly distributed, immobile SFTs in the case of gold.

#### *FCC-to-HCP phase transformation within Goldilocks zone*

In the case of 10-nm gold nanowires, our simulations reveal a different mechanism than the ones described above for smaller or larger diameters. In this case (see Figure 3.8(a)-(c)), our simulations show that a stable HCP phase (as identified though CNA) accumulates across the nanowire and bisects the entire wire as the damage level increases. A few distributed vacancies are sandwiched in-between the HCP regions. Our simulations show that the FCC-to-HCP phase transformation is initiated via radiation-induced stacking-fault lamellas forming across the wire and subsequently piling up as the radiation damage in-

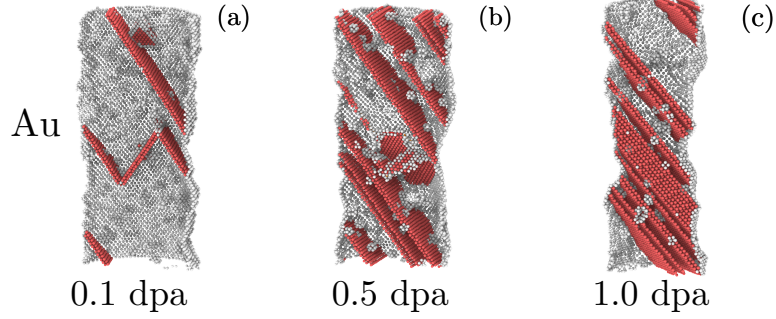


Figure 3.8: Defect structures in 10-nm gold nanowires at various damage levels (measured in dpa): (a) 0.1 dpa; (b) 0.5 dpa; and (c) 1.0 dpa. White atoms represent disordered structures and red atoms denote atoms in the HCP configuration. Lattice atoms are not shown.

creases. Such a mechanism is in agreement with phase transformation predicted in other FCC metals [162] and experimental observations of stacking faults and twin defects in gold nanowires [163] or gold nanocrystalline structures [122]. At high damage levels (*i.e.*,  $\text{dpa} \gtrsim 0.5$ ), the HCP region becomes thicker at the expense of the FCC crystalline phase. For gold nanowires with larger diameters (see for instance Figure 3.4(a)-(c)), our results show that SFTs and a few stacking faults are accumulating instead of a FCC-to-HCP phase transformation, while very small nanowires see their structure amorphized instead (see Figure 3.3). In the experimental observations by Suri et al. [122], a proposed mechanism for phase transformation is the motion of  $1/6\langle 112 \rangle$  Shockley dislocations along the  $\{111\}$  planes, converting two layers of FCC atoms to an HCP structure. We show evidence of this mechanism occurring in our simulations in Figure 3.9, where we observe a  $1/6\langle 112 \rangle$  Shockley dislocation gliding along a  $\{111\}$  plane of the nanowire while leaving behind a planar stacking fault. This stacking fault then merges with adjacent stacking faults, resulting in the formation of an HCP phase spanning the diameter of the nanowire. Since the motion of the  $1/6\langle 112 \rangle$  Shockley dislocations is along  $\{111\}$  glide planes and does not necessarily rely on surface orientation, it is unlikely that wire orientation would prevent the phase transformation from occurring. That being said, it is possible that different wire orientations might be more susceptible to the nucleation of  $1/6\langle 112 \rangle$  and thereby susceptible to the FCC-to-HCP phase transformation.

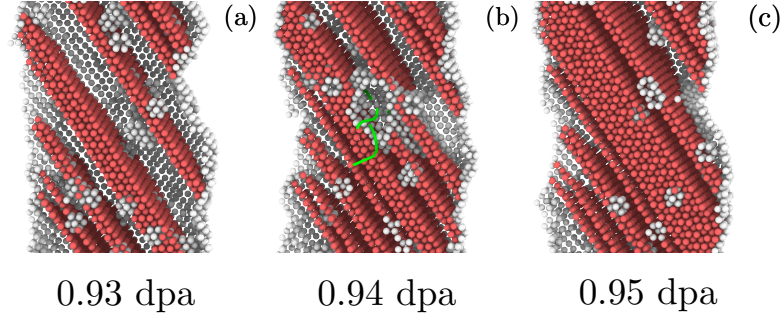


Figure 3.9: Mechanism of motion of  $1/6\langle 112 \rangle$  Shockley dislocation along  $\{111\}$  planes leading to FCC-to-HCP phase transformation: (a) state prior occurrence of  $1/6\langle 112 \rangle$  Shockley dislocation. (b) Motion of  $1/6\langle 112 \rangle$  Shockley dislocation along  $\{111\}$  plane. (c) Stacking fault merging with adjacent stacking faults. White atoms represent disordered structures and red atoms denote atoms in the HCP configuration. Lattice atoms are not shown. Green dislocation line corresponds to  $1/6\langle 112 \rangle$  Shockley dislocations.

The development of this phase transformation mechanism is a direct consequence of the confinement effect seen in the 10-nm nanowires preventing the formation of SFTs due to the relative size of cascades with respect to the diameter of the nanowire. The evolution of the HCP phase fraction as a function of the damage level presented in Figure 3.10 confirms that the FCC-to-HCP transformation occurs only in the 10-nm gold nanowire. Additionally, as illustrated in Figure 3.5, we observed that, for gold nanowires with a 10-nm diameter, the concentration of point defects accumulating in the nanowire was substantially smaller than in larger nanowires (see Figure 3.5(a)), confirming the prevalence of the FCC-to-HCP transformation at the expense of other damage mechanisms. Conversely, for larger diameters, the phase fraction of HCP phase is substantially smaller than in the 10-nm case but point defects and dislocation density increases as the dose increases (see Figure 3.5 (a) and (b)).

The FCC-to-HCP phase transformation has been observed experimentally in in-situ studies of nanocrystalline gold thin films for grain sizes with characteristic dimensions on the same order of those predicted in our simulation [122], but not in nanoparticles and nanorods [148, 149, 151, 153]. Experimentally, the irradiation of nanoparticles and nanorods [148, 149, 151, 153] has been conducted for sizes outside the range where we pre-

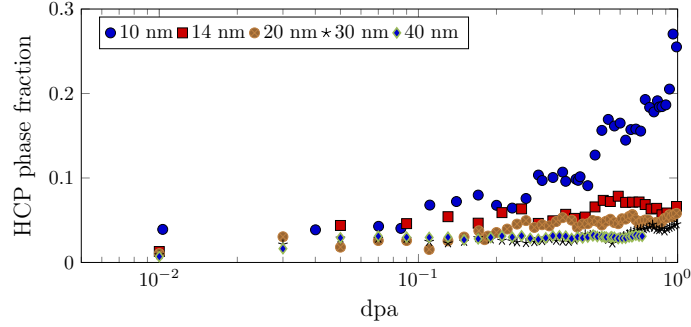


Figure 3.10: Evolution of the HCP phase fraction as a function of the damage level (measured in dpa) in gold nanowires of different sizes.

dict phase transformation from our simulations. In both the nanocrystalline and nanoparticles cases, the phase transformation has been observed at doses significantly higher than the dose predicted by our simulations. This discrepancy could be attributed to the significantly higher dose rate of  $\sim 1.0 \times 10^7 \text{ dpa.s}^{-1}$  used in our simulations as compared to typical dose rates for ion beam irradiation ( $\sim 1.0 \times 10^{-3} \text{ dpa.s}^{-1}$ ). A higher dose rate reduces the amount of time that defects have to anneal at sinks such as free surfaces in the case of nanowires, resulting in an accelerated rate of defect-defect interactions. This high density of defects interacting with each other results in an effective accelerated rate of dislocation formation.

#### *Surface roughening mechanism*

Finally, while not necessarily specific to the 10-nm gold nanowire, our simulation results in Figure 3.8 suggest that there is a large variation in the evolution of the surface roughness with increasing dose. This mechanism is especially well-captured when using the hybrid PKA/ROAC multi-cascades approach for simulating radiation damage accumulation which is only computationally amenable in the 10-nm range of wire sizes. Our atomistic results reveal that the origin of this irradiation-induced surface roughening is the consequence of two factors.

First, we note the presence of defect clusters in the vicinity of the free surface which interact with that surface. In this case, and this observation would be valid for larger diameters and for both FCC and BCC systems (see for example in Figure 3.4 (e) for Nb

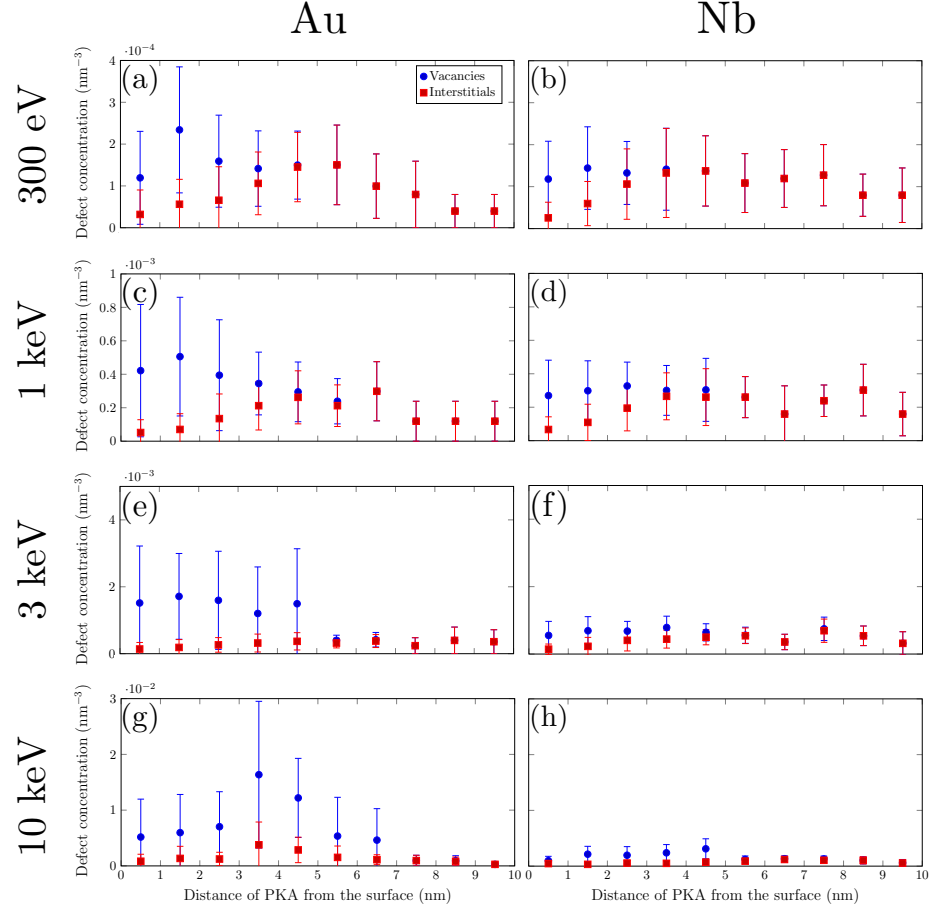


Figure 3.11: Point defect concentration (vacancies and interstitials) formed in Au and Nb 20-nm nanowires due to a single cascade at different recoil energies as a function of the distance between the initial location of the PKA and the free surface. Error bars show the standard deviation around the average values.

and Figure 3.8 (b) for gold), early-on in the damage accumulation process, the formation of predominantly vacancy clusters near the free surface ( $\sim 3$  to  $4$  nm below the free surface, see Supplementary Figure 1 in Note 8 of Appendix C) ensued from displacement cascades. As illustrated by our sputtering simulations in Figure 3.11, the concentration of vacancy defects is dependent on the recoil energy associated with the subsurface displacement cascade. As the dose increases, subsequent PKA or ROAC events may anneal the pre-existing clusters into smaller clusters (*e.g.* see distribution of defect clusters in Figure 3.4 (e)) or produce a displacement cascade near the pre-existing clusters, facilitating the formation of larger clusters. In both cases, the absorption of these defect clusters by the free surface of

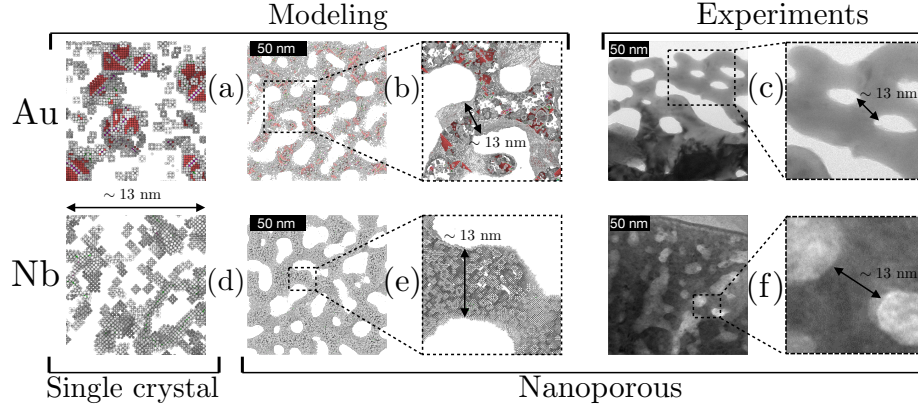


Figure 3.12: Defect structures at 0.10 dpa in a single crystal ((a) and (d)), and in the vicinity of a ligament within a nanoporous structure ((b) and (e)) in gold and niobium, as predicted from the atomistic simulations. White atoms represent disordered structures, and red atoms represent HCP atoms. Lattice atoms are not shown. (c) and (f) show corresponding TEM images of gold and niobium nanoporous structures respectively.

the nanowire induces surface roughness. Such mechanism corroborates with other studies showing that, during irradiation, displacement cascades can incur viscous flow and large sputtering events in the vicinity of the surface [128, 152, 164–166].

The second factor is related to the pinning of stacking faults at the free surface of the wire and is therefore expected to only occur in FCC systems. We note in Figure 3.8(b) and (c) or in Figure 3.4 (b) and (c) that some of the surface protrusions correspond to the pinning of sub-surface stacking faults spanning part or the entire cross section of the wire. In this case, the surface roughness also originates from surface steps due to the protruding stacking faults. For the 10-nm gold nanowire case, the pile-up of stacking-fault lamellas accentuates the surface roughness features. This is not necessarily the case for larger nanowires that instead tend to form SFTs and the surface roughness in this case is dominated by the interaction of vacancy clusters and individual stacking faults with the surface of the wire.

### 3.1.5 Discussion: Comparison of Radiation Tolerance Between Nanowires and Nanoporous Structures

The results above give an overview of the various mechanisms associated with defect accumulation in nanowires, where the nanowire structure is taken as a model system representative of ligaments present in nanoporous structures. However, actual nanoporous structures are more complex. Nanoporous structures include nodes connecting ligaments, and are composed of ligaments of different sizes, sometimes curved. We anticipate that, as the dose increases, the defect accumulation behavior of nanoporous structures as a whole will deviate more from that of nanowires due to different damage accumulation mechanisms between the nodes and ligaments. We show in Figure 3.12 a comparison of the radiation response and defect structures at 0.1 dpa between single crystal, nanowires, and nanoporous structures, for both gold and niobium. In this figure, we only represent surfaces (free surfaces) and atoms not in their lattice positions. In Figure 3.12, we also put our modeling predictions in perspective with observations of actual nanoporous gold and niobium made via in-situ ion irradiation TEM characterization. Note that, given the size of the nanoporous structures simulated ( $\sim 50$  million atoms) and the associated computational cost, we could only perform radiation damage simulations up to 0.1 dpa in those structures.

In the gold nanoporous structure, our simulations reveal that the defect structures in the nodes and ligaments are different. In the ligament, in agreement with our simulation predictions for the gold nanowires, the defects are composed of distributed vacancies as well as stacking faults and SFTs. However, our in-situ TEM observations show that the small, elongated ligaments within the nanoporous structure do not appear to have stacking faults that cut across the entire ligament, or SFTs (see inset for small ligaments in Figure 3.13 (a)). Instead, our experimental observations reveal that large visible SFTs are found in the ligaments with a thicker diameter and in the nodes connecting the ligaments (see insets for nodes and large ligaments in Figure 3.13 (a)). These observations confirm our atomistic



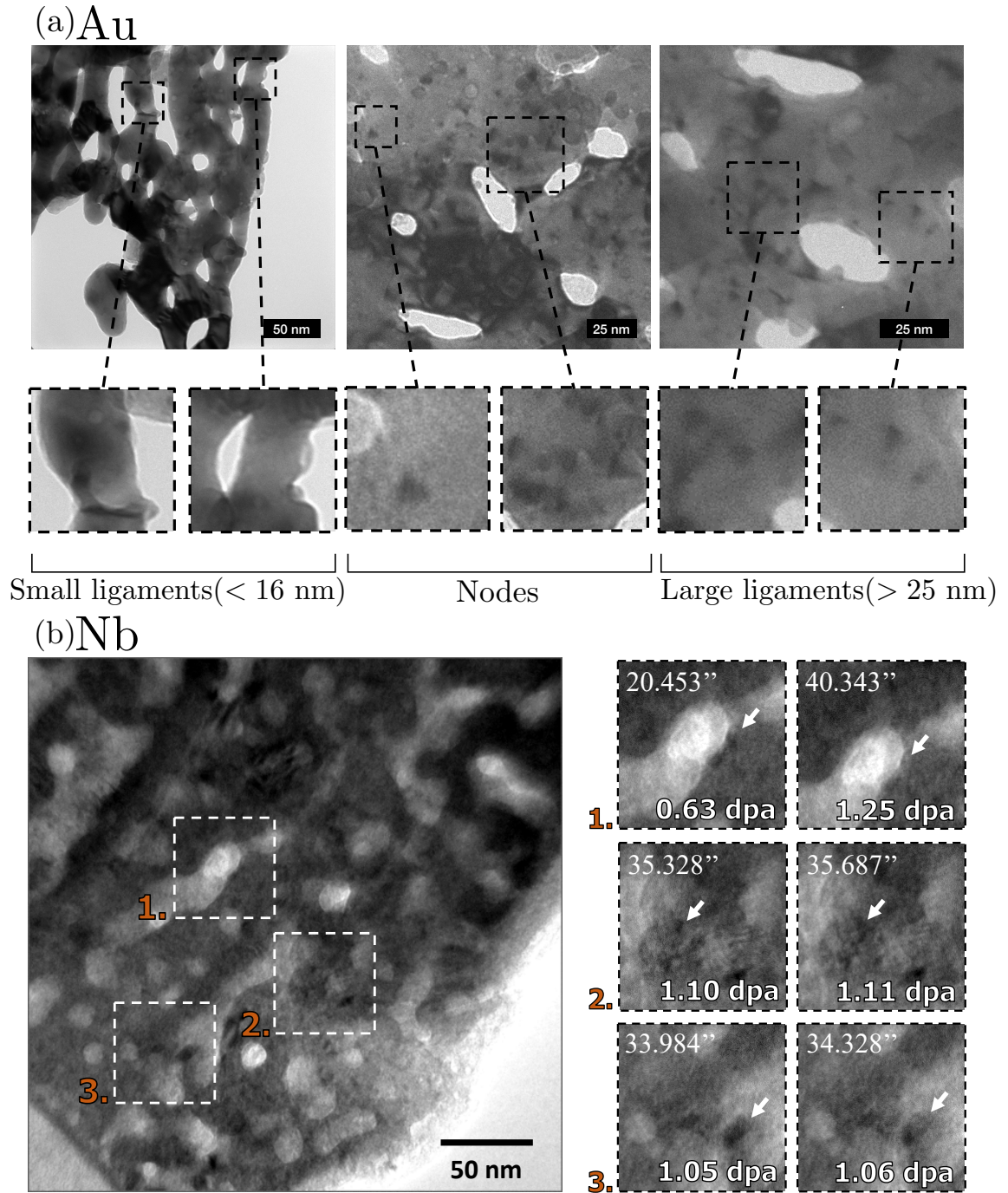


Figure 3.13: (a) Experimental characterization of radiation damage in nanoporous gold irradiated with 1.7 MeV  $\text{Au}^{3+}$  ions to 18.6 dpa (fluence  $5.49 \cdot 10^{14}$  ions/cm<sup>2</sup>). (b) Real-time TEM observations of the damage evolution in nanoporous niobium, irradiated with 1.7 MeV  $\text{Au}^{3+}$  ions for 40 s.



predictions for the nanoporous structure. In addition, both our experimental observations and simulation predictions show that the nodes contain not only SFTs, but also a higher density of small defect clusters, indicating that the ligaments accumulated less damage than the nodes. The experimental comparison of the defect structures in ligaments of various sizes and in nodes presented in Figure 3.13(a), and the comparison with the predictions of the defects seen in the single crystal case depicted in Figure 3.12(a) both indicate that the defects accumulated in the ligaments behave like those seen in large nanowires. Even if the damage level tested experimentally is beyond the one simulated with our atomistic model (18.61 dpa as compared to 0.1 dpa), we notice, both in the experimental observations and our simulation predictions, far more defects in the node than in the ligaments. In addition, our experimental observations (see Note 9 of Appendix C) indicate that upon irradiation some of the ligaments became decorated with small islands, where sputtered atoms can re-deposit on the surface of the ligaments as small clusters. Similar island formation has been reported for irradiated gold nanoparticles [149]. The difference between the experimentally observed island formation and predictions from our simulations is expected due to the nature of the ROAC method to insert cascade in the nanostructure in order to accelerate the damage accumulation for which redeposition of sputtered atoms is not permitted.

In the case of the niobium nanoporous structure, the primary damage consists of distributed vacancies and small vacancy clusters, with a few small dislocation segments. Defect densities and the size of the defect clusters do not appear to differ significantly from those observed for the niobium nanowires. The comparison with the defects observed in the niobium single crystal case (Figure 3.12(d)) show that large defect clusters and loops are formed, while the vacancies present in the niobium nanoporous structures tend to remain as single vacancies or form small clusters. Our simulation predictions correlate with our experimental observations for nanoporous niobium (see Figure 3.13(b)) in which little to no defects were visible (*i.e.*, below the resolution and detection limit of the microscopy instrumentation) in small ligaments.

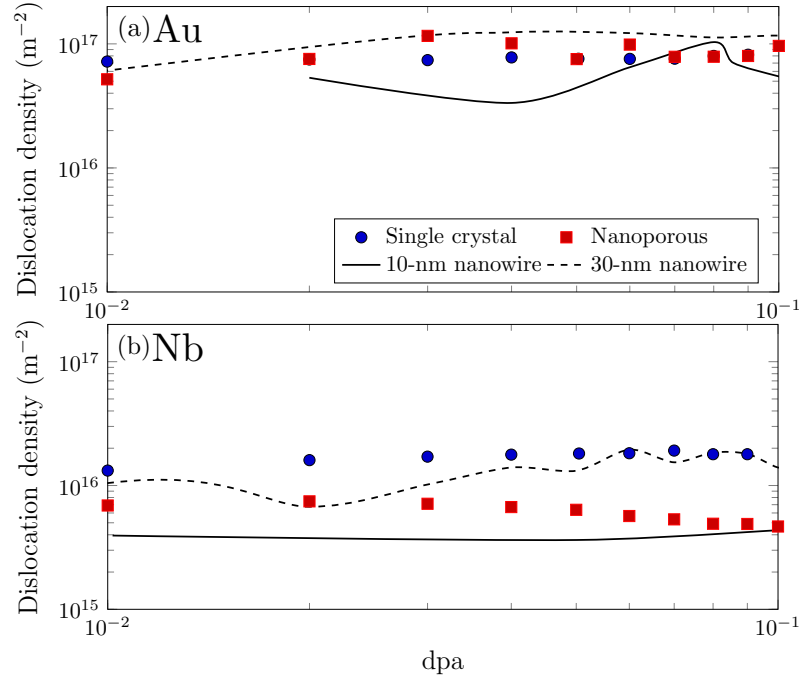


Figure 3.14: (a)-(b): Evolution of dislocation density as a function of the damage level (measured in dpa) in gold and niobium nanostructures.

Finally, in order to evaluate if any significant changes to the nanoporous structures occurred under irradiation, we compared the average ligament diameters in our simulations for both the gold and niobium nanoporous structures at 0.01 dpa intervals up to the final dose of 0.1 dpa as measured by the open-source OpenFoam software [143]. Our results show no statistically significant difference in the average ligament diameter before and after irradiation. See Note 2 of Appendix C for comparison of pre- post-irradiation ligament size distribution. Examination of the pre- and post-irradiation (0 dpa and 0.1 dpa) length measurement distributions showed a 0.1 nm upward shift of the distribution of ligament sizes. Therefore, we conclude that little to no radiation-induced coarsening occurred in the presented simulations. This is to be expected given the low damage level simulated.

Taken together, comparison of the experimentally observed features in Figure 3.13 with the nanoporous structures simulated in Figure 3.12 show many similarities, providing credence to the validity of the simulations performed and mechanisms observed. As such, we show in Figure 3.14 a comparison of the defect accumulation (point defect and dislocation

density) between a single crystal, a nanoporous structure, and nanowires with diameters that bound the size of ligaments seen in the nanoporous structure (10 nm and 30 nm). We point out that, despite the low level of damage simulated for the nanoporous structure, the small and large nanowire data provide adequate bounds for the dislocation densities seen in the nanoporous ligament region, and it is reasonable to hypothesize that the mechanisms and behavior seen at higher doses in nanowires will be seen in nanoporous ligament regions.

Further studies are needed to investigate the effect of damage accumulation on the mechanical response of these low-dimensional nanostructures. We expect a competition between the size effects seen in intrinsic properties of nanowires [167, 168] and the size-dependent transition of defect accumulation mechanisms reported in this study. Additionally, while the larger defect clusters observed in the structures studied in this manuscript may appear relatively static at the atomistic timescale, stress- or temperature-driven diffusion is expected over a period of seconds or hours. By replacing the source term used in classical rate theories [169, 170] with the defect structures and defect concentration observed in the present study, results obtained from this study could be upscaled to develop multiscale radiation effects models for instance.

### 3.1.6 Conclusions

This study gives insights into the atomistic processes at work during ion irradiation of nanostructures. We show that radiation-induced damage mechanisms in nanowires and nanoporous structures are size and crystallography dependent. For very small nanowires with a diameter less than 10 nm, the primary degradation mechanism under irradiation is sputtering. In this case, very small nanowires are not stable under irradiation. In contrast, for nanowires with larger diameters (greater than or equal to 14 nm), the mechanism of radiation damage accumulation is dominated by the rapid formation of small dislocations at low doses, followed by their saturation and coalescence. Our results establish

that the dose at which the mechanism transitions from the accumulation to the saturation of dislocations is size-dependent. The smaller the diameter, the lower the dose at which this transition occurs. In the case of gold nanowires, we reveal the existence of a narrow range of wire diameters (*i.e.*, nanowires with a diameter of approximately 10 nm), for which an FCC-to-HCP phase transformation occurs. This mechanism is not observed in smaller or larger nanowires. This phase-transformation mechanism stems from a confinement effect which promotes the formation and growth of radiation-induced stacking fault lamellas across the entire width of the wire to form a stable HCP phase. In addition to these mechanisms, we also show that these irradiation damage mechanisms are accompanied with radiation-induced surface roughening resulting from defect-surface interactions. Comparison between nanowires and nanoporous structures show that the behavior of damage accumulation seen in small and large nanowires provided adequate bounds for the defect accumulation seen in the nanoporous structure. The good agreement between the in-situ TEM characterization and prediction for the modeling provide credence to these conclusions.

## **3.2 Impact of Radiation Damage on the Mechanical Behavior of Nanoporous Metallic Foams Studied Via Atomistic Simulation Techniques**

### 3.2.1 Introduction

Interest in the use of nanostructured materials has grown in recent years due to the significant differences between the properties of these microstructures compared to their bulk phases [171–173]. One such property of interest is the improved radiation tolerance of nanostructured materials with high surface-to-volume ratios due to the ability of the material interfaces, grain boundaries, or free surfaces present in these nanostructures to serve as sinks for radiation-induced defects [4, 109, 111, 174]. Nanoporous metals have inherently high ratios of free surfaces to solid volume and it has been shown that, based on the size parameters of the structure and the irradiation conditions, there exists a zone of radiation tolerance where defects will not accumulate within the ligaments of a nanoporous metal [24, 112].

While these structures have been found to display radiation tolerance [24, 112], the microstructural evolution caused by irradiation can still impact the various behaviors and properties of the nanoporous material. Several experimental and computational studies of how radiation damage can impact the mechanical performance of nanoporous metals have been performed, but they have been limited in scope. Caro et al. [25] performed nanoindentation experiments after irradiating nanoporous gold with an average ligament diameter of approximately 40 nm up to a dose of 4 dpa, and observed a trend of increasing hardness with increasing dose. They also performed atomistic simulations to show that nanoporous structures fail initially at the nodes between the individual ligaments, which is why the yield stresses of nanoporous structures are significantly lower than the yield stresses of axially-loaded ligaments and nanowires with similar dimensions to those present in the nanoporous structures. However, the simulations performed by Caro et al. [25] only considered pristine structures, and did not include the presence of radiation damage. Zepeda-Ruiz et al. [26]

used molecular dynamics to examine how the compressive response of a 10 nm diameter Au nanowire changed due to the presence of an inserted SFT, and found that the presence of the defect led to a lower yield stress. This was found to be due to the unfauling of the inserted SFTs, resulting in a lowering of the dislocation nucleation stress. Currently there exists a need to determine the mechanisms by which radiation damage can change the mechanical performance of nanoporous metals with realistic representations of the damage that forms in these material systems under irradiation.

The purpose of this work is to use atomistic simulations to examine the mechanical behavior of irradiated nanoporous structures under compression and tension. This study will include doses that have not yet been considered in similar computational studies, and will examine this behavior in nanowires of varying diameters to determine if there are any size-dependent trends. In this study, two different material systems are considered. Nanoporous gold is an FCC material system that has been studied via both experiments [25, 112, 113, 117] and computational simulations [113, 125, 126], and has been shown to exhibit radiation tolerance depending on the irradiation conditions and the properties of the structure [24, 112]. Nanoporous niobium is a BCC material system that was synthesized relatively recently [175], and has not been studied extensively. Recent work was done to examine the radiation response of nanoporous niobium via atomistic simulations [24]; here we seek to expand on this previous work by including the impact of irradiation on its mechanical behavior. The comparison between the mechanical responses of nanoporous niobium to nanoporous gold also serves as an investigation into the differences in behavior between FCC and BCC nanoporous structures.

This work is organized as follows. The methods employed in the modelling of damage accumulation as well as the mechanical testing of gold and niobium nanowires are described in subsection 3.2.2. The results of the compression and tension simulations are reported in subsection 3.2.3. Finally, concluding remarks are provided in subsection 3.2.4.

### 3.2.2 Methodology

The methods employed in this work are organized as follows. First, information on general simulation details are provided. Then, the methods employed in the generation of gold and niobium nanowires are presented. Next, a short summary of the methods used to simulate the irradiation process are provided. Finally, the methodology employed in the performance of the tensile and compressive tests is presented.

#### *General Simulation Details*

All MD simulations performed for this work were performed with the MD code LAMMPS [15]. Simulations of gold nanowires were performed using an EAM potential for gold developed by Foiles, Baskes, and Daw [135]. The simulations involving ballistic collision cascades included the built-in ZBL potential found in LAMMPS to modify the close-range repulsion behavior, with splining parameters of  $r_1 = 0.4617 \text{ \AA}$  and  $r_2 = 1.20 \text{ \AA}$ . All gold systems were initialized in an FCC structure with a lattice constant of  $4.08 \text{ \AA}$ . This interatomic potential was fit to parameters relevant to radiation damage simulations, and was found to closely match low-index surface energies, which is relevant to the realistic modeling of nanoporous structures. Simulations of niobium nanowires were performed using an EAM potential for niobium developed by Ackland et al. [136] that has been modified to include close-range repulsion for radiation damage simulations, with all niobium systems being initialized in a BCC structure with a lattice constant of  $3.3008 \text{ \AA}$ . This interatomic potential was developed for the simulation of defects, free surfaces, and grain boundaries, making it the ideal potential for the simulation of radiation damage in nanoporous structures that have a high ratios of surface area to volume.

#### *Nanowire Generation*

All nanowires were produced by creating cylindrical columns with the desired length and diameter, then performing an energy minimization using the conjugate gradient method

with an energy stopping tolerance (unitless) and force stopping tolerance (eV/Å) of  $1.0 \times 10^{-15}$ . The cylinder axis of the nanowires lied along the  $\langle 001 \rangle$  direction, with the  $\langle 100 \rangle$  and the  $\langle 010 \rangle$  directions lying in the radial plane of the nanowire. After the initial minimization, the nanowires were equilibrated at zero pressure and 300 K under an NPT ensemble for at least 50 ps. All nanowires simulated in this work had an aspect ratio of 0.5 (i.e., each nanowire had a length that was equal to two times the diameter of the wire). Gold and niobium nanowires were produced with diameters of 10, 14, 20, 30 and 40 nm, with additional details of the nanowire microstructures provided in Table C.1 of Appendix C. The surfaces of the nanowires for both gold and niobium resolved into facets during the temperature and pressure equilibration, with longer  $\{100\}$  and  $\{110\}$  surfaces separated by small tiers of  $\{100\}$  and  $\{110\}$  surfaces.

#### *Irradiation Methods*

All of the Au and Nb nanowires examined in this work were irradiated up to a final dose of 1.0 dpa. The details of the methodology employed in performing the irradiation simulations, as well as an atomistic study of the defect accumulation mechanisms in nanowires and nanoporous systems, are provided in subsection 3.1.2 [24]. Prior to the performance of any mechanical simulations, all irradiated systems were equilibrated at zero pressure and 300 K under an NPT ensemble for a minimum of 50 ps.

#### *Mechanical Tests*

Simulations examining the mechanical response of nanowires were performed for both pristine structures as well as structures that had been damaged via the damage insertion methods described in subsection 3.1.2 [24]. All mechanical testing simulations were performed under an NVT ensemble at 300 K, with the total stress calculated from the standard virial expression for stress in LAMMPS.



**Compression** Uniaxial compression tests were performed along the primary axis of the nanowires by rescaling the width of the simulation cell as well as the atomic positions along the axis of choice every ten timesteps (0.01 ps) at a strain rate of 0.1 1/ns ( $1 \times 10^8$  1/s) using the `fix/deform` command within LAMMPS. Prior to beginning the process of the application of compressive strain, regions with thicknesses of 4.6 Å at the top and the bottom of the nanowires were frozen using the `fix/setforce` such that the atoms within these regions could only be moved by the `fix/deform` command. This was done to prevent the structures from rebounding after each application of compressive strain. All simulated systems were run to a maximum compressive strain of 0.15.

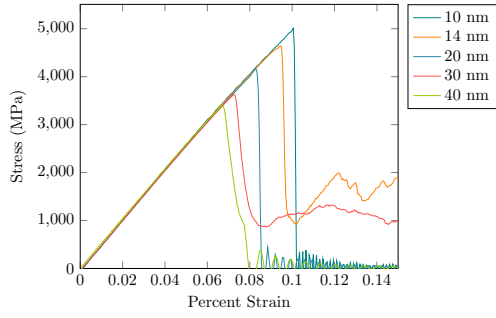
**Tension** Uniaxial tension tests were performed in a very similar manner to the uniaxial compression tests, with the exception that a tensile strain was applied rather than a compressive strain. The same strain rate of 0.1 1/ns ( $1 \times 10^8$  s) was applied in all tensile tests performed. The simulations of tension were kept fully periodic in the axis of the loading, with no capped regions on the top and bottom of the simulation cell. All simulated systems were run to a maximum tensile strain of 0.15.

### 3.2.3 Results

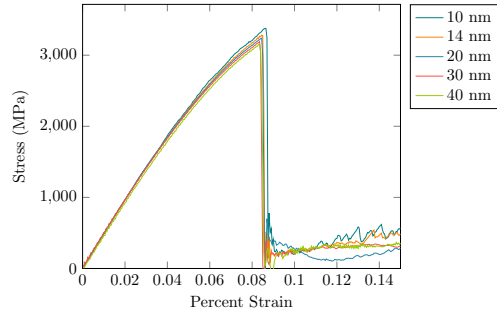
#### *Effect of Wire Diameter on Mechanical Properties*

Prior to examining the effects of radiation damage on the mechanical behavior of nanowires, it is important to establish a baseline understanding of their performance while in pristine condition. Figure 3.15 shows the stress-strain behavior of pristine gold and niobium nanowires of various diameters.

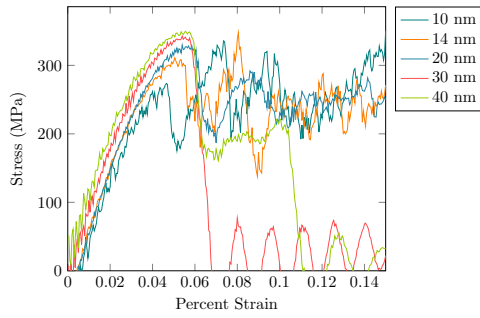
**Behavior Under Tension** For both gold and niobium nanowires, the size effect of diameter on the stress-strain behavior under tension is relatively small. In the case of the niobium nanowires, the yield stress and the yield strain decrease slightly with increasing diameter,



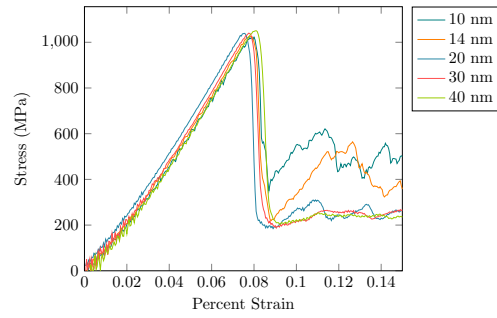
(a) Niobium Compression



(b) Niobium Tension



(c) Gold Compression



(d) Gold Tension

Figure 3.15: Stress-strain curves for pristine gold and niobium nanowires under tension and compression. Wire diameters are provided in the legends.

with the magnitude of this change appearing to decrease as the wire diameters increases. For the case of the gold nanowires under tension, there appears to be no size effect, with no discernible ordering of the yield stresses and yield strains based on nanowire diameters. The only observable trend in the gold nanowires under tension is in the behavior after the initial yield point at around 0.08 applied strain, where the second increase in stress is ordered such that the magnitude of the second peak decreases with increasing wire diameter.

Figure 3.16 shows cross-sections of 10 nm niobium and gold nanowires under tension prior to and after their failure. In both of the pre-failure images of Figure 3.16, there can be seen some atoms within the nanowires that are not being identified as the primary structure

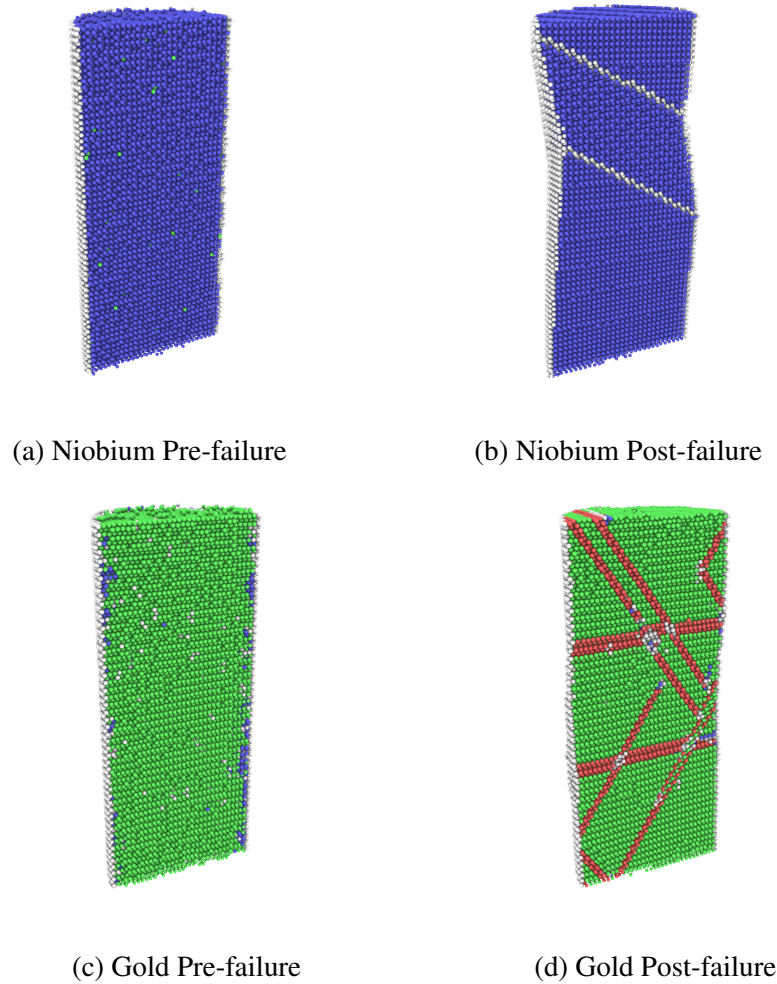


Figure 3.16: Images of 10 nm nanowires pre and post yielding under tension. Atoms are colored according to lattice type: blue is BCC, green is FCC, red is HCP, and white is disordered.

type. The quantity of these atoms increases as the system is loaded until the wires yield to relax the stress. The niobium nanowire yields through a slip mechanism, where a portion of the wire is rotated with respect to the original crystallographic direction which essentially results in the formation of a grain bisecting the wire. As strain is applied after the initial yield point, the rotated region grows in size as the boundaries between the two regions sweep along the axial direction of the nanowires. The gold nanowire yields through a similar mechanism, although instead of seeing the formation of a single rotated region the slip results in the formation of a series of stacking faults that bisect the wire. As strain is

applied to the gold nanowires after the initial yield point, some of the stacking faults merge or are removed as the wire begins to become thinner.

**Behavior Under Compression** In Figure 3.15, both niobium and gold nanowires displayed a stronger size effect under compression than under tension; however, the direction of the trend is reversed between the two materials. In niobium, there is a clear decrease in both the yield stress and the yield strain as the diameter of the nanowire increases. In the case of the gold nanowires, an opposite trend is observed where the yield strength increases with the diameter of the nanowire. The yield strain also seems to increase with wire diameter up to a diameter of 20 nm, where it appears that the yield strain remains constant with increasing wire diameter.

Figure 3.17 shows cross-sections of the niobium and gold nanowires under compression prior to and after their failure. In both material systems, the wires yield via a slip mechanism, similar to the failure mechanism shown in Figure 3.16, albeit with some slight differences. The niobium nanowire is shown to slip near the bottom of the wire; however, instead of forming a rotated region separate from the rest of the nanowire by disordered planes of atoms, the wire remains a single crystal with the deformation of the wire having formed a wider base. Increasing the applied strain after the initial failure of the niobium nanowires under compression resulted in additional deformation in the slip region. The gold wire similarly fails via a slip mechanism, however instead of forming a network of stacking faults like in Figure 3.16 (d), the gold nanowire under compression forms two parallel stacking faults along the slip plane of the failure ( $\langle 111 \rangle$ ). Continuing to apply additional strain to the gold wire results in motion of the stacking faults increasing the size of the region between the two faults bisecting the wire, as well as the formation of additional stacking faults.

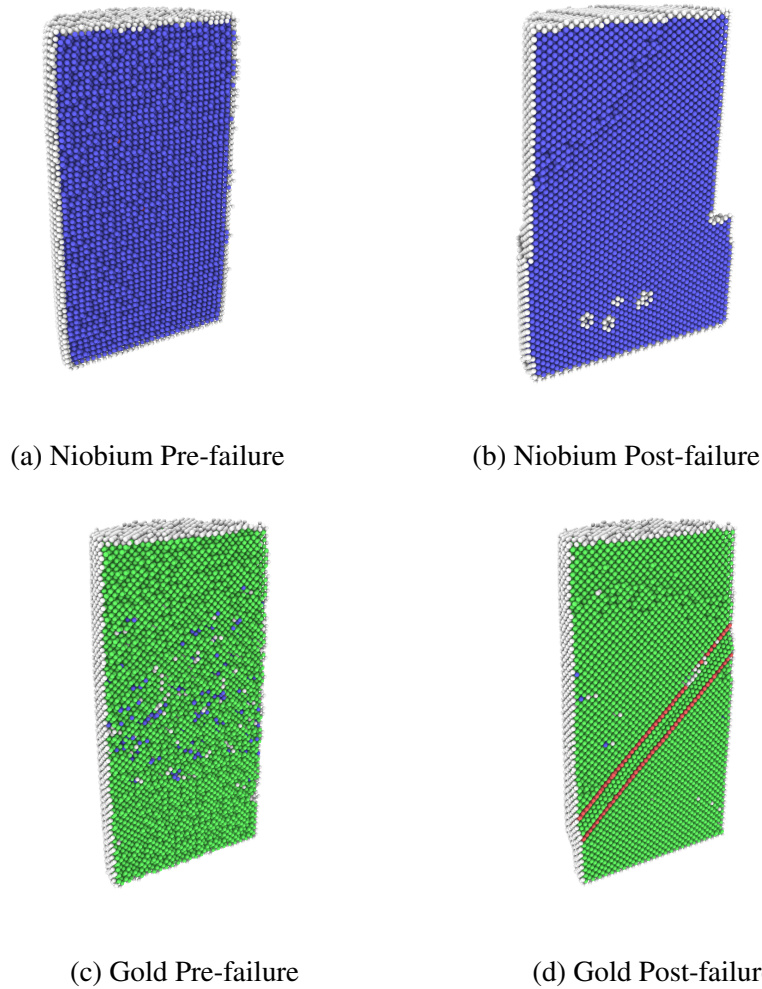
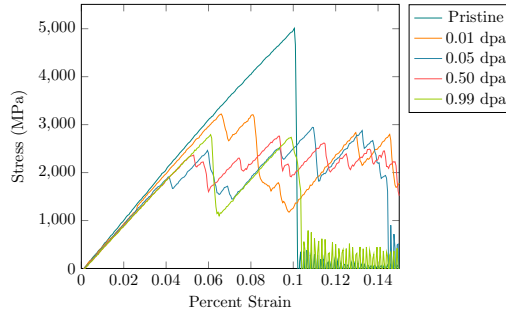


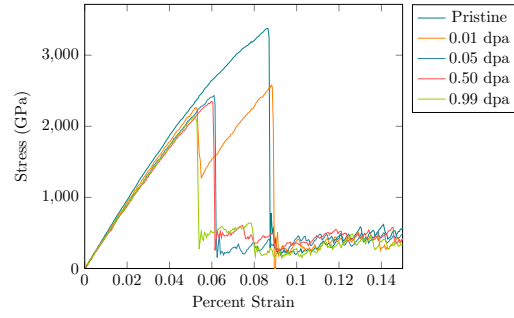
Figure 3.17: Images of 10 nm nanowires pre and post yielding under compression. Atoms are colored according to lattice type: blue is BCC, green is FCC, red is HCP, and white is disordered.

#### *Impact of Irradiation on the Mechanical Behavior of Nanowires*

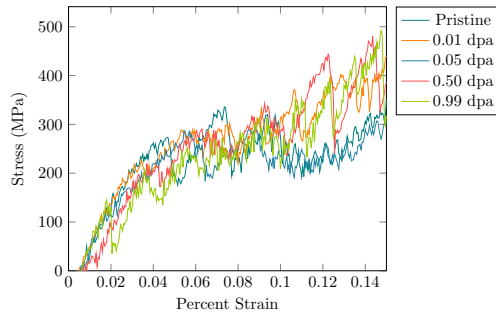
With respect to defect accumulation under irradiation in nanowires of various diameters, there exist several different material-dependent regimes of defect accumulation. In niobium these regimes include a regime where the concentration of defects is increasing, a regime where the concentration is steady with increasing dose, and regimes where the concentration of defects decreases with further irradiation. In gold, the density of defects initially increases with applied dose, and eventually reaches a plateau in concentration where ad-



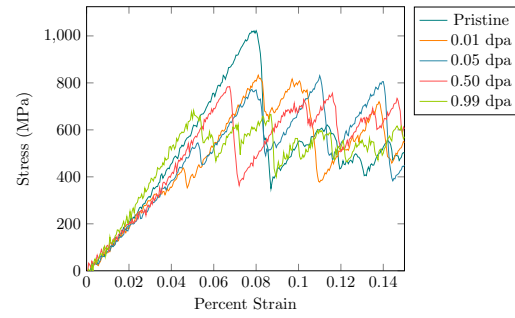
(a) Niobium Compression



(b) Niobium Tension



(c) Gold Compression



(d) Gold Tension

Figure 3.18: Stress-strain curves for irradiated gold and niobium nanowires with diameters of 10 nm under tension and compression. Dose levels are provided in the legends.

ditional radiation dose not change the density of defects. Further details of the defect accumulation observed in the irradiated nanowires can be found in section 3.1. In order to examine how the defects within these different accumulation regimes impact the mechanical behavior of the irradiated nanowires, dose levels representing each of these regimes were chosen for each nanowire diameter independently, as there was found to be a size effect on the transition between these different accumulation regimes [24].

Figure 3.18 shows the stress-strain data collected for the compression and tension of niobium and gold nanowires with diameters of 10 nm irradiated to four different dose levels as well as the pristine data for reference. Plots of the stress-strain behavior of the irradiated nanowires with diameters of 14, 20, and 30 nm are provided in Appendix D. In

the gold nanowire under compression ((c) in Figure 3.18), the impact of radiation damage on the stress-strain behavior is not discernible within the noise in the collected data. In the case of the gold 10 nm diameter nanowire under tension and the niobium 10 nm diameter nanowire under both compression and tension, the introduction of radiation damage to the system always resulted in a reduction of the yield stress and the yield strain relative to the behavior of the pristine nanowires. There is no consistent trend between the different dose levels, as the ordering of the different doses between compression and tension in the case of niobium is not consistent, and the different dose levels for the gold wire under tension also do not present a consistent trend with respect to the yield stress and the yield strain.

Figure 3.19 shows the stress-strain behavior observed at four different irradiation doses

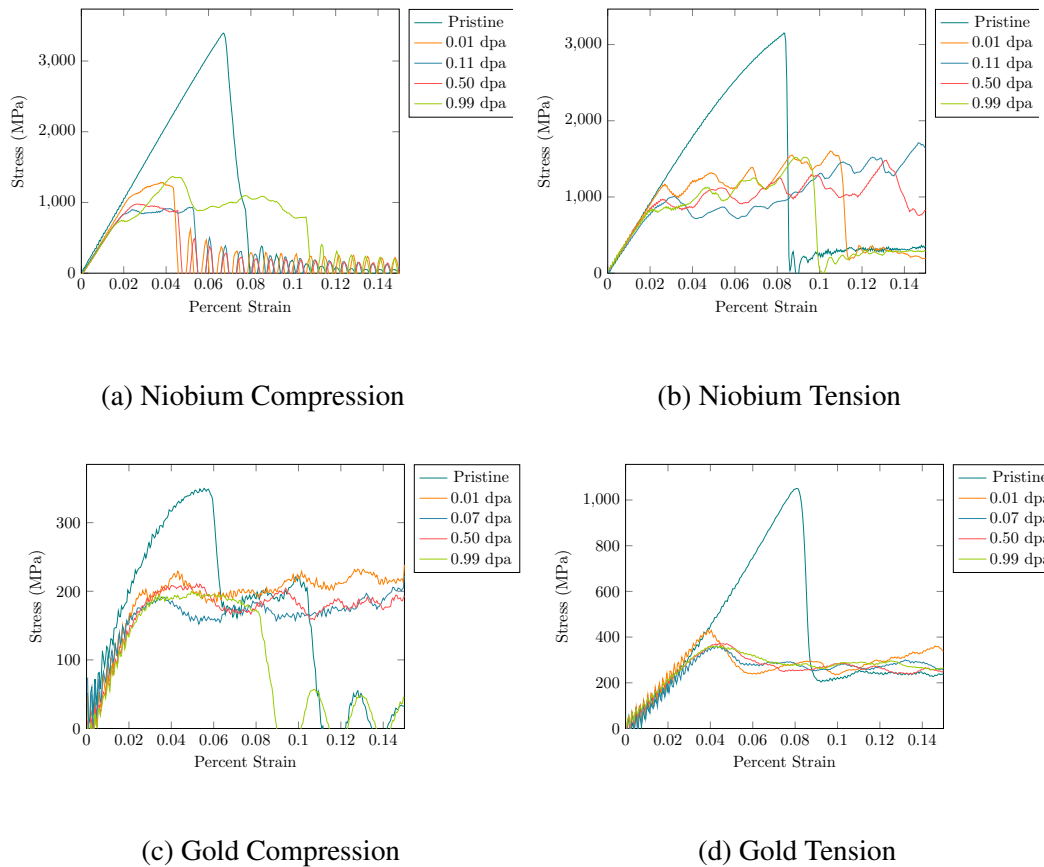


Figure 3.19: Stress-strain curves for irradiated gold and niobium nanowires with diameters of 40 nm under tension and compression. Dose levels are provided in the legends.

for nanowires with diameters of 40 nm. The length scale of these nanowires matches the characteristic ligament diameter of the nanoporous structure tested in the work of Caro et al. [25], where they observed radiation-induced hardening with increasing dose. As can be seen in the plots of Figure 3.19, the behavior at the largest length scale that was tested for this work is the same as that observed in Figure 3.18, where the introduction of any amount of radiation damage results in a reduction in the yield stress and the yield strain of the nanowires. Again, there is no clear trend within the data for the irradiated systems, indicating that the different defect accumulation regimes all have a similar effect on the mechanical behavior of the tested nanowires.

**Radiation-Induced Softening in Niobium Nanowires** The irradiation-induced softening that was observed in Figure 3.18 and Figure 3.19 was observed across all of the tested nanowire diameters at all dose levels, with all wires experiencing a significant reduction in the yield stress and yield strain under both tension and compression (additional stress-strain plots for gold and niobium nanowires can be seen in Figure D.1, Figure D.2, and Figure D.3). This effect appeared to not have a dependence on the applied dose to the nanowire, indicating that the effect was independent of both the defect density and the length-scale of the defects.

In the irradiated niobium nanowires, the mechanisms behind the relaxation of stress are not always the same compared to the pristine wires of the same size, which as noted in subsection 3.2.3 was initiated under both compression and tension by the nucleation of a dislocation at the surface of the nanowires. In the case of the 40 nm niobium nanowire under compression whose stress-strain behavior is shown in Figure 3.19, there were no catastrophic failure events resulting in significant deformation of the wire for any of the tested dose levels. Rather, despite the rapid relaxations of stress observed in Figure 3.19 (a), the nanowire relaxed its stress through small slip events and the migration and annihilation of defect clusters at the surface of the wire. Selected images are shown in Figure 3.20



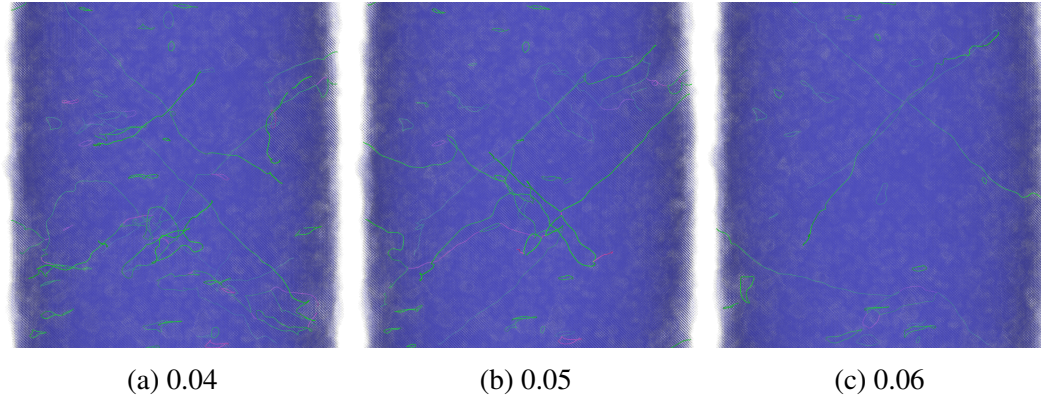


Figure 3.20: Cross-section of a 40 nm diameter niobium nanowire irradiated to a dose of 0.11 dpa under compression. Atoms have been made semi-transparent and are colored according to their structure: blue is BCC, white is disordered. Dislocations are colored according to their type: green is  $\frac{1}{2} \langle 111 \rangle$ , magenta is  $\langle 100 \rangle$ . The current applied strain to the nanowire is shown in the caption of each image.

of the 40 nm diameter niobium nanowire with an applied dose of 0.11 dpa around an applied strain of 0.05, showing the changes to the nanowire that occurred around the yield point of the wire under compression. There was no large deformation event like that observed in Figure 3.17, with very little changing from image to image. The most notable difference being a change in the dislocation network resulting in the annihilation of some dislocation lines and the merging of others. This type of stress relaxation mechanism under compression was observed for all of the irradiated niobium nanowires, indicating that the presence of radiation damage alters the failure mode of such systems from a single catastrophic deformation event to a series of smaller relaxations involving small slip events as well as defect and dislocation merger and annihilation.

The change to the failure mechanism observed in the compression of irradiated nanowires as well as the reduction in the yield stress and the yield strain is likely a result of the damage that occurs to the surfaces of the irradiated nanowires. The roughening of the surface caused by direct interactions of cascade events with the surface as well as the migration of radiation-induced defects to the surface induces some roughness that reduces the stress required to nucleate a dislocation. This lower nucleation stress allows for more gradual stress release in the case of compression, preventing catastrophic restructuring of the nanowires

under compression.

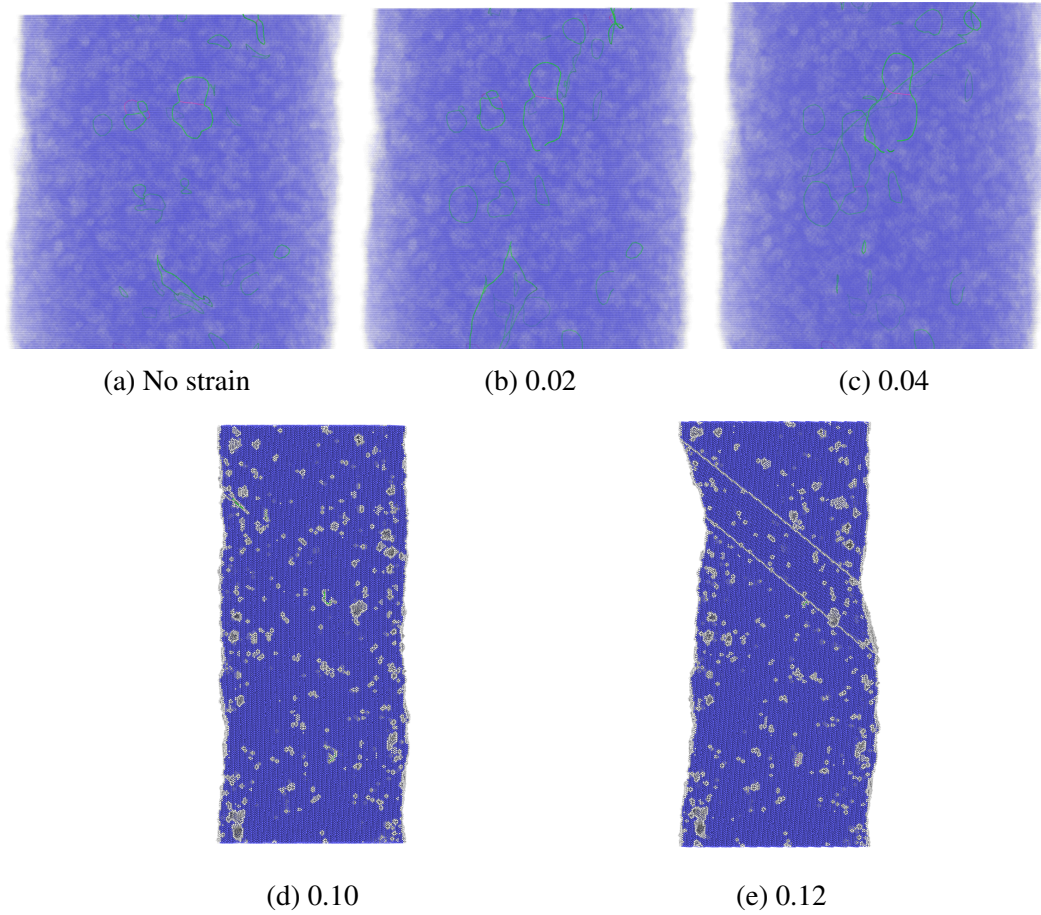


Figure 3.21: Renders of a 30 nm diameter niobium nanowire irradiated to a dose of 0.50 dpa under tension. Atoms are colored according to their structure: blue is BCC, white is disordered. Dislocations are colored according to their type: green is  $\frac{1}{2} \langle 111 \rangle$ , magenta is  $\langle 100 \rangle$ . The current applied strain to the nanowire is shown in the caption of each image.

Under tension, a similar behavior is observed where the large deformation following stress relaxation observed in pristine systems is replaced by smaller deformation events as well as dislocation annihilation and merger. However, as strain is continuously applied to the irradiated niobium nanowires under tension, several of the wires reach a point where they undergo the same type of deformation that was observed in the pristine 10 nm diameter niobium nanowire in Figure 3.16. Figure 3.21 shows the 30 nm diameter niobium nanowire irradiated to a final dose of 0.50 dpa around the point where its stress-strain curve deviates from elastic deformation (approximately 0.02 applied strain) as well as the point where its

stress rapidly relaxes (approximately 0.11 strain). In the images related to the lower strain level, the only observable changes are slight elongation of the wire as well as dislocation motion that results in the merging and annihilation of some dislocations. At the higher strain level, a large-scale deformation similar to that observed in Figure 3.16 occurs, with the formation of a rotated region separated from the rest of the wire by two disordered regions. This type of behavior was observed in all irradiated niobium nanowires under tension that experienced a rapid relaxation of stress to a near zero stress state at higher strain levels.

**Radiation-Induced Softening in Gold Nanowires** The gold nanowires also experienced radiation-induced softening across all nanowire diameters as well as all of the tested dose levels, with the only exception being the case of the 10 nm diameter gold nanowire under compression, where no radiation effect was observed on the stress-strain behavior. Within the gold nanowire system, there are two likely causes for the radiation-induced softening under both compression and tension. The first is the same as that observed in the niobium nanowires, where radiation damage has induced a degree of surface roughness which lowers the nucleation stress of dislocations and could lead to premature yielding of the nanowires. This mechanism is likely the primary cause of radiation-induced softening in wires irradiated to low doses, where the defect cluster sizes are small and the defect densities are low. The second mechanism is possible due to the ability of FCC systems to form SFTs, which can serve as sources for dislocations. As was mentioned in subsection 3.2.1, Zepeda-Ruiz et al. [26] observed softening of gold nanowires with diameters of 10 nm under compression when inserting an SFT into the center of the nanowire. Similar behavior has been observed in CuNb nanocomposites [176] and AuSi nanocomposites [177], where SFTs present in irradiated fcc nanostructures can unfault and serve as sources for dislocations, resulting in a reduction in the yield stress and yield strain. The simulations performed by Zepeda-Ruiz et al. [26] and Martinez, Caro, and Beyerlein [176] were performed in sys-

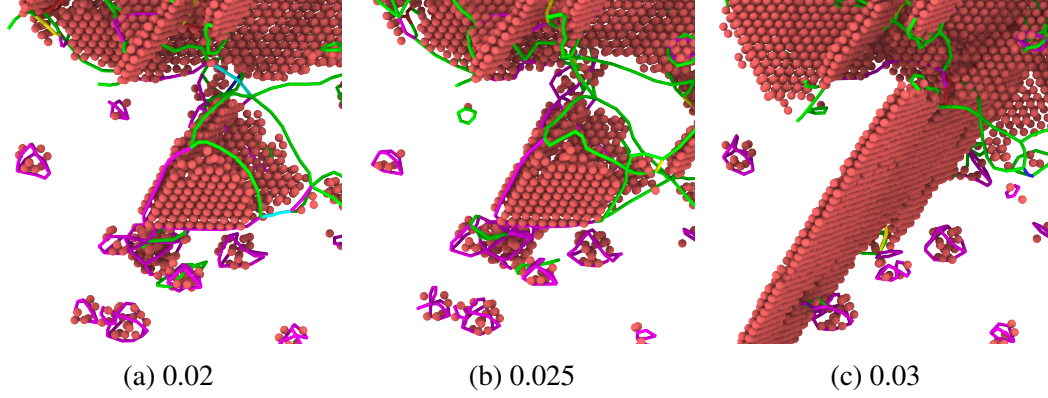


Figure 3.22: SFT found in a 20 nm diameter gold nanowire irradiated to a dose of 0.5 dpa under compression. Lattice atoms have been removed, with the atoms shown being HCP. Dislocations are colored according to their type: green is  $\frac{1}{2} \langle 111 \rangle$ , magenta is  $\langle 100 \rangle$ . The current applied strain to the nanowire is shown in the caption of each image.

tems where the only defects present were the manually inserted SFTs; however, the simulations performed for this work and those performed by Chen et al. [177] found a wide array of defect structures that can form in irradiated FCC systems, from SFTs and stacking faults to voids and isolated point defects. Despite the complexity of the defect structures observed in our simulations, the behavior of SFT unfauling was observed in our compression simulations of irradiated gold nanowires, as shown in Figure 3.22 which shows an SFT unfauling in a 20 nm diameter gold nanowire at a total dose of 0.5 dpa. In this series of images, an SFT unfaults after emitting a dislocation, leaving behind a large stacking fault. The strain at which this occurred was before the deviation of the stress-strain curve from elastic to plastic deformation (see Figure D.2 of Appendix D), indicating that this mechanism does not always result in the yielding of the material or a large relaxation of stress.

This behavior was also observed in nanowires under tension, as shown in Figure 3.23, where a 20 nm diameter gold nanowire irradiated to a final dose of 0.05 dpa is shown at several strain levels. In these images, a defect composed of overlapping SFTs begins to unfault, resulting in a ring of dislocations that eventually changes into a stacking fault. These images are provided with reference to the stress-strain plot for the simulation.

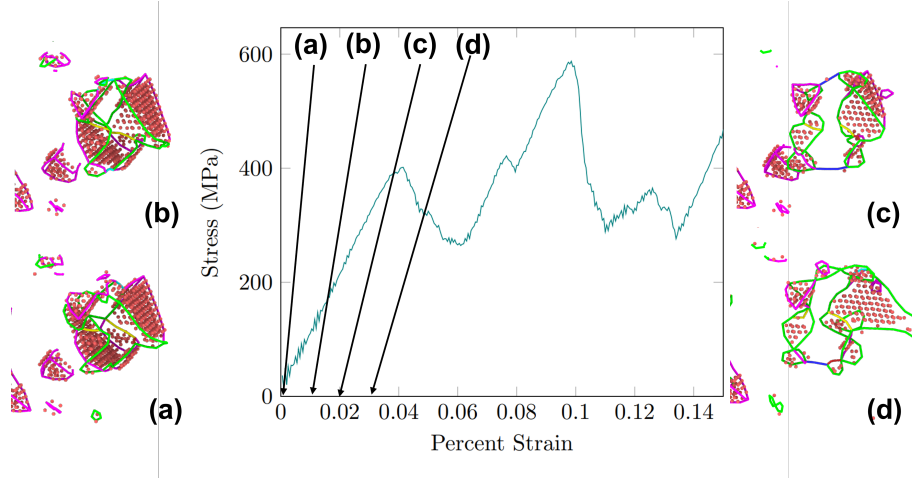


Figure 3.23: Stress-strain plot and renders of a 20 nm diameter gold nanowire irradiated to a final dose of 0.05 dpa under tension. In the renders, only HCP atoms are shown in red. Dislocations are colored according to their type: green is  $\frac{1}{2} \langle 111 \rangle$ , magenta is  $\langle 100 \rangle$ .

**Impact of Radiation-induced Phase Transformation on Mechanical Behavior** In subsection 3.1.4, a radiation-induced phase transformation was observed in a 10 nm diameter gold nanowire as the total dose approached 1 dpa [24]. Figure 3.10 shows the progression of the phase transformation, with approximately 5% of the wire having been converted from fcc to hcp around 0.05 dpa, 14% at 0.5 dpa, and 25% at 1 dpa. The stress-strain data for this nanowire under tension and compression can be seen in Figure 3.18. As was mentioned in subsection 3.2.3, there appears to be no clear impact of radiation damage on the stress-strain behavior of this particular nanowire under compression, whereas there is some degree of radiation-induced softening under tension with no consistent trend connecting the dose and the degree of softening.

Under compression, the 10 nm diameter gold nanowire irradiated to a final dose of 1 dpa behaves similarly to the other dose levels as well as the pristine nanowire, with the formation and annihilation of stacking faults occurring as the wire is strained. The region where the FCC-to-HCP phase transformation has occurred initially grows in size, but gradually shrinks as the system approaches the final applied strain of 0.15. Figure 3.24 shows cross-sections of the 10 nm gold nanowire at 1 dpa at various strain levels under compression, highlighting the growth and shrinkage of the HCP region. In this system, it



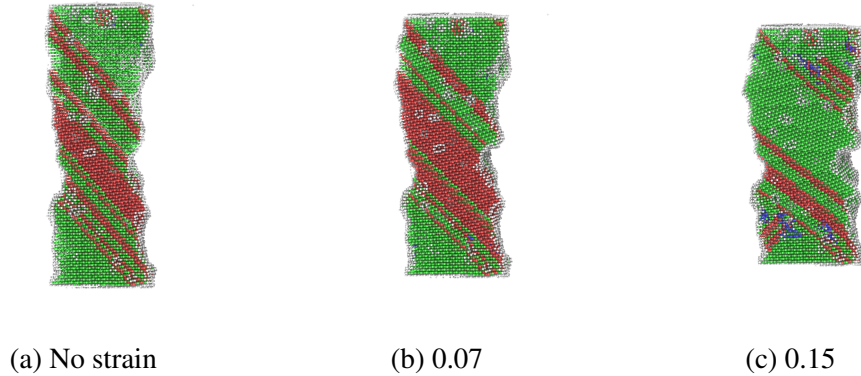


Figure 3.24: Cross-section images of a 10 nm gold nanowire at 1 dpa under compression. Applied strain is shown in the caption of each image. Atoms are colored by structure type: green is FCC, red is HCP, white is disordered.

appears that both the formation and annihilation of stacking faults and HCP regions can be mechanisms for the relaxation of stress.

Under tension, the behavior of the 10 nm Au nanowire at a dose level of 1 dpa is not noticeably different from the behavior of the nanowires at other dose levels. The primary stress relaxation mechanism appears to be the nucleation or annihilation of stacking faults. Unlike in the system under compression, under tension the size of the phase-transformed region does not change during the simulation. Figure 3.25 shows cross-section images of the nanowire under tension, where it can be seen that the phase-transformed region does not change under the applied strain, with the formation and annihilation of stacking faults occurring elsewhere in the nanowire.

#### 3.2.4 Conclusions

Simulations of irradiated nanowires under compression and tension have found that dose-independent radiation-induced softening was observed in both gold and niobium nanowires across a wide range of diameters. In niobium, this softening is believed to have been caused by the introduction of surface roughness brought on by interactions of radiation damage events with the surface as well as the migration of defects to the surface. In gold, radiation-induced softening is believed to be a result of a combination of radiation-induced

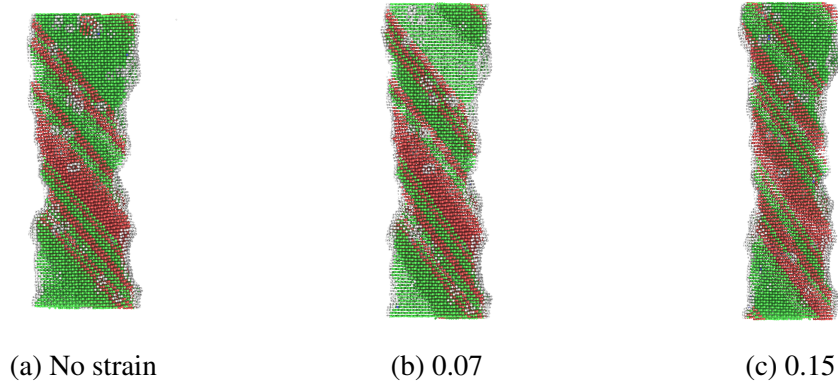


Figure 3.25: Cross-section images of a 10 nm gold nanowire at 1 dpa under tension. Applied strain is shown in the caption of each image.

surface roughness as well as the unfaulting of SFTs present within the interior regions of the nanowires.

The introduction of radiation damage to the nanowires was also found to change how stress relaxation occurs under both compression and tension. In niobium nanowires under compression, large deformation events were replaced with smaller slip events accompanied by the merging and annihilation of dislocations and defect clusters. For niobium nanowires under tension, the stress-strain behavior changed drastically, with the initial yielding of the pristine system being replaced by a regime where the stress remained relatively constant while additional strain was applied. Some of the irradiated niobium nanowires under tension did undergo the same deformation event observed in the pristine niobium nanowires, albeit at a much higher strain. In gold, the SFTs observed in irradiated nanowires were found to be possible sources of dislocations under both compression and tension.

The next of stage this work will be to perform compression and tension simulations with nanoporous structures that have been irradiated, in order to determine how the impact of radiation damage on mechanical behavior differs between nanowires and nanoporous structures. These computations and additional analysis will be provided in a publication of the work performed in this section.

### **3.3 Molecular Statics Investigation into the Stability of the 4H Phase of Gold at 0 K Using the EGTB Interatomic Potential**

#### **3.3.1 Introduction**

In molecular dynamics simulations, the interatomic potential is responsible for defining potential energies and interatomic forces based on the configuration of particles in the simulation. These interatomic potentials can vary significantly in their complexity, and even potentials of the same functional form for the same material can predict significantly different material behavior if the parameters of the potential were fit to different values, as was shown in section 2.2 [21]. Therefore, it is very important that careful consideration is taken when selecting interatomic potentials to ensure that the potential is capable of accurately recreating the characteristics of the intended simulation, such as free surfaces, grain boundaries, and microstructural defects.

The EGTB model is a phenomenological cohesion model, which is a model type known to be better than other potential formulations at reproducing thermally-averaged material properties, such as temperature-dependent lattice constants and atomic mean squared displacement [20]. In this model, the repulsive region of the potential energy curve is defined through an  $n$ -body term based on the Thomas-Fermi electron gas kinetic energy approximation [178], as well as a short-range spline term. This approach, compared to the approach used for EAM potential of using a Born-Meyer pair repulsion term, results in a more accurate prediction of the equation of state, the temperature dependant lattice constant, and the unstable stacking fault energy, which are all dependent on the first and second derivatives of the potential energy curve [20]. The equation of state and unstable stacking fault energy are related to the structural stability of the FCC versus HCP phases, meaning that the application of these approaches to the repulsive region of the potential allows for better reproduction of the phase stability of FCC materials with this potential form. The accuracy with which the EGTB potential is able to recreate the thermodynamic properties of



materials as well as its accurate reproduction of surface and stacking fault energies makes it an ideal potential for use in simulations of highly non-equilibrium conditions, such as simulations of shock or of radiation damage events. Therefore, improving the availability of the EGTB potential to the greater scientific community allows for more accurate MD simulations to be performed in the future.

This section is organized into the following sections. In subsection 3.3.2, the functional form of the EGTB potential is provided, and the implementation of the potential into the LAMMPS source code is discussed. In subsection 3.3.3, the validation of the implementation of the potential in LAMMPS is presented. Finally, subsection 3.3.4 provides an examination of the stability of the 4H hexagonal phase in gold nanoribbons using the EGTB potential. Concluding remarks are provided in subsection 3.3.5.

### 3.3.2 LAMMPS Implementation

In the EGTB potential formulation, the potential energy function consists of four terms, each with their own adjustable parameters [20]. The first term represents the cohesive part of the energy function, and is represented by the following equation,

$$U_{TB}^i = -\xi \left( \sum_{j \neq i} f_{FD}(r_{ij}) \exp \left[ -2q \left( \frac{r_{ij}}{d_2} - 1 \right) \right] \right)^{\frac{1}{2}}, \quad (3.4)$$

where  $\xi$  and  $q$  are adjustable parameters,  $d_2$  is the second nearest neighbor distance at 0 K,  $r_{ij}$  is the interatomic distance between atoms  $i$  and  $j$ , and  $f_{FD}(r_{ij})$  is defined as,

$$f_{FD}(r_{ij}) = \frac{1}{1 + \exp \left[ \epsilon \left( \frac{r_{ij}}{r_0} \right) \right]}, \quad (3.5)$$

where  $\epsilon$  and  $r_0$  are adjustable parameters. A repulsive energy term is defined by the expression

$$U_{rep}^i = A \left( \sum_{j \neq i} \exp \left[ -p \left( \frac{r_{ij}}{d_1} - q \right) \right] \right)^{\frac{5}{3}}, \quad (3.6)$$

where  $d_1$  is the first nearest neighbor distance and  $A$  and  $p$  are adjustable parameters. A long-range correction term is expressed as

$$U_{DJT}^i = \sum_{j \neq i} f_{FD}(r_{ij}) \left[ A_3 \frac{\cos\left(\frac{r_{ij}}{r_{DJT}}\right)}{\left(\frac{r_{ij}}{r_{DJT}}\right)^3} + A_4 \frac{\sin\left(\frac{r_{ij}}{r_{DJT}}\right)}{\left(\frac{r_{ij}}{r_{DJT}}\right)^4} + A_5 \frac{\cos\left(\frac{r_{ij}}{r_{DJT}}\right)}{\left(\frac{r_{ij}}{r_{DJT}}\right)^5} \right], \quad (3.7)$$

where  $A_3$ ,  $A_4$ ,  $A_5$ , and  $r_{DJT}$  are adjustable parameters. Finally, a short-range spline term is expressed as

$$U_s^i = \begin{cases} A_s \sum_{j \neq i} \left[ 1 - \frac{r_{ij}}{r_s} \right]^3 & \text{if } r_{ij} \leq r_s, \\ 0 & \text{otherwise} \end{cases}, \quad (3.8)$$

where  $A_s$  and  $r_s$  are adjustable parameters. Note that in the original paper [20], there is a typo in the expression for Equation 3.8 where the bound of the expression is written as  $r_{ij} \leq r_0$  instead of  $r_{ij} \leq r_s$ . The total potential energy function becomes

$$U_{tot} = \sum_i (U_s^i + U_{rep}^i + U_{DJT}^i + U_{TB}^i). \quad (3.9)$$

The first and second derivatives of this potential energy function provide the stress tensor and the elastic constants at 0 K, respectively.

In molecular dynamics simulations, the potential energy and total force on each atom is computed based on its interaction with other atoms within the system. It is in theory possible to compute the interaction between an atom and every other atom within the simulation; however, as the size of the simulation increases this dramatically increases the computational cost of such an approach. Also, as interatomic distances increase, the magnitude of their interactions with each other also decrease substantially. Therefore, each atom within LAMMPS is assigned a neighbor list of atoms that are within a certain cutoff distance, and only those atoms within the neighbor list are considered when calculating potential energies and interatomic forces.

In the EGTB formulation, Equation 3.4 and Equation 3.6 are considered many-body

terms due to the exponent performed on the summations. This means that in order to calculate the contributions of these functions to Equation 3.9, the sum must be calculated for all atoms within any given atom's neighbor list prior to computing the value of Equation 3.4 and Equation 3.6. This type of operation introduces additional computation cost, as each atom has a unique neighbor list and must be iterated through individually rather than iterating through the list of all possible pairs, as is possible in the case of pair-wise terms such as Equation 3.7 and Equation 3.8.

When adding a new interatomic potential style to LAMMPS, it is necessary to prepare the code such that each atom within the system is assigned a potential energy value and a force value broken into x, y, and z components. The potential energy terms are updated through changing the `eatom` and `eng_vdwl` variables, where `eatom` is a list containing one value for each atom within the simulation and `eng_vdwl` being a single variable that stores the total system potential energy. Interatomic forces are updated through the use of an `ev_tally` operation within LAMMPS, with different styles of the operation being available depending on the specific needs of the interatomic potential.

In order to use the EGTB potential within LAMMPS, the user must provide one input file. This input file contains pre-calculated values for the pair-wise elements of the total potential energy as well as the first derivatives of the potential energy equations, and is structured as follows. The code will ignore the first line of the input file, which can be used as a comment line. The second line holds the atomic number of the element, its atomic mass in amu, the lattice constant of the material in its most stable phase at 0 K, and the name of that phase (*i.e.*, FCC, BCC, etc.). The third line describes the positions where the pair-wise terms were pre-calculated. The first element of the third line defines the number of points where the values were pre-calculated, the second element describes the spacing between these points, and the third value defines the maximum distance where these pre-defined values have been calculated. This maximum distance is also used by the code to define the maximum distance at which interatomic forces and energies are calculated. The

Table 3.3: EGTB Potential Parameters

Quantity	Cu	Ag	Au
$a$ (nm)	0.36015	0.4056	0.406
$A_3$ (eV)	-25.14	-36.86	-69.138
$A_4$ (eV)	44.46	77.9	24.3169
$A_5$ (eV)	2745.52	2284.27	2520.99
$r_{DJT}$ ( $a$ -units)	0.0933	0.098932	0.098583
$A_s$ (eV)	0.0	-10.93	344.74
$r_s$ ( $a$ -units)	–	0.70709	0.66738
$A$ (eV)	$1.6753 \times 10^{-3}$	$2.8165 \times 10^{-3}$	$1.5922 \times 10^{-2}$
$p$	13.55	13.74	7.3956
$\xi$ (eV)	0.505	0.4963	0.6497
$q$	2.2	2.16	2.125
$\epsilon$	14.36	9.61	20.711
$r_0$ ( $a$ -units)	1.43	1.12	1.165

potential energy and force terms begin at an interatomic distance of zero, and increase in integer multiples of the spacing between the points. After these lines, the pre-calculated values for the potential energy terms are provided in the following order:  $U_s$ ,  $U_{DJT}$ ,  $U_{rep}$ ,  $U_{TB}$ ,  $F_s$ ,  $F_{DJT}$ ,  $F_{rep}^{pre}$ , and  $F_{TB}^{pre}$ .  $F_s$  and  $F_{DJT}$  are the first derivatives with respect to  $r_{ij}$  of the terms within the summations of Equation 3.8 and Equation 3.7, respectively.  $F_{rep}^{pre}$  and  $F_{TB}^{pre}$  are the first derivatives with respect to  $r_{ij}$  of the portions of Equation 3.6 and Equation 3.4 within their respective summations. For the pair-wise energy terms ( $U_s$  and  $U_{DJT}$ ), their contribution to the total force is equal to the negative of the derivative of the energy expression. However, for the many-body energy terms ( $U_{rep}$  and  $U_{TB}$ ), their contribution to the interatomic forces includes their final energy values; therefore, the repulsive and tight-binding force terms must be computed after the potential energies have been computed.

### 3.3.3 Interatomic Potential Validation

In order to test if the implementation of the EGTB potential into LAMMPS had been performed correctly, a large suite of simulations were performed calculating various material properties in copper, gold, and silver. The adjustable parameters used for these materials are provided in Table 3.3 [20].

Table 3.4: Defect Formation Energies

Material	$E_v^f$ (eV)	$E_i^{f,100}$ (eV)	$E_{ISF}$ (mJ m <sup>-2</sup> )	$E_C$ (eV)
Cu	1.431	2.901	46.5638	-3.48935
Cu [20]	1.43	3.11	47.7	-3.49
Au	0.844	4.6753	36.477	-3.84535
Au [20]	0.83	5.14	37.6	-3.85
Ag	1.041	2.796	23.124	-2.8854
Ag [20]	1.05	2.796	23.8	-2.93

The properties that were calculated to validate the implementation of the EGTB potential include defect formation energies (Table 3.4), surface energies (Table 3.5), and material elastic constants (Table 3.6). For reference, the values calculated for these properties by Pontikis et al. [20] using the EGTB potentials are also provided. All of the properties calculated for Table 3.4, Table 3.5, and Table 3.6 were determined in FCC lattices at temperatures of 0 K.

Slight differences in values are expected between the values calculated using LAMMPS and the values calculated by Pontikis et al. [20]. For most of the tested parameters, these differences come as a result of differences in the methods used to interpolate between the pre-calculated energy and force values. For the case of the interstitial formation energy  $E_i^{f,100}$ , the differences come as a result of the use of relaxed atomic positions in LAMMPS versus the unrelaxed atomic positions in the work by Pontikis et al. [20].

Table 3.5: Surface Energies (mJ/m<sup>-2</sup>)

Surface Orientation	Copper	Gold	Silver
{100}	1688.913	990.1274	926.4069
{100} [20]	1685.9	980.0	925.8
{110} 1x1	1780.513	1028.597	993.3372
{110} 1x1 [20]	1781.2	1029.8	990.2
{110} 2x1	1878.43	1038.69	1024.104
{110} 2x1 [20]	1878.8	1040.0	1026.2
{111}	1597.853	872.8553	862.5441
{111} [20]	1610.1	862.4	863.0

Table 3.6: Elastic Properties

Material	B (GPa)	$C_{44}$ (GPa)	$C'$ (GPa)
Cu	145.3364	72.776	23.66085
Cu [20]	145.4	72.8	23.7
Au	155.7232	53.565	15.88239
Au [20]	155.7	53.6	15.9
Ag	113.3963	47.05405	16.60766
Ag [20]	113.5	47.1	16.6

### 3.3.4 Investigation of the Stability of the 4H Hexagonal Phase in Gold

One of the strong points of the EGTB potential is excellent recreation of experimentally measured surface energies. As an example use case of the EGTB potential, simulations were performed to examine the stability of the 4H hexagonal phase for gold, which has been experimentally observed as a stable phase in nanoribbons [179] and nanowires [180] that are precipitated in solution. Experimental studies have found that the 4H gold nanoribbons and nanowires can remain stable when removed from the fabrication solution, and it was observed that these structures remained in the 4H phase even when heated, with one study observing a phase transformation to FCC at approximately 800 K [181], while another study observed this phase transformation at 800 °C (1073.15 K) [180]. The 4H hexagonal phase has a characteristic stacking sequence of ‘ABCB’, compared to the stacking sequence of ‘ABC’ for FCC materials. The simulations of the 4H hexagonal phase of gold were performed with lattice constants of 2.86 Å, 4.94 Å, and 9.524 Å for  $a$ ,  $b$ , and  $c$ , respectively ( $a$ ,  $b$ , and  $c$  correspond to the  $[110]$ ,  $[1\bar{1}0]$ , and  $[001]$  directions).

Prior to performing simulations with nanoribbons, it is important to determine the surface energies so that the ribbon is oriented correctly. As described by Fan et al. [179], the nanoribbons are oriented such that they grow along the  $[001]$  axis, with exposed  $\{110\}$  ( $\{11\bar{2}0\}$ ) and  $\{1\bar{1}0\}$  ( $\{1100\}$ ) surfaces, as shown in Figure 3.26. The energies for the  $\{110\}$  and  $\{1\bar{1}0\}$  surfaces as calculated using EGTB and EAM [135] potentials are provided in Table 3.7.

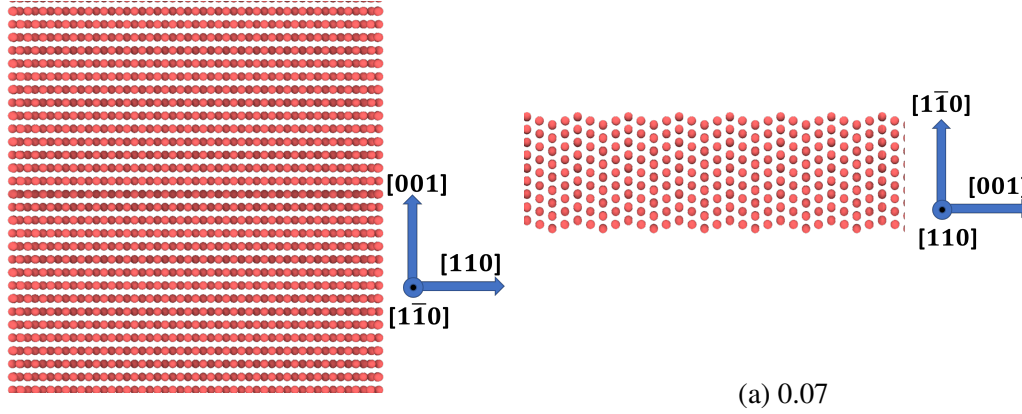


Figure 3.26: Renders of a 2x6 nm 4H hexagonal phase gold nanoribbon. Lattice orientations are provided for each image.

Table 3.7: 4H Surface Energies

Surface Orientation	EGTB (mJ/m <sup>2</sup> )	EAM (mJ/m <sup>2</sup> )
{001}	682.564	730.301
{110}	1041.493	1054.163
{110}	912.040	837.463

Based on the surface energies in Table 3.7 it can be predicted that, in a vacuum, the larger face of the nanoribbon should be oriented to expose the  $\{1\bar{1}0\}$  surface, with the thinner surface exposing the  $\{110\}$  surface, assuming the growth axis of the nanoribbon is along the  $[001]$  direction as has been observed experimentally [179–181]. However, if the conditions of the system were different, such as those described by Fan et al. [179] where there are numerous chemical compounds in solution, it is possible that the interaction of these compounds with the surfaces of the nanoribbons may alter the surface energies and result in different orientations.

Comparing the 4H surface energies from Table 3.7 with those for FCC in Table 3.5, it can be seen that the lowest energy surface predicted by the EGTB potential is the  $\{001\}$  surface of the 4H phase, followed by the  $\{111\}$  surface of the FCC phase, then the  $\{1\bar{1}0\}$  surface of the 4H phase. Based on these surface energies, an FCC nanoribbon with exposed  $\{111\}$  surfaces would have lower energy surfaces than a 4H hexagonal phase nanoribbon with exposed  $\{1\bar{1}0\}$  and  $\{110\}$  surfaces, assuming the nanoribbons have the same exposed

surface area.

The cohesive energy was calculated for both bulk structures as well as nanoribbons with various dimensions in order to examine which phase would be preferred for any of the tested structures. Any system with a lower cohesive energy would be considered more stable, although it is important to note again that these simulations assume a vacuum environment, while the experimental conditions described in Fan et al. [179] involve a specific chemical environment which will adjust the energies. Based on the surface energies shown in Table 3.7, the larger face of the 4H hexagonal phase nanoribbons were oriented such that the  $\{1\bar{1}0\}$  surface would be along the larger face, with the smaller face being oriented to expose the  $\{110\}$  surface. These simulations were performed with both the EGTB potential described above as well as an EAM interatomic potential for gold by Foiles, Baskes, and Daw [135]. This calculated cohesive energies are tabulated in Table 3.8, with the final entry in the table switching the orientations of the surfaces. In the table, entries for the measured cohesive energies of the nanoribbons are listed in the structure column by their dimensions. Values in parentheses represent fcc structures with exposed  $\{100\}$  surfaces, values in brackets represent FCC structures with exposed  $\{110\}$  surfaces, while values with no parentheses represent 4H structures with the larger face of the nanoribbon exposing the  $\{1\bar{1}0\}$  surface.

Table 3.8: Structure Cohesive Energies

Structure	EGTB (eV)	EAM (eV)
4H bulk	-3.84104	-3.92716
fcc bulk	-3.84535	-3.93
2x15 (nm)	-3.74305 (-3.75481) [-3.74358]	-3.83781 (-3.84664) [-3.83234]
2x30 (nm)	-3.74997 (-3.76118) [-3.75089]	-3.84429 (-3.85248) [-3.93927]
4x15 (nm)	-3.78266 (-3.78430) [-3.78592]	-3.87429 (-3.87339) [-3.87301]
4x30 (nm)	-3.78949 (-3.79064) [-3.79306]	-3.88123 (-3.87923) [-3.87980]
6x15 (nm)	-3.79698 (-3.80102) [-3.80067]	-3.88747 (-3.88872) [-3.88714]
15x2 (nm)	-3.74120	-3.83322

Examining the data collected using the EGTB potential in Table 3.8, it can be seen that there were no nanoribbon configurations where the 4H hexagonal structure had a lower



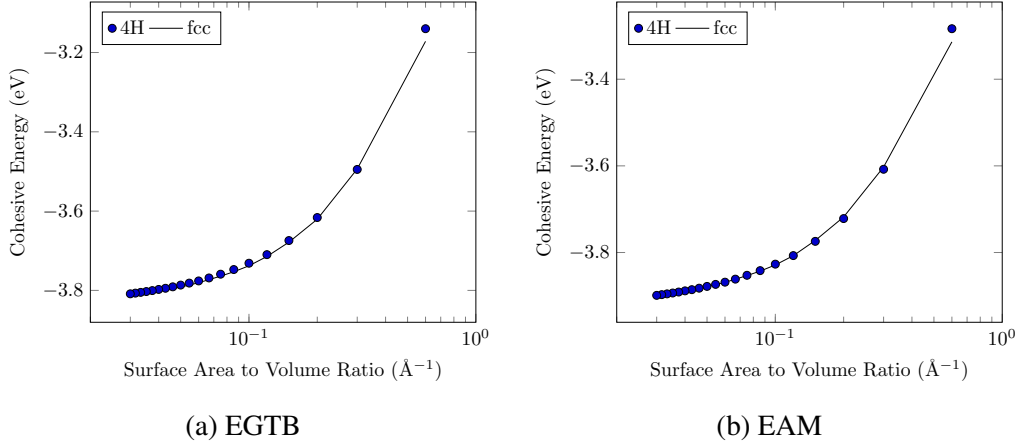


Figure 3.27: Plots of the calculated cohesive energy for spheres with different radii. The x axis represents the ratio of the surface area to the solid volume of the sphere, and is equivalent to three divided by the radius.

cohesive energy than the similarly sized FCC structures. With the EAM potentials, all nanoribbons with thicknesses greater than 2 nm were observed to have a lower cohesive energy than the FCC structures regardless of the orientation of the exposed surfaces, indicating that the 4H hexagonal phase was the preferred phase for those specific configurations. Therefore, it can be understood that the results of the EGTB potential indicate that FCC is the preferred phase for the nanoribbons, while the EAM potential by Foiles, Baskes, and Daw [135] predicts that some nanoribbon configurations are intrinsically more stable in the 4H hexagonal phase than the FCC phase.

Comparing the differences between the cohesive energies of the nanoribbons with different phases, it can be observed that these differences change as the ratio of surface area to solid volume changes. In order to examine how the cohesive energy changes with this ratio, simulations were performed where the cohesive energy was calculated for spheres of various sizes in order to see if there was a ratio where the 4H hexagonal phase would be preferred over the FCC phase. Figure 3.27 shows graphs comparing the calculated cohesive energies as a function of the sphere radius for both EGTB and EAM potentials.

In Figure 3.27, it can be seen that for both of the tested potentials there are surface to volume ratios where the 4H phase is lower in energy than the FCC phase. For the EGTB

potential, the only tested data point where the 4H hexagonal phase was lower in energy than the FCC phase had a surface area to volume ratio of  $0.3 \text{ \AA}^{-1}$ , which is equivalent to a radius of  $10 \text{ \AA}$ . The data captured using the EAM potential had three points where the 4H hexagonal phase was preferred, with surface to volume ratios of 0.3, 0.2, and  $0.15 \text{ \AA}^{-1}$  (equivalent radii of 10, 15, and  $20 \text{ \AA}$ ). For reference, the nanoribbon with the highest surface area to volume ratio was the nanoribbon with a thickness of 2 nm and a width of 15 nm, which had a surface to volume ratio of  $0.1133 \text{ \AA}^{-1}$ .

### 3.3.5 Conclusions

The EGTB potential has been implemented as a `pair_style` within the molecular dynamics code LAMMPS, with the intention of adding that functionality to the official version of the code at a later date. This implementation has been validated through comparisons to calculation performed by Pontikis et al. [20] in gold, silver, and copper.

The EGTB potential was then used to study the stability of the 4H hexagonal phase in gold nanoribbons, with comparisons made to simulations performed using an EAM potential for gold from Foiles, Baskes, and Daw [135]. This examination found that the EAM potential predicted a preference for the 4H hexagonal phase for nanoribbons with certain size characteristics, but the EGTB potential always favored the FCC phase over the 4H hexagonal phase. The behavior predicted by the EGTB potential aligns with experimental observations [179–181], where the 4H hexagonal phase gold nanoribbons were found to only form under very specific chemical conditions, with FCC phase structures being preferred when those conditions were absent.

Future work include the necessary optimization and documentation to get the EGTB `pair_style` added to the distribution version of LAMMPS. Also, the EGTB potential could be used to examine the temperature at which the 4H hexagonal phase of gold transitions to FCC, to see if the predicted transition temperature aligns with those observed by Wang et al. [180] and [181].

## CHAPTER 4

### COMPUTATIONAL STUDY OF RADIATION-INDUCED SEGREGATION MECHANISMS IN METALLIC ALLOYS

In this chapter, we seek to address the third question posed in Chapter 1,

**Q3** How do defect characteristics effect continuum scale models of radiation-induced degradation mechanisms, such as radiation induced segregation?

In the following section, we propose a phase field model for radiation induced segregation in a binary alloy. This model serves as an example of how continuum scale methods rely on accurate quantification of the characteristics of radiation-induced defects, which were examined in Chapter 2. The proposed model allows for the examination of how irradiation conditions can impact the accumulation of radiation-induced defects and the radiation-induced degradation mechanism of radiation-induced segregation.

#### **4.1 Phase Field Examination of Radiation Induced Segregation in Binary Alloy Systems**

##### 4.1.1 Introduction

Materials exposed to a radiation environment can experience changes to their microstructures due to the local atomic shuffling and defect formation that occurs as a result of radiation damage events [1–5]. These microstructural changes can lead to the degradation of the material’s properties through a variety of mechanisms, including radiation-induced hardening and embrittlement, radiation-induced and -modified solute segregation and phase stability, irradiation creep, void swelling, and high temperature helium embrittlement [3, 6]. In metallic alloys, RIS leads to changes in the local composition of the alloy which can eventually lead to de-alloying of the material or local phase transformations [29, 182–185].

Due to the drastic consequences of radiation-induced segregation on the properties of alloyed materials, there exists a need for predictive models that can assist in the selection and design of materials that can delay or resist the onset of RIS.

The damage mechanism known as RIS occurs as a result of several phenomena over a wide range of time and length scales [28, 29]. At a time-scale of picoseconds and a length-scale of nanometers, radiation damage events evolve through stages of ballistic collisions and thermal equilibration, ultimately resulting in the formation of defects as well as some short-range atomic shuffling. Over short time and length-scales, this local atomic mixing disrupts the distribution of elements within the alloy and can cause localized regions to become solute-rich or solute-poor. Over greater length and time-scales, preferential diffusion of solute atoms can lead to growth of these heterogeneous regions, potentially leading to phase changes and stress fields created through lattice mismatch at the aggregate-matrix interface. This process is enhanced via the diffusion of radiation-induced defects, which have a tendency to migrate towards and either accumulate or annihilate at pre-existing defect sinks such as dislocations and grain boundaries [28, 182].

The same conditions that play a role in determining the quantity and type of radiation-induced defects present within a microstructure also play a role in determining the onset and development of RIS. Averback et al. [186] found that increasing the irradiation temperature lead to an increase in the thickness of the precipitate layer that would form in the Ni-12.7 at.% Si sample. They also observed a temperature threshold effect, where above 590 °C the growth rate of the precipitate region ceased to depend on dose rate, while below that temperature the growth rate was dose rate dependent. Etienne et al. [187] performed irradiation experiments in ultrafine-grained and conventional 316 austenitic stainless steels, and observed reduced RIS development at the same doses in the ultrafine-grained sample compared to the conventional sample. This serves as an example that microstructural features that suppress radiation damage formation and accumulation, such as a high density of grain boundaries in the case of the ultrafine-grained 316, also impede the development

of RIS. Allen et al. [188] examined neutron-irradiated samples of stainless steels as well as samples irradiated with protons and observed that RIS was enhanced at lower displacement rates under neutron irradiation. Was and Allen [189] compared several experiments performed in stainless steels irradiated by neutrons, protons, or ions, and noted that the development of RIS in terms of dose dependence and segregation profile differs depending on the type of incident particle. Therefore, any attempts to develop predictive models of radiation-induced segregation should have the capacity of considering the effects of temperature, pre-existing microstructural features, dose rate, and incident particle type.

Atomistic simulation techniques such as MD or kMC provide unique and necessary insight into the formation of defects and the local atomic mixing that occurs during radiation damage events [23]; however, these simulation techniques operate on length and time-scales that are too small to observe the longer length and time-scale mechanisms of RIS [24]. An alternative to atomistic methods would be the use of continuum methods such as phase-field or cluster dynamics, where the evolution of a material over time is modeled as the evolution of a set of field equations solved over a set of discrete nodes. These equations rely on the atomistic properties of materials in order to simulate time-dependent material processes, including grain growth, corrosion, de-alloying, or radiation-induced segregation [27–29].

In a cluster dynamics model, the evolution of defect clusters over time is described through a series of ordinary differential equations where each equation represents the number density of defect clusters of a given size [190, 191]. Cluster dynamics allows for the simulation of defect clustering under irradiation over very long time-scales, but becomes more computationally expensive as the range of considered cluster sizes is expanded. Cluster dynamics simulations are also limited to modeling systems with few mobile defects or chemical species unless simplifying assumptions are made [169, 190]. Such techniques have been used to study the accumulation of radiation damage in materials [169, 190, 191], as well as to study phase changes and precipitate growth under irradiation [192, 193].

In a phase field model, the evolution over time of the elemental species, point defect species, and any other species considered by the model are all represented individually by coupled partial differential equations, where interactions between the different species are described via rate terms [28, 29, 170, 194, 195]. Several phase field models of radiation-induced segregation have been produced previously; however each of those came with limitations that prevented them from being used to simulate materials under realistic irradiation and microstructural conditions. The model presented by Dubey and El-Azab [194, 195] examines the radiation-induced segregation behavior of a binary alloy with a free surface as a sink. This model includes a unique consideration of interstitial dumbbells, where different field variables are used to represent different dumbbell configurations; however, this model does not include the formation and growth of defect clusters. The model presented by Badillo, Bellon, and Averback [28] includes the presence of vacancy and interstitial clusters, but does not allow for the presence of any additional defect sinks, such as free surfaces or dislocations. The model presented by Piochaud et al. [29] includes a calculation of diffusion parameters from accelerated kinetic Monte Carlo simulations, and utilizes a variable time-step approach to accelerate the simulation. However, this model does not include the formation of defect clusters and does not include additional discrete defect sinks, such as dislocations, grain boundaries, or free surfaces.

The intent of the proposed phase field model is to provide a method that can be used to examine radiation-induced segregation behavior in binary alloy systems while including as few simplifications to the system as possible. Therefore, the proposed model includes the formation and evolution of defect clusters, the presence of additional defect sinks in the form of dislocations (which also interact with the chemical potentials of the point defect species through an applied stress field), and two different methods of radiation damage insertion, which are intended to simulate either electron beam or ion beam irradiation. A quick comparison between the proposed model and some of the previously developed phase field models of radiation induced segregation is provided in Table 4.1.

Table 4.1: Comparison of existing phase field radiation-induced segregation models

	Defect Clusters	Additional Sinks	Damage Insertion	Additional Features
Model 1 [195]	None	Free Surface	Cascade-like	Considers Dumbbell Orientation
Model 2 [28]	Yes	None	FP Insertion	None
Model 3 [29]	None	Arbitrary Sink	Uniform Source	Multi-timescale solver
Model 4 [170]	None	Dislocations	Uniform Source	Stress-Chemical Potential Coupling
Proposed Model	Yes	Dislocations	FP and Cascade-like Insertion	Stress-Chemical Potential Coupling

This work is organized into the following sections. A complete description of the radiation-induced segregation phase field model presented in this work is provided in subsection 4.1.2. An examination of the effect of dose rate on the development of RIS is provided in subsubsection 4.1.3. A comparison in the RIS behavior of systems modeled using two different radiation damage insertion methods is provided in subsubsection 4.1.4. A summary of the results produced using the proposed model and concluding remarks are provided in subsection 4.1.5.

#### 4.1.2 Phase Field Model for Radiation-Induced Segregation in Binary Alloys

##### *Kinetic Equations*

This model considers a binary alloy with self-interstitials of both alloy species as well as vacancies. Included in this model are also clusters of each point defect species. The evolution of the atomic, point defect, and defect cluster concentrations through time and space are modeled using Cahn-Hilliard style equations. These equations have been modified to include a variety of defect-defect and defect-defect cluster interactions, which will be defined below. Each node within the simulation volume is assumed to be a cube with each side dimension being  $L$  unit cells across. Therefore, each node would contain  $L^2$  or  $L^3$  unit cells, depending on whether the simulation is two or three dimensional, respectively. The concentration within each node for any given species is thereby determined by dividing a number of atoms or point defects within the node by the number of lattice sites within the node.

In total, there are eight fields that are represented within this model, representing the

two alloy species ( $X_A, X_B$ ), the three point defect species ( $X_V, X_{iA}, X_{iB}$ ), and the three defect cluster species ( $X_{VC}, X_{iAC}$ , and  $X_{iBC}$ ). For some of the equations used in this model, adjusted concentrations are used in order to account for the presence of defect clusters within specific nodes, which reduces the number of available sites. The expressions used in the proposed model have been modified from the expressions presented in Badillo, Bellon, and Averback [28]:

$$\tilde{X}_\gamma = \frac{X_\gamma}{1 - X_{VC} - X_{iAC} - X_{iBC}}; \text{ for } \gamma = A, B, V, \quad (4.1)$$

$$\tilde{X}_{i\alpha} = \frac{X_{i\alpha}}{1 - X_{VC} - X_{iAC} - X_{iBC}}; \text{ for } \alpha = A, B. \quad (4.2)$$

The change in the alloy species (described in the equations as  $\alpha$  and  $\beta$ , each representing species  $A$  or  $B$ ) and the point defect concentrations (described in the equations as  $d$ , representing either vacancies or either of the two self-interstitial atom concentrations) are described by the following equations [29]:

$$\frac{dX_\alpha}{dt} = \nabla \cdot \left[ \sum_d \sum_\beta \frac{\ell_{\alpha\beta}^d X_d}{k_B T} (\nabla \mu_\beta + \text{sign}(d) \nabla \mu_d) \right] + R_{V,i\alpha} + R_{VC,i\alpha} + R_{V,i\alpha C}, \quad (4.3)$$

$$\frac{dX_d}{dt} = \nabla \cdot \left[ \sum_\alpha \sum_\beta \frac{\ell_{\alpha\beta}^d X_d}{k_B T} (\text{sign}(d) \nabla \mu_\beta + \nabla \mu_d) \right] - R_{recom} - R_{d,sink}. \quad (4.4)$$

In these equations,  $\text{sign}(d)$  has a value of  $-1$  for vacancies and a value of  $1$  for the two interstitial species,  $\mu_\beta$  is the chemical potential of the alloy species,  $\mu_d$  is the chemical potential of a point defect species,  $T$  is the temperature of the system in Kelvin, and  $k_B$  is the Boltzmann constant.  $R_{recom}$  and  $R_{d,sink}$  depend on which point defect  $d$  and which sinks are being considered. The term  $\ell_{\alpha\beta}^d$  represents a normalized Onsager coefficient, and is defined by the equation

$$\ell_{\alpha\beta}^d = \frac{V_{at} k_B T}{X_d} L_{\alpha\beta}^d, \quad (4.5)$$



where  $V_{at}$  is the atomic volume normalized by the number of lattice cells per simulation node. The expressions for  $L_{\alpha\beta}^d$  can be found in Tucker et al. [196], with the parameters used in this work tabulated in Appendix E.

Recombination of the point defect species is handled using the below equations [28]:

$$\left(\frac{dX_{iA}}{dt}\right)_{recom} = R_{V,iA} = -4\pi r_c \tilde{X}_V \tilde{X}_{iA} [\bar{\Gamma}_V + \nu_c^{iA} \exp(-\beta E_{iA}^m)], \quad (4.6)$$

$$\left(\frac{dX_{iB}}{dt}\right)_{recom} = R_{V,iB} = -4\pi r_c \tilde{X}_V \tilde{X}_{iB} [\bar{\Gamma}_V + \nu_c^{iB} \exp(-\beta E_{iB}^m)], \quad (4.7)$$

and

$$\left(\frac{dX_V}{dt}\right)_{recom} = \left(\frac{dX_{iA}}{dt}\right)_{recom} + \left(\frac{dX_{iB}}{dt}\right)_{recom} \quad (4.8)$$

In the above equations,  $\bar{\Gamma}_V$  is defined by the below equation [28]:

$$\bar{\Gamma}_V = \nu_c \tilde{X}_A \exp(-\beta E_{VA}^m) + \nu_c \tilde{X}_B \exp(-\beta E_{VB}^m). \quad (4.9)$$

The expression  $4\pi r_c$  in Equation 4.6 and Equation 4.7 is for three dimensional simulations, and is replaced by the expression  $2\pi / [r_c^2/2 - \ln(r_c) - 1/2]$  for two dimensional simulations. In the above equations,  $r_c$  refers to the recombination radius for interstitials and vacancies normalized by the size of the node,  $\nu_c$  refers to the jump attempt frequency of isolated vacancies divided by  $L^2$  (i.e.  $\frac{\nu}{L^2}$ ),  $E_{VA}^m$  and  $E_{VB}^m$  are the vacancy migration barriers in pure metals of species A or B, and  $E_{iA}^m$  and  $E_{iB}^m$  are the migration barriers for interstitials of type A and type B atoms, respectively. A discussion on why the vibrational frequency  $\nu$  must be normalized by the dimension of the nodes can be found in Badillo, Bellon, and Averback [28].

The change in the concentrations of the defect clusters are described by the following equations

$$\frac{dX_{VC}}{dt} = R_{V,VC} - \sum_{\alpha} R_{i\alpha,VC}, \quad (4.10)$$

$$\frac{dX_{i\alpha C}}{dt} = R_{i\alpha, iAC} + R_{i\alpha, iBC} - R_{V, i\alpha C}. \quad (4.11)$$

For all cluster types, growth of the cluster occurs via interactions with defects of the same type (i.e., vacancy absorption at a vacancy cluster) and shrinkage of the cluster occurs via absorption of the opposite defect type (i.e., vacancy absorption at an interstitial cluster). Vacancy-vacancy cluster interactions are described by the equation,

$$R_{V, VC} = \nu_c \left( \tilde{X}_A \exp(-\beta E_{VA}^m) + \tilde{X}_B \exp(-\beta E_{VB}^m) \right) \left\{ \tilde{X}_V - \frac{\exp(-\beta E_{N-1 \rightarrow N}^b)}{1 - X_{VC}} \right\}. \quad (4.12)$$

In the above equation,  $E_{N-1 \rightarrow N}^b$  is the binding energy of a single vacancy to a vacancy cluster of size  $N$ , which is approximated using the following equation:

$$E_{N-1 \rightarrow N}^b = E_V^f + \frac{E_{2V}^b - E_V^f}{2^\sigma - 1} [N^\sigma - (N-1)^\sigma], \quad (4.13)$$

where  $E_V^f$  is the vacancy formation energy,  $E_{2V}^b$  is the divacancy binding energy, and  $\sigma$  is related to the spacial dimension via the expression  $\sigma = (d-1)/d$  where  $d$  is the dimensionality of the simulation. Equation 4.12 includes both vacancy capture at vacancy clusters (represented by the first term in the curly brackets) as well as thermal emission of vacancies from vacancy clusters (represented by the second term in the curly brackets).

The expression for vacancy loss at interstitial clusters is

$$R_{V, i\alpha C} = \nu_c \left( \tilde{X}_A \exp(\beta E_{VA}^m) + \tilde{X}_B \exp(\beta E_{VB}^m) \right) \tilde{X}_V, \quad (4.14)$$

and the expressions for interstitial loss at vacancy clusters and interstitial clusters are described by the equations

$$R_{i\alpha, i\alpha C} = \nu_c^{i\alpha} \tilde{X}_{i\alpha} \left( 1 - \tilde{X}_{iA} - \tilde{X}_{iB} \right) \exp(-\beta E_{i\alpha}^m). \quad (4.15)$$

A constraint was applied to the simulation such that vacancy clusters and interstitial clusters could not be in the same node at the same time.

### *Driving Forces*

The diffusion behaviors of the different mobile species are described by the first term on the right hand side of Equation 4.3 and Equation 4.4. The chemical potentials  $\mu_\alpha$  and  $\mu_d$  are functions of the chemical energy of the system, which can be divided into homogeneous and heterogeneous parts according to the equation [29]

$$F^{chem}(X_d, X_\alpha) = F_{hom}^{chem}(X_d, X_\alpha) + F_{het}^{chem}(X_\alpha), \quad (4.16)$$

expressions for which can be found in Piochaud et al. [29]. The chemical potential of the alloy and defect mixture  $\mu$  can be derived from the expressions for chemical energy through a partial derivative, as shown in the following equations;

$$\mu_\alpha = V_{at} \frac{\delta F^{chem}}{\delta X_\alpha}, \quad (4.17)$$

and

$$\mu_d^0 = V_{at} \frac{\delta F^{chem}}{\delta X_d}. \quad (4.18)$$

Equation 4.17 and Equation 4.18, as well as Equation 4.5 tend towards infinity when the species concentration approaches zero. Due to this limitation, the defect species were not allowed to fall below their thermal equilibrium concentration as defined by the expression  $e^{-E_d^f/k_bT}$ , and the concentrations of the A and B species were not allowed to fall below 0.001 within any single node.

In this model, the chemical potential for vacancies and interstitials is modified by a stress term [170]. The expressions for the total chemical potential of vacancies and inter-

stitials are below:

$$\mu_V = \mu_V^0 - V_m \eta_V \sigma_{kk}, \quad (4.19)$$

and

$$\mu_{i\alpha} = \mu_{i\alpha}^0 - V_m \eta_{i\alpha} \sigma_{kk}. \quad (4.20)$$

In Equation 4.19 and Equation 4.20,  $V_m$  is the molar volume of the pure solid,  $\eta_V$  and  $\eta_{i\alpha}$  are the coefficients of compositional expansion for vacancies and interstitial respectively, and  $\sigma_{kk}$  is the trace of the stress tensor calculated for each node of the simulation volume.

All simulations discussed in this work were performed with zero-flux boundary conditions applied to the edges of the simulated volume.

#### *Method for Calculating Stress*

Due to the nature of the simulated system, there will be an inherent non-zero residual stress field throughout the simulated volume. This stress field is produced due to microstructural defects (i.e., dislocations or grain boundaries) as well as eigenstrain caused by the point defects [170]. Since this model also includes the formation and growth of defect clusters, the concentration of these clusters were also included when computing the stress. The total stress field within the simulated volume can be considered as a sum of the intrinsic stress and the stress associated with the elastic response and compositional eigenstrain,

$$\sigma_{ij} = \sigma_{ij}^{(in)} + \hat{\sigma}_{ij}. \quad (4.21)$$

The second term in Equation 4.21 can be summarized as the product of the stiffness tensor  $C_{ijkl}$  and the sum of two distinct terms that represent the strain due to the elastic response and the compositional eigenstrain, respectively,

$$\hat{\sigma}_{ij} = C_{ijkl} \left( \varepsilon_{kl}^{(el)} + \varepsilon_{kl}^{(c)} \right). \quad (4.22)$$

The compositional strain is defined by the equation,

$$\varepsilon^{(c)} = (\eta_i X_i + \eta_v X_v) \begin{bmatrix} 1 \\ 1 \\ 0 \end{bmatrix}, \quad (4.23)$$

where  $\eta_i$  and  $\eta_v$  are the coefficients of compositional expansion for interstitials and vacancies, respectively. In Equation 4.23,  $X_i$  and  $X_v$  including both the concentrations of their respective point defects as well as the concentrations of their respective defect clusters.

The strains  $\hat{\varepsilon}_{ij}$  are calculated using the nodal displacements  $\hat{u}_i$  using the compatibility equation,

$$\hat{\varepsilon}_{ij} = \frac{1}{2} (\hat{u}_{i,j} + \hat{u}_{j,i}). \quad (4.24)$$

The elastic strain can then be calculated using the following expression,

$$\varepsilon^{(el)} = \hat{\varepsilon} - \varepsilon^{(c)}. \quad (4.25)$$

Using Equation 4.22, Equation 4.23, Equation 4.24, and Equation 4.25, the  $\hat{\sigma}_{ij}$  term in Equation 4.21 can be determined.

For a system containing no dislocations, the intrinsic stress term  $\sigma_{ij}^{(in)}$  is zero, and the total stress is equal to Equation 4.22. However, the proposed phase field model also allows for the presence of an edge dislocation as a defect sink, alongside its intrinsic stress field. The following equations describe the stress field for an edge dislocation centered at  $(0, 0)$  [197].

$$\sigma_{11}^{\perp} = -D_0 b \frac{y(3x^2 + y^2)}{x^2 + y^2}, \quad (4.26)$$

$$\sigma_{22}^{\perp} = D_0 b \frac{y(x^2 - y^2)}{x^2 + y^2}, \quad (4.27)$$

$$\sigma_{12}^{\perp} = D_0 b \frac{y(x^2 - y^2)}{x^2 + y^2}, \quad (4.28)$$

$$D_0 = \frac{\mu}{2\pi(1 - \nu)}, \quad (4.29)$$

where  $\mu$  is the shear modulus of the material,  $\nu$  is the Poisson's ratio, and  $b$  is the Burgers vector of the dislocation. The matrix form of Equation 4.26, Equation 4.27, and Equation 4.28 takes the place of the first term in Equation 4.21. Finally, the out-of-plane stress is calculated as:

$$\sigma_{33} = \nu(\sigma_{11} + \sigma_{22}) \quad (4.30)$$

The total stress is then entered into Equation 4.19 and Equation 4.20 in order to determine the chemical potentials for the point defect species.

#### *Additional Considerations*

**Defect Cluster Migration** Migration of defect clusters was managed through a random shuffling step. Vacancy clusters containing more than the equivalent concentration of five vacancies were considered immobile [198]. Interstitial clusters that were smaller than half the node size were allowed to migrate, as well as vacancy clusters smaller than five vacancies. For every mobile defect cluster, a random number was generated during each simulated time step and that number was compared to a threshold value that determined the migration frequency. For the simulations performed in this work, this threshold was chosen such that on average each cluster would migrate once every 100 timesteps. Mobile defect clusters were allowed to migrate to any adjacent node, as long as that motion would not lead to the concentration of that defect species to exceed one. When considering the migration of vacancy clusters, a proportionate amount of A and B species would be placed in the node originally containing the vacancy cluster, based on the original concentrations of A and B species in the target node. Defect clusters trapped at dislocations were not

allowed to be displaced. If through a migration step defect clusters of opposite types ended up in the same node, the clusters were set to annihilate with each other, leaving behind the excess of the larger cluster.

**Simulation Parameters** All simulation parameters used in this work are provided in Appendix E.

**Handling Excess Defect Cluster Growth** If an interstitial defect cluster grew to a sufficient size that it filled an entire node, the excess cluster concentration was shuffled to adjacent nodes, based on the ratio of interstitial atoms of species A and B.

#### *Radiation Damage Insertion Methods*

This model allows for two different methods of inserting radiation damage. The first and simplest of the methods is Frenkel pair (FP) insertion, which is meant to resemble electron irradiation [29]. In this method, the vacancy field variable within a target node is increased by the equivalent value of a single vacancy. Based on the local atomic composition, an interstitial atom of either type A or type B is created in either the same node as the vacancy or one of the immediately adjacent nodes. These FP insertion events occur at a frequency determined by a target dpa rate.

The second method of radiation damage insertion can be considered as a cascade-like insertion method, which is meant to resemble ion beam irradiation [23, 195]. This methodology uses the ARC-dpa and ARC-rpa method of determining the number of defects and the size of the mixing region that form as a result of a damage cascade initiated by a particle with energy  $T$  [145]. The equations for this method were defined in subsubsection 3.1.2 of Chapter 3. This method approximates a radiation damage cascade as a core-shell structure that is described by two different damage estimators. The first estimator is an athermal recombination corrected dpa that occurs in the shell of the approximated cascade, which is meant to capture the formation of long-range ballistic damage near the periphery of the

thermal spike. The second estimator is a short-range thermal spike mixing damage that occurs within the hot cascade core. The number of atoms involved in either the core or the shell of the approximated damage cascade initiated by a PKA with energy  $T$  are determined using Equation 3.1, Equation 3.2, and Equation 3.3.

In the proposed phase field model,  $N_{dpa}$  vacancies are created within the randomly selected node, and  $N_{dpa}$  interstitials are created either in the same node or any of the adjacent nodes. The fraction of interstitials that are of species A or B are sampled from the selected node's concentrations of species A or B. In order to account for recombination of pre-existing defects that exist within the node where the damage event occurred, the fraction of the node that is participating in the cascade is determined by dividing  $N_{rpa}$  by the number of atoms per node. Then, the minimum defect fraction is determined by comparing the total vacancy concentration (i.e. the sum of the isolated vacancy concentration and the vacancy cluster concentration) in the event node to the total interstitial concentration. A random number between 0 and 1 is multiplied by the product of the minimum defect concentration and the fraction of the node that is participating in the cascade. This fraction of the minimum defect concentration is recombined with the other defect species according to the local distribution of point defects to defect clusters and interstitials of species A and B.

A maximum recoil energy is provided as an input into the model, and an event energy is sampled based on that maximum energy using the primary recoil spectrum calculated using the below equations [199].

$$P(E, T) = \frac{\int_{E_d}^T \sigma(E, T') dT'}{\int_{E_d}^{\hat{T}} \sigma(E, T') dT'}. \quad (4.31)$$

Equation 4.31 represents the fractional number of recoils between the minimum displacement energy  $E_d$  and energy  $T$ , where  $\hat{T}$  is the maximum possible recoil energy,  $E$  is the incident ion energy, and  $\sigma(E, T)$  is the scattering cross section for heavy, slow ions with



incident energy  $E$  and PKA energy  $T$ . The scattering cross-section can be approximated using the following equation,

$$\sigma(E, T) = \frac{\pi^2 a^2 E_a \gamma^{1/2}}{8 E^{1/2} T^{3/2}}, \quad (4.32)$$

where  $a = \frac{0.8853a_0}{(Z_1 Z_2)^{1/6}}$  ( $Z_1$  and  $Z_2$  are the atomic numbers of the interacting atoms and  $a_0$  is the Bohr radius),  $\gamma = \frac{4M_1 M_2}{(M_1 + M_2)^2}$  ( $M_1$  and  $M_2$  are the masses of the interacting atoms), and  $E_a = 13.6 (Z_1 Z_2)^{7/6} \frac{(M_1 + M_2)}{(M_2 \epsilon)}$  ( $\epsilon$  is the unit charge). For the ARC-dpa insertion method, the dpa rate is controlled by using the average recoil energy from the spectrum described by Equation 4.31 and its  $N_{dpa}$  to determine an appropriate event rate. For the simulations performed in this work, the maximum cascade size was limited such that  $N_{rpa}$  did not exceed the number of lattice sites within any one node. A potential improvement of this model would be to allow for cascade events that are sufficiently high enough in energy to be spread across multiple nodes at once.

### 4.1.3 Results

For the simulations performed for this work, the nickel-chrome alloy system was used as a reference for the physical constants [196]. All simulations were performed with a temperature of 673.15 K, a 32x32x1 grid of nodes with  $L$  equal to 14, a simulated time-step of one second, and an 80-20 average alloy concentration with a 5% amplitude noise applied to the solute concentration. A complete list of all simulation parameters are provided in Appendix E.

#### *Dose Rate Effect on Radiation-Induced Segregation*

The accumulation of defects and the evolution of radiation-induced degradation mechanisms such as RIS is closely related to the irradiation conditions, including the flux of the incident radiation, the irradiation particle type, and the dose rate that the material experi-

ences. Displacement rates can vary significantly depending on the conditions of irradiation. Intentional irradiation via ion beam exposure can produce displacement rates on the order of  $10^{-2}$  to  $10^{-5}$  dpa/s, while exposure to neutron flux across a nuclear reactor can produce displacement rates on the order of  $10^{-7}$  to  $10^{-12}$  dpa/s [198]. In this section we examine the impact of the dose rate on the accumulation of radiation-induced defects as well as the onset and progression of RIS in a binary alloy.

In order to study the relationship between dose rate and RIS, simulations were performed using the proposed phase field model with three different dose rates, 1 dpa/day ( $1.1574 \times 10^{-5}$  dpa/s), 1 dpa/month ( $3.858 \times 10^{-7}$  dpa/s), and 1 dpa/year ( $3.171 \times 10^{-8}$  dpa/s). These simulations were performed using cascade-like damage insertion, which replicates the production of radiation damage in systems undergoing irradiation by heavy ions. No defect clusters were present in these systems at the beginning of irradiation, but defect clusters were allowed to form during damage insertion events as described in subsubsection 4.1.2, with all other simulation parameters provided in Appendix E.

Figure 4.1 shows the evolution of the point defect concentrations in systems irradiated at the three mentioned dose rates up to a final dose of 10 dpa. Comparing the scales representing the magnitude of the point defect concentrations for the three graphs, we can observe that defect concentrations within these systems vary depending on the incident dose rate, with the concentration increasing with an increase in the dose rate. Second, across all three simulations the point defect concentrations appear to reach a steady state value prior to the interstitial and vacancy concentrations diverging. For the 1 dpa/day simulation, this meta-stable equilibrium concentration is reached very quickly, at around a dpa of 0.01 or a simulated time of approximately 100 seconds. At 1 dpa/month, this equilibrium defect concentration is reached roughly around 0.003 dpa (a simulated time of around 2 hours), and at 1 dpa/year this equilibrium concentration is reached at around  $4 \times 10^{-4}$  dpa (a simulated time of around 3 hours). A similar trend with dose rate is observed with the dose at which the vacancy and interstitial concentrations diverge. Due to differences in diffusion

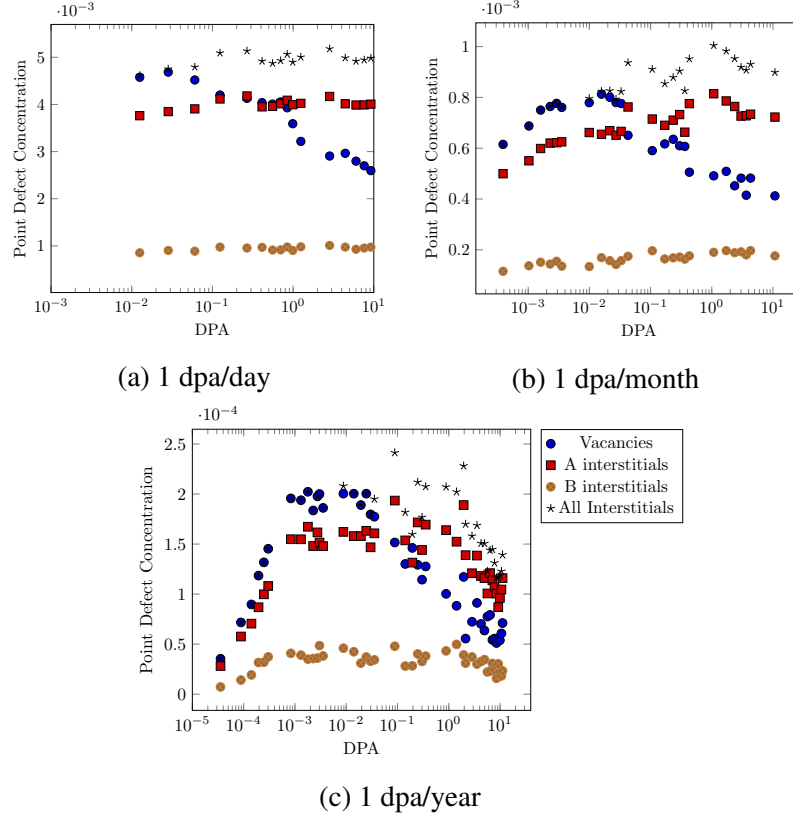


Figure 4.1: Plot of point defect concentrations as a function of dose for three different dose rates. The legend for (c) describes the marks for (a) and (b).

behavior between the two defect species, it is expected that the concentrations of vacancies and interstitials should diverge as one of the two species should diffuse to defect sinks at a higher rate. In the proposed model, defect concentrations are conserved, meaning that the number of free and trapped vacancies and interstitials must always be the same. Because of this imposition on the model, we observe across all three dose rates the behavior of the free vacancy concentration decreasing below that of the free interstitials, as a greater number of vacancies become preferentially trapped in vacancy clusters. The dose at which this deviation begins follows the same trend as was observed with the reaching of the metastable defect concentrations, where increasing the dose rate increases the dose at which this transition occurs.

This behavior where the concentration of free vacancies decreases below that of the free interstitials in the proposed model does deviate from the behavior described in traditional

rate-equation models such as those shown in Was [199]. This is likely due to the previously mentioned conservatory nature of the proposed model. In real material systems, defect sinks do not necessarily conserve the species that the proposed model tracks. For example, defect migration to a defect sink such as a dislocation does not necessarily preserve the integrity of the defect type (i.e., vacancy loss at a dislocation does not necessarily return a trapped interstitial to a standard lattice position). Depending on the simulation parameters, the preference of the simulation to store more defects in the form of interstitial or vacancy clusters will determine which point defect has a higher concentration.

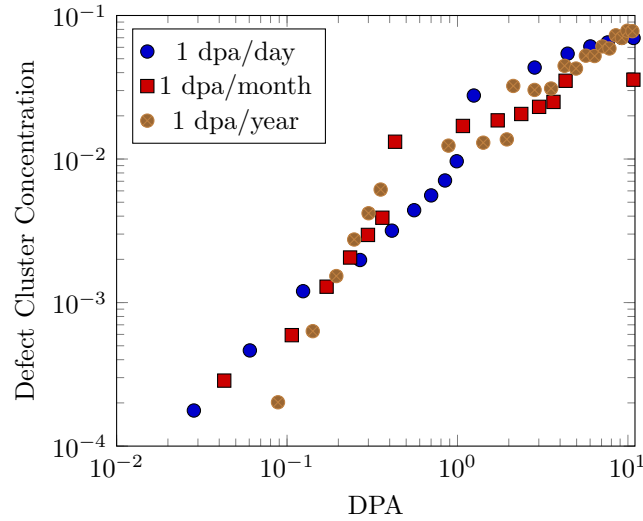


Figure 4.2: Plot of the total defect cluster concentration (i.e., the sum of the concentrations of vacancy clusters and interstitial clusters) for simulations with different dose rates.

Differences between the defect accumulation behavior of the proposed phase field model and the behavior seen in other phase field models [28, 29] and the simple rate-theory model proposed by Was [199] are also due to how the density of defect sinks is handled. In some phase field models [29, 170] and the rate theory model proposed by Was [199], defect sink densities are static and cannot be changed by the annihilation of defects at those sinks. In Badillo, Bellon, and Averback [28], the results shown for defect densities were of simulations where pre-existing defect clusters were present at the beginning of the simulation, and the parameters were tuned such that these clusters did not change in size

significantly throughout the course of the simulation. The simulations whose results are shown in Figure 4.1 and Figure 4.2 allowed the formation of new clusters during irradiation, and these clusters were changing in size throughout the course of the simulation. This change in the sink density with respect to defect clusters as sinks is a more realistic but imperfect representation of how defect clusters evolve in irradiated systems.

The dose rate also plays a role in how the concentrations of defect clusters evolves, which is shown in Figure 4.2. No consistent trends are observed at lower doses, as in this regime defect clusters are beginning to form and grow and haven't trapped a significant number of point defects yet. As the dose approached 10 dpa, the fluctuations in cluster concentration stabilized, with the 1 dpa/year simulation having the highest concentration of defect clusters, then the 1 dpa/day simulation, then the 1 dpa/month. This behavior indicates that the dependence on dose rate of the formation and growth of defect clusters follows an inverse parabolic trend, where very high and very low dose rates encourage cluster formation and growth, while intermediate dose rates are less favorable for the formation and growth of defect clusters. It also appears that across all three dose rates the sink density is beginning to approach a steady-state value.

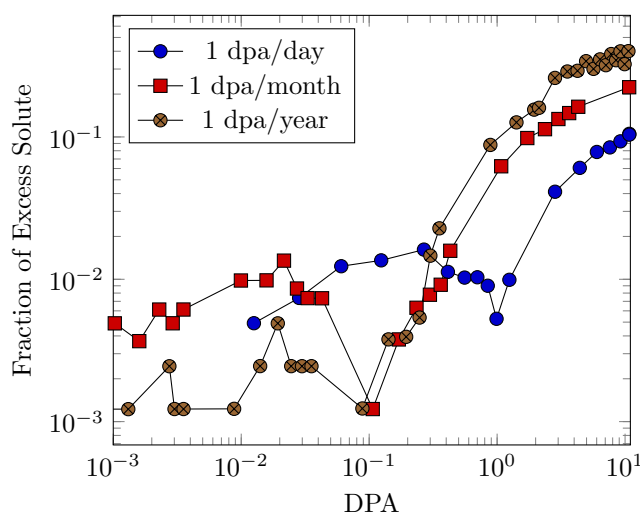


Figure 4.3: Plot of the fraction of solute trapped at segregation sites. Segregation sites are nodes where the concentration of the solute is greater than 0.25%, which is the maximum initial concentration.

Figure 4.3 shows the evolution of the amount of solute that has been trapped at segregation sites versus dose for three different dose rates. Here we clearly observe the impact that dose rate has on the development of RIS. At low doses, the amount of solute contained in nodes with concentrations higher than the highest initial concentration remains low, indicating that any increase in solute concentration at those doses is likely due to the random atomic displacements that occur as a result of the damage insertion steps. After a rate-dependent incubation period, a clear increase in the fraction of concentrated solute is observed. As a function of dose, Figure 4.3 shows that the progression of RIS increases as the dose rate decreases. When considering the development of RIS in time rather than by dose, RIS will begin to develop at an earlier time in systems irradiated at a higher dose rate. For the simulation at 1 dpa/year, there is some oscillation in the amount of segregated solute at high doses. This oscillation is likely driven by the motion of defect clusters, which serve as sinks for defects as well as the primary nucleation sites for segregation. As the clusters migrate, the rates of defect annihilation and recombination change significantly, which leads to segregation sites either increasing or decreasing in solute concentration depending on the type of cluster that has either entered or left each individual node.

Figure 4.4 shows several images of the solute concentration field at various doses for the three different dose rates. These images taken into consideration with Figure 4.3 allow us to examine the impact that dose rate has had on RIS behavior. For the high dose rate system (1 dpa/day), very little segregation has developed at the final dose of 10 dpa, with the solute concentration at the segregation sites having increased by only around 5 to 15 percent above the initial solute concentration. This is likely due to the rapid rate at which solute atoms are shuffled around due to interstitial formation, which at this dose rate is enough to work against diffusion to impede RIS. Decreasing the dose rate to 1 dpa/month, a significant increase in RIS behavior is observed, with many segregation sites spread across the simulated system. Going from 1 dpa/month to 1 dpa/year, both the number of segregation sites as well as the concentration within those segregation sites increase. Segregation in

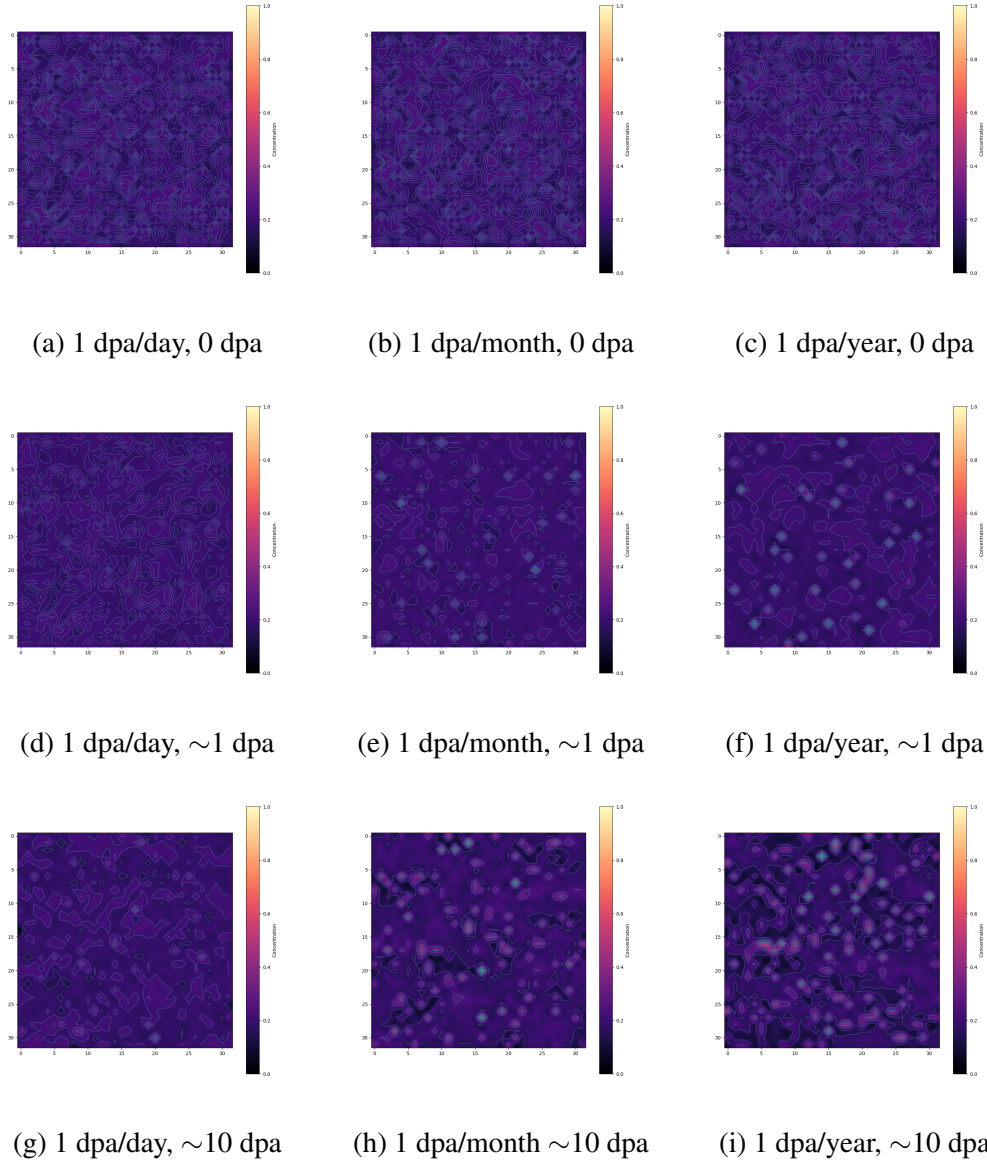


Figure 4.4: Plots of the concentration of the solute species at three different dose levels for simulations with different dose rates.

both the 1 dpa/month and 1 dpa/year systems seems to be confined to individual nodes, with an exponential decay in the concentration of the solute species in adjacent nodes. In all of these simulations, segregation sites also contain interstitial clusters which have served as the nucleation site for the development of RIS.

### *Effect of Dislocation on Radiation-Induced Segregation*

Through our examination of dose rate, we have determined that within the presented model RIS initiates within nodes containing defect sinks. Another common type of defect sink present within metallic systems is dislocations, which can be in the form of isolated line or loop dislocations or in the form of organized or random networks such as those present in grain boundaries and highly irradiated systems, respectively. In order to examine the effect of a dislocation on RIS behavior, simulations were performed using the proposed model with an edge dislocation inserted into a central node within the simulated volume. Simulations with dislocations were performed at the dose rates of 1 dpa/day, 1 dpa/month/ and 1 dpa/year, as described in subsubsection 4.1.3.

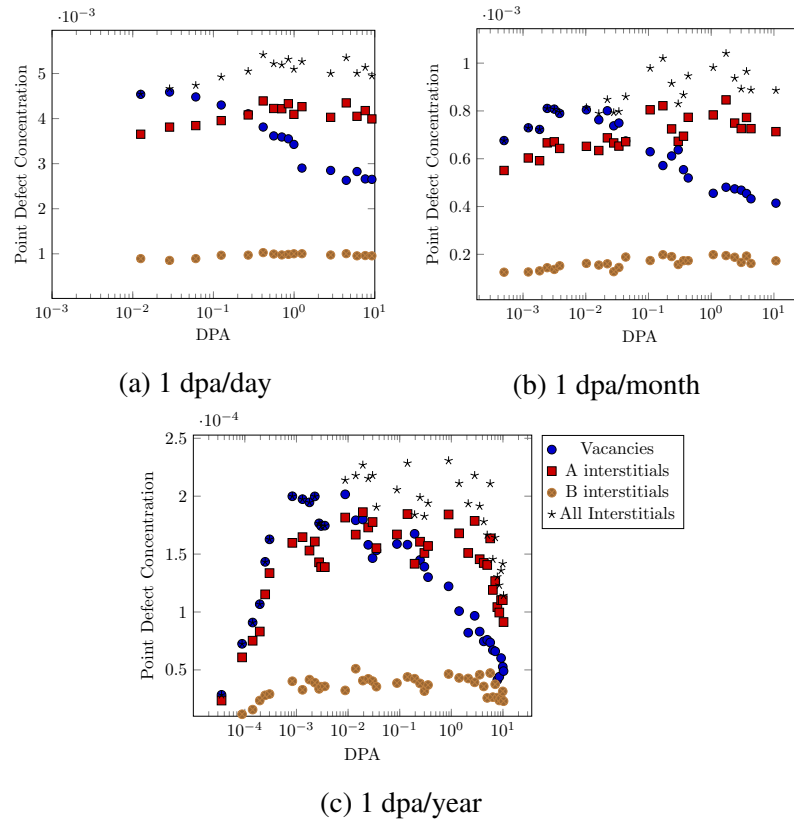


Figure 4.5: Plot of point defect concentrations as a function of dose for three different dose rates in systems containing a dislocation. The legend for (c) describes the marks for (a) and (b).

Figure 4.5 shows the evolution of the point defect concentrations for systems containing



one dislocation irradiated at three different dose rates. Comparing the defect concentrations found in Figure 4.5 with those in Figure 4.1, no immediate differences are noticeable due to the noise in the collected data. Looking at the behavior as a whole, it can be noted that the presence of the dislocation as an additional defect sink does not appear to drastically change the concentrations of point defects within the systems. There are two possible reasons why the introduction of a dislocation had a minimal impact on the progression of the simulations. The first is the way the dislocation serves as a sink for defects, as described in subsection 4.1.2, where the dislocation only serves as a sight for enhanced recombination. This was done to maintain the balance of defects and lattice positions within the system, which was a necessary condition for the proposed phase field equations. In real systems, annihilation of defects at defect sinks such as dislocations would not necessarily conserve defect counts and which may lead to different behavior in the evolution of the concentrations of defects. The second is the low density of dislocations within the performed simulations. With the simulation size used here, the equivalent dislocation density is only  $2.67 \times 10^{-13} \text{m}^{-2}$ . An examination of how increasing the dislocation density effects the progression of RIS will be presented in a later section.

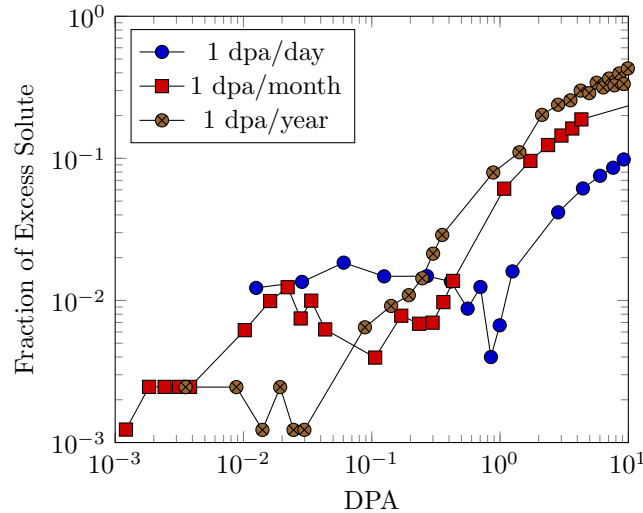


Figure 4.6: Plot of the fraction of solute trapped at segregation sites for simulations containing dislocations. Segregation sites are nodes where the concentration of the solute is greater than 0.25%, which is the maximum initial concentration.

Figure 4.6 compares the amount of segregated solute for systems containing a dislocation for three different dose rates. Similar to the discussion of Figure 4.5, comparisons between Figure 4.6 and Figure 4.3 do not show an immediately observable change in the progression of RIS due to the presence of the dislocation. Again, the progression of RIS with dose shows a strong dose rate effect, where lowering the dose rate results in an increase in the quantity of solute that has become segregated versus dose. When comparing individual points, it is consistently observed that the system containing the dislocation did have a slightly higher amount of the total solute present in segregation sites for both the 1 dpa/month and 1 dpa/day simulations. The same oscillation behavior that was observed in Figure 4.3 is observed in the 1 dpa/year data from Figure 4.6. In the simulation with the dislocation present, these oscillations have a higher amplitude, with the lows being slightly lower and the highs being slightly higher. Overall, it can be said that the presence of the dislocation was found to increase the rate at which RIS developed within the simulated systems, although that increase was relatively subtle.

Figure 4.7 shows snapshots of the solute field for simulations containing a dislocation in one of the central nodes irradiated at 1 dpa/day, 1 dpa/month, and 1 dpa/year at three different dose levels. Comparing Figure 4.7 to Figure 4.4, the key difference that can be observed is the dislocation near the center of the simulation, which for all three dose rates served as the highest concentration segregation site. The number of segregation sites in the simulations containing the dislocation are very similar compared to the results of the simulations without dislocations; however the average solute concentration at these segregation sites is slightly higher in the simulations containing dislocations, which explains the higher fraction of excess solute observed in Figure 4.6.

The presence of the dislocation within the phase field simulations was found to slightly enhance RIS progression for all three of the tested dose rates. This increase in the amount of segregated solute was on the order of 2 to 3 percent of the total initial quantity of solute. The dislocation also served as a segregation site due to the ability of the dislocation to trap

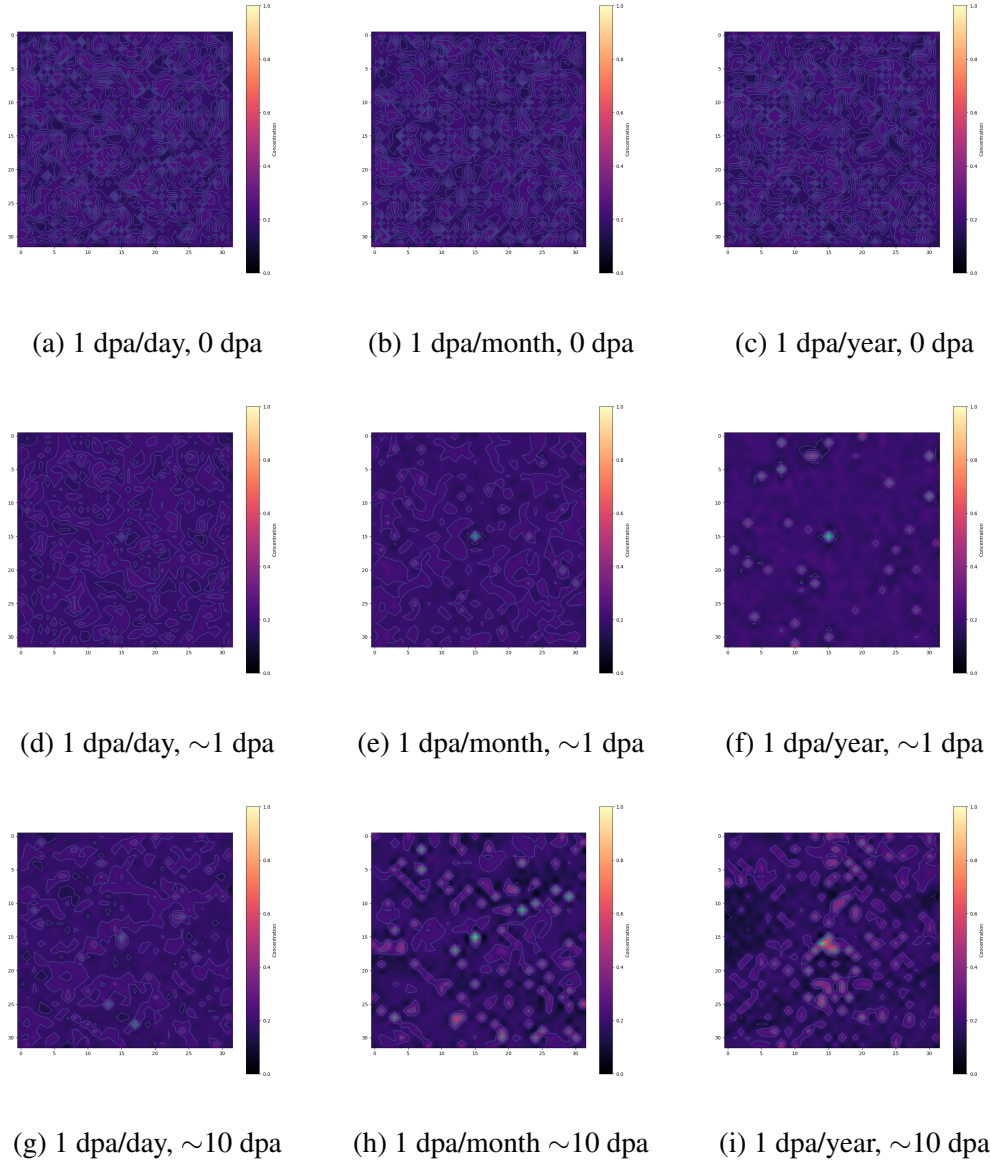


Figure 4.7: Plots of the concentration of the solute species at three different dose levels for simulations with dislocations and different dose rates.

defect clusters, which themselves serve as nucleation sites for segregation. This behavior could be modified through changes to how defects and defect clusters interact with the dislocation, as well as changes to the constants that control the diffusion of the various species.

The previous simulations were all performed with the same number of nodes representing the same physical dimensions for the simulated volume. For simulations performed

without any externally applied sinks, this will have little to no impact on the evolution of the system under irradiation, since all of the rate terms as well as the damage insertion are scaled via the dimensions of the simulation. However, once an externally defined sink is applied that is independent of the conserved fields, the density of those applied sinks can have an impact on the evolution of the systems. Therefore, we've performed simulations at a dose rate of 1 dpa/month in three systems with different dimensions (32x32, 25x25, 18x18) in order to examine the impact that the effective dislocation density has on the evolution of defect accumulation and RIS.

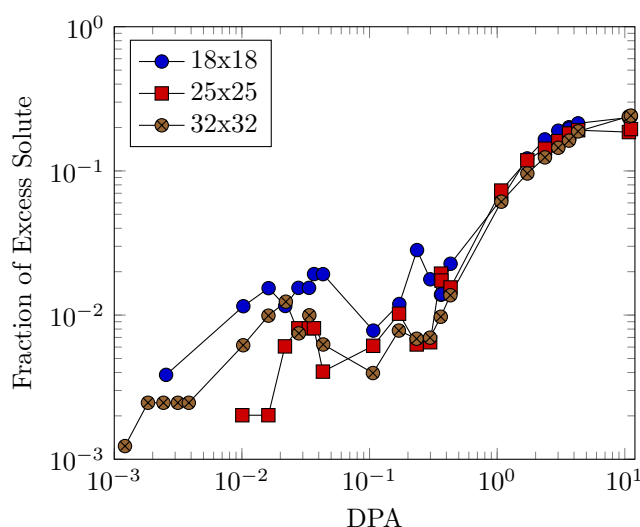


Figure 4.8: Plot of the fraction of solute trapped at segregation sites for simulations with varying grid sizes. Segregation sites are nodes where the concentration of the solute is greater than 0.25%, which is the maximum initial concentration.

Figure 4.8 shows the progression of RIS in three different simulations with different grid sizes, each irradiated at 1 dpa/month and having a dislocation near the center of the simulated volume. At low doses, the change in the simulated volume and thereby the density of dislocations does not have a noticeable impact on the development of RIS. This trend continues throughout the course of the simulation, with the final results at a dose of 10 dpa having the largest and smallest grid size being roughly the same, and the middle grid size being slightly lower. Ultimately, with the current implementation of dislocations as sinks, increasing the density of dislocations by changing the size of the simulated volume does not

appear to result in a significant change to the quantity of solute that becomes trapped at segregation sites. There also wasn't a trend in the concentration of solute in the same node as the dislocation with simulation grid size, as the simulation with a 25x25 grid had the highest solute concentration at 10 dpa, followed by the 32x32 grid and then the 18x18 grid. It is important to note that while the reduction in the grid size did result in an increase in the dislocation density, the simulated dislocation densities within these simulations were still quite low, with the dislocation densities being  $2.67 \times 10^{13} \text{m}^{-2}$ ,  $1.03 \times 10^{14} \text{m}^{-2}$ , and  $1.98 \times 10^{14} \text{m}^{-2}$  for the simulations with grid sizes of 32x32, 25x25, and 18x18, respectively. It is possible that with additional increases to the dislocation densities a stronger effect could be observed.

The lack of correlation between the density of dislocations and the progression of RIS in the proposed model is also likely linked to how RIS in the model is reliant on defect clusters as nucleation sites. Since the dislocations primarily enhances RIS by pinning defect clusters and enhancing defect recombination, the effect of the dislocation as a sink is confined to the node containing the dislocation. Also, due to the physical size attributed to the nodes is large, the impact of the stress field on the diffusion of point defects is also quite low compared to simulations with much smaller physical dimensions [170].

#### 4.1.4 Discussion

##### *Impact of incident particle type on RIS*

In this section we examine the impact that different radiation damage insertion methods have on the onset and development of RIS in a binary alloy. As discussed in subsection 4.1.2, different irradiation methods create radiation damage in different ways. Irradiation by high energy electrons tends to result in the formation of distributed FPs, since each collision between the ballistic electron and the atoms within the material lack the necessary energy to produce collision cascades. Conversely, irradiation by ballistic ions results in the formation of collision cascades, which are capable of producing both FPs as well as defect

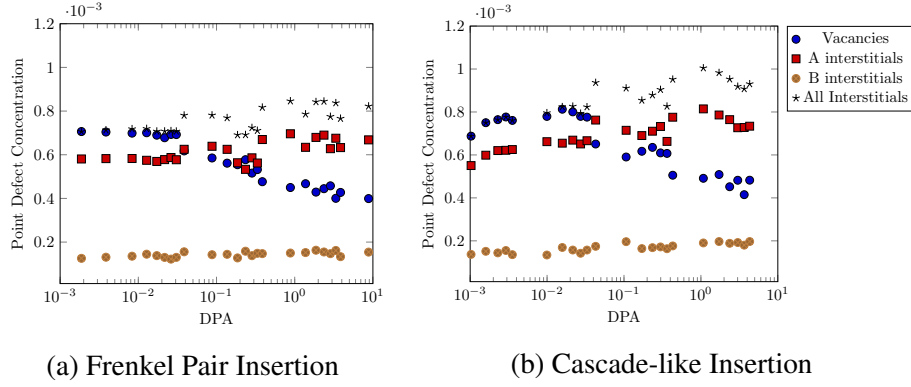


Figure 4.9: Plot of point defect concentrations as a function of dose for two different damage insertion methods at a dose rate of 1 dpa/month ( $3.858\ 02 \times 10^{-7}$  dpa/s)

clusters within individual damage events. Damage cascades also result in a greater amount of atomic mixing than FP insertion, which can lead to redistribution of the local alloy as well as recombination of any pre-existing defects that are trapped within the thermal spike of the cascade.

Figure 4.9 compares the evolution of the concentrations of point defects in systems irradiated with a dose rate of 1 dpa/month via FP insertion and cascade-like insertion. The change in damage insertion mechanism does not result in a drastic change in the evolution of the concentrations of the point defects, with the most noticeable change being a slightly higher concentration of both interstitials and vacancies in the system irradiated via cascade-like damage insertion. The difference between the concentrations of vacancies and the total concentration of interstitials is also slightly higher in the system irradiated via cascade-like insertion.

Figure 4.10 shows the evolution of the concentrations of defect clusters versus dose for two different dose rates in systems irradiated using Frenkel pair insertion. The relative behavior between the 1 dpa/day simulation and the 1 dpa/month simulation shown in Figure 4.10 is similar to the behavior observed in Figure 4.2 for those dose rates, with the concentration of defect clusters for the 1 dpa/month simulation being higher than that of the 1 dpa/day simulation until about 1 dpa, and then dropping below. Comparing the magnitude of the data shown in Figure 4.10 to that shown in Figure 4.2, it can be seen defect

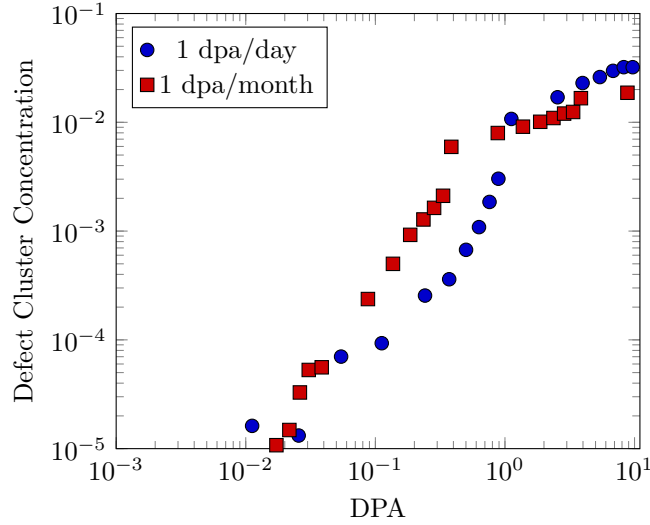


Figure 4.10: Plot of the total defect cluster concentration for simulations irradiated using Frenkel pair insertion.

cluster concentration in the simulations irradiated via FP insertion are lower than those observed in the simulations irradiated using cascade-like damage insertion. It can also be seen that the slope of the 1 dpa/month data near 10 dpa is closer to a flat line in the case of FP insertion, which indicates that systems irradiated via FP insertion may reach an equilibrium state with respect to their sink densities at an earlier stage than systems irradiated via cascade-like damage insertion.

Figure 4.11 shows the progression of solute segregation versus dose for simulations irradiated via FP insertion at 1 dpa/day and 1 dpa/month. Comparing the data found in Figure 4.11 with the data in Figure 4.3 for simulations with cascade-like damage insertion and the same dose rate, it can be seen that the development of RIS is very similar between the two damage insertion methods. There is a slight difference in the magnitudes of the fraction of excess solute at higher doses, with the data for FP insertion having a one percent higher fraction of excess solute at 10 dpa for the 1 dpa/day simulation, and a three percent lower fraction of excess solute at 10 dpa for the 1 dpa/month simulation. It is possible that FP insertion is more efficient at inducing RIS at very high dose rates due to the reduced amount of atomic mixing that occurs when only one atom is displaced at a time for each

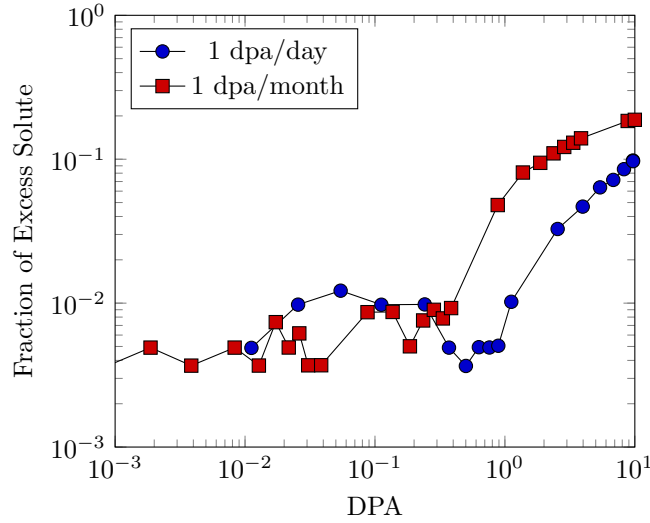


Figure 4.11: Plot of the fraction of solute trapped at segregation sites for simulations irradiated using Frenkel pair insertion. Segregation sites are nodes where the concentration of the solute is greater than 0.25%, which is the maximum initial concentration.

damage event. The decrease in the amount of excess solute observed at 1 dpa/month when using FP insertion is likely connected with the lower defect cluster concentration observed in Figure 4.10, where a lower concentration of defect clusters results in a reduction in the number and efficiency of possible nucleation sites for segregation.

#### 4.1.5 Conclusions

In the proposed phase field model, RIS was found to develop primarily at defect clusters that were produced under irradiation. This type of behavior was been observed experimentally for both voids [200] and interstitial clusters [184], indicating that the proposed model does a good job of recreating experimentally observed RIS behavior in bulk regions of the microstructure away from microstructural defects such as grain boundaries and free surfaces.

The results of the proposed phase field model showed that the rate and way in which RIS develops in a binary alloy depends strongly on the dose rate of the irradiation. Very high dose rates lead to the higher concentrations of radiation-induced defects, but impede the development of RIS due to the large amount of atomic mixing introduced via the damage



events. Lowering the dose rate from 1 dpa/day to 1 dpa/month and 1 dpa/year lowered the concentration of radiation-induced defects but enhanced the development of RIS as a function of dose.

Through the introduction of dislocations as defect sinks into the phase field models, it was observed that dislocations can serve as nucleation sites for RIS. This behavior in the proposed model is likely tied to the ability of the dislocation to trap migrating defect clusters, which were found in our simulations to be the primary source of solute segregation. Through modifications to the way that the dislocation behaved as a defect sink, this behavior could be tuned to introduce segregation or depletion of a solute species at the dislocation.

Comparing FP insertion with cascade-like damage insertion, it was observed that the different damage insertion techniques resulted in measurable differences in the concentrations of both point defects as well as defect sinks. The reduction in the amount of atomic mixing that occurs as a result of FP insertion increased the progression of RIS at the high dose rate of 1 dpa/day. At lower dose rates, such as the tested 1 dpa/month, FP insertion results in a lower concentration of defect clusters and a reduced amount of RIS.

All together, the proposed phase field model provides a good starting point for the analysis of the development of RIS in binary alloy systems while considering different material systems, irradiation conditions, and initial microstructural states. However, there are several opportunities for improvement within the proposed model that would improve the accuracy of the performed simulations as well as improve the flexibility of the model. The current implementation of defect cluster migration was controlled through a flat rate term, with no consideration of the impact of cluster size or type on the rate of migration. Migration direction was also not controlled, which is less accurate for the migration of interstitial clusters, which tend to move in either 1D lines or 2D planes. This could be improved through the introduction of a diffusive model for cluster migration, or a more refined rate approach based on the results of experiments or molecular dynamics simula-

tions. The requirement imposed on the model to maintain the number of lattice positions and atoms within the simulated volume is another aphysical limitation that could be improved through changes to the boundary conditions at the edges of the simulated volume, as well as changes to the way the dislocations were handled as defect sinks.

Future work using the proposed model will involve the revision of some of the presented results with additional simulations. This also includes some planned improvements to the model, including the addition of free surfaces as potential defect sinks, modification of the code to allow for multiple dislocations at once, and the coupling of the model with other phase field models, such as grain growth or corrosion models.

## CHAPTER 5

### CONCLUSIONS

The goal of this dissertation was to use computational techniques to explore the formation and accumulation behavior of radiation damage in various material systems with the intent to gaining an understanding of how some microstructures can display resistance to radiation damage. In order to address this complex and multi-scale question, a series of semi-independent studies that explored radiation damage formation and accumulation across a wide range of length and time-scales were performed.

In Chapter 2, molecular statics simulations were used to explore the properties of radiation induced defects within two different material systems. In the uranium-zirconium alloy, the vacancy formation energy was calculated as a function of the general alloy composition as well as a function of the local configuration of elements around the vacancy site [22]. Through this examination, we observed how defect formation properties can be affected by both global and local alloy composition, which can provide insight into how alloy homogeneity and composition will effect defect formation under irradiation. In elemental niobium, an investigation was performed to examine how the formation and binding energies of vacancy and interstitial clusters depended on the size and configuration the cluster[21]. We showed the importance of including defect configuration when characterizing the properties of defect clusters, especially as cluster size increases, and proposed a statistical method for predicting defect properties from a characterization of the cluster configuration.

In Chapter 3, molecular dynamics simulations were used to examine defect accumulation mechanisms in nanoporous niobium and gold as a function of the characteristic length scale of the nanoporous structure [24]. In this study, we confirmed the dependence of the radiation tolerance of nanoporous structures on the characteristic length scale of the struc-

ture, and found that the cut-off for the maximum diameter that displays radiation tolerance is material dependent. We observed that the radiation-tolerance of the structures does not imply a complete immunity to the formation of radiation-induced defects, but rather that the size of the defects is constrained within such systems, preventing the formation of defect clusters large enough to be visible with experimental imaging techniques. This study was followed with an examination of the impact of radiation damage on the mechanical behavior of gold and niobium nanowires. We observed radiation-induced softening across all of the tested nanowire diameters, with the change in the yield strength and yield strain appearing to be dose-independent. The cause of this radiation-induced softening in the niobium nanowires was deemed to be due to radiation-induced surface roughness, while in the gold nanowires the softening was deemed to be due to a combination of radiation-induced surface roughness as well as the unfauling of SFTs. Finally, we presented the implementation and validation of the recently developed EGTB interatomic potential through an examination of the stability of gold 4H phase nanoribbons. The accuracy of the EGTB potential with recreating the surface energies and phonon properties of materials makes it an ideal potential for simulating microstructures with high densities of defects such as grain boundaries and free surfaces under highly non-equilibrium conditions, such as irradiation.

Lastly, a phase field model for radiation induced segregation in binary alloys is proposed in Chapter 4. Included in the model are two different methods for inserting radiation-induced defects meant to mimic different irradiation conditions, as well as the inclusion of a dislocation as an external sink for defects. This model allows for the examination of the impact of irradiation conditions, material properties, and defect characteristics on a complex radiation-induced degradation process. The model predicts that radiation-induced segregation in a miscible alloy can be seeded by clusters of radiation-induced defects, and that this process is enhanced when the clusters are pinned at a dislocation. Simulations at a wide range of dose rates showed the progression of radiation-induced segregation increased as the dose rate was reduced.

# **Appendices**

## APPENDIX A

### APPENDIX FOR SECTION 2.1

#### A.1 MEAM Potential Description

Molecular dynamics simulations determine the interactions of atoms by utilizing inter-atomic potential functions that can be used to calculate the force on any atom in the system that is caused by the N-1 atoms in the system. The total energy of the system is described in both EAM and MEAM potential forms as the following equation

$$E = \sum_i [F_i(\bar{\rho}_i) + \frac{1}{2} \sum_{j \neq i} \phi_{ij}(R_{ij})] \quad (\text{A.1})$$

where the embedding function  $F_i$  is the energy required to embed an atom of type  $i$  into the background electron density at site  $i$ , shown as  $\bar{\rho}_i$ , and  $\phi_{ij}$  is a pairwise interaction between atoms  $i$  and  $j$  that are separated by a distance  $R_{ij}$  [201]. The pairwise interaction term  $\phi_{ij}$  [19] is defined by the following equation:

$$\phi(R) = \frac{2}{z} [E^u(R) - F(\frac{\bar{\rho}_i^0(R)}{z})] \quad (\text{A.2})$$

where  $z$  is the number of first nearest neighbors,  $\bar{\rho}_i^0$  is the background electron density, and  $E^u(R)$  is the per atom energy of the reference structure as a function of nearest-neighbor distance  $R$ , which can be obtained from first principle calculation or the universal equation of state of Rose *et al* [202]. Using the latter in Equation A.2:

$$E^u(R) = -E_c(1 + a^* + \delta x(\frac{r_e}{r}x(a^*)^3)e^{-a^*}) \quad (\text{A.3})$$

with

$$a^* = \alpha \left( \frac{R}{r_c} - 1 \right) \quad (\text{A.4})$$

and

$$\alpha^2 = \frac{9\omega B}{E_c} \quad (\text{A.5})$$

where  $E_c$ ,  $r_e$ ,  $\omega$ , and  $B$  are the cohesive energy, nearest neighbor distance, atomic volume, and bulk modulus, respectively, evaluated in the reference structure at equilibrium. In  $\gamma$ -U-Zr, the reference structure is face-centered cubic, resulting in the equation:

$$\bar{\rho}_i^0(R) = z\rho^{a(0)}(R) \quad (\text{A.6})$$

where  $\rho^{a(0)}$  is the atomic electron density. The embedding function  $F_i$  from Equation A.1 is defined as:

$$F(\bar{\rho}) = AE_c \frac{\bar{\rho}}{z} \ln \frac{\bar{\rho}}{z} \quad (\text{A.7})$$

In a traditional EAM potential, the background electron density is a simple linear supposition of spherically averaged atomic electron densities, shown as

$$\rho_i^{(0)} = \sum_{j \neq i} \rho_j^{a(0)}(R_{ij}) \quad (\text{A.8})$$

whereas in the MEAM potential, there are additional angularly dependent terms  $\rho_i$  such as shown in Equation A.9 through Equation A.11 [19].

$$\begin{aligned} (\rho_i^{(1)})^2 &= \sum_{\alpha} \left\{ \sum_{j \neq i} x_{ij}^{\alpha} \rho_i^{a(1)} R_{ij} \right\}^2 \\ &= \sum_{j, k \neq i} \rho_j^{a(1)}(R_{ij}) \rho_k^{a(1)}(R_{ik}) \cos(\theta_{ijk}) \end{aligned} \quad (\text{A.9})$$

$$\begin{aligned}
(\rho_i^{(2)})^2 = \sum_{\alpha, \beta} \left\{ \sum_{j \neq i} x_{ij}^\alpha x_{ij}^\beta \rho_j^{a(2)}(R_{ij}) \right\}^2 \\
- \frac{1}{3} \sum_{j \neq i} [\rho_j^{a(2)}(R_{ij})]^2
\end{aligned} \tag{A.10}$$

$$\begin{aligned}
(\rho_i^{(3)})^2 = \sum_{\alpha, \beta, \gamma} \left\{ \sum_{j \neq i} x_{ij}^\alpha x_{ij}^\beta x_{ij}^\gamma \rho_j^{a(3)}(R_{ij}) \right\}^2 \\
- \frac{3}{5} \sum_{j \neq i} [\rho_j^{a(3)}(R_{ij})]^2
\end{aligned} \tag{A.11}$$

In these equations,  $\rho^{a(l)}$  are the atomic densities which represent the decrease in the contribution with distance  $R_{ij}$  to the site of interest, and the  $\alpha, \beta, \gamma$  summations are each over the three coordinate directions with  $x_{ij}^\alpha$  being the ratio  $R_{ij}^\alpha / R_{ij}$ , with  $R_{ij}^\alpha$  being the  $\alpha$  component of the distance vector between atoms  $i$  and  $j$  [19]. Equation A.7 and Equation A.8 can be re-written in a form that has a dependence on the angle between atoms  $i, j$ , and  $k(\theta_{ijk})$ , which has been performed by I. Baskes, S. Nelson, and Wright [203]. It is assumed that atomic electron densities decrease exponentially:

$$\rho_i^{(a(l))}(R) = e^{-[\beta^{(l)}(\frac{R}{r_e} - 1)]} \tag{A.12}$$

where  $\beta^{(l)}$  are the decay lengths. To obtain the background electron densities from the partial electron densities, it is assumed that the angular terms are only a small correction to the EAM potential:

$$(\rho_i^{(0)})^2 = \sum_{l=0}^3 t_i^{(l)} (\rho_i^{(l)})^2 \tag{A.13}$$

Many-body screening is implemented through a screening function,  $S_{ik}$ , that quantifies screening between two atoms  $i$  and  $k$  due to other atoms in the system,  $j$ . The pair potentials and atomic electron densities are multiplied by this function. This screening function is



dependent on all other atoms in the system, such that:

$$S_{ik} = \prod_{j \neq i, k} S_{ijk} \quad (\text{A.14})$$

where  $S_{ijk}$  is determined using a simple geometric construction. The screening factor  $S_{ijk}$  is defined as:

$$S_{ijk} = f_c \left[ \frac{C - C_{min}}{C_{max} - C_{min}} \right] \quad (\text{A.15})$$

where  $C$  is a geometric parameter, and  $C_{min}$  and  $C_{max}$  are limiting values of  $C$ . The smooth cutoff function is defined as:

$$f_c = \begin{cases} 1 & x \geq 1 \\ [1 - (1 - x)^6]^2 & 0 < x < 1 \\ 0 & x \leq 0 \end{cases} \quad (\text{A.16})$$

A radial cutoff function is also applied to the pair potentials and atomic electron densities, and is given by  $f_c[(r_c - r)/\lambda]$  where  $r_c$  is the cutoff distance of 4.5 Å and  $\lambda$  gives the cutoff region.

## A.2 Tabulated Data

Table A.1: Uranium vacancy formation energy in SQS and random structures

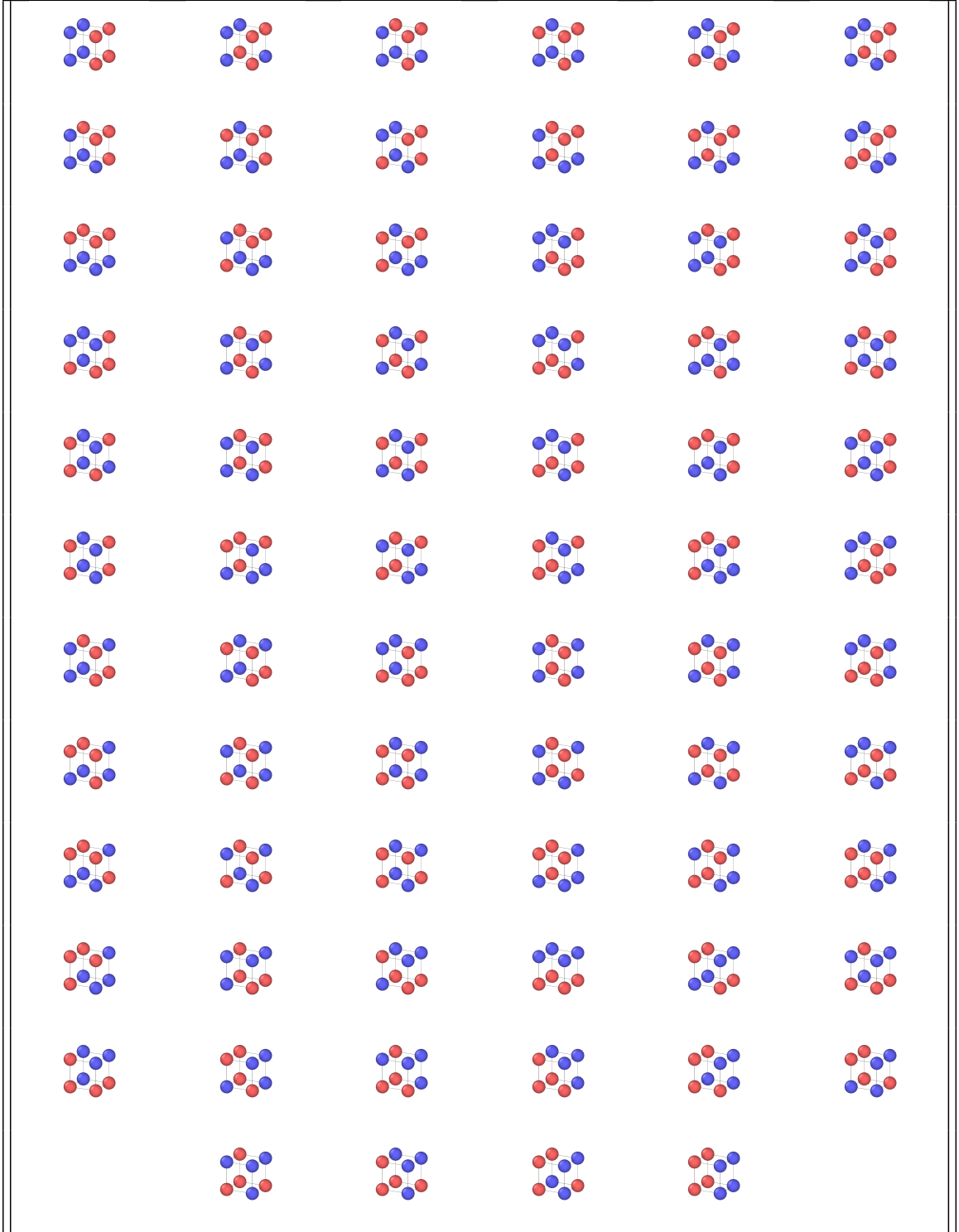
Atom % U	SQS (2000 atoms)	SQS (2000 atoms) Std. Dev.	SQS (250 atoms) (eV)	SQS (250 atoms) Std. Dev.	Random $E_v$	Random Std. Dev.
0	N/A	N/A	N/A	N/A	1.665	N/A
10	1.804	0.307	1.850	0.167	1.555	0.245
20	1.669	0.352	1.734	0.278	1.654	0.321
30	1.529	0.437	1.551	0.452	1.379	0.516
40	1.520	0.394	1.556	0.392	1.187	0.397
50	1.270	0.332	1.393	0.357	1.317	0.411
60	1.278	0.342	1.462	0.248	1.245	0.313
70	1.192	0.446	1.289	0.177	1.068	0.294
80	1.196	0.149	1.365	0.237	1.356	0.223
90	0.913	0.339	1.162	0.217	1.135	0.182
100	N/A	N/A	N/A	N/A	1.34	N/A

Table A.2: Zirconium vacancy formation energy in SQS and random structures

Atom % U	SQS (2000 atoms) (eV)	SQS (2000 atoms) Std. Dev.	SQS (250 atoms) (eV)	SQS (250 atoms) Std. Dev.	Random $E_v$ (eV)	Random Std. Dev.
0	N/A	N/A	N/A	N/A	2.074	N/A
10	2.255	0.331	2.048	0.253	2.205	0.336
20	2.132	0.466	2.363	0.350	2.204	0.386
30	2.376	0.476	2.328	0.272	2.312	0.493
40	2.609	0.437	2.440	0.334	2.344	0.320
50	2.466	0.353	2.491	0.431	2.474	0.307
60	2.388	0.342	2.586	0.209	2.328	0.412
70	2.262	0.282	2.547	0.148	2.366	0.194
80	2.387	0.255	2.620	0.128	2.680	0.176
90	2.028	0.241	2.384	0.122	2.148	0.269
100	N/A	N/A	N/A	N/A	1.76	N/A

## A.3 Images of Nearest Neighbor Configurations

Table A.1: All possible nearest neighbor configurations with 4 Zr and 4 U around a vacancy



## APPENDIX B

### APPENDIX FOR SECTION 2.2

#### B.1 Existing formation and binding energies of defects in bulk Nb in the literature

Table B.1: Formation,  $E^f$ , and binding,  $E^b$  energies of defects in bulk Nb investigated via DFT in the literature. NNS: nearest neighboring site; 2NNS: second nearest neighboring site.

Defect type	Energy Type	Energy (eV)
Vacancy	$E^f$	2.99 [61] 2.67 [60] 2.99 [62] 2.72 [91]
Divacancy (nns)	$E^f$	5.62 [61] 5.09 [60]
	$E^b$	0.36 [61] 0.24 [60]
Divacancy (2nns)	$E^f$	5.57 [61]
	$E^b$	0.41 [61] 0.40 [60]
Trivacancy	$E^f$	7.10 [60]
	$E^b$	0.66 [60]
Tetravacancy	$E^f$	8.83 [60]
	$E^b$	0.93 [60]
$\langle 100 \rangle$ SIA dumbbell	$E^f$	5.02 [60] 5.949 [62] 4.76 [91]
$\langle 110 \rangle$ SIA dumbbell	$E^f$	4.65 [60] 5.597 [62] 4.31 [91]
$\langle 111 \rangle$ SIA dumbbell	$E^f$	4.34 [60] 5.253 [62] 3.95 [91]
$\langle 111 \rangle$ SIA crowdion	$E^f$	4.35 [60] 5.254 [62] 3.99 [91]
Tetrahedral SIA	$E^f$	4.90 [60] 5.758 [62] 4.56 [91]
Octahedral SIA	$E^f$	5.08 [60] 6.060 [62] 4.89 [91]
He <sub>tet</sub> Interstitial	$E^f$	3.15 [60] 3.05 [70] 3.45 [106]
He <sub>oct</sub> Interstitial	$E^f$	3.43 [60] 3.26 [70] 3.71 [106]

Table B.1 (continued)

Defect type	Energy Type	Energy (eV)
2 He <sub>tet</sub> Interstitials	$E^f$	6.24 [60]
	$E^b$	0.34 [60]
3 He Interstitials	$E^f$	9.25 [60]
	$E^b$	0.47 [60]
4 He Interstitials	$E^f$	11.69 [60]
	$E^f$	4.27 [60]
He <sub>1</sub> V <sub>1</sub> cluster	$E^b$	1.54 [60]
	$E^f$	5.91 [60]
He <sub>2</sub> V <sub>1</sub> cluster	$E^b$	1.50 [60]
	$E^f$	7.77 [60]
He <sub>3</sub> V <sub>1</sub> cluster	$E^b$	(1 He) 1.29 [60] (2 He) 2.74 [60]
	$E^f$	9.68 [60]
He <sub>4</sub> V <sub>1</sub> cluster	$E^f$	6.19 [60]
	$E^b$	(He) 2.05 [60] (V) 0.75 [60]
He <sub>1</sub> V <sub>2</sub> cluster	$E^f$	7.43 [60]
	$E^b$	(He) 1.90 [60]
He <sub>2</sub> V <sub>2</sub> cluster	$E^f$	9.10 [60]
He <sub>3</sub> V <sub>2</sub> cluster	$E^f$	10.20 [60]
He <sub>4</sub> V <sub>2</sub> cluster	$E^f$	7.86 [60]
	$E^b$	(He) 2.38 [60] (V) 0.99 [60]
He <sub>1</sub> V <sub>3</sub> cluster	$E^f$	8.96 [60]
He <sub>2</sub> V <sub>3</sub> cluster	$E^f$	9.99 [60]
He <sub>3</sub> V <sub>3</sub> cluster	$E^f$	11.05 [60]
He <sub>4</sub> V <sub>3</sub> cluster	$E^f$	9.29 [60]
	$E^b$	(He) 2.30 [60] (HeV) 1.70 [60] (HeV <sub>2</sub> ) 1.99 [60]

Table B.1 (continued)

Defect type	Energy Type	Energy (eV)
He <sub>2</sub> V <sub>4</sub> cluster	$E^f$	10.07 [60]
He <sub>3</sub> V <sub>4</sub> cluster	$E^f$	11.04 [60]
He <sub>4</sub> V <sub>4</sub> cluster	$E^f$	11.95 [60]

Table B.2: Formation,  $E^f$ , and binding,  $E^b$  energies of defects in Nb via MD in the literature. NNS: nearest neighboring site; 2NNS: second nearest neighboring site.

Defect type	Energy Type	Energy (eV)
Vacancy	$E^f$	2.75 [89] 3.27 [77] 2.76 [72] 3.10 [91] 2.48 [71] 2.75 [63]
Divacancy (nns)	$E^f$	5.15 [89] 6.07 [77] 5.16 [72] 5.107 [63]
	$E^b$	0.36 [89] 0.46 [77] 0.393 [63]
Divacancy (2nns)	$E^f$	6.12 [77] 5.20 [72] 5.107 [63]
	$E^b$	0.48 [77] 0.393 [63]
Trivacancy	$E^f$	7.19 [89]
	$E^b$	0.71 [89]
Tetravacancy	$E^f$	9.53 [89]
	$E^b$	0.42 [89]
$\langle 100 \rangle$ SIA dumbbell	$E^f$	4.80 [92] 4.821 [93] 4.50 [91] 4.44 [72] 4.85 [71]
$\langle 110 \rangle$ SIA dumbbell	$E^f$	4.85 [92] 4.482 [93] 3.83 [91] 4.39 [72] 4.54 [71]
$\langle 111 \rangle$ SIA dumbbell	$E^f$	4.60 [92] 4.795 [93] 4.09 [91] 4.74 [72] 4.88 [71]
$\langle 111 \rangle$ SIA crowdion	$E^f$	4.857 [93] 4.02 [91] 4.93 [72] 4.95 [71]
Octahedral SIA	$E^f$	4.36 [91] 4.43 [72] 4.91 [71]
Tetrahedral SIA	$E^f$	3.26 [89] 4.37 [91] 4.73 [72] 4.95 [71]
He <sub>tet</sub> Interstitial	$E^f$	3.55 [89]
He <sub>1</sub> V <sub>1</sub> cluster	$E^f$	3.74 [89]
	$E^b$	2.57 [89]
He <sub>1</sub> V <sub>2</sub> cluster	$E^f$	5.90 [89]
	$E^b$	(He) 2.80 [89] (V) 0.59 [89]
He <sub>1</sub> V <sub>3</sub> cluster	$E^f$	7.70 [89]
	$E^b$	(He) 3.04 [89] (V) 0.95 [89]
He <sub>2</sub> V <sub>3</sub> cluster	$E^f$	8.96 [60]
He <sub>3</sub> V <sub>3</sub> cluster	$E^f$	9.99 [60]

Table B.2 (continued)

Defect type	Energy Type	Energy (eV)
He <sub>4</sub> V <sub>3</sub> cluster	$E^f$	11.05 [60]



## B.2 Atomistic simulation setup

Table B.1: Supercell size ( $L$ ) and number of atoms ( $N$ ) used for point defect formation energy simulations. Supercell sizes are given in units of lattice constants.

Type of Defect	$L$	$N$
Single Vacancy	$16 \times 16 \times 16$	8,192
Single Interstitial	$20 \times 20 \times 20$	16,000
He Interstitial	$10 \times 10 \times 10$	2,000

Table B.2: Supercell size ( $L$ ) and number of atoms ( $N$ ) used for vacancy cluster formation energy simulations as a function of the cluster size ( $V_n$ ). Supercell sizes are given in units of lattice constants.

$V_n$	$L$	$N$
2-4	$16 \times 16 \times 16$	8,192
5-10	$24 \times 24 \times 24$	27,648
11-15	$36 \times 36 \times 36$	93,312
16-30	$50 \times 50 \times 50$	250,000
31-40	$60 \times 60 \times 60$	432,000
41-50	$70 \times 70 \times 70$	686,000

Table B.3: Supercell size ( $L$ ) and number of atoms ( $N$ ) used for interstitial cluster formation energy simulations as a function of the cluster size ( $I_n$ ). Supercell sizes are given in units of lattice constants.

$I_n$	$L$	$N$
2-4	$20 \times 20 \times 20$	16,000
5-9	$30 \times 30 \times 30$	54,000
10-19	$50 \times 50 \times 50$	250,000
20-29	$60 \times 60 \times 60$	432,000
30-39	$70 \times 70 \times 70$	686,000
40-50	$80 \times 80 \times 80$	1,024,000

### B.3 Formation energies of vacancy and interstitial clusters in bulk Nb from this study

Table B.1: Formation energies of single vacancies and vacancy clusters containing up to four vacancies. NNS: nearest neighboring site; 2NNS: second nearest neighboring site.

Type of Defect	Johnson	Ackland	Fellinger	Literature
Single Vacancy	2.753	2.508	3.054	2.99[61, 62] 2.67[60] 2.72[91] 2.7[63] 2.75[89] 3.27[77] 2.76[72] 3.10[91] 2.48[71]
Divacancy (nns)	5.149	4.738	5.755	5.62[61] 5.15[89] 6.07[77] 5.16[72] 5.107[63]
Divacancy (2nns)	5.186	4.778	5.843	5.09[60] 5.57[61] 6.12[77] 5.20[72] 5.107[63]
Trivacancy (a)	7.192	6.673	8.117	7.10[60] 7.19[89]
Trivacancy (b)	7.577	7.006	8.543	
Trivacancy (c)	7.561	7.000	8.499	
Trivacancy (d)	7.542	6.964	8.455	
Trivacancy (e)	7.615	7.052	8.618	
Trivacancy (f)	7.654	7.112	8.725	
Tetravacancy (g)	8.815	8.215	9.985	8.83[60] 9.53[89]
Tetravacancy (h)	9.237	8.613	10.477	
Tetravacancy (i)	9.247	8.639	10.516	
Tetravacancy (j)	9.580	8.900	10.816	

Table B.2: Formation energy,  $E^f(V_n)$ , (in eV) for vacancy clusters as a function of the size ( $V_n$ ) for three interatomic potential tested.

$V_n$	Johnson	Ackland	Fellinger
5	10.434	9.752	11.845
10	17.362	16.360	19.827
15	23.498	21.532	26.905
20	27.943	26.961	32.524
30	36.904	36.150	43.713
40	44.608	46.679	52.289
50	52.497	56.507	62.065

Table B.3: Formation energies of self-interstitial point defects.

<b>Configuration</b>	<b>Johnson</b>	<b>Ackland</b>	<b>Fellinger</b>	<b>Literature</b>
$\langle 100 \rangle$ dumbbell	3.111	4.758		5.02[60] 5.949[62] 4.76[91] 4.80[92] 4.821[93] 4.50[91] 4.44[72] 4.85[71]
$\langle 110 \rangle$ dumbbell	3.126	4.397	3.978	4.65[60] 5.597[62] 4.31[91] 4.85[92] 4.482[93] 3.83[91] 4.39[72] 4.54[71]
$\langle 111 \rangle$ dumbbell	3.248	4.730	4.208	4.34[60] 5.253[62] 3.95[91] 4.60[92] 4.795[93] 4.09[91] 4.74[72] 4.88[71]
Octahedral	3.144	4.813	4.513	5.08[60] 6.060[62] 4.90[91] 4.36[91] 4.43[72] 4.91[71]
Tetrahedral	3.210	4.397	3.976	4.90[60] 5.758[62] 4.56[91] 3.26[89] 4.37[91] 4.73[72] 4.95[71]

Table B.4: Formation energy,  $E^f(I_n)$ , (in eV) of interstitial clusters as a function of the cluster size ( $I_n$ ) for three interatomic potential tested.

$I_n$	<b>Johnson</b>	<b>Ackland</b>	<b>Fellinger</b>
2	5.682	7.962	7.284
	5.910	8.270	7.331
	6.337	8.783	7.441
3	7.751	11.014	10.003
	8.589	11.286	10.435
	9.127	12.164	11.332
4	9.397	13.528	12.257
	10.177	13.977	13.144
	11.285	15.160	14.267
5	11.285	16.168	14.558
	12.266	16.629	15.754
	13.692	17.793	17.564
10	18.672	25.328	23.101
	21.930	28.309	27.815
	23.648	30.503	29.817

Table B.4 (continued)

$I_n$	<b>Johnson</b>	<b>Ackland</b>	<b>Fellinger</b>
15	27.854	33.539	31.164
	31.128	38.282	38.753
	33.579	42.386	42.221
20	30.751	40.127	37.754
	39.425	46.508	48.847
	42.389	52.574	54.753
25	42.892	46.137	43.967
	48.017	55.351	59.672
	50.833	63.772	64.887
30	48.841	52.181	51.271
	56.009	63.962	68.508
	61.066	73.420	74.341
40	64.069	63.869	75.204
	72.330	80.977	90.102
	76.055	93.337	95.223
50	80.540	73.025	92.847
	87.717	95.641	109.800
	91.017	113.478	114.764

\* For each column and number of defects, the values shown are the minimum, average, and maximum formation energies found for clusters containing that number of defects.

#### B.4 Binding energies of vacancy and interstitial clusters in bulk Nb from this study

Table B.5: Binding energies for small vacancy clusters of up to size four. NNS: nearest neighbor site; 2NNS: second nearest neighbor site. For vacancy clusters of size three or four, results correspond to configuration (a) illustrated in Figure 2.7 (a) and Figure 2.7 (g).

Reaction	Johnson	Ackland	Fellinger	Literature
$V + V \rightarrow V_2(\text{nns})$	0.357	0.278	0.353	0.24[60] 0.36[61, 89] 0.39[77] 0.36[72] 0.393[63]
$V + V \rightarrow V_2(2\text{nns})$	0.32	0.238	0.265	0.40[60] 0.39[77] 0.41[61] 0.32[72] 0.393[63]
$V + V_2(\text{nns}) \rightarrow V_3(\text{a})$	0.710	0.573	0.692	0.66[60] 0.71[89]
$V + V_2(2\text{nns}) \rightarrow V_3(\text{a})$	0.747	0.613	0.78	
$V + V + V \rightarrow V_3(\text{a})$	1.067	0.851	1.045	0.90[60]
$V + V_3(\text{a}) \rightarrow V_4(\text{g})$	1.130	0.966	1.186	0.93[60] 0.42[89]
$V + V + V + V \rightarrow V_4(\text{g})$	2.197	1.817	2.231	1.83[60]
$V_2(\text{nns}) + V_2(\text{nns}) \rightarrow V_4(\text{g})$	1.483	1.261	1.525	
$V_2(2\text{nns}) + V_2(2\text{nns}) \rightarrow V_4(\text{g})$	1.557	1.341	1.701	1.35[60]

Table B.6: Minimum binding energy,  $E^b(V_n)$ , (in eV) for vacancy clusters as a function of the cluster size ( $V_n$ ) for three interatomic potentials.

$V_n$	Johnson	Ackland	Fellinger
5	0.935	0.970	1.193
10	1.503	1.310	1.591
15	1.502	1.312	1.451
20	1.936	1.243	1.546
30	1.935	1.310	1.650
40	2.036	1.310	1.613
50	1.925	1.310	1.461

Table B.7: Minimum, average, and maximum binding energies,  $E^b(I_n)$ , (in eV) for interstitial clusters as a function of the cluster size ( $I_n$ ).

$I_n$	Johnson	Ackland	Fellinger
2	0.837	0.831	0.668
3	1.197	1.546	1.204
	1.398	1.598	1.278
	1.535	1.613	1.433
4	1.645	1.882	1.731
	2.604	2.072	1.893
	5.527	2.214	2.096
5	1.229	1.798	1.689
	3.655	2.399	2.281
	5.843	2.972	2.815
10	1.174	3.257	2.954
	3.122	3.733	3.548
	5.513	4.381	4.981
15	0.587	3.340	2.984
	2.239	4.240	4.065
	4.177	5.766	5.847
20	1.510	3.404	3.021
	3.636	4.657	4.385
	5.423	6.388	6.279
25	1.015	3.428	3.027
	3.099	4.863	4.646
	5.428	6.501	6.350
30	1.816	3.464	3.116
	3.130	5.036	4.683

Table B.7 (continued)

$I_n$	<b>Johnson</b>	<b>Ackland</b>	<b>Fellinger</b>
	5.097	6.541	6.401
40	1.307	2.569	1.853
	3.402	5.301	4.001
	5.437	6.573	6.412
50	1.261	2.629	1.866
	3.191	5.523	4.170
	5.356	6.619	6.600

## APPENDIX C

### APPENDIX FOR SECTION 3.1

#### Supplementary Note 1: Generation of nanowire structures

Gold (Au) and niobium (Nb) nanowires were produced by creating cylindrical columns of atoms of the desired length and diameter, and then performing an energy minimization using the conjugate gradient method with an energy stopping tolerance (unitless) and force stopping tolerance of  $1.0 \times 10^{-15} \text{ eV.}\text{\AA}^{-1}$ . The cylindrical axis of the nanowires was oriented along the  $\langle 001 \rangle$  direction, with the  $\langle 100 \rangle$  and the  $\langle 010 \rangle$  directions lying in the radial plane of the cylinder. After the initial minimization, the nanowires were equilibrated at zero pressure and 300 K under an NPT ensemble for at least 50 ps. All nanowires simulated in this work had an aspect ratio of 0.5 (*i.e.*, each nanowire had a length twice the diameter of the wire). Details of the nanowire microstructures produced are listed in Table C.1.

Table C.1: Diameters, lengths, and numbers of atoms in simulations of Au and Nb nanowires

Diameter (nm)	Length (nm)	Number of Atoms	
		Au	Nb
3	6	2,478	2,466
7	14	31,722	29,274
10	20	94,650	86,940
14	24	251,940	235,956
20	40	742,154	702,842
30	60	2,517,924	236,1086
40	80	5,929,588	5,578,826



## Supplementary Note 2: Generation of nanoporous structures

Au and Nb nanoporous structures were created from a porous structure template produced by a phase-field model simulating the spinodal decomposition of a binary alloy.[27, 141] This templates was then populated with single crystal atomic lattices using nanoSCULPT.[142] The nanoporous structures utilized in this study had an average ligament size of 12 nm for both Au and Nb. Descriptions of the size of these models are provided in Table C.2.

Table C.2: Structure parameters for nanoporous simulations

Average Ligament Size (nm)	Simulation Cell Dimension (nm <sup>3</sup> )		Number of Atoms	
	Au	Nb	Au	Nb
12.0	124.4 <sup>3</sup>	124.8 <sup>3</sup>	52,748,478	50,204,722

An additional method of quickly approximating the average ligament diameter of nanoporous structures is provided by the following expression: [204]

$$L = \frac{1.63 (1.25 - \phi) (1.89 + \phi (0.505 + \phi))}{\alpha}, \quad (\text{C.1})$$

where  $\alpha$  is the ratio of the surface area of the nanoporous structure to its solid volume, and  $\phi$  is the solid volume fraction of the nanoporous structure. The surface area, solid volume, and solid volume fraction of the nanoporous structures were calculated using the surface mesh modifier in OVITO [101]. All nanoporous structures were run under an NPT ensemble held at 300 K and zero pressure until their temperatures and pressures had stabilized around their respective targets.

### Supplementary Note 3: Generation of single crystal structures

Cubic single-crystal structures of Au and Nb with the same side dimensions as the nanocrystalline structures were also used. Exact cell dimensions and atom counts are provided in Table C.3. The single crystal systems were run under an NPT ensemble at 300 K and zero pressure until their temperatures and pressures had stabilized.

Table C.3: Structure parameters for bulk simulations

Structure Type	Simulation Cell Dimension (nm <sup>3</sup> )		Number of Atoms	
	Au	Nb	Au	Nb
Single crystal	59.0	59.0	11,943,936	10,701,875

#### **Supplementary Note 4: Single cascade simulations: Primary Knock-on Atoms (PKA)**

Single cascade simulations were performed by randomly selecting an atom from the atomistic system, and assigning this atom a velocity in a randomly selected direction. The velocity to a specified recoil kinetic energy  $T$  was calculated using  $T = \frac{1}{2}mv^2$ . The kinetic energies used in this work were sufficiently low such that relativistic effects in the conversion between kinetic energy and velocity could be ignored. The system was run with an adaptive time step such that no atom within the system would move more than 0.02 Å in a single time step. The simulation was progressed with an adaptive time step until 0.3 ps of simulation time had passed, after which the system was allowed to progress with the standard time step of 1 fs to a total simulation time of 50 ps. Single cascade simulations were performed with all atoms under an NVE ensemble, with an electronic drag force applied as defined by Lee et al. [140]. All atoms that were within a lattice constant of the surface of the nanowires were held under an over-damped Langevin thermostat at 300 K. During the cascade evolution, the system was held with periodic boundaries along the primary axis of the nanowire ( $\langle 001 \rangle$ ) and fixed boundary conditions in the other two coordinate directions. This was done to prevent sputtered atoms from wrapping around periodic boundaries and depositing on the nanowire surface. We performed one hundred individual cascade simulations for recoil energies of 300 eV, 1 keV, 3 keV, and 10 keV, for each diameter, in both Au and Nb respectively, resulting in a total of 4,000 cascade simulations per nanowire diameter and material.

### Supplementary Note 5: Consecutive cascades simulations

Consecutive cascades simulations consisted of repeated single PKA event, with the method of PKA selection and cascade evolution as described in Note 4. For the consecutive cascades, PKA energies were sampled from the primary recoil energy spectra calculated using the following equation [199],

$$P(E, T) = \frac{\int_{E_d}^T \sigma(E, T') dT'}{\int_{E_d}^{\hat{T}} \sigma(E, T') dT'}. \quad (\text{C.2})$$

Equation C.2 represents the fractional number of recoils between the minimum displacement energy  $E_d$  and energy  $T$ , where  $\hat{T}$  is the maximum possible recoil energy,  $E$  is the incident ion energy, and  $\sigma(E, T)$  is the scattering cross section for heavy, slow ions with incident energy  $E$  and PKA energy  $T$ . The scattering cross-section can be approximated using the following equation,

$$\sigma(E, T) = \frac{\pi^2 a^2 E_a \gamma^{1/2}}{8 E^{1/2} T^{3/2}}, \quad (\text{C.3})$$

where  $a = \frac{0.8853 a_0}{(Z_1 Z_2)^{1/6}}$  ( $Z_1$  and  $Z_2$  are the atomic numbers of the interacting atoms and  $a_0$  is the Bohr radius),  $\gamma = \frac{4 M_1 M_2}{(M_1 + M_2)^2}$  ( $M_1$  and  $M_2$  are the masses of the interacting atoms), and  $E_a = 13.6 (Z_1 Z_2)^{7/6} \frac{(M_1 + M_2)}{(M_2 \epsilon)}$  ( $\epsilon$  is the unit charge). These spectra are shown in Fig. 2 of the manuscript for 1 MeV Au ions into Au and Nb ions into Nb. The sampling of these spectra was truncated to ignore the highest five percent of recoil energies, which resulted in a maximum possible PKA energy of approximately 13 keV for Au and 20.5 keV for Nb.

Similar to single cascade simulations, consecutive cascade simulations were performed under an NVE ensemble with all atoms within a lattice constant of the nanowire surface being held under an overdamped Langevin thermostat at 300 K. An electronic drag force meant to replicate energy loss to electrons was also applied to all atoms in the system [140].

Due to required adaptive time stepping used to track the development the cascades,

these simulation are computationally expensive. Achieving the goal dose of 1 dpa using this method was too costly for nanowires with a diameter greater or equal to 10 nm. We performed consecutive cascades simulations for nanowires with a diameter of 3 and 7 nm up to 1 dpa. For these two systems, we only needed a total number of 100 PKAs initiated in each system. Examples of results for these simulations are presented in Note 9.

## Supplementary Note 6: Accelerated cascade simulations

Simulating a series of consecutive single PKA events as described in Note 5 is computationally too expensive to reach large damage levels as the ones observed in experiments and targeted in this study. Instead we used an accelerated damage insertion technique, in this case the Reduced Order Atomistic Cascade (ROAC) method [23], to simulate damage accumulation in nanowires with a diameter greater than 10 nm and for the nanofoam, nanocrystalline and single crystal structures.

The ROAC method introduces collision cascades as core-shell atomic structures approximating a displacement cascade by considering the athermal-recombination-corrected displacements-per-atom (arc-dpa) in the shell, and the replacements-per-atom (rpa) atomic mixing in the core. The arc-dpa is meant to capture the formation of long-range ballistic damage near the periphery of the thermal spike. The rpa is a short-range thermal spike mixing damage that occurs within the hot cascade core, and it is meant to capture both the recombination of existing defects within the lattice as well as the formation of larger defect clusters within a single cascade. The number of atoms involved in either the core or the shell of the approximated damage cascade initiated by a PKA with energy  $T$  are determined using the following equations [145],

$$N_{\text{dpa/rpa}} = \begin{cases} 0 & \text{for } T < E_d \\ 1 & \text{for } E_d < T < \frac{2E_d}{0.8} \\ \frac{0.8T}{2E_d} \xi_{\text{dpa/rpa}} & \text{for } \frac{2E_d}{0.8} < T < \infty \end{cases} \quad (\text{C.4})$$

and,

$$\xi_{\text{dpa}}(T) = \frac{1 - c_{\text{dpa}}}{(2E_d/0.8)^{b_{\text{dpa}}}} T^{b_{\text{dpa}}} + c_{\text{dpa}}, \quad (\text{C.5})$$

$$\xi_{\text{rpa}}(T) = \left[ \frac{b_{\text{rpa}}^{c_{\text{rpa}}}}{(2E_d/0.8)^{c_{\text{rpa}}}} + 1 \right] \frac{T^{c_{\text{rpa}}}}{b_{\text{rpa}}^{c_{\text{rpa}}} + T^{c_{\text{rpa}}}}, \quad (\text{C.6})$$

where  $E_d$  is the threshold displacement energy, and  $b_{\text{dpa}}$ ,  $c_{\text{dpa}}$ ,  $b_{\text{rpa}}$ , and  $c_{\text{rpa}}$  are material specific constants determined from explicit PKA simulations or from experiments. The coefficients used in this work are shown in Table C.4, with the coefficients for Nb being taken directly from Chen et al. [23] The threshold displacement energy for Nb was taken from Chen et al.,[23] while the threshold displacement energy for Au was taken from Bauer and Anderman.[146]

Table C.4: Material constants for the modified NRT defect production model in Equation C.4, Equation C.5, and Equation C.6

	$E_d$ (eV)	$b_{\text{dpa}}$	$c_{\text{dpa}}$	$b_{\text{rpa}}$ (eV)	$c_{\text{rpa}}$
<b>Au</b>	35.0	$-1.044 \pm 0.0957$	$0.220 \pm 0.0095$	$801.54 \pm 16.50$	$1.773 \pm 0.0134$
<b>Nb</b>	56.0	$-0.485 \pm 0.0270$	$0.172 \pm 0.0155$	$2627.5 \pm 311.1$	$1.11 \pm 0.0403$

To fit the material coefficients for Au in the model described by Equation C.4, Equation C.5, and Equation C.6, we performed 600 single PKA for displacement cascades across a broad range of recoil energies from 0.5 keV to 50 keV in fully periodic bulk systems. The dimensions of the simulation cell were chosen such that cascade self-interactions across periodic boundaries would not occur (simulation cell sizes and other simulation parameters are provided in Table C.5). Values for Nb are available in Chen et al.[23] The protocol to perform these explicit PKA simulations is described in Note 4. Additional details on the ROAC method are provided in Chen et al.[23]

Table C.5: List of MD PKA simulation parameters:  $E_{\text{PKA}}$  - initial energy of recoil,  $N_{\text{simulation}}$  - Number of simulations performed,  $L^{\text{Au}}$  - Simulation cell size in lattice units for gold,  $N_{\text{atoms}}^{\text{Au}}$  - Total number of atoms within the computation domain.

$E_{\text{PKA}}$ (keV)	$N_{\text{simulation}}$	$L^{\text{Au}}$	$N_{\text{atoms}}^{\text{Au}}$
0.5	100	$30^3$	108,000
1	100	$40^3$	256,000
2	100	$50^3$	500,000
5	100	$60^3$	864,000
10	100	$60^3$	864,000
20	50	$70^3$	1,372,000
50	50	$80^3$	2,048,000

## Supplementary Note 7: Hybrid cascade simulations

The ROAC method was developed for atomistic simulations of radiation damage events in bulk systems, and was used for damage accumulation simulations in the large nanowires (diameters greater than 10 nm and assuming the cascade event did not overlap with the free surface of the wire) and bulk structures. In the case of the 10-nm nanowires, due to the small size of the system and the associated high probability of a cascade interacting with the free surface, we adopted a hybrid simulation strategy. Employing such a hybrid methodology allowed for the acceleration of the simulation when a damage event would occur in the bulk of the system while fully capturing the interactions of damage events that occurred near free surfaces. We determined that the computational cost of using this hybrid methodology for atomic systems containing several hundred thousand atoms or more made reaching the desired damage level of 1 dpa not feasible. Therefore we only used this hybrid strategy for nanowires with diameters less than 10 nm. Damage accumulation simulations in larger nanowires or the nanoporous structures used only the ROAC method.

The hybrid ROAC-PKA method consists of the following steps:

1. The atomic system is first equilibrated at 300 K and zero pressure under an NPT ensemble for a minimum of 50 ps prior to performing any damage steps.
2. A recoil event with energy  $T$  was randomly sampled from the recoil spectrum of a given material.
3. The number of atoms that would be displaced to form defects ( $N_{\text{dpa}}(T)$ ) and the number of atoms involved in thermal mixing ( $N_{\text{rpa}}(T)$ ) are calculated using Equation C.4, Equation C.5, and Equation C.6 in order to determine the size of the cascade:  $N_{\text{core}} = N_{\text{dpa}} + N_{\text{rpa}}$ .
4. A random atom within the nanowire is selected as the center of the ROAC core, and the atoms that are at a distance less than the previously determined radius from the



central atom were grouped as part of the core.

- If that core region did not contain atoms belonging to a free surface, then the event would be progressed as an ROAC event.
- If the core region did contain atoms that were part of a free surface, then that event would be replaced with a full PKA simulation.

The established end conditions for the loop where ROAC events are initiated are either: (i) the number of currently queued ROAC events reaching an arbitrary maximum limit of consecutive ROAC events, or (ii) the presence of surface atoms within an event region.

- If an end condition was met and ROAC events had been successfully introduced into the system, the entire system with all of the displaced atoms and rescaled temperature regions from the queued ROAC events was progressed for 20 ps under an NVE ensemble with all atoms not identified as belonging to an event core being held under an over-damped Langevin thermostat held at 300 K.
- If the end condition that had been met was the presence of surface atoms within an event region, then the energy and location from that event would be used as inputs for a full PKA simulation (see Note 4) after any previously queued ROAC events had been run to completion. Once the full PKA simulation had run to completion, a new search for ROAC events began.

In between insertions of  $N$  number of cascades, the entire system was evolved under an NVT ensemble at 300 K for 50 ps. This procedure of generating ROAC events and full PKA events was repeated until reaching 1 dpa, as calculated by the total number of displaced atoms calculated using Equation C.4 and Equation C.5 divided by the total number of atoms in the system.

### Supplementary Note 8: Defect types in Au and Nb nanowires due to single cascades

Figure C.1 shows examples of defect structures left behind in the core region of Au and Nb nanowires, 50 ps after the initiation of a 3 keV PKA event. Defect structures were identified using common neighbor analysis in OVITO [101], with FCC and BCC atoms removed in the case of Au and Nb, respectively. In the Au nanowires, a 3 keV PKA is sufficient to create stacking faults and disordered regions in the 3nm diameter nanowire that span across the entire wire, while in the 10nm diameter nanowire the cascade creates isolated vacancies as well as a small SFT. In The Nb nanowire , the 3 keV PKA produces isolated vacancies in both the 3nm and 10nm diameter nanowires, with more defects being produced in the larger diameter nanowire.

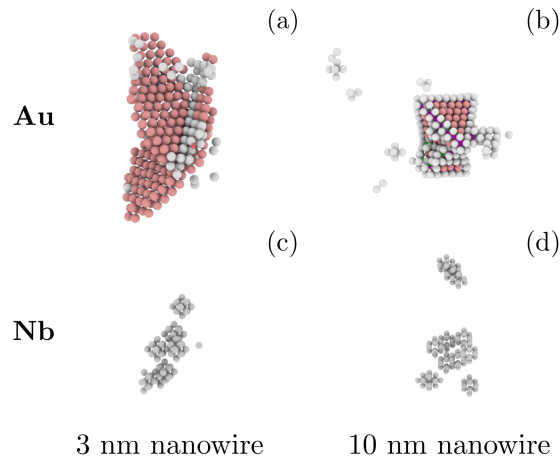


Figure C.1: Examples of defect structures left behind in the core region of Au and Nb nanowires, 50 ps after the initiation of a 3 keV PKA event. Red atoms are HCP, and white atoms are disordered atoms.

### Supplementary Note 9: Radiation damage in small nanowires ( $\leq 7$ nm)

Figure C.2 and Figure C.3 show the evolution of the defect structures in small (3-nm and 7-nm wires) Au and Nb nanowires after multiple consecutive cascades based on the methodology presented in Note 5. Both systems see amorphization of the entire wire upon being struck by consecutive cascades, especially for the smaller nanowires.

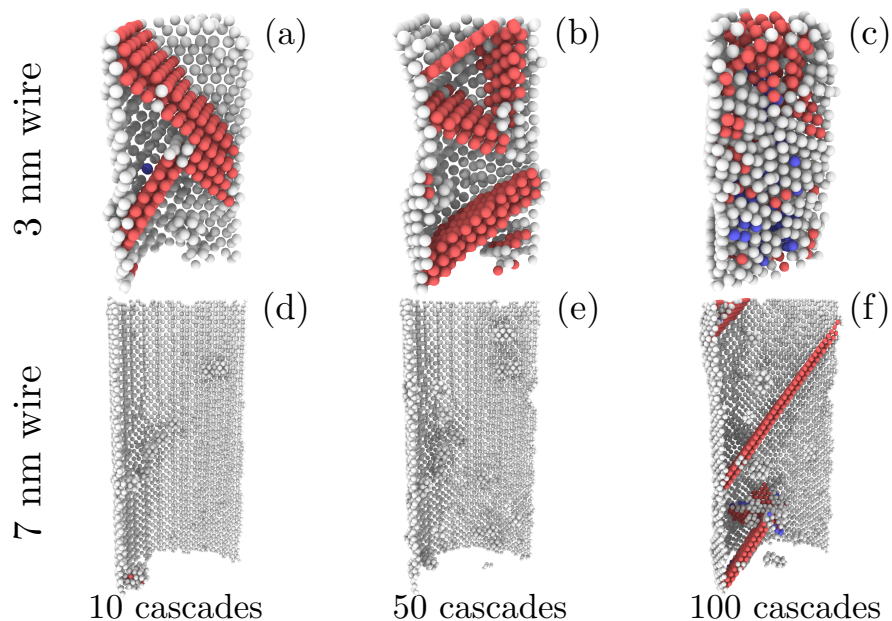


Figure C.2: Evolution of defect accumulation after multiple consecutive cascades in small FCC Au nanowires. (a) After 10 cascades, (b) after 50 cascades, and (c) after 100 cascades.

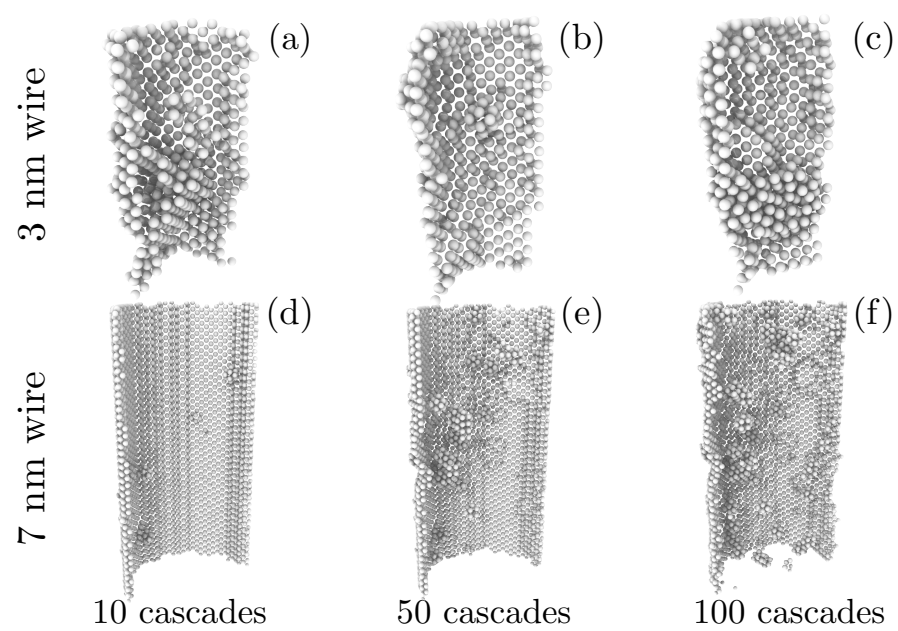


Figure C.3: Evolution of defect accumulation after multiple consecutive cascades in small BCC Nb nanowires. (a) After 10 cascades, (b) after 50 cascades, and (c) after 100 cascades.

## APPENDIX D

### APPENDIX FOR SECTION 3.2

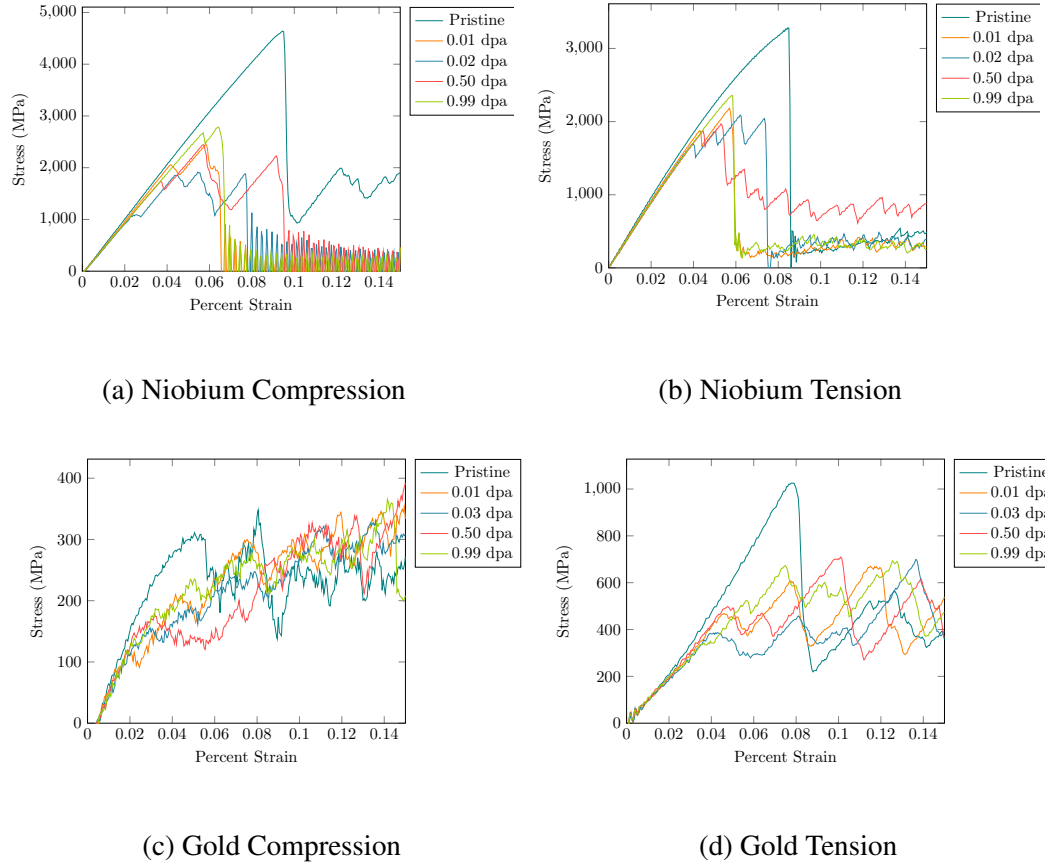
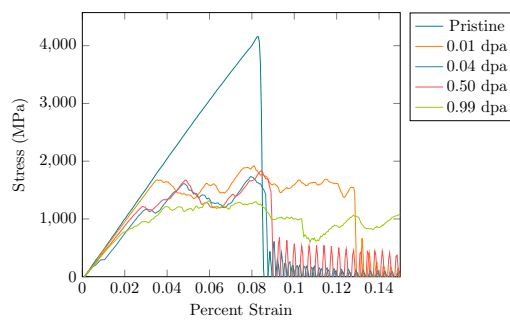
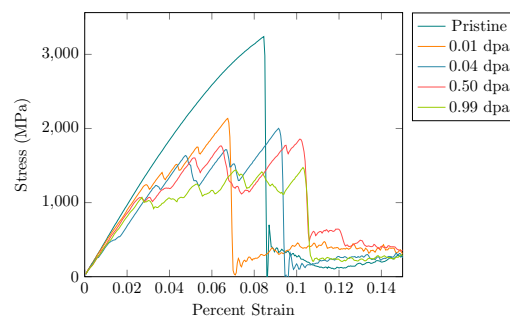


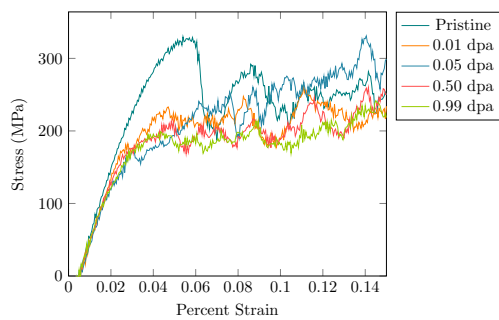
Figure D.1: Stress-strain curves for irradiated gold and niobium nanowires with diameters of 14 nm under tension and compression. Dose levels are provided in the legends.



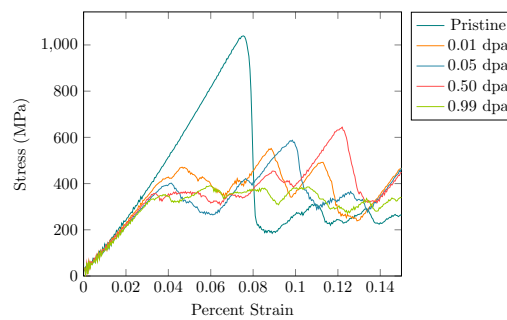
(a) Niobium Compression



(b) Niobium Tension

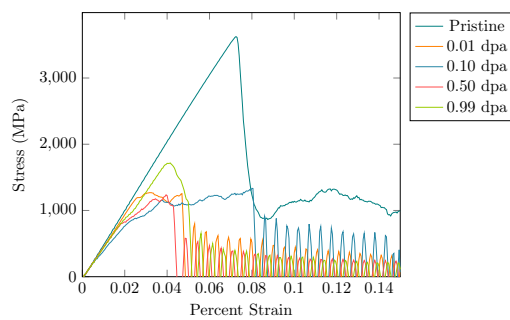


(c) Gold Compression

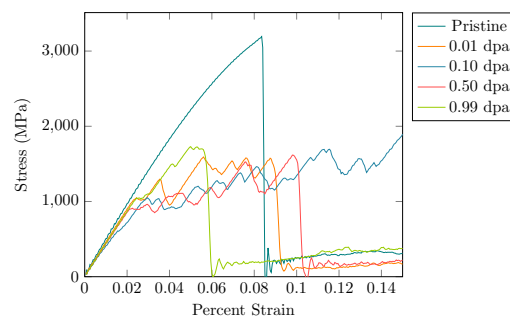


(d) Gold Tension

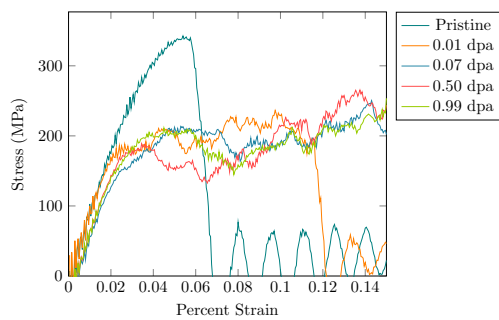
Figure D.2: Stress-strain curves for irradiated gold and niobium nanowires with diameters of 20 nm under tension and compression. Dose levels are provided in the legends.



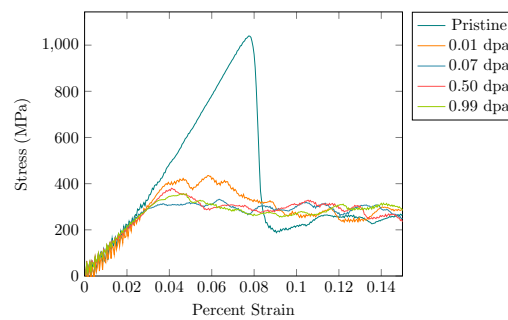
(a) Niobium Compression



(b) Niobium Tension



(c) Gold Compression



(d) Gold Tension

Figure D.3: Stress-strain curves for irradiated gold and niobium nanowires with diameters of 30 nm under tension and compression. Dose levels are provided in the legends.

# APPENDIX E

## APPENDIX FOR CHAPTER 4

### E.1 General Simulation Parameters

Table E.1: List of General Parameters

Parameter	Value	unit
$T$	673.15	K
$\nu_c$	$4.48 \times 10^{12}$	$s^{-1}$
$\nu_c^{iA}$	$4.48 \times 10^{12}$	$s^{-1}$
$\nu_c^{iB}$	$4.92 \times 10^{12}$	$s^{-1}$
$E_{VA}^m$	1.537	eV
$E_{VB}^m$	1.537	eV
$E_{iA}^m$	1.520	eV
$E_{iB}^m$	1.520	eV
$E_f^V$	1.9	eV
$E_f^{iA}$	4.07	eV
$E_f^{iB}$	4.07	eV
$E_{2V}^b$	0.5	eV
$a_A^{lat}$	3.5239	Å
$a_B^{lat}$	2.91	Å
$V_m$	$7.092329 \times 10^{-6}$	$m^3/mol$
$V_{at}$	$9.111 \times 10^{-5}$	unitless



## E.2 Elastic Parameters

Table E.2: List of Elastic Parameters

Parameter	Value for A	Value for B	unit
$\nu_V$	-0.19305	-0.19305	unitless
$\nu_I$	0.484783	0.484783	unitless
$C_{11}$	230.01	413.81	MPa
$C_{12}$	130.01	108.09	MPa
$C_{13}$	130.01	108.09	MPa
$C_{14}$	0	0	MPa
$C_{15}$	0	0	MPa
$C_{16}$	0	0	MPa
$C_{22}$	230.01	413.81	MPa
$C_{23}$	130.01	108.09	MPa
$C_{24}$	0	0	MPa
$C_{25}$	0	0	MPa
$C_{26}$	0	0	MPa
$C_{33}$	230.01	230.01	MPa
$C_{34}$	0	0	MPa
$C_{35}$	0	0	MPa
$C_{36}$	0	0	MPa
$C_{44}$	130	105.16	MPa
$C_{45}$	0	0	MPa
$C_{46}$	0	0	MPa
$C_{55}$	130	130	MPa
$C_{56}$	0	0	MPa
$C_{66}$	130	105.16	MPa

### E.3 Parameters for Cascade-Like Damage Insertion

Table E.3: Parameters for ARC-DPA Equations

Parameter	Value	unit
$b_{dpa}$	-0.485	unitless
$c_{dpa}$	0.172	unitless
$b_{rpa}$	2627.5	unitless
$c_{rpa}$	1.11	unitless
$E_d$	56	eV
$T_{max}^{PKA}$	1	keV

### E.4 Parameters for Simulations with Dislocations

Table E.4: Dislocation Parameters

Parameter	Value	unit
$b$	0.24855	nm

## E.5 Parameters for the Calculation of Onsager Coefficients

Table E.5: Coefficients for Determining Onsager Coefficients

Parameter	Value	unit
$w_0^v$	1.09	eV
$w_1^v$	0.98	eV
$w_2^v$	0.83	eV
$w_3^v$	1.04	eV
$w_4^v$	1.06	eV
$w_R$	0.75	eV
$w_I$	0.08	eV
$w_0^i$	0.14	eV
$w_1^i$	$\infty$	eV
$w_2^i$	0.31	eV
$w_3^i$	0.26	eV
$w_4^i$	0.15	eV
$w_1'$	0.16	eV
$w_2'$	0.00	eV
$w_3'$	0.21	eV
$w_4'$	0.10	eV
$B_1$	180.3	unitless
$B_2$	924.3	unitless
$B_3$	1338.1	unitless
$B_4$	30.1	unitless
$B_5$	253.3	unitless
$B_6$	596.0	unitless
$B_7$	453.3	unitless
$\mu$	70.0	GPa
$\nu$	0.3	unitless

## **APPENDIX F**

### **FRENCH SUMMARY**

L'objectif ultime de cette thèse est d'utiliser des techniques informatiques pour explorer les mécanismes atomistiques et les caractéristiques de la formation de dommages dus aux rayonnements, et comment ces propriétés et comportements contribuent à la tolérance aux rayonnements des matériaux nanostructurés. Le besoin de matériaux capables de résister aux environnements radiatifs pendant de longues périodes s'est accru à mesure que nous développons des technologies nucléaires plus avancées. Les expériences et les simulations informatiques ont montré que les matériaux nanostructurés avec des densités élevées de puits de défauts tels que les joints de grains ou les surfaces libres ont une tolérance aux rayonnements améliorée, étant capables de résister à des doses de rayonnement élevées sans accumuler de dommages dus aux rayonnements de la même manière que les matériaux structurés de manière conventionnelle. Afin de comprendre les mécanismes par lesquels ces matériaux présentent une tolérance aux rayonnements, ainsi que de pouvoir prédire comment ces matériaux évolueront dans le temps lorsqu'ils sont exposés à un environnement de rayonnement, une caractérisation approfondie des propriétés, du comportement de formation et du comportement d'accumulation du rayonnement des dommages sont nécessaires. À cette fin, nous avons utilisé des techniques de calcul pour étudier les dommages dus aux rayonnements sur toute la gamme d'échelles de longueur et de temps dans lesquelles ils se développent, en mettant l'accent sur l'impact de la microstructure et de la configuration des défauts sur la formation et l'évolution des dommages dus aux rayonnements.

Nous avons commencé par un examen des propriétés des défauts radio-induits. Dans l'alliage uranium-zirconium, nous avons examiné comment les arrangements des atomes dans le réseau ainsi que la composition de l'alliage ont eu un impact sur la valeur de l'énergie de formation de lacunes. Les lacunes sont l'un des deux défauts ponctuels fon-

damentaux produits sous irradiation, et elles jouent un rôle important dans l'évolution des matériaux sous irradiation en raison de l'importance des lacunes dans le processus de diffusion. Grâce à cette étude, nous avons observé comment les propriétés de base des matériaux peuvent être très sensibles aux petits changements dans les configurations atomiques locales et avons montré l'importance de considérer à la fois la composition de l'alliage et la configuration atomique locale lors de la caractérisation des propriétés des matériaux dans les alliages.

Nous avons ensuite examiné comment les propriétés des amas de défauts variaient avec la taille de l'amas ainsi que la configuration de l'amas dans le niobium pur. Des études antérieures sur les propriétés des clusters de défauts se sont principalement concentrées sur les propriétés de l'état fondamental de ces clusters et ont exploré une gamme limitée de tailles de clusters. Dans les systèmes dans des conditions de non-équilibre tels que les systèmes à température ou les systèmes sous irradiation, il existe une forte probabilité que certains défauts ne soient pas dans leur configuration à l'état fondamental. Par conséquent, l'objectif principal de cette étude était d'examiner comment les propriétés des amas de défauts, telles que les énergies de formation et de liaison, variaient à la fois avec la taille et la configuration de l'amas, et a découvert que les configurations à l'état non fondamental peuvent être thermiquement stables en fonction de sur la config.

Partant de l'étude des propriétés des défauts, nous avons ensuite réalisé une étude des mécanismes d'accumulation des dommages causés par les radiations dans le niobium et l'or nanoporeux. Les structures nanoporeuses ont des rapports surface-volume très élevés où les surfaces libres sont capables de servir de puits parfaits pour tout dommage dû au rayonnement produit dans le volume solide de la structure. Dans cette étude, nous avons examiné l'impact de l'échelle de longueur de la structure nanoporeuse sur les mécanismes d'accumulation des dommages causés par le rayonnement et observé un effet de taille important où les systèmes nanoporeux avec l'échelle de longueur correcte pour les conditions d'irradiation afficheraient un degré de tolérance aux rayonnements. Nous avons également

observé des mécanismes d'endommagement dépendant de la taille où les systèmes avec certaines caractéristiques de taille subiraient des changements uniques dans leur microstructure. Nous avons ensuite suivi cette étude par un examen de la façon dont le comportement mécanique de ces systèmes nanoporeux était affecté par le processus d'irradiation. Nous avons constaté que, bien que les systèmes nanoporeux puissent être résistants au comportement d'accumulation des dommages causés par les rayonnements dans les matériaux conventionnels, il y avait un effet sur la réponse mécanique des structures nanoporeuses en raison des dommages causés aux surfaces au sein de la nanostructure ainsi que de la formation de divers rayonnements défauts induits au sein des ligaments et des nœuds des structures. Par conséquent, bien que le rayonnement puisse ne pas affecter ces matériaux de la même manière qu'il affecte les matériaux structurés de manière conventionnelle, il a un impact sur la microstructure qui peut affecter négativement les propriétés des matériaux.

Nous nous sommes ensuite concentrés sur la technique informatique de la dynamique moléculaire et avons travaillé sur la mise en œuvre et la validation du potentiel interatomique EGTB nouvellement développé dans le code de dynamique moléculaire LAMMPS. Les potentiels interatomiques contrôlent la précision des simulations de dynamique moléculaire, et il est d'une importance vitale que des précautions appropriées soient prises lors de la sélection d'un potentiel interatomique pour s'assurer que les caractéristiques de la simulation prévue seront correctement reproduites par le potentiel choisi. Le potentiel EGTB est capable de prédire avec précision les énergies de surface, les caractéristiques fondamentales des défauts et le comportement des phonons des matériaux, ce qui en fait un potentiel interatomique idéal pour la simulation de microstructures complexes dans des conditions de non-équilibre, telles que les matériaux nanostructurés sous irradiation.

Enfin, nous fournissons un exemple de la façon dont les caractéristiques déterminées atomistiquement des dommages dus aux rayonnements peuvent être utilisées en proposant un modèle de champ de phase pour la ségrégation induite par le rayonnement. Les techniques de champ de phase utilisent des équations aux dérivées partielles couplées pour

simuler l'évolution spatio-temporelle des espèces, où les interactions entre les espèces sont décrites via des termes de taux. Le modèle proposé permet d'étudier l'impact des propriétés des matériaux ainsi que des conditions de rayonnement sur le développement de la ségrégation induite par les rayonnements, un processus de dégradation dans lequel les éléments mélangés de manière homogène dans un alliage commencent à se séparer, ce qui peut avoir un impact considérable sur les propriétés mécaniques de l'alliage. Matériel. Ce modèle a été utilisé pour étudier l'impact des conditions de rayonnement telles que le débit de dose et le type de particules incidentes sur le développement de la ségrégation induite par le rayonnement.

## REFERENCES

- [1] F. Seitz. “On the disordering of solids by action of fast massive particles”. In: *Discussions of the Faraday Society* 5.271-282 (1949). DOI: 10.1039/DF9490500271.
- [2] C. A. Bruch, W. E. McHugh, and R. W. Hockenbury. “Variations in Radiation Damage to Metals”. In: *JOM* 8.10 (1956), pp. 1362–1372. DOI: 10.1007/BF03377887.
- [3] S.J. Zinkle and G.S. Was. “Materials challenges in nuclear energy”. In: *Acta Materialia* 61.3 (2013), pp. 735–758. DOI: 10.1016/j.actamat.2012.11.004.
- [4] X. Zhang et al. “Radiation damage in nanostructured materials”. In: *Progress in Materials Science* 96 (2018), pp. 217–321. DOI: 10.1016/j.pmatsci.2018.03.002.
- [5] S.J. Zinkle and K. Farrel. “Void swelling and defect cluster formation in reactor-irradiated copper”. In: *Journal of Nuclear Materials* 168.3 (1989), pp. 262–267. DOI: 10.1016/0022-3115(89)90591-6.
- [6] S.J. Zinkle. “Radiation-induced effects on microstructure”. In: *Comprehensive Nuclear Materials*. Ed. by Konings RJM. Vol. 1. Elsevier, 2012. Chap. 1.03, pp. 65–98.
- [7] R. J. Reda, S. L. A. Hana, and J. L. Kelly. “Intergranular attack observed in radiation-enhanced corrosion of mild steel”. In: *Corrosion Science* 44.9 (1987), pp. 632–637. DOI: 10.5006/1.3584976.
- [8] C. Cawthorne and E. J. Fulton. “Voids in irradiated stainless steel”. In: *Nature* 216 (1967), pp. 575–576. DOI: 10.1038/216575a0.
- [9] M. Eldrup et al. “Dose dependence of defect accumulation in neutron irradiated copper and iron”. In: *Journal of Nuclear Materials* 307-311 (2002), pp. 912–917. DOI: 10.1016/S0022-3115(02)01160-1.
- [10] C. Deo, E. Chen, and R. Dingreville. “Atomistic modeling of radiation damage in crystalline materials”. In: *Modelling and Simulation in Materials Science and Engineering* (2021). DOI: 10.1088/1361-651X/ac2f83.
- [11] F. F. Abraham. “Computational statistical mechanics: methodology, applications, and supercomputing”. In: *Advances in Physics* 35 (1986), pp. 1–111. DOI: 10.1080/00018738600101851.
- [12] M. P. Allen and D. J. Tildesley. *Computer Simulation of Liquids*. Oxford: Clarendon Press, 1987.



- [13] K. Binder et al. “Molecular dynamics simulations”. In: *Journal of Physics: Condensed Matter* 16.S429 (2004). DOI: 10.1088/0953-8984/16/5/006.
- [14] F. Ercolessi. *Introductory Molecular Dynamics*. Tech. rep. IAEA, 1997.
- [15] S. Plimpton. “Fast parallel algorithms for short-range molecular dynamics”. In: *Journal of Computational Physics* 117 (1995), pp. 1–19. DOI: 10.1006/jcph.1995.1039.
- [16] B. Beeler et al. “Atomistic properties of  $\gamma$  uranium”. In: *Journal of Physics: Condensed Matter* 24.7 (2012), p. 075401. DOI: 10.1088/0953-8984/24/7/075401.
- [17] Stephen M. Foiles and Michael I. Baskes. “Contributions of the embedded-atom method to materials science and engineering”. In: *MRS Bulletin* 37.5 (2012), pp. 485–491. DOI: 10.1557/mrs.2012.93.
- [18] C. S. Gardner and C. Radin. “The infinite-volume ground state of the Lennard-Jones potential”. In: *Journal of Statistical Physics* 20 (1979), pp. 719–724. DOI: 10.1007/BF01009521.
- [19] M. I. Baskes. “Modified embedded-atom potentials for cubic materials and impurities”. In: *Phys. Rev. B* 46 (5 1992), pp. 2727–2742. DOI: 10.1103/PhysRevB.46.2727.
- [20] V. Pontikis et al. “Near transferable phenomenological  $n$ -body potentials for noble metals”. In: *Journal of Physics: Condensed Matter* 29.355701 (2017). DOI: 10.1088/1361-648X/aa7766.
- [21] D. Vizoso, C. Deo, and R. Dingreville. “Scaling laws and stability of nano-sized defect clusters in niobium via atomistic simulations and statistical analysis”. In: *Journal of Materials Science* 54 (2019), pp. 14002–14028. DOI: 10.1007/s10853-019-03885-y.
- [22] D. Vizoso and C. Deo. “Determination of vacancy formation energies in binary UZr alloys using special quasirandom structure methods”. In: *Frontiers in Materials* 8.692660 (2021). DOI: 10.3389/fmats.2021.692660.
- [23] E.Y. Chen, C. Deo, and R. Dingreville. “Reduced-order atomistic cascade method for simulating radiation effects in metals”. In: *Journal of Physics: Condensed Matter* 32.4 (2019). DOI: 10.1088/1361-648X/ab4b7c.
- [24] D. Vizoso et al. “Size-dependent radiation damage mechanisms in nanowires and nanoporous structures”. In: *Acta Materialia* 215.117018 (2021). DOI: 10.1016/j.actamat.2021.117018.

- [25] M. Caro et al. “Radiation induced effects on mechanical properties of nanoporous gold foams”. In: *Applied Physics Letters* 104.23 (2014), p. 233109. DOI: 10.1063/1.4882275.
- [26] L. A. Zepeda-Ruiz et al. “Deformation mechanisms of irradiated metallic nanofoams”. In: *Applied Physics Letters* 103.3 (2013), p. 031909. DOI: 10.1063/1.4813863.
- [27] J. A. Stewart and R. Dingreville. “Microstructure morphology and concentration modulation of nanocomposite thin-films during simulated physical vapor deposition”. In: *Acta Materialia* 188 (2020), pp. 181–191. DOI: 10.1016/j.actamat.2020.02.011.
- [28] A. Badillo, P. Bellon, and R. S. Averback. “A phase field model for segregation and precipitation induced by irradiation in alloys”. In: *Modelling and Simulation in Materials Science and Engineering* 23.035008 (2015). DOI: 10.1088/0965-0393/23/3/035008.
- [29] J. B. Piochaud et al. “Atomic-based phase-field method for the modeling of radiation induced segregation in Fe-Cr”. In: *Computational Materials Science* 122 (2016), pp. 249–262. DOI: 10.1016/j.commatsci.2016.05.021.
- [30] L.-Q. Chen. “Phase-field models for microstructure evolution”. In: *Annual Review of Materials Research* 32 (2002), pp. 113–140. DOI: 10.1146/annurev.matsci.32.112001.132041.
- [31] P. L. Freddolino et al. “Ten-microsecond molecular dynamics simulation of a fast-folding WW domain”. In: *Biophysical Journal* 94.10 (2008), pp. L75–L77. DOI: 10.1529/biophysj.108.131565.
- [32] M. Pasi et al. “ $\mu$ ABC: a systematic microsecond molecular dynamics study of tetranucleotide sequence effects in B-DNA”. In: *Nucleic Acids Research* 42.19 (2014), pp. 12272–12283. DOI: 10.1093/nar/gku855.
- [33] F. Soisson. “Kinetic Monte Carlo simulations of radiation induced segregation and precipitation”. In: *Journal of Nuclear Materials* 349 (2006). DOI: 10.1016/j.jnucmat.2005.11.003.
- [34] H. Matter, J. Winter, and W. Triftshäuser. “Investigation of vacancy formation and phase transformations in uranium by positron annihilation”. In: *Journal of Nuclear Materials* 88 (Feb. 1980), pp. 273–278. DOI: 10.1016/0022-3115(80)90283-4.
- [35] P. A. Korzhavyi et al. “First-principles calculations of the vacancy formation energy in transition and noble metals”. In: *Physical Review B* 59 (18 1999), pp. 11693–11703. DOI: 10.1103/PhysRevB.59.11693.

- [36] O. Le Bacq, F. Willaime, and A. Pasturel. “Unrelaxed vacancy formation energies in group-IV elements calculated by the full-potential linear muffin-tin orbital method: Invariance with crystal structure”. In: *Physical Review B* 59 (13 1999), pp. 8508–8515. DOI: 10.1103/PhysRevB.59.8508.
- [37] A. P. Moore et al. “Atomistic modeling of high temperature uranium–zirconium alloy structure and thermodynamics”. In: *Journal of Nuclear Materials* 467 (2015), pp. 802–819. DOI: 10.1016/j.jnucmat.2015.10.016.
- [38] B. Beeler et al. “First principles calculations of the structure and elastic constants of  $\alpha$ ,  $\beta$  and  $\gamma$  uranium”. In: *Journal of Nuclear Materials* 433 (2013), pp. 143–151. DOI: 10.1016/j.jnucmat.2012.09.019.
- [39] D. E. Smirnova et al. “A ternary EAM interatomic potential for U-Mo alloys with xenon”. In: *Modelling and Simulations in Materials Science and Engineering* 21 (2013). DOI: 10.1088/0965-0393/21/3/035011.
- [40] D. E. Smirnova, S. V. Starikov, and V. V. Stegailov. “Interatomic potential for uranium in a wide range of pressures and temperatures”. In: *Physical Review B* 24 (2011). DOI: 10.1088/0953-8984/24/1/015702.
- [41] S. Xiang, H. Huang, and L. Hsiung. “Quantum mechanical calculations of uranium phases and niobium defects in  $\gamma$ -uranium”. In: *Journal of Nuclear Materials* 375 (2008). DOI: 10.1016/j.jnucmat.2007.11.003.
- [42] F. Willaime and C. Massobrio. “Development of an N-body interatomic potential for hcp and bcc zirconium”. In: *Physical Review B* 43 (1991), pp. 11653–11665. DOI: 10.1103/PhysRevB.43.11653.
- [43] S. H. Wei et al. “Electronic properties of random alloys: special quasirandom structures”. In: *Physical Review B* 42 (15 1990), pp. 9622–9649. DOI: 10.1103/PhysRevB.42.9622.
- [44] A. van de Walle et al. “Efficient stochastic generation of special quasirandom structures”. In: *Calphad* 42 (2013), pp. 13–18. DOI: 10.1016/j.calphad.2013.06.006.
- [45] S. Zhao, G. M. Stocks, and Y. Zhang. “Defect energetics of concentrated solid-solution alloys from ab initio calculations:  $\text{Ni}_{0.5}\text{Co}_{0.5}$ ,  $\text{Ni}_{0.5}\text{Fe}_{0.5}$ ,  $\text{Ni}_{0.8}\text{Fe}_{0.2}$  and  $\text{Ni}_{0.8}\text{Cr}_{0.2}$ ”. In: *Physical Chemistry Chemical Physics* 18 (34 2016), pp. 24043–24056. DOI: 10.1039/C6CP05161H.
- [46] S. M. Kim. “Vacancy formation energies in disordered alloys”. In: *Physical Review B* 30 (8 1984), pp. 4829–4832. DOI: 10.1103/PhysRevB.30.4829.

- [47] A. V. Ruban. “Thermal vacancies in random alloys in the single-site mean-field approximation”. In: *Physical Review B* 93 (2016). DOI: 10.1103/PhysRevB.93.134115.
- [48] X. Zhang and M. H. F. Sluiter. “*Ab initio* prediction of vacancy properties in concentrated alloys: The case of fcc Cu-Ni”. In: *Physical Review B* 91 (2015), p. 174107. DOI: 10.1103/PhysRevB.91.174107.
- [49] A. van de Walle, M. Asta, and G. Ceder. “The alloy theoretic automated toolkit: A user guide”. In: *Calphad* 26.4 (2002), pp. 539–553. DOI: 10.1016/S0364-5916(02)80006-2.
- [50] E. del Rio et al. “Formation energy of vacancies in FeCr alloys: Dependence on Cr concentration”. In: *Journal of Nuclear Materials* 408.1 (2011), pp. 18–24. DOI: 10.1016/j.jnucmat.2010.10.021.
- [51] B. Beeler et al. “First principles calculations for defects in U”. In: *Journal of Physics: Condensed Matter* 22.50 (2010), p. 505703. DOI: 10.1088/0953-8984/22/50/505703.
- [52] SJ Zinkle. “1.03-Radiation-Induced effects on microstructure”. In: *Comprehensive Nuclear Materials* 1 (2012), pp. 65–98. DOI: 10.1016/B978-0-08-056033-5.00003-3.
- [53] M.-C. Marinica, F. Willaime, and J.-P. Crocombette. “Irradiation-induced formation of nanocrystallites with C15 laves phase structure in bcc iron”. In: *Phys. Rev. Lett.* 108.2 (2012), p. 025501. DOI: 10.1103/PhysRevLett.108.025501.
- [54] K Morishita, R Sugano, and B. D. Wirth. “MD and kMC modeling of the growth and shrinkage mechanisms of helium–vacancy clusters in Fe”. In: *J. Nucl. Mater.* 323.2-3 (2003), pp. 243–250. DOI: 10.1016/j.jnucmat.2003.08.019.
- [55] F. Soisson et al. “Atomistic kinetic Monte Carlo studies of microchemical evolutions driven by diffusion processes under irradiation”. In: *J. Nucl. Mater.* 406.1 (2010), pp. 55–67. DOI: 10.1016/j.jnucmat.2010.05.018.
- [56] I. Martin-Bragado et al. “MMonCa: An Object Kinetic Monte Carlo simulator for damage irradiation evolution and defect diffusion”. In: *Comput. Phys. Commun.* 184.12 (2013), pp. 2703–2710. DOI: 10.1016/j.cpc.2013.07.011.
- [57] T. Jourdan and J. P. Crocombette. “Rate theory cluster dynamics simulations including spatial correlations within displacement cascades”. In: *Phys. Rev. B* 86.5 (2012), p. 054113. DOI: 10.1103/PhysRevB.86.054113.

- [58] N. M. Ghoniem et al. “On dislocation interaction with radiation-induced defect clusters and plastic flow localization in fcc metals”. In: *Philos. Mag. A* 81.11 (2001), pp. 2743–2764. DOI: 10.1080/01418610108216667.
- [59] A. Arsenlis et al. “A dislocation dynamics study of the transition from homogeneous to heterogeneous deformation in irradiated body-centered cubic iron”. In: *Acta Mater.* 60.9 (2012), pp. 3748–3757. DOI: 10.1016/j.actamat.2012.03.041.
- [60] M. A. Cerdeira et al. “*Ab initio* simulations of the structure, energetics and mobility of radiation-induced point defects in bcc Nb”. In: *J. Nucl. Mater.* 478 (2016), pp. 185–196. DOI: 10.1016/j.jnucmat.2016.06.013.
- [61] P. M. Derlet, D. Nguyen-Manh, and S. L. Dudarev. “Multiscale modeling of crowdion and vacancy defects in body-centered-cubic transition metals”. In: *Phys. Rev. B* 76.5 (2007), p. 054107. DOI: 10.1103/PhysRevB.76.054107.
- [62] D. Nguyen-Manh, A. P. Horsfield, and S. L. Dudarev. “Self-interstitial atom defects in bcc transition metals: Group-specific trends”. In: *Phys. Rev. B* 73.2 (2006), p. 020101. DOI: 10.1103/PhysRevB.73.020101.
- [63] Z. Bangwie et al. “An analytic MEAM model for all BCC transition metals”. In: *Physica B Condens. Matter* 262.3-4 (1999), pp. 218–225. DOI: 10.1016/S0921-4526(98)01156-9.
- [64] D. Farkas and C. Jones. “Interatomic potentials for ternary Nb-Ti-Al alloys”. In: *Model. Simul. Mater. Sci. Eng.* 4.1 (1996), p. 23. DOI: 10.1088/0965-0393/4/1/004.
- [65] Y. N. Osetsky et al. “Structure and properties of clusters of self-interstitial atoms in fcc copper and bcc iron”. In: *Philos. Mag.* 80.9 (2000), pp. 2131–2157. DOI: 10.1080/01418610008212155.
- [66] L. Dézerald et al. “Stability of self-interstitial clusters with C15 Laves phase structure in iron”. In: *J. Nucl. Mater.* 449.1-3 (2014), pp. 219–224. DOI: 10.1016/j.jnucmat.2014.02.012.
- [67] R. Alexander et al. “*Ab initio* scaling laws for the formation energy of nanosized interstitial defect clusters in iron, tungsten, and vanadium”. In: *Phys. Rev. B* 94.2 (2016), p. 024103. DOI: 10.1103/PhysRevB.94.024103.
- [68] Y. N. Osetsky et al. “Computer simulation of vacancy and interstitial clusters in bcc and fcc metals”. In: *J. Nucl. Mater.* 251 (1997), pp. 34–48. DOI: 10.1016/S0022-3115(97)00255-9.

- [69] A. R. Akbarzadeh, Z. Z. Chen, and N. Kioussis. “Crucial role of surface in stability and mobility of vacancy clusters in metals”. In: *Phys. Rev. B* 79.19 (2009), p. 195404. DOI: 10.1103/PhysRevB.79.195404.
- [70] A. K. Bandyopadhyay and S. K. Sen. “Calculation of self-interstitial formation energy (both split and non-split) in noble metals”. In: *Phys. Status Solidi B* 157.2 (1990), pp. 519–530. DOI: 10.1002/pssb.2221570204.
- [71] J. M. Harder and D. J. Bacon. “The structure of small interstitial clusters in b.c.c. metals modelled with  $N$ -body potentials”. In: *Philos. Mag. A* 58.1 (1988), pp. 165–178. DOI: 10.1080/01418618808205181.
- [72] W. Hu, X. Shu, and B. Zhang. “Point-defect properties in body-centered cubic transition metals with analytic EAM interatomic potentials”. In: *Comput. Mater. Sci.* 23.1-4 (2002), pp. 175–189. DOI: 10.1016/S0927-0256(01)00238-5.
- [73] D.R. Mason, D. Nguyen-Manh, and C.S. Becquart. “An empirical potential for simulating vacancy clusters in tungsten”. In: *J. Phys. Condens. Matter* 29.50 (2017), p. 505501. DOI: 10.1088/1361-648X/aa9776.
- [74] J. Marian et al. “Dynamics of self-interstitial cluster migration in pure  $\alpha$ -Fe and Fe-Cu alloys”. In: *Phys. Rev. B* 65.14 (2002), p. 144102. DOI: 10.1103/PhysRevB.65.144102.
- [75] Y. N. Osetsky et al. “Stability and mobility of defect clusters and dislocation loops in metals”. In: *J. Nucl. Mater.* 276.1-3 (2000), pp. 65–77. DOI: 10.1016/S0022-3115(99)00170-1.
- [76] N. Soneda and T. Diaz de la Rubia. “Migration kinetics of the self-interstitial atom and its clusters in bcc Fe”. In: *Philos. Mag. A* 81.2 (2001), pp. 331–343. DOI: 10.1080/01418610108214307.
- [77] S. Uniyal et al. “Divacancy binding energy, formation energy and surface energy of bcc transition metals using MEAM potentials”. In: vol. 1728. 1. 2016, p. 020194. DOI: 10.1063/1.4946245.
- [78] X. T. Zu et al. “Properties of helium defects in bcc and fcc metals investigated with density functional theory”. In: *Phys. Rev. B* 80.5 (2009), p. 054104. DOI: 10.1103/PhysRevB.80.054104.
- [79] T. Muroga. *Structural Materials for Generation IV Nuclear reactors*. Ed. by P. Yvon. Woodhead Publishing, 2017.
- [80] R. H. Cooper Jr. “Potential refractory alloy requirements for space nuclear reactors”. In: *Refractory Alloy Technology for Space Nuclear Power Applications*. Ed.

- by R.H. Cooper Jr. and E. E. Hoffman. Vol. CONF-8308130. Oak Ridge National Laboratories. Oak Ridge, TN, 1984, pp. 14–17.
- [81] S. J. Zinkle and F. W. Wiffen. “Radiation effects in refractory alloys”. In: *STAI/F 2004*. Ed. by M. S. El-Genk. Vol. 699. AIP Conference Proceedings. 2004, pp. 733–740.
  - [82] J. T. Busby and K. J. Leonard. “Space fission reactor structure materials: choices past, present, and future”. In: *JOM* 59.4 (2007), pp. 20–26. DOI: 10.1007/s11837-007-0049-9.
  - [83] S. J. Zinkle, F. W. Wiffen, and J. R. DiStefano. *Historical basis for selection of Nb-1Zr cladding for space reactor applications*. Tech. rep. TN Report ORNL/LTR/NR-JIMO/04-05. Oak Ridge, TN: Oak Ridge National Laboratories, 2004.
  - [84] M. S. El-Genk and J. Tournier. “A review of refractory metal alloys and mechanically alloyed-oxide dispersion strengthened steels for space nuclear power systems”. In: *J. Nucl. Mater.* 340.1 (2005), pp. 93–112. DOI: 10.1016/j.jnucmat.2004.10.118.
  - [85] F. W. Wiffen. “Effects of irradiation on properties of refractory alloys with emphasis on space power reactor applications”. In: *Refractory Alloy Technology for Space Nuclear Power Applications*. Ed. by R. H. Cooper Jr. and E. E. Hoffman. CONF-8308130. Oak Ridge National Laboratories. Oak Ridge, TN, 1984, pp. 252–277.
  - [86] K. D. Weaver. *GenIV Nuclear Energy Systems Gas-Cooled Fast Reactor (GFR) FY-04 Annual Report*. Tech. rep. INEEL/EXT-04-02361. Idaho Falls, ID: Idaho National Engineering and Environmental Laboratory, 2004.
  - [87] L. J. Pionke and J. W. Davis. *Technical Assessment of Niobium Alloys Data Base for Fusion Reactor Applications*. Tech. rep. C00-4247-2. McDonnell Douglas, 1979.
  - [88] S.J. Zinkle. “Advanced materials for fusion technology”. In: *Fusion Engineering and Design* 74.1-4 (2005), pp. 31–40. DOI: 10.1016/j.fusengdes.2005.08.008.
  - [89] A. Y. Dunn et al. “A rate theory study of helium bubble formation and retention in Cu-Nb nanocomposites”. In: *J. Nucl. Mater.* 435.1-3 (2013), pp. 141–152. DOI: 10.1016/j.jnucmat.2012.12.041.
  - [90] A. Dunn et al. “Synchronous parallel spatially resolved stochastic cluster dynamics”. In: *Comput. Mater. Sci.* 120 (2016), pp. 43–52. DOI: 10.1016/j.commatsci.2016.04.013.

- [91] M. R. Fellingner, H. Park, and J. W. Wilkins. “Force-matched embedded-atom method potential for niobium”. In: *Phys. Rev. B* 81.14 (2010), p. 144119. DOI: 10.1103/PhysRevB.81.144119.
- [92] D. Finkenstadt et al. “Vibrational modes and diffusion of self-interstitial atoms in body-centered-cubic transition metals: a tight-binding molecular-dynamics study”. In: *Phys. Rev. B* 74.18 (2006), p. 184118. DOI: 10.1103/PhysRevB.74.184118.
- [93] G. J. Ackland and R. Thetford. “An improved N-body semi-empirical model for body-centered cubic transition metals”. In: *Philos. Mag. A* 56.1 (1987), pp. 15–30. DOI: 10.1080/01418618708204464.
- [94] S. Plimpton. “Fast parallel algorithms for short-range molecular dynamics”. In: *J. Comput. Phys.* 117.1 (1995), pp. 1–19. DOI: 10.1006/jcph.1995.1039.
- [95] L. Zhang et al. “Liquid-phase thermodynamics and structures in the Cu-Nb binary system”. In: *Model. Sim. Mater. Sci. Eng.* 21.2 (2013), p. 025005. DOI: 10.1088/0965-0393/21/2/025005.
- [96] M. J. Demkowicz and R. G. Hoagland. “Simulations of collision cascades in Cu-Nb layered composites using an EAM interatomic potential”. In: *Int. J. Appl. Mech.* 1.3 (2009), pp. 421–442. DOI: 10.1142/S1758825109000216.
- [97] R. A. Johnson and D. J. Oh. “Analytic embedded atom method model for bcc metals”. In: *J. Mater. Res.* 4.5 (1989), pp. 1195–1201. DOI: 10.1557/JMR.1989.1195.
- [98] Erin Hayward and Chaitanya Deo. “Energetics of small hydrogen–vacancy clusters in bcc iron”. In: *J. Phys. Condens. Matter* 23.42 (2011), p. 425402. DOI: 10.1088/0953-8984/23/42/425402.
- [99] Nicholas Metropolis et al. “Equation of state calculations by fast computing machines”. In: *J. Chem. Phys.* 21.6 (1953), pp. 1087–1092. DOI: 10.1063/1.1699114.
- [100] Günther Leibfried and Nikolaus Breuer. *Point defects in metals I: introduction to the theory*. Vol. 81. Springer, 2006.
- [101] A. Stukowski. “Visualization and analysis of atomistic simulation data with OVITO - the Open Visualization Tool”. In: *Modelling and Simulation in Materials Science and Engineering* 18.1 (2010). DOI: 10.1088/0965-0393/18/1/015012.
- [102] H. Xu et al. “Solving the puzzle of <100> interstitial loop formation in bcc iron”. In: *Phys. Rev. Lett.* 110.26 (2013), p. 265503. DOI: 10.1103/PhysRevLett.110.265503.



- [103] D. R. Mason et al. “Relaxation volumes of microscopic and mesoscopic irradiation-induced defects in tungsten”. In: *Journal of Applied Physics* 126 (7 2019). DOI: 10.1063/1.5094852.
- [104] Ian Jolliffe. *Principal component analysis*. Springer, 2011. DOI: 10.1007/978-3-642-04898-2\_455.
- [105] M. J. Demkowicz et al. “The effect of excess atomic volume on He bubble formation at fcc-bcc interfaces”. In: *Appl. Phys. Lett.* 97.16 (2010), p. 161903. DOI: 10.1063/1.3502594.
- [106] A. Kashinath and M. J. Demkowicz. “A predictive interatomic potential for He in Cu and Nb”. In: *Modelling and Simulation in Materials Science and Engineering* 19.035997 (2011). DOI: 10.1088/0965-0393/19/3/035007.
- [107] K Morishita et al. “Thermal stability of helium–vacancy clusters in iron”. In: *Nucl. Instrum. Methods Phys. Res. B* 202 (2003), pp. 76–81. DOI: 10.1016/S0168-583X(02)01832-3.
- [108] A. Dunn et al. “Identification of dominant damage accumulation processes at grain boundaries during irradiation in nanocrystalline  $\alpha$ -Fe: A statistical study”. In: *Acta Materialia* 110 (2016), pp. 306–323. DOI: 10.1016/j.actamat.2016.03.026.
- [109] A.V. Krashenninnikov and K. Nordlund. “Ion and electron irradiation-induced effects in nanostructured materials”. In: *Journal of Applied Physics* 107.071301 (2010). DOI: 10.1063/1.3318261.
- [110] J. Li, H. Wang, and X. Zhang. “A review on the radiation response of nanoporous metallic materials”. In: *JOM* 70 (2018), pp. 2753–2764. DOI: 10.1007/s11837-018-3111-x.
- [111] I.J. Beyerlein et al. “Radiation damage tolerant nanomaterials”. In: *Materials today* 16.11 (2013), pp. 443–440. DOI: 10.1016/j.mattod.2013.10.019.
- [112] E.M. Bringa et al. “Are nanoporous materials radiation resistant?” In: *Nano Letters* 12.7 (2011), pp. 3351–3355. DOI: 10.1021/nl201383u.
- [113] E.G. Fu et al. “Surface effects on the radiation response of nanoporous Au foams”. In: *Applied Physics Letters* 101 (2012), p. 191607. DOI: 10.1063/1.4764528.
- [114] C. Sun et al. “In situ study of defect migration kinetics in nanoporous Ag with enhanced radiation tolerance”. In: *Scientific Reports* 4 (2014), p. 3737. DOI: doi.org/10.1038/srep03737.

- [115] J. Li et al. “In situ heavy ion irradiation studies of nanopore shrinkage and enhanced radiation tolerance of nanoporous Au”. In: *Sci. Rep.* 7.1 (2017), pp. 1–10. DOI: 10.1038/srep39484.
- [116] C.J. Ruestes et al. “Nanoindentation tests of heavy-ion-irradiated Au foams—molecular dynamics simulation”. In: *J. Appl. Phys.* 123.22 (2018), p. 225903. DOI: 10.1063/1.5027191.
- [117] N.J. Briot et al. “In situ TEM investigation of self-ion irradiation of nanoporous gold”. In: *Journals of Material Science* 54 (2019), pp. 7271–7287. DOI: 10.1007/s10853-019-03385-z.
- [118] D.R. Gomes et al. “Size-dependent ion-induced densification of nanoporous gold”. In: *Scripta Mater.* 164 (2019), pp. 17–20. DOI: 10.1016/j.scriptamat.2019.01.033.
- [119] Z.Y. Hu et al. “The radiation effect of ion species on the microstructure of nanoporous gold”. In: *Scripta Mater.* 190 (2021). DOI: 10.1016/j.scriptamat.2020.08.042.
- [120] D.J. Sprouster et al. “fcc-hcp phase transformation in Co nanoparticles induced by swift heavy-ion irradiation”. In: *Phys. Rev. B* 80.11 (2009), p. 115438. DOI: 10.1103/PhysRevB.80.115438.
- [121] V. Siva et al. “Ion irradiation induced phase transition of Co in Co/Au multilayers”. In: *J. Alloys Compd.* 680 (2016), pp. 722–728. DOI: 10.1016/j.jallcom.2016.04.155.
- [122] P.K. Suri et al. “Ion irradiation induced phase transformation in gold nanocrystalline films”. In: *Sci. Rep.* 10.1 (2020), pp. 1–10. DOI: 10.1038/s41598-020-74779-2.
- [123] S. Rajasekhara, P.J. Ferreira, and K. Hattar. “Microstructural evolution of nanocrystalline nickel thin films due to high-energy heavy ion irradiation”. In: *AIP Conf. Proc.* 1525 (2013), pp. 630–635. DOI: 10.1063/1.4802404.
- [124] C. Anders, E.M. Bringa, and H.M. Urbassek. “Sputtering of a metal nanofoam by Au ions”. In: *Nuclear Instruments and Methods in Physics Research B* 342 (2015), pp. 234–239. DOI: 10.1016/j.nimb.2014.10.005.
- [125] C. G. Zhang et al. “Anti-radiation mechanisms in nanoporous gold studied via molecular dynamics simulations”. In: *Journal of Nuclear Materials* 466 (2015), pp. 328–333. DOI: 10.1016/j.jnucmat.2015.08.003.
- [126] W. Liu et al. “A molecular dynamics simulation study of irradiation induced defects in gold nanowire”. In: *Nucl. Instrum. Methods Phys. Res. B* 405 (2017), pp. 22–30. DOI: 10.1016/j.nimb.2017.05.016.

- [127] M. Zhang et al. “The effect of PKA directions on the primary radiation damage in the alpha iron nanowires”. In: *Mater. Chem. Phys.* 232 (2019), pp. 16–22. DOI: 10.1016/j.matchemphys.2019.04.038.
- [128] J. Grossi, J. Kohanoff, and E.M. Bringa. “MeV irradiation of tungsten nanowires: structural modifications”. In: *Mater. Res. Express* 7.5 (2020), p. 055015. DOI: 10.1088/2053-1591/ab9254.
- [129] D.J. Bacon, F. Gao, and Yu.N. Osetsky. “The primary damage state in fcc, bcc and hcp metals as seen in molecular dynamics simulations”. In: *J. Nucl. Mater.* 276.1-3 (2000), pp. 1–12. DOI: 10.1016/S0022-3115(99)00165-8.
- [130] A. Iwase and S. Ishino. “Comparison between radiation effects in some fcc and bcc metals irradiated with energetic heavy ions – A review”. In: *J. Nucl. Mater.* 276.1 (2000), pp. 178–185. DOI: 10.1016/S0022-3115(99)00177-4.
- [131] M. Samaras et al. “Atomic scale modelling of the primary damage state of irradiated fcc and bcc nanocrystalline metals”. In: *J. Nucl. Mater.* 351.1-3 (2006), pp. 47–55. DOI: 10.1016/j.jnucmat.2006.02.030.
- [132] S.J. Zinkle and F.W. Wiffen. “Radiation effects in refractory alloys”. In: *AIP Conference Proceedings* 699 (2004), pp. 733–740. DOI: 10.1063/1.1649637.
- [133] T. Muroga. “Refractory metals as core materials for Generation IV nuclear reactors”. In: *Structural Materials for Generation IV Nuclear Reactors*. Ed. by P. Yvon. United Kingdom: Woodhead Publishing, 2017. Chap. 11, pp. 415–441.
- [134] A. Stukowski, V.V. Bulatov, and A. Arsenlis. “Automated identification and indexing of dislocations in crystal interfaces”. In: *Modelling and Simulation in Materials Science and Engineering* 20.8 (2012). DOI: 10.1088/0965-0393/20/8/085007.
- [135] S.M. Foiles, M.I. Baskes, and M.S. Daw. “Embedded-atom-method functions for the metals Cu, Ag, Au, Ni, Pd, Pt, and their alloys”. In: *Physical Review B* 37 (1986), p. 10378.
- [136] G.J. Ackland et al. “Simple n-body potentials for the noble metals and nickel”. In: *Philosophical Magazine A* 56.6 (1987), pp. 735–756. DOI: 10.1080/01418618708204485.
- [137] J.F. Ziegler, J.P. Biersack, and U. Littmark. *The Stopping and Range of Ions in Matter, Vol. 1*. Pergamon, New York, 1985.
- [138] J.F. Ziegler, M.D. Ziegler, and J.P. Biersack. “SRIM—The stopping and range of ions in matter (2010)”. In: *Nucl. Instrum. Methods Phys. Res. B* 268.11-12 (2010), pp. 1818–1823. DOI: 10.1016/j.nimb.2010.02.091.

- [139] J.A. Stewart et al. “Characterizing single isolated radiation-damage events from molecular dynamics via virtual diffraction methods”. In: *J. Appl. Phys.* 123.16 (2018), p. 165902. DOI: 10.1063/1.5022471.
- [140] C.-W. Lee et al. “Multiscale simulations of electron and ion dynamics in self-irradiated silicon”. In: *Physical Review B* 102.024107 (). DOI: 10.1103/PhysRevB.102.024107.
- [141] R. Dingreville, J.A. Stewart, and E.Y. Chen. *Benchmark problems for the Mesoscale Multiphysics Phase Field Simulator (MEMPHIS)*. Tech. rep. SAND2020-4015. Albuquerque, NM (United States): Sandia National Laboratories, 2020. DOI: 10.2172/1615889.
- [142] A. Prakash et al. “NanoSCULPT: A methodology for generating complex realistic configurations for atomistic simulations”. In: *MethodsX* 3 (2016), pp. 219–230. DOI: 10.1016/j.mex.2016.03.002.
- [143] E. Aparicio et al. “FoamExplorer: Automated measurement of ligaments and voids for atomistic systems”. In: *Comput. Mater. Sci.* 185 (2020), p. 109942. DOI: 10.1016/j.commatsci.2020.109942.
- [144] M.T. Robinson and I.M. Torrens. “Computer simulation of atomic-displacement cascade in solids in the binary-collision approximation”. In: *Physical Review B* 9.5008 (1974). DOI: 10.1103/PhysRevB.9.5008.
- [145] K. Nordlund et al. “Improving atomic displacement and replacement calculations with physically realistic damage models”. In: *Nature Communications* 9.1084 (2018). DOI: 10.1038/s41467-018-03415-5.
- [146] W. Bauer and A.I. Anderman. “Atomic Displacement Process in Gold”. In: *Physical Review* 185.870 (1969). DOI: 10.1103/PhysRev.185.870.
- [147] M. Kosmidou et al. “Vacuum thermal dealloying of magnesium-based alloys for fabrication of nanoporous refractory metals”. In: *MRS Commun.* 9.1 (2019), pp. 144–149. DOI: 10.1557/mrc.2019.15.
- [148] D.C. Bufford and K. Hattar. “Physical response of gold nanoparticles to single self-ion bombardment”. In: *J. Mater. Res.* 29.20 (2014), pp. 2387–2397. DOI: 10.1557/jmr.2014.259.
- [149] J.A. Hinks et al. “Effects of crystallographic and geometric orientation on ion beam sputtering of gold nanorods”. In: *Sci. Rep.* 8.1 (2018), pp. 1–10. DOI: 10.1038/s41598-017-17424-9.

- [150] K. Hattar, D.C. Bufford, and D.L. Buller. “Concurrent in situ ion irradiation transmission electron microscope”. In: *Nucl. Instrum. Methods Phys. Res. B* 338 (2014), pp. 56–65. DOI: 10.1016/j.nimb.2014.08.002.
- [151] G. Greaves et al. “Enhanced sputtering yields from single-ion impacts on gold nanorods”. In: *Phys. Rev. Lett.* 111.6 (2013), p. 065504. DOI: 10.1103/PhysRevLett.111.065504.
- [152] Z. Shang et al. “In situ study on surface roughening in radiation-resistant Ag nanowires”. In: *Nanotechnology* 29.21 (2018), p. 215708. DOI: 10.1088/1361-6528/aab537.
- [153] S.A. Briggs and K. Hattar. “Evolution of gold nanoparticles in radiation environments”. In: *Gold Nanoparticles-Reaching New Heights*. IntechOpen, 2018.
- [154] W.A. Grant. “Amorphous metals and ion implantation”. In: *J. Vac. Sci. Technol.* 15.5 (1978), pp. 1644–1649. DOI: 10.1116/1.569822.
- [155] Y. Cheng et al. “Surface modification and damage of MeV-energy heavy ion irradiation on gold nanowires”. In: *Nanomaterials* 7.5 (2017), p. 108. DOI: 10.3390/nano7050108.
- [156] R.C. Rau, F.S. D’aragona, and R.L. Ladd. “Neutron damage in molybdenum irradiated at high temperatures”. In: *Philos. Mag.* 21.171 (1970), pp. 441–452. DOI: 10.1080/14786437008238430.
- [157] P.M. Rice and S.J. Zinkle. “Temperature dependence of the radiation damage microstructure in V–4Cr–4Ti neutron irradiated to low dose”. In: *J. Nucl. Mater.* 258 (1998), pp. 1414–1419. DOI: 10.1016/S0022-3115(98)00208-6.
- [158] D.E. Peacock and A.A. Johnson. “Stage III recovery in neutron irradiated molybdenum and niobium”. In: *Philos. Mag. A* 8.88 (1963), pp. 563–577. DOI: 10.1080/14786436308211156.
- [159] E. Alonso et al. “Simulation of damage production and accumulation in vanadium”. In: *J. Nucl. Mater.* 276.1-3 (2000), pp. 221–229. DOI: 10.1016/S0022-3115(99)00181-6.
- [160] I. Ipatova et al. “Structural defect accumulation in tungsten and tungsten-5wt.% tantalum under incremental proton damage”. In: *J. Nucl. Mater.* 501 (2018), pp. 329–335. DOI: 10.1016/j.jnucmat.2017.11.030.
- [161] S.E. Ferry et al. “Inferring radiation-induced microstructural evolution in single-crystal niobium through changes in thermal transport”. In: *J. Nucl. Mater.* 523 (2019), pp. 378–382. DOI: 10.1016/j.jnucmat.2019.06.015.

- [162] P. Tolédano et al. “Theory of the martensitic transformation in cobalt”. In: *Phys. Rev. B* 64.14 (2001), p. 144104. DOI: 10.1103/PhysRevB.64.144104.
- [163] D.A. Moraes et al. “Gold nanowire growth through stacking fault mechanism by oleylamine-mediated synthesis”. In: *Nanoscale* 12 (2020), p. 13316. DOI: 10.1039/d0nr03669b.
- [164] M. Ghaly and R.S. Averback. “Effect of viscous flow on ion damage near solid surfaces”. In: *Phys. Rev. Lett.* 72.3 (1994), p. 364. DOI: 10.1103/PhysRevLett.72.364.
- [165] R.C. Birtcher and S.E. Donnelly. “Plastic flow induced by single ion impacts on gold”. In: *Phys. Rev. Lett.* 77.21 (1996), p. 4374. DOI: 10.1103/PhysRevLett.77.4374.
- [166] S.E. Donnelly and R.C. Birtcher. “Heavy ion cratering of gold”. In: *Phys. Rev. B* 56.21 (1997), p. 13599. DOI: 10.1103/PhysRevB.56.13599.
- [167] R. Dingreville, J. Qu, and M. Cherkaoui. “Surface free energy and its effect on the elastic behavior of nano-sized particles, wires and films”. In: *J. Mech. Phys. Solids* 53.8 (2005), pp. 1827–1854. DOI: 10.1016/j.jmps.2005.02.012.
- [168] R. Dingreville et al. “A semi-analytical method for quantifying the size-dependent elasticity of nanostructures”. In: *Model. Simul. Mater. Sci. Eng.* 16.2 (2008), p. 025002. DOI: 10.1088/0965-0393/16/2/025002.
- [169] A. Dunn et al. “Synchronous parallel spatially resolved stochastic cluster dynamics”. In: *Computational Materials Science* (2016). DOI: 10.1016/j.commatsci.2016.04.013.
- [170] P. D. Zarnas, R. Dingreville, and J. Qu. “Mechanics of point defect diffusion near dislocations and grain boundaries: A chemomechanical framework”. In: *Computational Materials Science* 144 (2018), pp. 99–112. DOI: 10.1016/j.commatsci.2017.12.006.
- [171] Y. Kondo, Q. Ru, and K. Takaynagi. “Thickness induced structural phase transition of gold nanofilm”. In: *Physical Review Letters* 82.751 (1999). DOI: 10.1103/PhysRevLett.82.751.
- [172] A. Hasmy and E. Medina. “Thickness induced structural transition in suspended fcc metal nanofilms”. In: *Physical Review Letters* 88.096103 (2000). DOI: 10.1103/PhysRevLett.88.096103.
- [173] C. A. Volkert and E. T. Lilleodden. “Approaching the theoretical strength in nanoporous Au”. In: *Applied Physics Letters* 89.061920 (2006). DOI: 10.1063/1.2240109.

- [174] A. Johannes, H. Holland-Moritz, and C. Ronning. “Ion beam irradiation of nanostructures: sputtering, dopant incorporation, and dynamic annealing”. In: *Semiconductor Science and Technology* 30.3 (2015), p. 033001. DOI: 10.1088/0268-1242/30/3/033001.
- [175] N. Briot et al. “Irradiation of Nanoporous Gold and Niobium - Effects on Mechanical Properties”. In: *MS&T Annual Meeting*. United States, Apr. 2017.
- [176] E. Martinez, A. Caro, and I. J. Beyerlein. “Atomistic modeling of defect-induced plasticity in CuNb nanocomposites”. In: *Physical Review B* 90.054103 (2014). DOI: 10.1103/PhysRevB.90.054103.
- [177] E. Y. Chen et al. “Origin of the change in mechanical strength of silicon/gold nanocomposites during irradiation”. In: *Sci. Rep.* 11.19526 (2021). DOI: 10.1038/s41598-021-98652-y.
- [178] Y. S. Kim and R. G. Gordon. “Study of the electron gas approximation”. In: *The Journal of Chemical Physics* 60 (5 1974). DOI: 10.1063/1.1681283.
- [179] Z. Fan et al. “Stabilization of 4H hexagonal phase in gold nanoribbons”. In: *Nature Communications* 6.7684 (2015). DOI: 10.1038/ncomms8684.
- [180] Q. Wang et al. “Ultra-stable 4H-gold nanowires up to 800°C in a vacuum”. In: *Journal of Materials Chemistry A* 7 (41 2019), pp. 23812–23817. DOI: 10.1039/C9TA01306G.
- [181] P. Li et al. “Thermal effect and Rayleigh instability of ultrathin 4H hexagonal gold nanoribbons”. In: *Matter* 2 (3 2020), pp. 658–665. DOI: 10.1016/j.matt.2019.10.003.
- [182] P. R. Okamoto and L. E. Rehn. “Radiation-induced segregation in binary and ternary alloys”. In: *Journal of Nuclear Materials* (1979). DOI: 10.1016/0022-3115(79)90587-7.
- [183] Z. Jiao and G. S. Was. “Novel features of radiation-induced segregation and radiation-induced precipitation in austenitic stainless steels”. In: *Acta Materialia* (2011). DOI: 10.1016/j.actamat.2010.10.055.
- [184] C. Lu et al. “Radiation-induced segregation on defect clusters in single-phase concentrated solid-solution alloys”. In: *Acta Materialia* 127 (2017), pp. 98–107. DOI: 10.1016/j.actamat.2017.01.019.
- [185] T. R. Allen et al. “Swelling and radiation-induced segregation in austenitic alloys”. In: *Journal of Nuclear Materials* 342 (2005). DOI: 10.1016/j.jnucmat.2005.02.008.

- [186] R. S. Averback et al. “Kinetics of radiation-induced segregation in Ni-12.7 at.% Si”. In: *Physical Review B* 28.3100 (1983). DOI: 10.1103/PhysRevB.28.3100.
- [187] A. Etienne et al. “Comparison of radiation-induced segregation in ultrafine-grained and conventional 316 austenitic stainless steels”. In: *Ultramicroscopy* 111 (2011), pp. 659–663. DOI: 10.1016/j.ultramic.2010.12.026.
- [188] T. R. Allen et al. “Analyzing the effect of displacement rate on radiation-induced segregation in 304 and 316 stainless steels by examining irradiated EBR-II components and samples irradiated with protons”. In: *Journal of Nuclear Materials* 376 (2008), pp. 169–173. DOI: 10.1016/j.jnucmat.2008.01.025.
- [189] G. S. Was and T. Allen. “Radiation-induced segregation in multicomponent alloys: effect of particle type”. In: *Materials Characterization* (1994). DOI: 10.1016/1044-5803(94)90101-5.
- [190] E. Meslin et al. “Cluster-dynamics modelling of defects in  $\alpha$ -iron under cascade damage conditions”. In: *Journal of Nuclear Materials* (2008). DOI: 10.1016/j.jnucmat.2008.08.010.
- [191] J. Marian and V. V. Bulatov. “Stochastic cluster dynamics method for simulations of multispecies irradiation damage accumulation”. In: *Journal of Nuclear Materials* (2011). DOI: 10.1016/j.jnucmat.2011.05.045.
- [192] F. Christien and A. Barbu. “Cluster dynamics modelling of irradiation growth of zirconium single crystals”. In: *Journal of Nuclear Materials* (2009). DOI: 10.1016/j.jnucmat.2009.05.016.
- [193] J. Ke et al. “Cluster dynamics modeling of Mn-Ni-Si precipitates in ferritic-martensitic steel under irradiation”. In: *Journal of Nuclear Materials* (2018). DOI: 10.1016/j.jnucmat.2017.10.008.
- [194] S. Dubey and A. El-Azab. “Computational modeling of radiation-induced segregation in concentrated binary alloys”. In: *Symposium TT - Defects and Microstructure Complexity in Materials*. 2013. DOI: 10.1557/opl.2013.493.
- [195] S. Dubey and A. El-Azab. “A defect-based model of radiation-induced segregation to free surfaces in binary alloys”. In: *Computational Materials Science* (2015). DOI: 10.1016/j.commatsci.2015.04.040.
- [196] J. D. Tucker et al. “*Ab initio*-based diffusion theory and tracer diffusion in Ni-Cr and Ni-Fe alloys”. In: *Journal of Nuclear Materials* 405 (2010), pp. 216–234. DOI: 10.1016/j.jnucmat.2010.08.003.



- [197] J. P. Hirth, J. Lothe, and T. Mura. *Theory of dislocations*. Wiley, 1983. DOI: 10.1115/1.3167075.
- [198] A. Dunn et al. “Displacement rate and temperature equivalence in stochastic cluster dynamics simulations of irradiated pure  $\alpha$ -Fe”. In: *Journal of Nuclear Materials* (2016). DOI: 10.1016/j.jnucmat.2016.08.018.
- [199] Gary Was. *Fundamentals of Radiation Materials Science*. Springer-Verlag, 2007.
- [200] H. Takahashi, S. Ohnuki, and T. Takeyama. “Radiation-induced segregation at internal sinks in electron irradiated binary alloys”. In: *Journal of Nuclear Materials* 104 (1981), pp. 1415–1419. DOI: 10.1016/0022-3115(82)90798-X.
- [201] M. S. Daw and M. I. Baskes. “Semiempirical, quantum mechanical calculation of hydrogen embrittlement in metals”. In: *Physical Review Letters* 50 (1983), pp. 1285–1288. DOI: 10.1103/PhysRevLett.50.1285.
- [202] M. I. Baskes. “Atomistic model of plutonium”. In: *Physical Review B* 62 (23 2000), pp. 15532–15537. DOI: 10.1103/PhysRevB.62.15532.
- [203] M I. Baskes, J S. Nelson, and AF Wright. “Semiempirical modified embedded-atom potentials for silicon and germanium”. In: *Physical review. B, Condensed matter* 40 (Oct. 1989), pp. 6085–6100. DOI: 10.1103/PhysRevB.40.6085.
- [204] B.-N.D. Ngô et al. “Anomalous compliance and early yielding of nanoporous gold”. In: *Acta Materialia* 93 (2015), pp. 144–155. DOI: 10.1016/j.actamat.2015.04.021.